CRANFIELD UNIVERSITY

ANDREW PIDCOCK

CONTROL OF MAGNESIUM ALLOY CORROSION THROUGH THE USE OF ENGINEERED INTERMETALLICS

SCHOOL OF APPLIED SCIENCES

PhD
Academic Year: 2011-2014

Supervisors: Dr Michael Robinson, Dr Sue Impey
December 2014

CRANFIELD UNIVERSITY

SCHOOL OF APPLIED SCIENCES

PhD

Academic Year: 2011-2014

ANDREW PIDCOCK

Control of Magnesium Alloy Corrosion through the Use of Engineered Intermetallics

Supervisors: Dr Michael Robinson, Dr Sue Impey
December 2014

This thesis is submitted in partial fulfilment of the requirements for the degree of PhD

ABSTRACT

The low density and high relative strength of Mg alloys means they can offer engineering benefits over steels or Al alloys. However, the susceptibility of Mg alloys to corrosion has limited their exploitation and restricted their use to more benign environments.

An Mg-Al intermetallic surface layer is a good candidate for a robust corrosion protection method. This work demonstrates their development by using a novel ionic liquid electroplating process to deposit Al on to Mg substrates that when heat treated diffuses to form discrete intermetallic layers.

Examination of three Mg-Al-Zn alloys showed that the amount of Mg-Al intermetallic phases in their microstructures was linked to the quantity of Al they contained. Subsequent self-corrosion measurements using electrochemical impedance spectroscopy demonstrated that their performance was connected to the amount of intermetallic present, and in particular the strength of the micro-galvanic couples generated between the anodic and cathodic phases.

Measurements of the self-corrosion behaviour of manufactured samples of the Mg-Al intermetallics confirmed that they could provide significant improvements, but it was acknowledged that their noble nature compared to an Mg substrate would encourage galvanic corrosion if a surface layer was damaged. As such, the galvanic activity of the Mg-Al-Zn alloys and Mg-Al intermetallics was compared against a pure Mg standard using zero resistance ammetry and the resistance box technique. Galvanic models of alloy self-corrosion and a damaged intermetallic surface layer were also used to assess the potential problem. These measurements demonstrated that the intermetallics could act as strong cathodes, but further discussion on the nature of the behaviour suggested means by which galvanic corrosion might self-limit or self-repair.

The galvanic corrosion experiments also revealed how the combination of current flow and a solution saturated with Mg^{2+} ions could lead to the formation of a highly protective $Mg(OH)_2$ film with promising characteristics.

Keywords: magnesium, aluminium, intermetallics, electroplating, microstructure, EIS, galvanic

ACKNOWLEDGEMENTS

For your valued wisdom, expert guidance, and unwavering support.

Thank You

“Fall in love with some activity, and do it! Nobody ever figures out what life is all about, and it doesn’t matter. Explore the world. Nearly everything is really interesting if you go into it deeply enough. Work as hard and as much as you want to on the things you like to do the best. Don’t think about what you want to be, but what you want to do.”

– Richard P. Feynman

TABLE OF CONTENTS

LIST OF FIGURES

LIST OF TABLES

LIST OF EQUATIONS

LIST OF ABBREVIATIONS

AC	Alternating current
ASTM	American Society for Testing and Materials
B	Stern-Geary constant
b_a	Anodic Tafel slope
b_c	Cathodic Tafel slope
BMIm	1-butyl-3 methyl imidazolium heptachloroaluminate
C_{dl}	Double layer capacitance
CE	Counter electrode
CIP	Cold isostatic pressing
C_{pf}	Surface layer capacitance
CVD	Chemical vapour deposition
DC	Direct current
E_{anode}	Anode electrode potential
EBSD	Electron backscatter diffraction
$E_{cathode}$	Cathode electrode potential
EDX	Energy dispersive X-ray spectroscopy
EIS	Electrochemical impedance spectroscopy
EPMA	Electron probe X-ray micro analyser
FIB	Focused ion beam
HCP	Hexagonal close packed
I_{corr}	Corrosion current density
IL	Ionic liquid
IM	Intermetallic
IPA	Isopropyl alcohol
KAP	Potassium acid phthalate
LPR	Linear polarisation resistance
MAO	Micro-arc oxidation
OCP	Open circuit potential
PEO	Plasma electrolytic oxidation
PVD	Physical vapour deposition
R-box	Resistance box
R_{ct}	Charge transfer resistance
RE	Reference electrode
R_p	Polarisation resistance
R_{pf}	Surface layer resistance
R_0	Electrolyte/solution resistance
SCE	Saturated calomel electrode

SEM	Scanning electron microscope
SHE	Standard hydrogen electrode
SMAT	Surface mechanical attrition treatment
TEM	Transmission electron microscope
WE	Working electrode
XRD	X-ray diffraction
ZRA	Zero resistance ammetry
Z_ω	Warburg diffusion impedance

1 INTRODUCTION

Magnesium is one of the lightest engineering materials and as a consequence it has significant appeal to the aerospace and automotive industries, where maximising product performance is a key aim. Its density is 1.74 g/cm^3, which is under a quarter that of steel (7.86 g/cm^3) and around two thirds that of aluminium (2.70 g/cm^3). All three materials have comparable specific stiffness, but the specific strength of magnesium is more than three times that of steel and a sixth greater than aluminium [1,2]. These properties allow substantial weight savings, yield improvements in component stiffness and provide better noise, vibration, and harshness characteristics [3–12]

1.1 History and Limitations

Magnesium has been exploited by the aerospace industry since the 1940s, and one of the primary users has been the military. Its applications have included airframes and skins, wing and door structures, as well as gearbox housings, and engine and brake components [13–15]. In some cases the quantities used have reached 8600 kg, and a reported weight saving of 862 kg on one aircraft extended its range by 190 miles [14,15].

The first extensive application of Mg in the automotive industry was on the rear mounted engine of the original Volkswagen Beetle, which was conceived in the 1930s. The use of Mg alloys, instead of cast iron, for the crank case and gearbox housing resulted in an assembly that was some 50 kg lighter [16]. Mercedes-Benz achieved a claimed weight saving of 27 kg by using Mg alloys instead of comparable steel components for a seat frame, and the greater stiffness also allowed the safety belt mechanism to be incorporated into the back rest [16]. Fiat produced a single piece Mg dashboard component to replace an 18 piece steel one, resulting in a 50% weight saving as well as substantial improvements in bending and torsional stiffness [4]. Both Volkswagen and the Ford Motor Company have also developed Mg body parts in an effort to reduce vehicle weight and improve fuel efficiency [17,18].

An important considerations when designing a product is its behaviour to in-service conditions [8,17–20]. There are often clear mechanical benefits to using Mg instead of other materials, but its ‘active’ nature causes problems that are apparent from the initial material processing stages, through to component manufacture, and during its service life [16]. Magnesium alloys tend to have a corrosion resistance lower than that of Al

alloys, and as a consequence their use is restricted to relatively undemanding environments, such as shorter term military aircraft applications, component housings, or vehicle interiors, where general corrosion resistance is adequate [14,15,19,21]. In exposed locations, or when they are connected to other materials, Mg alloys must be carefully selected and treated to avoid severe corrosion problems [12,19,22–24].

1.2 Magnesium Alloys

Magnesium is available commercially with purities exceeding 99.8%, but when employed as an engineering material it is nearly always alloyed [16]. Although no international code exists for designating Mg alloys, the alphanumeric system defined by the American Society for Testing and Materials (ASTM) is often seen [25]. The first two letters of this code denote the principle alloying elements according to Table 1-1, with the element present in the greatest quantity listed first, or alphabetically when they are equal. The subsequent two numbers designate the nominal proportions of these alloying elements in wt%, rounded off to the nearest whole number. Any following letters define variations in composition within that alloy range [16,25].

Table 1-1 – Element identification letters used in the ASTM alphanumeric Mg alloy designation system [16,25].

A	Aluminium	F	Iron	M	Manganese	S	Silicon
B	Bismuth	G	Magnesium	N	Nickel	T	Tin
C	Copper	H	Thorium	P	Lead	W	Yttrium
D	Cadmium	K	Zirconium	Q	Silver	Y	Antimony
E	Rare earths	L	Lithium	R	Chromium	Z	Zinc

The various applications of Mg alloys have resulted in a wide variety of elements being incorporated to improve their physical properties, and the general effects of some of these are listed in Table 1-2.

Table 1-2 – General effects of some Mg alloying elements [16].

Alloying element	Melting and casting behaviour	Mechanical and technological properties	Corrosion behaviour
Ag	-	Improves elevated temperature tensile and creep properties in the presence of rare earths	Detrimental influence on corrosion behaviour
Al	Improves castability, tendency to micro-porosity	Solid solution hardener, precipitation hardening at low temperatures (<120°C)	Minor influence
Be	Significantly reduces oxidation of melt surface at very low concentrations (<30 ppm), leads to coarse grains	-	-
Ca	Effective grain refining effect, slight suppression of oxidation of the molten metal	Improves creep properties	Detrimental influence on corrosion behaviour
Cu	System with easily forming metallic glasses, improves castability	-	Detrimental influence on corrosion behaviour, limitation necessary
Fe	Magnesium hardly reacts with mild steel crucibles	-	Detrimental influence on corrosion behaviour, limitation necessary
Li	Increases evaporation and burning behaviour, melting only in protected and sealed furnaces	Solid solution hardener at ambient temperatures, reduces density, enhances ductility	Decreases corrosion properties strongly, coating to protect from humidity is necessary
Mn	Control of Fe content by precipitating Fe-Mn compound, refinement of precipitates	Increases creep resistance	Improves corrosion behaviour due to iron control effect
Ni	System with easily forming metallic glasses	-	Detrimental influence on corrosion behaviour, limitation necessary
Rare earths	Improves castability, reduces micro-porosity	Solid solution and precipitation hardening at ambient temperatures, improve elevated temperature tensile and creep properties	Improve corrosion behaviour
Si	Decreases castability, forms stable silicide compounds with many other alloying elements, compatible with Al, Zn, and Ag, weak grain refiner	Improves creep properties	Detrimental influence
Th	Supresses micro-porosity	Improves elevated temperature tensile and creep properties, improves ductility, most efficient alloying element	-
Y	Grain refining effect	Improves elevated temperature tensile and creep properties	Improves corrosion behaviour
Zn	Increases fluidity of the melt, weak grain refiner, tendency to micro-porosity	Precipitation hardening, improves strength at ambient temperatures, tendency to brittleness and hot shortness unless Zr refined	Minor influence, sufficient Zn content compensates for the detrimental effect of Cu
Zr	Most effective grain refiner, incompatible with Si, Al, and Mn, removes Fe, Al, and Si from the melt	Improves ambient temperature tensile properties slightly	-

Some of the most commonly used Mg alloys are those containing Al and Zn, and additions typically range between 3-10 wt% and 1-3 wt% respectively, with quantities of other elements added or limited to further enhance mechanical and corrosion properties [16,26,27]. The Mg-Al-Zn alloys AZ31B, AZ61A, and AZ91D contain approximately 3, 6, and 9 wt% Al respectively and all have around 1 wt% Zn. Table 1-3 lists the ASTM composition specifications for these alloys, and also gives the forms in which they are used.

Table 1-3 – Composition breakdown for some Mg-Al-Zn alloys compiled by the author from ASTM standards [28–36].

ASTM Alloy[A]	Source[B]	Form	Al	Be	Ca	Cu	Fe	Mn	Ni	R.E.	Si	Th	Zn	Zr	Others Each	Total Others	Mg
AZ31B	ASTM B90/B90M-07	Sheet and plate	2.5-3.5	n/a	0.04	0.05	0.005	0.20-1.0	0.005	…	0.10	…	0.6-1.4	… min	…	0.30	Remainder
AZ31B	ASTM B91-07	Forgings	2.5-3.5	n/a	0.04	0.05	0.005	0.20-1.0	0.005	…	0.10	n/a	0.6-1.4	… min	n/a	0.30	Remainder
AZ31B	ASTM B107/B107M-01	Extruded bars, rods, tubes, profiles, and wires	2.5-3.5	n/a	0.04	0.05	0.005	0.20-1.0	0.005	n/a	0.10	n/a	0.6-1.4	… min	n/a	0.30	Remainder
AZ31B	ASTM B843-07	Anodes for cathodic protection	2.5-3.5	n/a	0.04	0.05	0.005	0.20-1.0	0.005	n/a	0.10	n/a	0.6-1.4	n/a	…	0.30	Remainder
AZ31D	ASTM B843-07	Anodes for cathodic protection	2.5-3.5	n/a	0.04	0.04	0.002	0.20-1.0	0.0010	n/a	0.05		0.6-1.4	n/a	0.01	0.30	Remainder
AZ61A	ASTM B91-07	Forgings	5.8-7.2	n/a	…	0.05	0.005	0.15-0.5	0.005	…	0.10	n/a	0.40-1.5	… min	n/a	0.30	Remainder
AZ61A	ASTM B107/B107M-01	Extruded bars, rods, tubes, profiles, and wires	5.8-7.2	n/a	…	0.05	0.005	0.15-0.5	0.005	n/a	0.10	n/a	0.40-1.5	…	n/a	0.30	Remainder
AZ91D	ASTM B93/B93M-09	Alloys used for die castings	8.5-9.5	0.0005-0.0015	n/a	0.03	0.004	0.17-0.40	0.001	…	0.08	n/a	0.45-0.9	n/a	0.1	…	Remainder
AZ91D	ASTM B94-07	Die castings	8.3-9.7	n/a	n/a	0.30	0.005[C]	0.15-0.50[C]	0.002	…	0.10	n/a	0.35-1.0	n/a	0.02	n/a	Remainder
AZ91E	ASTM B80-09	Sand castings	8.1-9.3	n/a	n/a	0.02	0.005[D]	0.17-0.35	0.0010	…	0.20	n/a	0.40-1.0	…	0.01	0.3	Remainder
AZ91E	ASTM B93/B93M-09	Alloy ingot for remelt to sand, permanent mould, and investment castings	8.3-9.2	n/a	n/a	0.02	0.005	0.17-0.50	0.0010	…	0.20	n/a	0.45-0.9	…	0.01	0.30	Remainder
AZ91E	ASTM B199-07	Permanent mould castings	8.1-9.3	n/a	n/a	0.02	0.005[D]	0.17-0.35	0.0010	…	0.20	n/a	0.40-1.0	…	0.01	0.30	Remainder
AZ91E	ASTM B403-07	Investment castings	8.1-9.3	n/a	n/a	0.02	0.005[D]	0.17-0.35	0.0010	…	0.20	…	0.40-1.0	…	0.01	0.30	Remainder

A - All values in weight %.
B - Included elements listed as '…' for which no specific limit is shown. Elements listed as 'n/a' were not in the specification table for that alloy.
C - If the minimum manganese limit or the maximum iron limit is not met, then the iron/manganese ratio shall not exceed 0.032.
D - If iron exceeds 0.005%, the iron to manganese ratio must not exceed 0.032.

1.3 Corrosion Behaviour

Research into improving the corrosion behaviour of Mg alloys can be split into two broad areas: modification of material composition and microstructure, and surface treatments. Work in these fields has led to significant enhancements in corrosion characteristics, and the results of both streams of research generally come together to deliver an optimised solution [12,17,18].

1.3.1 Composition and Microstructure

Some of the earliest research into Mg and its alloys established that corrosion behaviour is strongly linked to the presence of other elements, either as intended alloying components, or as undesirable impurities. Hanawalt *et al*. 1941 [26] identified three critical impurity elements — Fe, Ni, and Cu — that can significantly increase the corrosion rate of Mg if the quantities exceed particular tolerance limits. The plots in Figure 1-1 are taken from this work and show the limits to be 0.0017 wt% Fe, 0.0005 wt% Ni, and 0.1 wt% Cu when alloyed with pure Mg. These plots also show the influence of the common alloying elements Mn and Zn on the effect of each impurity. Additions of Mn and Zn do not change the tolerance limits for Fe and Cu, but they do reduce the increase in corrosion rate observed beyond their respective limits. Both Mn and Zn increase the tolerance limit for Ni and also reduce the rise in corrosion rate seen once this limit is reached. With 0.2 wt% Mn the tolerance limit for Ni rises to 0.001 wt%, and with 2.0 wt% Mn it is around 0.015 wt%. Adding Zn also had a similar effect.

The influence of alloying elements on the corrosion rate of Mg was later studied by Reichek *et al*. 1987 [27]. This research investigated the interactions that occur between elements in an alloy, and described how the tolerance limit for Fe could be defined as a 0.032 ratio with Mn. The formation of ‘sludge’ in the melts, which consisted of Fe-Al-Mn intermetallic phases, led to the conclusion than Mn had the effect of limiting the Fe content by controlling its solubility. By understanding these interactions it was possible to propose new compositional limits, the result being an alloy with a corrosion performance 10 to 100 times better than previous. Further work by Lunder *et al.* 1987 [37] established that Fe-Al precipitates were more corrosion resistant than the bulk alloy, and acted to increase the overall corrosion rate. It was also shown that additions of Mn led to the preferential formation of Fe-Al-Mn precipitates, which do not have such a significant effect.

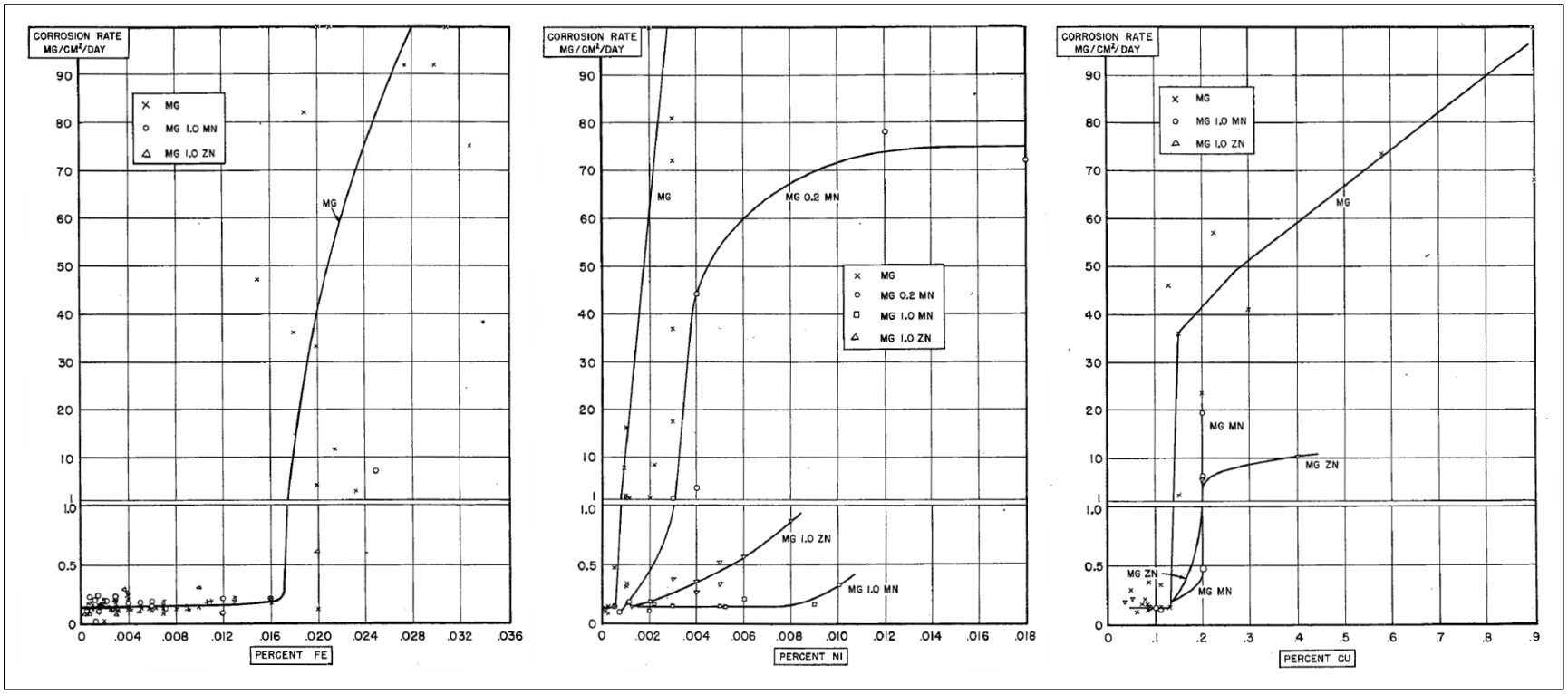

Figure 1-1 – Plots taken from Hanawalt *et al*. 1941 [26] showing the influence of Fe, Cu, and Ni on the corrosion rate of Mg. A rapid rise is observed once the quantity of each impurity element reaches a particular 'tolerance limit'. These are shown as being 0.0017 wt% Fe, 0.0005 wt% Ni, and 0.1 wt% Cu when individually alloyed with pure Mg. Additions of Mn and Zn do not change the tolerance limits for Fe and Cu, but do reduce the observed rise in corrosion once the limit is reached. Both Mn and Zn increased the tolerance limit for Ni, and also reduced the associated rise in the corrosion rate.

The concept of second phases affecting corrosion performance is important for the Mg-Al-Zn alloys AZ31B, AZ61A, and AZ91D that were mentioned in Section 1.2. The microstructures of these alloys are dominated by the Mg-Al system, and the boundaries defined by the binary phase diagram that is described later in Section 4.2.2.2. Differences in Al content and variations in processing and heat treatment lead to different microstructures, and where conditions allow the intermetallic phase $Mg_{17}Al_{12}$ can form [38–41]. This phase tends to develop more readily in AZ91D due to its higher Al content, and an example of an AZ91D microstructure containing $Mg_{17}Al_{12}$ is given in Figure 1-2. Three distinct phases can be seen: primary α-Mg and eutectic α-Mg — both Mg solid solutions containing Al — and the intermetallic $Mg_{17}Al_{12}$.

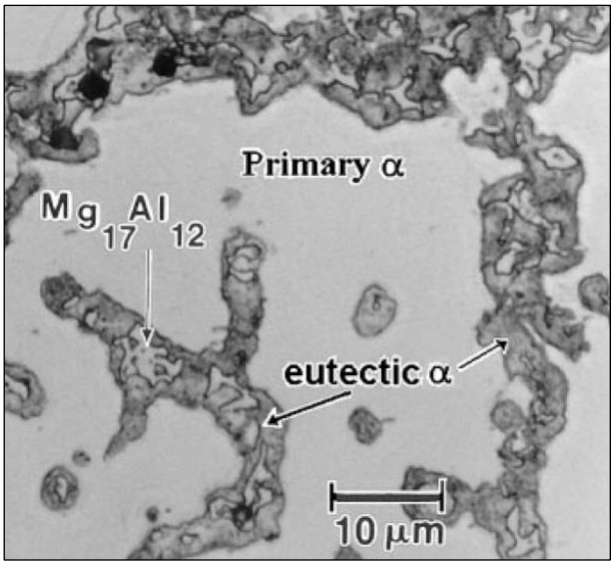

Figure 1-2 – Example of the microstructure of a die cast AZ91D Mg alloy showing three distinct phases [38].

Lunder *et al.* 1989 [42] took another step by showing that the $Mg_{17}Al_{12}$ phase in AZ91D can act to increase corrosion rate in the same manner as the Fe-Al precipitates described previously. The characteristics of Mg-Al-Zn alloy corrosion have continued to be investigated, and each study has concluded that corrosion behaviour is determined by the microstructure and the amount and distribution of $Mg_{17}Al_{12}$ [21,38,43–53].

1.3.2 Surface Treatments

Another method of improving corrosion performance is to apply a surface treatment, or coating. Gray and Luan 2002 [54] provide a comprehensive review of the multitude of protective coatings that have been used for Mg and its alloys, and their work divides these into the following categories, which are discussed further in Section 2.1.

- Electro/electrochemical deposition
- Conversion coatings
- Anodising
- Gas phase deposition processes
- Laser surface alloying and cladding
- Organic/polymer coatings

The application of coatings can significantly improve corrosion performance, but their other benefits, such as improvements to hardness and wear resistance, or an aesthetically pleasing finish, must also be considered. To ensure the most desirable properties are obtained it is not uncommon for several coating methods to be employed to create a multistep protective system.

Schreckenberger *et* al 2000 [17] shows an example of this practice in the development of a corrosion protection system for a hybrid Mg-Al component for Volkswagen. In this work fourteen different coating systems were examined and these consisted of combinations of conversion coatings, anodising, E-coatings, powder coatings, and wet painting; all of which are discussed later in Section 2.1. It was concluded that E-coating plus powder coating was most suitable for this application. A similar methodology was used by Bretz *et al 2004* [18] when investigating corrosion protection systems for a die cast Mg door for the Ford Motor Company, and this research also showed that no single method is entirely suitable. Each process has its benefits and weaknesses, and a small weakness in one part of a carefully engineered protective system can lead to rapid failure.

1.3.3 Engineered Intermetallics

The work referred to previously that described the detrimental effect of the intermetallic $Mg_{12}Al_{17}$ in Mg-Al-Zn alloys also highlighted that, when suitably distributed throughout the microstructure, it has the benefit of acting as a corrosion barrier [38,42–45,48,55]. This effect has led researchers to investigate ways of engineering Mg-Al intermetallic surface layers, with the aim of improving the corrosion properties of Mg alloys [46,56–68].

Each of the techniques developed to produce an Mg-Al intermetallic layer relies on diffusion between the Mg substrate and an Al source at its surface. In the work of Spencer & Zhang 2009 [65] a cold spray technique was used to deposit Al on an AZ91E alloy. During subsequent heat treatment at 400°C for 20 h diffusion resulted in the formation of distinct layers of Mg-Al intermetallics as shown in Figure 1-3. The rates of diffusion and the proportions of Mg and Al meant that both intermetallics — $Mg_{17}Al_{12}$ and Mg_2Al_3 (Figure 4-20) — were able to form. The voids seen between the Mg_2Al_3 layer and unreacted Al are caused by the Kirkendall effect, and are a consequence of the different diffusion rates of Mg and Al.

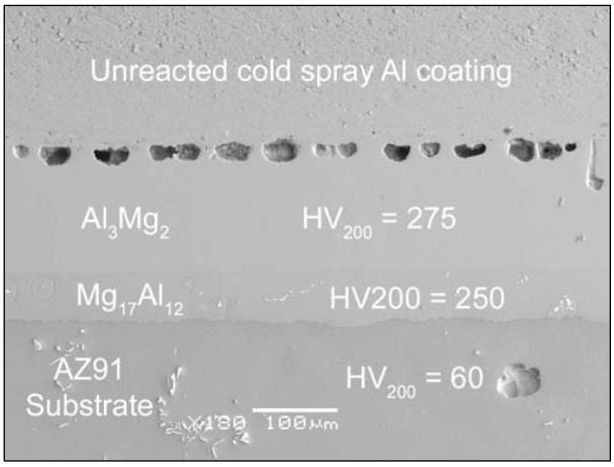

Figure 1-3 – Example of an engineered Mg-Al intermetallic layer produced by Spencer & Zhang 2009 [65] through the heat treatment of AZ91 with a thermally sprayed Al coating at 400°C for 20 h.

The use of engineered intermetallics over conventional coatings is desirable for a number of reasons, not only because of the improved corrosion performance. They also possess greater hardness and wear resistance and, as they are physically part of the material rather than simply a layer on its surface, they are likely to be more robust

and would perform better in situations where the Mg alloy was bonded to another material [65,69]. These properties mean a single intermetallic surface layer may be able to replace the complex multi-step systems that are currently used.

The attractiveness of intermetallic surface layers means numerous production techniques have been developed. A comprehensive review of these, as well as the corrosion benefits they confer, is provided later in Section 2.2. In producing these layers however, the possible consequences must not be overlooked. Research originally showed that Mg-Al intermetallic phases could be detrimental to the behaviour of an Mg alloys by causing the surrounding α-Mg solid solution to preferentially corrode. Therefore, by creating a surface layer of Mg-Al intermetallic, it is conceivable that damage penetrating through to the substrate could lead to a similar effect, and result in a severe loss of corrosion performance.

1.4 Aim and Objectives

The aim of this research is to investigate the formation of Mg-Al intermetallic surface layers on Mg substrates, and provide a comprehensive understanding of how they affect the corrosion performance of an Mg-Al-Zn alloy, both as part of its microstructure and as a protective surface layer.

The following objectives have been set:

1. To produce Mg-Al intermetallic surface layers on an Mg alloy substrate, and describe how formation and structure is controlled by changes in process parameters.

2. To analyse the microstructures of samples of the Mg-Al-Zn alloys AZ31B, AZ61A, and AZ91D, and describe how these are related to typical processing and heat treatment stages during manufacture.

3. To measure the self-corrosion behaviour of samples of the Mg-Al-Zn alloys AZ31B, AZ61A, and AZ91D, and describe how corrosion rate is linked to material microstructure and the presence of the intermetallic phase $Mg_{17}Al_{12}$.

4. To produce samples of the Mg-Al intermetallics $Mg_{17}Al_{12}$ and Mg_2Al_3, and measure their self-corrosion behaviour.

5. To compare the galvanic corrosion behaviour of samples of the Mg-Al-Zn alloys AZ31B, AZ61A and AZ91D, and the Mg-Al intermetallics $Mg_{17}Al_{12}$ and Mg_2Al_3, and use these to model the micro-galvanic component of AZ91D self-corrosion, and the galvanic effect resulting from damage to an Mg-Al intermetallic surface layer.

6. To discuss the implications the experimental findings have for the practical application of Mg-Al intermetallic layers as a means of improving Mg alloy corrosion performance.

2 LITERATURE REVIEW

Section 1.3 described how the corrosion behaviour of Mg and Mg alloys is strongly linked to composition and microstructure, and showed that a greater understanding of the effects of alloying elements has led to significant improvements in corrosion properties. However, because the corrosion resistance of Mg alloys is often still not sufficient for many applications, it is common for further enhancements to be sought through surface modification and the application of protective films and coatings [70]. As such this review examines the use of conventional surface treatments as outlined in Section 1.3.2, and discusses the current research into engineered intermetallic surface layers that were introduced in Section 1.3.3.

The electrochemical terms and techniques referred to in this section — such as open circuit potential (OCP), corrosion current density (I_{corr}), anodic/cathodic polarisation, Tafel extrapolation, electrochemical impedance spectroscopy (EIS), and charge transfer resistance (R_{ct}) — are discussed fully in Section 4.3.2.2.

2.1 Conventional Surface Treatments

This review of conventional surface treatments used for the corrosion protection of Mg and its alloys builds on the work of Gray and Luan 2002 [54], who provide a detailed discussion of the benefits and weaknesses of various techniques. Their work breaks these down into six categories — electro/electrochemical deposition, conversion coatings, anodising, gas phase deposition processes, laser surface alloying and cladding, and organic/polymer coatings — and this appraisal uses the same structure to compare the electrochemical corrosion behaviour in NaCl solution of pure Mg and Mg-Al-Zn alloys with different surface treatments.

2.1.1 Electro/Electrochemical Deposition

Electro/electrochemical deposition is described as one of the most cost effective and simplest techniques for applying a metallic coating [54]. It can be split into two types, electroplating and electroless plating, but both involve the reduction of a metal salt in solution to its metallic form on the surface of a substrate [54]. In electroplating the electrons for reduction are supplied from an external source, whereas in electroless plating they either come from a chemical reducing agent in the solution or from the substrate in the case of immersion plating [54].

2.1.1.1 Electroplating

Electroplating has been used by a number or authors to apply protective coatings to Mg-Al-Zn alloys, and the corrosion behaviours of those discussed here are summarised in Table 2-1 and also plotted alongside other surface treatments in Section 2.1.7. Other examples, which did not fit the criteria for this review, include the work of Huang *et al.* 2010 [71] and Lei *et al.* 2010 [72].

Zhao *et al*. 2010 [73] applied a Ni coating to an AZ91D alloy with a Zn immersion pretreatment. Anodic/cathodic polarisation and Tafel extrapolation yielded a substrate OCP of −1.418 V_{SCE} and I_{corr} of 1126 μA/cm^2. After Ni coating the OCP was more noble at −0.355 V_{SCE}, and I_{corr} was three orders of magnitude lower at 4.579 μA/cm^2. A three layer Cu/Ni coating (two thin Cu pretreatment layers and a Ni outer layer) was used by Huang *et al*. 2008 [74] to improve the corrosion performance of an AZ31 Mg alloy. Anodic/cathodic polarisation showed that prior to treatment the alloy had an OCP of −1.547 V_{SCE} and I_{corr} of 2000 μA/cm^2, and this shift to a more active OCP and greater I_{corr}, compared to the AZ91D examined by Zhao *et al*. 2010 [73], is consistent with what might be expected for an Mg-Al-Zn alloy with a lower concentration of more corrosion resistant Al [70]. After coating with Ni a more noble OCP of −0.297 V_{SCE} was observed and I_{corr} had reduced by two orders of magnitude to 20 μA/cm^2.

A combination of Cu and Zn pretreatments on AZ91D were employed by Zhang *et al*. 2011 [75] prior to the electrodeposition of a Ni-P coating, and anodic/cathodic polarisation and EIS were used to determine corrosion behaviour. The AZ91D substrate was shown to have an OCP of −1.62 V_{SCE} and I_{corr} of 30.67 μA/cm^2. After a single Zn pretreatment and Ni-P electrodeposition a more noble OCP of −1.45 V_{SCE} was recorded and I_{corr} was significantly greater at 6758 μA/cm^2. This

suggests that corrosion had been accelerated by galvanic interactions between the substrate and coating, which was described as rough and defective [76]. The addition of a Cu pretreatment step resulted in a more uniform layer, and shifted the OCP to −0.32 V_{SCE} and reduced I_{corr} by two orders of magnitude against AZ91D to 0.30 μA/cm^2. Although the corrosion rates measured by Zhao *et al*. 2010 [73] and Zhang *et al*. 2011 [75] for AZ91D before and after Ni electroplating are different, both show reductions of over 100 times.

Jiang *et al*. 2005 [77,78] employed a pulse plating technique to deposit a protective Zn-Ni coating on to an AZ91 Mg alloy pretreated by Zn immersion plating and Zn-Cu plating, with corrosion performance assessed by anodic/cathodic polarisation and subsequent Tafel extrapolation. The resulting OCP of −1.391 V_{SCE} is described as noble and an I_{corr} of 2620 μA/cm^2 is shown, although no information on the behaviour of the substrate is provided for comparison. The work already discussed indicates that a good Ni coating would have an OCP in the region of −0.300 V_{SCE} and an I_{corr} below 10 μA/cm^2, and so the values given by this research suggest that the presence Zn, which could introduce galvanic effects, has had a detrimental influence on coating performance [76].

Zhang *et al*. 2009 [79] electroplated various Al-Mn alloys from a molten salt at 170°C on to AZ31B that had been pretreated with a thin Zn layer. A corrosion assessment using anodic/cathodic polarisation showed that prior to treatment the AZ31B substrate had an OCP of −1.523 V_{SCE} and I_{corr} of 16 μA/cm^2. Consistent improvements were observed as the Mn content of the coating increased, with the largest proportion of Mn (29.3 wt%) yielding an OCP of −0.713 V_{SCE} and an I_{corr} four orders of magnitude lower at 0.00371 μA/cm^2.

Perhaps one of the more novel methods of improving the corrosion performance of an Mg substrate is through the electrodeposition of Al from a room temperature ionic liquid [80–82]. This technique was first reported by Chang *et al.* 2007 [83], who used the acidic ionic liquid 1-ethyl-3methyllimidazolium chloride combined with aluminium chloride ($AlCl_3$-EMIC) to coat AZ91D. Anodic/cathodic polarisation and EIS showed that the AZ91D substrate had an OCP of −1.6 V_{SCE} and I_{corr} of 24 μA/cm^2. After electroplating with Al the OCP was −1.42 V_{SCE} and I_{corr} was reduced by an order of magnitude to 2.4 μA/cm^2. These values are different to what might be expected, with an OCP of −1.02 V_{SCE} and I_{corr} of 0.5 μA/cm^2 reported for pure Al, suggesting that coating porosity might have introduced detrimental galvanic effects [76,84].

Liu *et al.* 2011 [76] also electroplated Al but used aluminium chloride and the room temperature ionic liquid trimethyl-phenyl-ammonium, or $AlCl_3$-TMPAC, to apply a coating on to AZ31. The I_{corr} of the substrate before treatment was measured as 24 μA/cm^2 but the OCP is not provided, although values below −1.5 V_{SCE} were seen earlier for this alloy. Three Al coatings were subsequently deposited using different combinations of current density and duration. The sample electroplated at 5.8 mA/cm^2 for 60 min had an OCP of −1.23 V_{SCE} and an I_{corr} of 240 mA/cm^2, which is a corrosion rate 10 times greater than the alloy alone. This was explained by galvanic effects resulting from a porous coating that allowed NaCl solution to permeate though to the substrate. With an electroplating current density of 12.3 mA/cm^2 applied for 60 min a thicker and denser coating was formed, and an OCP of −1.28 V_{SCE} and I_{corr} of 11 mA/cm^2 were recorded. An even greater reduction was seen when the plating duration was doubled to 120 min with the I_{corr} dropping by two orders of magnitude to 5.7 μA/cm^2, which is similar to those given by Chang *et al.* 2007 [83].

Table 2-1 – Table listing OCP and I_{corr} values for Mg substrates treated by various electroplating methods.

Substrate	Surface Treatment	Electrolyte	Open Circuit Potential[A] (V_{SCE})	Corrosion Rate		Reference
				Technique	Current Density[A] ($\mu A/cm^2$)	
AZ91D	None	3.5% NaCl	−1.418	Tafel	1126	Zhao et al. 2010 [73]
AZ91D	Electrodeposited Ni (Zn pretreatment)	3.5% NaCl	−0.355	Tafel	4.579	
AZ31	None	3.5% NaCl	−1.547	Tafel	2000	Huang *et al.* 2007 [74]
AZ31	Electrodeposited Ni (Cu pretreatment)	3.5% NaCl	−0.297	Tafel	20	
AZ91D	None	3.5% NaCl	−1.62	Tafel	30.67	Zhang et al. 2011 [75]
AZ91D	Electrodeposited Ni-P (Zn pretreatment)	3.5% NaCl	−1.45	Tafel	6758	
AZ91D	Electrodeposited Ni-P (Zn + Cu pretreatment)	3.5% NaCl	−0.32	Tafel	0.30	
AZ91	Pulse plated Zn-Ni (Zn and Zn-Cu pretreatments)	3.5% NaCl	−1.391	Tafel	2620	Jiang *et al.* 2005 [78]
AZ31B	None	3.5% NaCl	−1.523	Tafel	16	Zhang *et al.* 2009 [79]
AZ31B	Electrodeposited Zn	3.5% NaCl	−1.463	Tafel	202	
AZ31B	Electrodeposited Zn + Al-Mn(9.2 wt%)	3.5% NaCl	−1.276	Tafel	51.5	
AZ31B	Electrodeposited Zn + Al-Mn(22.7 wt%)	3.5% NaCl	−1.271	Tafel	0.289	
AZ31B	Electrodeposited Zn + Al-Mn(25.4 wt%)	3.5% NaCl	−1.162	Tafel	0.0259	
AZ31B	Electrodeposited Zn + Al-Mn(29.3 wt%)	3.5% NaCl	−0.713	Tafel	0.00371	
AZ91D	None	3.5% NaCl	−1.6	EIS	24[B]	Chang et al. 2007 [83]
AZ91D	Electrodeposited Al (−0.2 V)	3.5% NaCl	−1.42	EIS	2.4[B]	
AZ91D	Electrodeposited Al (−0.4 V)	3.5% NaCl	−1.52	EIS	6.0[B]	
AZ31	None	3.5% NaCl	-	EIS	24[B]	Liu et al. 2011 [76]
AZ31	Electrodeposited Al (5.8 mA/cm^2, 60 min)	3.5% NaCl	−1.23	EIS	240[B]	
AZ31	Electrodeposited Al (12.3 mA/cm^2, 60 min)	3.5% NaCl	−1.28	EIS	11[B]	
AZ31	Electrodeposited Al (12.3 mA/cm^2, 120 min)	3.5% NaCl	-	EIS	5.7[B]	

A – Where listed the value from the reference is given. Where none were available the plots from the reference were digitised and a value extrapolated.
B – Value converted from R_{ct} to I_{corr} as described in Section 4.3.2.2.

2.1.1.2 Electroless Plating

Electroless plating has also been widely explored as a means of protecting Mg-Al-Zn alloys and examples of this, which all use Ni based coating systems, are summarised in Table 2-2, with corrosion measurements plotted for comparison in Section 2.1.7. An electroless Ni-P layer with a conversion coating pretreatment was used by Huo *et al.* 2004 [85] to improve the corrosion performance of AZ91D. Anodic/cathodic polarisation and Tafel extrapolation showed that the alloy had an OCP of −1.52 V_{SCE} and I_{corr} of 14 μA/cm^2. With the electroless Ni-P coating the OCP shifted to a more noble −0.58 V_{SCE} and I_{corr} was one order of magnitude lower at 6.2 μA/cm^2. A typical OCP for Ni of around −0.300 V_{SCE} was suggested earlier and so the more active value recorded here indicates that something else, possibly the porosity that was observed in the conversion coating pretreatment, has influenced the behaviour.

Jia *et al.* 2007 [86] also applied an Ni-P treatment to AZ91D and used anodic/cathodic polarisation to assess the corrosion behaviour. In this example the bare alloy had an OCP of −1.45 V_{SCE}, while that of the coated material was more typical of a Ni layer at −0.36 V_{SCE}. A single order of magnitude reduction in corrosion rate was also recorded, with the AZ91D substrate and the Ni-P treated specimen having I_{corr} values of 5.8 μA/cm^2 and 0.25 μA/cm^2 respectively. These findings are supported by Cheong *et al.* 2007 [87], who showed similar OCPs (−0.367 to −0.463 V_{SCE}) and I_{corr} values ranging between 0.31 and 1.4 μA/cm^2 for electroless Ni-P treated AZ91D. Similar work was also described by Mahallawy *et al.* 2008 [88], although the presented corrosion behaviour results are not suitable for this comparison.

Zhang *et al.* 2008 [89] also investigated the corrosion protection of AZ91D using electroless plating, but applied a duplex Ni-P/Ni-B coating (Ni-P inner layer, Ni-B outer layer). Anodic/cathodic polarisation measurements showed that AZ91D had an OCP of −1.549 V_{SCE} and I_{corr} of 411.8 μA/cm^2, and these changed to −0.700 V_{SCE} and 3.97 μA/cm^2 (two orders of magnitude lower) with a Ni-P layer. The addition of a Ni-B layer resulted in a more active OCP of −1.063 V_{SCE} and a greater I_{corr} of 36.67 μA/cm^2, although it is reasoned that the underlying Ni-P will result in the same corrosion protection but with improvements to hardness and wear resistance from the secondary layer. A similar argument was put forward by Araghi *et al.* 2010 [90], who created a Ni-P-B_4C composite coating on AZ91D by adding B_4C particles to an Ni-P electroless plating bath. Anodic/cathodic polarisation gave an OCP and I_{corr} of −1.683 V_{SCE} and 350 μA/cm^2 respectively for AZ91D, and −0.855 V_{SCE} and 7 μA/cm^2 respectively

following Ni-P plating. An OCP of −1.078 V_{SCE} and a single order of magnitude reduction in I_{corr} to 84 μA/cm^2 were measured when the coating contained B_4C particles, but again significant improvements to hardness were also recorded.

It is also interesting to note that Huo *et al.* 2004 [85], Jia *et al.* 2007 [86], Cheong *et al.* 2007 [87], Zhang *et al.* 2008 [89], and Araghi *et al.* 2010 [90] all either observe preferential deposition on different phases of the AZ91D substrate, or acknowledge the need for a pretreatment to reduce the electrochemical heterogeneous nature of the surface [91].

Table 2-2 – Table listing OCP and I_{corr} values for Mg substrates treated by various electroless plating methods.

Substrate	Surface Treatment	Electrolyte	Open Circuit Potential[A] (V_{SCE})	Corrosion Rate		Reference
				Technique	Current Density[A] (μA/cm^2)	
AZ91D	None	3.5% NaCl	−1.52	Tafel	14	Huo *et al.* 2004 [85]
AZ91D	Chemical conversion + electroless Ni-P	3.5% NaCl	−0.58	Tafel	6.2	
AZ91D	None	3.5% NaCl	−1.45	Tafel	5.8	Jia *et al.* 2007 [86]
AZ91D	Electroless Ni-P	3.5% NaCl	−0.36	Tafel	0.25	
AZ91D	Electroless Ni-P	5% NaCl	−0.367 to −0.463	EIS	0.31 to 1.4[B]	Cheong *et al.* 2007 [87]
AZ91D	None	3% NaCl	−1.549	Tafel	411.8	Zhang et al. 2008 [89]
AZ91D	Electroless Ni-P	3% NaCl	−0.700	Tafel	3.97	
AZ91D	Electroless Ni-P/Ni-B	3% NaCl	−1.063	Tafel	36.67	
AZ91D	None	3% NaCl	−1.683	Tafel	350	Araghi et al. 2010 [90]
AZ91D	Electroless Ni-P	3% NaCl	−0.855	Tafel	7	
AZ91D	Electroless Ni-P-B_4C	3% NaCl	−1.078	Tafel	84	

A – Where listed the value from the reference is given. Where none are available the plots from the reference were digitised and a value extrapolated.
B – Value converted from R_{ct} to I_{corr} as described in Section 4.3.2.2.

2.1.2 Conversion Coatings

Gray and Luan 2002 [54] describe the production of conversion coatings as the chemical or electrochemical treatment of a metal to produce a superficial layer of substrate metal oxides, chromates, phosphates or other compounds that are chemically bonded to the surface. The corrosion behaviours of those discussed here are summarised in Table 2-3 and also compared with other surface treatments in Section 2.1.7. Other examples, which did not fit the criteria for this review, include the work of Rudd *et al.* 2000 [92], Blawert *et al.* 2007 [93], Ardelean *et al.* 2008 [94], Liu *et al.* 2010 [95], Frignani *et al.* 2010 [96], and Rocca *et al.* 2010 [97].

Huo *et al.* 2004 [85] used a stannate conversion coating as a pretreatment for electroless Ni-P plating of AZ91D, and measured its corrosion performance by anodic/cathodic polarisation. Before treatment the bare alloy had a characteristic OCP of −1.52 V_{SCE} and I_{corr} of 14 μA/cm^2, but after submerging in the stannate solution the OCP and I_{corr} were −1.43 V_{SCE} and 0.28 μA/cm^2 respectively. It is argued that the more noble OCP of the conversion coating is closer to that of the Ni-P layer (−0.58 V_{SCE}), and so reduces the driver for galvanic corrosion between Ni and the AZ91D substrate. However, as the conversion coating is acknowledged as being porous, this possible benefit may not be substantial.

Jianrui *et al.* 2006 [98] compared the corrosion performance of AZ91D with a phytic acid conversion coating and a less environmentally friendly chromate conversion treatment. The anodic/cathodic polarisation plots showed that the alloy had an OCP of −1.3110 V_{SCE} and I_{corr} of 4800 μA/cm^2, which are uncharacteristic of the more common OCP for this alloy of less than −1.5 V_{SCE} and I_{corr} values of 5 to 500 μA/cm^2. Chromate conversion provided the greatest improvements in corrosion performance with an OCP and I_{corr} of −1.1719 V_{SCE} and 2700 μA/cm^2 respectively, compared to −1.2151 V_{SCE} and 3200 μA/cm^2 for the phytic acid solution. However, compared to the bare substrate, these represent reductions of less than 50%, which is low considered other surface treatments have exhibited 2 to 3 order of magnitude improvements.

The corrosion benefits offered by four conversion coating methods — stannate, cerium oxide, chromate, and galvanic black anodising — applied to AZ31B were examined by Shashikala *et al.* 2008 [99]. Anodic/cathodic polarisation and EIS were used to assess performance, although measurements for the bare alloy were not reported. Of the four surface treatments the lowest corrosion rate was obtained with galvanic black

anodising (−0.91 V_{SCE} OCP and 4.8 μA/cm^2 I_{corr}), followed by chromate (−0.98 V_{SCE} OCP and 5.06 μA/cm^2 I_{corr}), cerium oxide (−1.09 V_{SCE} OCP and 8.05 μA/cm^2 I_{corr}), and finally stannate (−1.24 V_{SCE} OCP and 11.4 μA/cm^2 I_{corr}). A typical OCP for this substrate appears to be less than −1.5 V_{SCE}, with I_{corr} normally sitting between 10 and 1000 μA/cm^2, and so despite no results being given it is possible to conclude that corrosion rate improvements of at least one or two orders of magnitude were achieved. However, because three of the coatings are described as having cracked morphologies, their long term performance might need to be examined.

Yu *et al.* 2010 [100] investigated the corrosion behaviour of AZ91D with a calcite conversion hard coating using anodic/cathodic polarisation and EIS. Although the OCP of the bare substrate and coated material were identical (−1.48 V_{SCE}) the I_{corr} was reduced from 250 μA/cm^2 to 7 μA/cm^2, or a three order of magnitude improvement.

The effect of zirconate solution concentration on the performance of Zr conversion coatings on AZ31D was examined by Hamdy and Farahat 2010 [101] using anodic/cathodic polarisation and EIS. The bare alloy exhibited an OCP of −1.570 V_{SCE}, and this was not significantly altered by any of the treatments, with zirconate concentrations of 5, 10, 20, and 50 g/l resulting in OCPs of −1.505 V_{SCE}, −1.560 V_{SCE}, −1.557 V_{SCE}, and −1.547 V_{SCE} respectively. Compared to the bare alloy, which had an I_{corr} of 5.7 μA/cm^2, three of the zirconate solutions led to an increase in corrosion rate. After treatment with a 5 g/l concentration an I_{corr} of 9.6 μA/cm^2 was recorded, and at 10 and 50 g/l the I_{corr} was 8.6 μA/cm^2. At 20 g/l, however, the I_{corr} reduced by almost a factor of eight to 0.75 μA/cm^2, and this was attributed to a greater resistance to pit formation offered by the more uniform and compact Zr-rich oxide film. The authors also conclude that these zirconate coatings are only intended as a pretreatment, and that a final painted top coat is crucial for adequate corrosion protection.

The corrosion of AZ31 was also examined by Chen *et al.* 2011 [102], who applied a Mg-Al hydrotalcite conversion film using a two-step method. The alloy was firstly immersed in carbonic acid, to which had been added Na_2CO_3 solution saturated with Al compounds, for 30 min at 60°C. Following this pretreatment the pH of the carbonic acid mix was raised by adding NaOH and the solution was left for a further 1.5 h at 80°C to form the final Mg-Al hydrotalcite film. Anodic/cathodic polarisation was used to determine corrosion performance, and prior to treatment the alloy exhibited an OCP of −1.52 V_{SCE} and I_{corr} was 59.4 μA/cm^2. After treatment the OCP was more noble at −1.47 V_{SCE} and I_{corr} had reduced by a single order of magnitude to 4.53 μA/cm^2.

Table 2-3 – Table listing OCP and I_{corr} values for Mg substrates treated by various conversion coating methods.

Substrate	Surface Treatment	Electrolyte	Open Circuit Potential[A] (V_{SCE})	Corrosion Rate		Reference
				Technique	Current Density[A] (μA/cm^2)	
AZ91D	None	3.5% NaCl	−1.52	Tafel	14	Huo *et al.* 2004 [85]
AZ91D	Stannate	3.5% NaCl	−1.43	Tafel	0.28	
AZ91D	None	3.5% NaCl	−1.3110	Tafel	4800	Jianrui *et al.* 2005 [98]
AZ91D	Phytic acid	3.5% NaCl	−1.2151	Tafel	3200	
AZ91D	Chromate	3.5% NaCl	−1.1719	Tafel	2700	
AZ31B	Stannate	5% NaCl	−1.24	Tafel	11.4	Shashikala *et al.* 2008 [99]
AZ31B	Cerium oxide	5% NaCl	−1.09	Tafel	8.05	
AZ31B	Chromate	5% NaCl	−0.98	Tafel	5.06	
AZ31B	Galvanic black anodising	5% NaCl	−0.91	Tafel	4.8	
AZ91D	None	3.5% NaCl	−1.48	Tafel	250	Yu et al. 2010 [100]
AZ91D	Calcite ($CaCO_3$)	3.5% NaCl	−1.48	Tafel	7	
AZ31D	None	3.5% NaCl	−1.570	EIS	5.7[B]	Hamdy & Farahat 2010 [101]
AZ31D	5 g/l zirconate	3.5% NaCl	−1.505	EIS	9.6[B]	
AZ31D	10 g/l zirconate	3.5% NaCl	−1.560	EIS	8.6[B]	
AZ31D	20 g/l zirconate	3.5% NaCl	−1.557	EIS	0.75[B]	
AZ31D	50 g/l zirconate	3.5% NaCl	−1.547	EIS	8.6[B]	
AZ91D	None	0.1 M NaCl	−1.52	Tafel	59.4	Chen et al. 2011 [102]
AZ91D	Mg-Al hydrotalcite	0.1 M NaCl	−1.47	Tafel	4.53	

A – Where listed the value from the reference is given. Where none were available the plots from the reference were digitised and a value extrapolated.
B – Value converted from R_{ct} to I_{corr} as described in Section 4.3.2.2.

2.1.3 Anodising

Anodising is an electrolytic process used to produce protective oxide films on metal substrates [54,103]. This is achieved by passing a current through a component submerged in an electrolyte such that it becomes the anode in the circuit. The resulting controlled corrosion causes the growth of an oxide surface film that is thicker, and more stable, than the native oxide that would normally form [54]. Anodised magnesium films are characterised by a porous oxide surface layer, the depth of which is determined by the type of electrolyte, its concentration and temperature, and the magnitude of the current density and applied voltage [54,104]. The porous structure means sealing is necessary to ensure good corrosion resistance, and this can be achieved through the precipitation of hydrated base metal species inside the pores by boiling in water, steam treatment, dichromate sealing, or lacquer sealing [54,104]. As with the surface treatments already discussed it in known that enhanced corrosion can occur if the coating contains defects [54]. The corrosion performances of anodised materials taken from the work examined here are summarised in Table 2-4 and also discussed alongside other surface treatments in Section 2.1.7. Other examples, which did not fit the criteria for this review, include the work of Shi *et al.* 2006 [105], Hino *et al.* 2008 [106], and Ardelean *et al.* 2009 [107].

Manavbasi and Nibhanupudi 2011 [108] produced anodised films on AZ31B using an alkaline-silicate electrolyte containing different amounts of an unspecified organic additive at 150 V and constant current of 70 A. Corrosion behaviour was assessed by anodic/cathodic polarisation, which showed that the alloy had an OCP of −1.49 V_{SCE} and I_{corr} of 6520 μA/cm^2. Without the organic additive the anodising treatment yielded a more active OCP (−1.56 V_{SCE}) and a two order of magnitude reduction in I_{corr} (31.8 μA/cm^2). With 0.2% organic additive the OCP of the anodised alloy was −1.54 V_{SCE} and I_{corr} was 28.5 μA/cm^2, and with 0.8% the OCP became −1.51 V_{SCE} and I_{corr} dropped to 12.4 μA/cm^2. The lower corrosion rates associated with the organic additive were explained by a reduction in the size of the pores in the anodised film.

Plasma electrolytic oxidation (PEO), also known as micro-arc oxidation (MAO), is a modification to the anodising process that uses higher voltages to breakdown a substrate's native oxide film and replace it with a more stable one, which is formed as a result of plasma discharges at the surface [109–114]. This type of treatment was employed by Arrabal *et al.* 2008 [109], who produced a protective film on AZ91D in an

alkaline-phosphate electrolyte using a potential of around 500 V and current density of 0.3 A/cm^2. Corrosion properties were assessed by a combination of anodic/cathodic polarisation and EIS. The OCP of the bare substrate was recorded as −1.490 V_{SCE}, while that of the treated alloy was −1.569 V_{SCE}. An order of magnitude reduction in corrosion rate was also observed, with I_{corr} for the untreated AZ91D ranging from 10 to 80 µA/cm^2 and treated between 0.2 and 0.5 µA/cm^2.

Protective films were formed on AZ31B and AZ91D by Cakmak *et al.* 2010 [110] using the commercial Keronite G3M PEO process. The corrosion behaviour was investigated by anodic/cathodic polarisation and subsequent Tafel extrapolation. Before treatment AZ31B and AZ91D exhibited OCPs of −1.543 and −1.512 V_{SCE} respectively, while afterwards both saw similar noble shifts to −1.518 and −1.491 V_{SCE} respectively. Almost identical changes between the alloys were also seen for the corrosion rates, with AZ31B exhibiting an I_{corr} of 8.9 µA/cm^2 prior to treatment and 0.086 µA/cm^2 afterwards, and the I_{corr} of AZ91D also reducing by two orders of magnitude from 6.2 µA/cm^2 to 0.067 µA/cm^2.

Liu *et al.* 2012 [111] also used PEO to form protective films on AZ91D, but examined the effect of different concentrations of potassium acid phthalate (KAP) additive on those produced in a borate-biphthalate electrolyte. Corrosion performance was measured by anodic/cathodic polarisation and EIS and, although no results are given for the bare alloy, other work has shown that a typical OCP is less than −1.5 V_{SCE} and I_{corr} values range between 5 and 500 µA/cm^2. Without the KAP additive the PEO film had an OCP of −1.502 V_{SCE} and I_{corr} of 3.092 µA/cm^2, while at 2.0 g/l KAP the OCP was −1.443 V_{SCE} and I_{corr} was 1.992 µA/cm^2. At greater concentrations the behaviour appears to stabilise, with OCPs of −1.372 and −1.375 V_{SCE}, and I_{corr} values of 0.2001 and 0.2028 µA/cm^2, at 4.0 and 6.0 g/l KAP respectively. At best this treatment has led to a single order of magnitude reduction in corrosion rate. The improvements associated with the addition of KAP were explained by its ability to moderate the PEO process and allow greater control of oxide growth, resulting in the formation of a more compact film.

Table 2-4 – Table listing OCP and I_{corr} values for Mg substrates treated by various anodising methods.

Substrate	Surface Treatment	Electrolyte	Open Circuit Potential[A] (V_{SCE})	Corrosion Rate		Reference
				Technique	Current Density[A] ($\mu A/cm^2$)	
AZ31B	None	3.5% NaCl	−1.49	Tafel	6520	Manavbasi & Nibhanupudi 2011 [108]
AZ31B	Alkaline-silicate (no organic additive)	3.5% NaCl	−1.56	Tafel	31.8	
AZ31B	Alkaline-silicate (0.2% organic additive)	3.5% NaCl	−1.54	Tafel	28.5	
AZ31B	Alkaline-silicate (0.8% organic additive)	3.5% NaCl	−1.51	Tafel	12.4	
AZ91D	None	3.5% NaCl	−1.490	Tafel	10 to 80	Arrabal et al. 2008 [109]
AZ91D	Alkaline-phosphate PEO	3.5% NaCl	−1.569	Tafel	0.2 to 0.5	
AZ31B	None	3.5% NaCl	−1.543	Tafel	8.9	Cakmak et al. 2010 [110]
AZ31B	Keronite G3M PEO	3.5% NaCl	−1.518	Tafel	0.086	
AZ91D	None	3.5% NaCl	−1.512	Tafel	6.2	Cakmak et al. 2010 [110]
AZ91D	Keronite G3M PEO	3.5% NaCl	−1.491	Tafel	0.067	
AZ91D	Borate-biphthalate PEO (0.0 g/L KAP)	3.5% NaCl	−1.502	Tafel	3.092	Liu et al. 2012 [111]
AZ91D	Borate-biphthalate PEO (2.0 g/L KAP)	3.5% NaCl	−1.443	Tafel	1.992	
AZ91D	Borate-biphthalate PEO (4.0 g/L KAP)	3.5% NaCl	−1.372	Tafel	0.2001	
AZ91D	Borate-biphthalate PEO (6.0 g/L KAP)	3.5% NaCl	−1.375	Tafel	0.2028	

A – Where listed the value from the reference is given. Where none were available the plots from the reference were digitised and a value extrapolated.

2.1.4 Gas Phase Deposition

Gas phase deposition techniques include thermal spray, chemical vapour deposition (CVD), physical vapour deposition (PVD), and ion implantation. Work showing the use of CVD or PVD to protect Mg is available, but the combinations of substrate and corrosion assessment were not suitable for consideration here [115,116]. As such only the corrosion behaviours of thermal spray and ion implantation techniques are discussed, and these are summarised in Table 2-5 and also compared with other surface treatments in Section 2.1.7. Other examples, which did not fit the criteria for this review, include the work of DeForce *et al.* 2007 [12], Carboneras *et al.* 2010 [117], Tao *et al.* 2010 [118], and Li *et al.* 2010 [119].

Thermal spray can be used to produce numerous types of coatings — including metallic, ceramic, metallic/ceramic composite, or polymeric — and involves heating the coating material to near, or above, its melting point in a torch or gun and accelerating the resulting droplets onto the substrate in a high velocity gas stream [54,120]. Two complementary works, both examining the corrosion protection of 99.9% Mg and Mg-Al-Zn alloys, used a thermal spray technique to deposit Al (Pardo *et al.* 2009 [121]) and Al/SiC composite (Pardo *et al.* 2009 [122]) powders. Anodic/cathodic polarisation showed that without a coating 99.9% Mg had an OCP of −1.527 to −1.55 V_{SCE} and I_{corr} of between 4410 and 5275 μA/cm^2, the OCP of AZ31 was between −1.46 and −1.497 V_{SCE} and I_{corr} between 250 and 376 μA/cm^2, and AZ91D had an OCP of −1.53 to −1.587 V_{SCE} and I_{corr} of 43 to 68 μA/cm^2.

The application of an Al thermal spray coating resulted in a noble OCP shift in all cases, with 99.9%, AZ31, and AZ91D exhibiting potentials of −1.35, −1.34, and −1.31 V_{SCE} respectively. However, as was observed for Al electrodeposition in Section 2.1.1.1, these OCP values are more active than that of the −1.02 V_{SCE} measured for pure Al [84]. Similarly the I_{corr} magnitudes were not a low as the 0.5 μA/cm^2 that might be expected, with values of 629, 1245, and 463 μA/cm^2 given for 99.9%, AZ31, and AZ91D respectively [84]. This again suggests that coating porosity might have introduced detrimental galvanic effects, which is also acknowledged by the authors who go on to investigate how subsequent cold isostatic pressing (CIP) can create a more compact layer structure. As a result of this further processing the recorded OCP and I_{corr} values became much closer to the expected Al values, at −1.05, −1.09, and −1.11 V_{SCE}, and 3.1, 1.7, and 1.6 μA/cm^2 respectively for 99.9%, AZ31, and AZ91D, which correspond to one to three order of magnitude reductions depending on the substrate.

The addition of SiC particles to the Al powder allowed the deposition of an Al/SiC composite coating, which is suggested might offer greater wear resistance over Al alone. With the inclusion of 5-30% by volume of SiC there was also a noble shift in OCP to between −1.387 and −1.457 V_{SCE} for 99.9% Mg, −1.357 to −1.447 V_{SCE} for AZ31, and −1.407 to −1.457 V_{SCE} for AZ91D. The I_{corr} measurements also demonstrated improvements, and values of 274 to 456 μA/cm^2 were recorded for 99.9% Mg, 173 to 1008 μA/cm^2 for AZ31, and 88 to 1529 μA/cm^2 for AZ91D. The smallest current densities all relate to the lowest SiC concentrations, which is likely to be an effect of stronger galvanic couples caused by the introduction of noble SiC

particles [123]. Samples coated with Al/SiC were also subjected to CIP, which again yielded more noble OCPs of −1.097 to −1.247 V_{SCE}, −1.147 to −1.237 V_{SCE}, and −1.167 to −1.207 V_{SCE}, and I_{corr} values of 5.4 to 31 μA/cm^2, 2.6 to 22 μA/cm^2, and 2.6 to 18 μA/cm^2, for 99.9%, AZ31, and AZ91D respectively. Although these rates are not as low as Al coating alone, they still represent reductions of between one and three orders of magnitude.

A novel process that combined thermal spray and cast infiltration was used by Zhang *et al.* 2010 [124] to apply a Zn coating to AZ91D. This involved depositing Zn onto the inner surface of a ceramic mould before filling with the alloy melt. Anodic/cathodic polarisation showed that bare AZ91D had an OCP of −1.58 V_{SCE} and I_{corr} of 2160 μA/cm^2, whereas the alloy cast with a Zn coating exhibited a less active OCP of −1.50 V_{SCE} and I_{corr} that was a single order of magnitude lower at 313 μA/cm^2.

Ion implantation is described by Gray and Luan 2002 [54] as a process that involves the exposure of a surface to beam of ionised particles, resulting in ions being embedded and neutralised at interstitial positions in the substrate to form a solid solution. Tian *et al.* 2005 [125] used nitrogen plasma ion implantation, with variations of acceleration voltage and implantation duration, as a means of improving the corrosion performance of an AZ31B Mg alloy. Before treatment the OCP of the alloy was −1.55 V_{SCE} and I_{corr} was 1734 μA/cm^2. After treatment at 20 kV for 2 h the OCP was identical but I_{corr} had risen to 3385 μA/cm^2, although no explanation for this was given. With ion implantation at 40 kV for 2 h the OCP shifted to −1.41 V_{SCE} and I_{corr} was 188 μA/cm^2, and at 40 kV for 4 h the OCP was −1.51 V_{SCE} and I_{corr} slightly greater at 257 μA/cm^2, which are both single order of magnitude reductions.

Table 2-5 – Table listing OCP and I_{corr} values for Mg substrates treated by various gas phase deposition methods.

Substrate	Surface Treatment	Electrolyte	Open Circuit Potential[A] (V_{SCE})	Corrosion Rate		Reference
				Technique	Current Density[A] ($\mu A/cm^2$)	
99.9% Mg	None	3.5% NaCl	−1.55	Tafel	4410	Pardo et al. 2009 [121]
99.9% Mg	Thermal sprayed Al	3.5% NaCl	−1.35	Tafel	629	
99.9% Mg	Thermal sprayed Al + CIP	3.5% NaCl	−1.05	Tafel	3.1	
AZ31	None	3.5% NaCl	−1.46	Tafel	376	Pardo et al. 2009 [121]
AZ31	Thermal sprayed Al	3.5% NaCl	−1.34	Tafel	1245	
AZ31	Thermal sprayed Al + CIP	3.5% NaCl	−1.09	Tafel	1.7	
AZ91D	None	3.5% NaCl	−1.53	Tafel	68	Pardo et al. 2009 [121]
AZ91D	Thermal sprayed Al	3.5% NaCl	−1.31	Tafel	463	
AZ91D	Thermal sprayed Al + CIP	3.5% NaCl	−1.11	Tafel	1.6	
99.9% Mg	None	3.5% NaCl	−1.527	Tafel	5275	Pardo et al. 2009 [122]
99.9% Mg	Thermal sprayed Al/SiC(5-30%)	3.5% NaCl	−1.387 to −1.457	Tafel	274 to 456	
99.9% Mg	Thermal sprayed Al/SiC(5-30%) + CIP	3.5% NaCl	−1.097 to −1.247	Tafel	5.4 to 31	
AZ31	None	3.5% NaCl	−1.497	Tafel	250	Pardo et al. 2009 [122]
AZ31	Thermal sprayed Al/SiC(5-30%)	3.5% NaCl	−1.357 to −1.447	Tafel	173 to 1008	
AZ31	Thermal sprayed Al/SiC(5-30%) + CIP	3.5% NaCl	−1.147 to −1.237	Tafel	2.6 to 22	
AZ91D	None	3.5% NaCl	−1.587	Tafel	43	Pardo et al. 2009 [122]
AZ91D	Thermal sprayed Al/SiC(5-30%)	3.5% NaCl	−1.407 to −1.457	Tafel	88 to 1529	
AZ91D	Thermal sprayed Al/SiC(5-30%) + CIP	3.5% NaCl	−1.167 to −1.207	Tafel	2.6 to 18	
AZ91D	None	5% NaCl	−1.58	Tafel	2160	Zhang et al. 2010 [124]
AZ91D	Thermal sprayed Zn + cast infiltration	5% NaCl	−1.50	Tafel	313	
AZ31B	None	3% NaCl	−1.55	Tafel	1734	Tian et al. 2010 [125]
AZ31B	Nitrogen ion implantation (20 kV, 2 h)	3% NaCl	−1.55	Tafel	3385	
AZ31B	Nitrogen ion implantation (40 kV, 2 h)	3% NaCl	−1.41	Tafel	188	
AZ31B	Nitrogen ion implantation (40 kV, 4 h)	3% NaCl	−1.51	Tafel	257	

A – Where listed the value from the reference is given. Where none were available the plots from the reference were digitised and a value extrapolated.

2.1.5 Laser Surface Alloying and Cladding

Laser surface alloying encompasses a number of techniques, from simple melting of the surface of an otherwise untreated material to modify its structure, to the inclusion of other elements/compounds in the melted region to create an alloyed/composite structure, or the re-melting of a coating deposited by another method to form a more adherent layer [54]. Laser cladding is similar to thermal spray techniques in that a metallic or metallic/ceramic power is heated and deposited onto a component. However, unlike thermal spray methods, the powder is fully melted with the result being lower porosity and a coating that is fully fused to the substrate [126]. The corrosion behaviours of laser treated materials in the work examined here are summarised in Table 2-6 and also discussed alongside other surface treatments in Section 2.1.7.

A laser melting technique was used by Abbas *et al.* 2005 [127] to modify the surfaces of AZ31 and AZ61 Mg alloys. Measurements of the OCP before and after treatment showed small noble shifts in both cases, with AZ31 changing from −1.585 V_{SCE} to −1.530 V_{SCE}, and AZ61 moving from −1.050 V_{SCE} to −1.030 V_{SCE}. Corrosion rate was assessed by weight loss, which indicated a 30% reduction in corrosion rate for AZ31 and a 66% drop for AZ61.

Qian *et al.* 2010 [128] laser re-melted a thermally sprayed Al-Si coating that had been applied to AZ91D. Anodic/cathodic polarisation revealed that bare AZ91D had an OCP of −1.527 V_{SCE} and I_{corr} of 65.4 μA/cm^2, while thermally sprayed Al-Si without laser re-melting exhibited a less active OCP of −1.344 V_{SCE}, and a lower I_{corr} of 23.9 μA/cm^2. After laser treatment there was a further noble shift in potential to −1.137 V_{SCE}, and I_{corr} reduced to 17.4 μA/cm^2. As seen with other methods a less porous structure reduces any galvanic interactions between the substrate and the coating, which results in better corrosion performance.

Table 2-6 –Table listing OCP and I_{corr} values for Mg substrates treated by various laser surface alloying and cladding methods.

Substrate	Surface Treatment	Electrolyte	Open Circuit Potential[A] (V_{SCE})	Corrosion Rate		Reference
				Technique	Current Density[A] ($\mu A/cm^2$)	
AZ31	None	5% NaCl	−1.585	-	-	Abbas et al. 2005 [127]
AZ31	Laser surface melting	5% NaCl	−1.530	-	-	
AZ61	None	5% NaCl	−1.050	-	-	Abbas et al. 2005 [127]
AZ61	Laser surface melting	5% NaCl	−1.030	-	-	
AZ91D	None	3.5% NaCl	−1.527	Tafel	65.4	Qian et al. 2010 [128]
AZ91D	Thermal sprayed Al-Si	3.5% NaCl	−1.344	Tafel	23.9	
AZ91D	Thermal sprayed Al-Si + laser re-melting	3.5% NaCl	−1.137	Tafel	17.4	

A – Where listed the value from the reference is given. Where none were available the plots from the reference were digitised and a value extrapolated.

2.1.6 Organic/Polymer Coatings

Gray and Luan 2002 [54] describe how organic/polymer finishes are typically used in the final stages of a coating process, and are applied to enhance corrosion resistance, abrasion and wear properties, and for decorative purposes. The methods available include painting, powder coating, and E-coating, as well as the application of lacquers, enamels, and varnishes. These can have any number of bases including acrylic, alkyd, butyrate, cellulose acetate , cellulose acetate butyrate, chlorinated polyethers, epoxies, fluorocarbons, nitrocellulose, nylon, polyesters, polyethylene, polypropylene, polyurethanes, rubber resins, silicones, and vinyls [54].

The assertion that organic/polymer treatments are used as a final protection system is also reflected in the work discussed here. A spin coating process was used by Conceicao *et al.* 2010 [129] and Conceicao *et al.* 2010 [130] to coat AZ31 with poly(ether imide) and, although this showed good corrosion performance, the correct selection of pretreatments was highlighted as an important step. E-coating is a commonly used industrial painting process, which involves the deposition of charged colloidal particles from a liquid medium. The application of a suitable electric field causes these charged particles to migrate towards a metallic surface and deposit to form a stable coating [131]. Two works by Song and Liu 2011 [132] and Song and Liu 2012 [131] demonstrated the use of a novel ‘electroless’ E-coating technique to protect Mg alloys. As well as examining the effects of various

pretreatments they also investigated how the coating's corrosion performance changed with different substrates, and they concluded that this was directly related to the corrosion resistance of the base material.

The sol-gel process is another method of protecting materials by producing polymeric networks of inorganic/organic composite layers [54]. The corrosion resistance offered by this technique is confirmed by Lamaka *et al.* 2008 [133] and Wang *et al.* 2011 [133], who examined its use to protect an AZ31 alloy. As highlighted for other methods though, careful pretreatment of the substrate was an important part of achieving good performance.

2.1.7 Summary of Conventional Surface Treatments

The electrochemical corrosion characteristics of the conventional surface treatments discussed here are summarised in the plots in Figure 2-1and Figure 2-2. These show a varying degree of corrosion performance improvements compared to the substrates, with up to three or four order of magnitude changes observed in some cases. However, the larger reductions in corrosion rate tend to be associated with much more noble OCPs. This is a concern when applied to an active material such as Mg because there is potential for severe galvanic corrosion if the protective coating is damaged. There may also be further consequences of this effect, as it could lead to less well adhered treatments becoming undermined and breaking away.

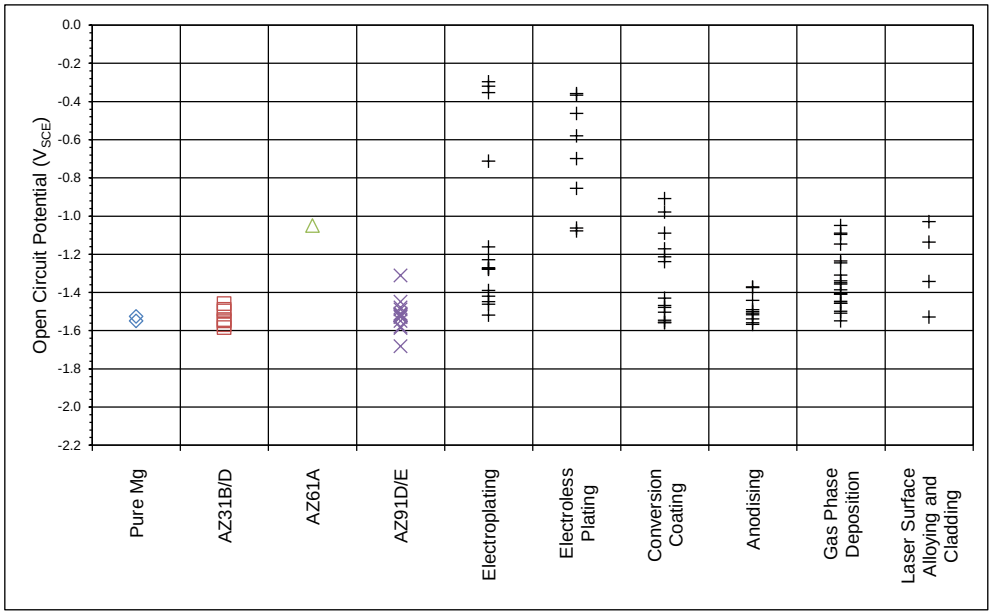

Figure 2-1 – Comparison of OCP values for the substrates and associated conventional surface treatments listed in Table 2-1, Table 2-2, Table 2-3, Table 2-4, Table 2-5, and Table 2-6.

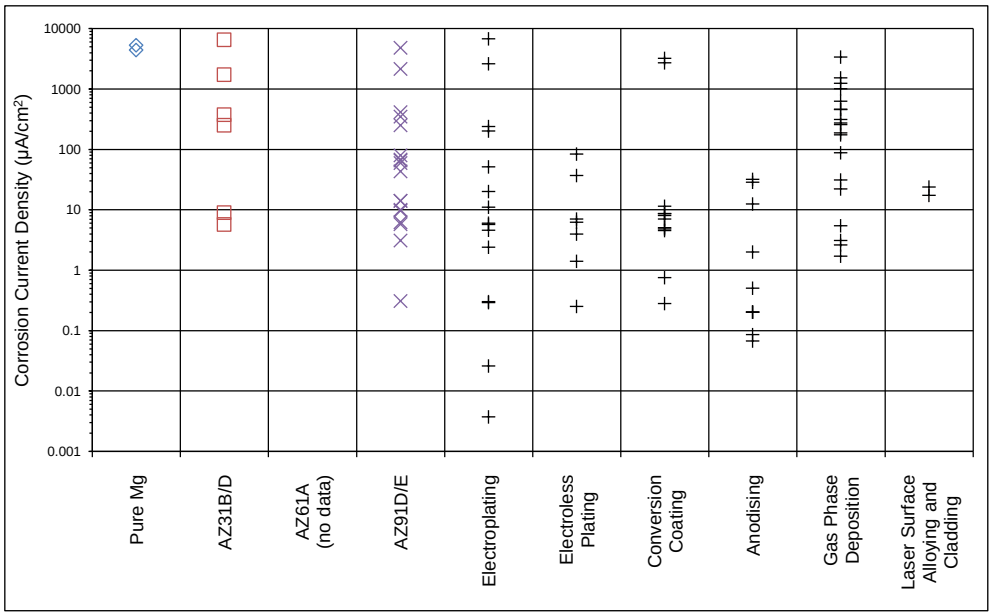

Figure 2-2 – Comparison of I_{corr} values for the substrates and associated conventional surface treatments listed in Table 2-1, Table 2-2, Table 2-3, Table 2-4, Table 2-5, and Table 2-6.

2.2 Engineered Intermetallic Surface Layers

The production of Mg-Al intermetallic (IM) surface layers on Mg and Mg alloys has been demonstrated in the literature using a number of methods, all of which involve the heating of a substrate material that has Al available at its surface. This promotes metal diffusion and, as was described in Section 1.3.3, leads to the formation of Mg-Al intermetallics when the correct compositions are reached. For the purposes of this review the various techniques used to form protective surface layers have been grouped together as follows: contact diffusion, powder diffusion, sputtering, molten salts, and electrodeposition. The structures of the layers produced by each method are examined and the corrosion protection they offer is discussed. The findings of this review are also summarised in Section 2.2.7.

2.2.1 Contact Diffusion

In this context contact diffusion is taken to mean any method where Mg and Al are simply brought together in close contact prior to undergoing heat treatment. In all the cases reviewed diffusion was achieved by applying pressure, in the range of 0.08-30 MPa, to the materials to achieve good face to face contact and then heating to 300-500°C for between 5 min and 18 h [56,57,134–138]. The aim of the majority of research on contact diffusion was to study the formation of Mg-Al phases and/or create a structural bond between two materials rather than form a protective surface layer [134–138]. The parameters used for bonding tended to be at the higher end of the temperature range (380-500°C) compared to other techniques and for shorter durations (5-100 min), with a greater emphasis on joint strength rather than the microstructure of the diffused region.

Li *et al.* 2009 [56], although still primarily concerned with bonding, looks more closely at the microstructure and goes on to discuss improvements to corrosion performance. In this example a 200 µm ‘Mg-eutectic powder solder’ is added between the pure Mg and pure Al coupons prior to heat treatment at 450°C for 1-2 h. Scanning electron microscope (SEM) and energy dispersive X-ray spectroscopy (EDX) analysis of the diffused region revealed three distinct zones, as shown in Figure 2-3, between the original Mg and Al samples consisting of a two-phase area deemed to be the eutectic solder, a layer of the $Mg_{17}Al_{12}$ intermetallic, and a layer of the Mg_2Al_3 intermetallic, which is consistent with that seen by others [134–138].

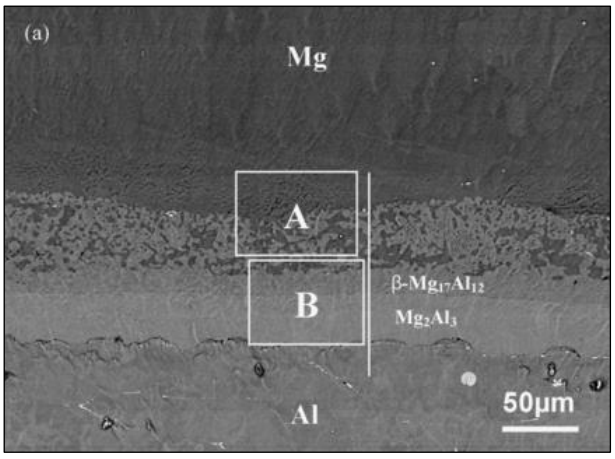

Figure 2-3 – Example of an engineered Mg-Al intermetallic layer produced by Li *et al.* 2009 [56] through the heat treatment of pure Mg in contact with pure Al foil and a Mg-Al eutectic powder solder at 450°C for 2 h.

To investigate improved corrosion properties the Al coupon was replaced by foil to create a thin bonded layer. Polarisation measurements in 5% NaCl solution were subsequently taken for pure Mg, pure Al, and Mg coated with Al foil. Pure Mg and Al exhibited OCPs of −1.250 V_{SCE} and −0.760 V_{SCE} respectively. The Mg coated with Al foil had an OCP of −0.887 V_{SCE}, which is more noble than the substrate and closer to that of pure Al. This is reflected in an I_{corr} of 0.2 μA/cm^2, which is the same as that measured for pure Al and an order of magnitude less than the 1 μA/cm^2 for the pure Mg substrate.

The work of Yang *et al.* 2011 [57] is similar to that of Li *et al.* 2009 [56] but the main theme is the use of contact diffusion as a means of improving corrosion performance. Continuous intermetallic compound coatings where produced by heat treating AZ91D that was in contact with pure Al for between 2-18 h at 300°C. X-ray diffraction (XRD), SEM and EDX analysis of a sample that had been heat treated for 6 h revealed a continuous two-layer diffusion region, as shown in Figure 2-4, consisting of $Mg_{17}Al_{12}$ and Mg_3Al_2 intermetallics similar to that described by Li *et al.* 2009 [56]. Yang *et al.* 2011 [57] also observed that the Al plate remaining at the surface was separated from the rest of the layer by voids, and could therefore be easily removed. In explaining this Yang *et al.* 2011 [57] refers to the work of Spencer & Zhang 2009 [139] who, as described later in Section 2.2.4, attribute this to the Kirkendall effect that arises from asymmetrical diffusion.

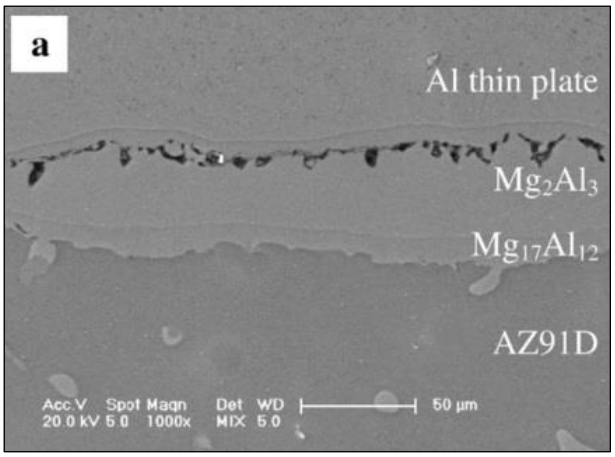

Figure 2-4 – Example of an engineered Mg-Al intermetallic layer produced by Yang *et al.* 2011 [57] through the heat treatment of AZ91D in contact with a thin Al plate at 300°C for 6 h.

Open circuit potential, anodic/cathodic polarisation, and EIS measurements were taken to compare the corrosion properties of the AZ91D substrate and the intermetallic coating. AZ91D exhibited an OCP of −1.66 V_{SCE} and I_{corr} of 5.57 µA/cm^2. This is compared to −1.29 V_{SCE} and 0.21 µA/cm^2 for the coating, which is of the same order as that measured by Li *et al.* 2009 [56]. However, Li *et al.* 2009 [56] appears to assume that the composition of the surface is Al whereas Yang *et al.* 2011 [57] highlights a weekly bonded Al layer and uses the Mg_2Al_3 intermetallic below this to compare corrosion performance.

2.2.2 Powder Diffusion

A modification to simple contact diffusion is the use of powdered material as an Al source at the surface of the substrate. There are a number of examples of the use of this method as a way of improving the corrosion performance of Mg, with variations to powder composition, application technique, and heat treatment used in an effort to improve diffusion. Shigematsu *et al.* 2000 [58] produced a 750 µm Mg-Al 'intermetallic compound layer' on AZ91D Mg alloy by heat treatment in 99.5% pure Al powder that was mixed with an unspecified amount of ZrO_2 powder to prevent sintering. The AZ91D and Al powder were then placed into an Al crucible and heated to 450°C for 1 h. Surface XRD identified α-Mg and $Mg_{17}Al_{12}$ and cross-section examination by SEM and an electron probe X-ray micro analyser (EPMA) revealed a hypoeutectic structure consisting of $Mg_{17}Al_{12}$ crystals and lamellae of α-Mg and $Mg_{17}Al_{12}$ as shown in Figure 2-5. The corrosion performance was not assessed.

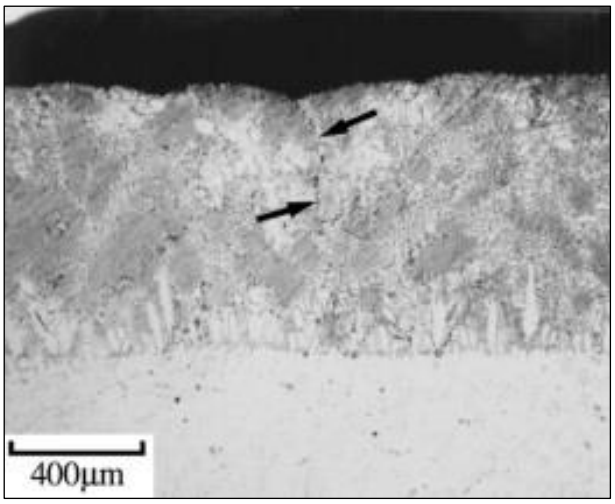

Figure 2-5 – Example of an engineered Mg-Al intermetallic layer produced by Shigematsu *et al.* 2000 [58] through the heat treatment of AZ91D in contact with Al powder at 450°C for 1 h.

The work of Zhang *et al.* 2002 [59] describes a similar process but with 30 wt% Zn added to the powder mix. A cross-section of the resulting layer formed at 430°C for 12 h is given in Figure 2-6. Subsequent electron probe analysis and XRD revealed a single layer, three component, microstructure consisting of α-Mg solid solution plus Zn, $Mg_{17}Al_{12}$ with some Al atoms replaced by Zn, and a eutectic structure of $Mg_{17}Al_{12}$ and $Al_5Mg_{11}Zn_4$. Again, no corrosion measurements were carried out.

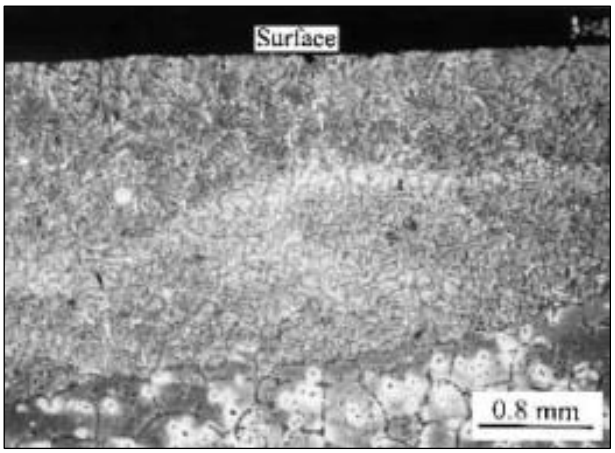

Figure 2-6 – Example of an engineered Mg-Al intermetallic layer produced by Zhang *et al.* 2002 [59] through the heat treatment of AZ91D in contact with a mixture of Al and Zn powder at 430°C for 12 h.

Zhu & Song 2006 [60] investigated the use of paste consisting of 99.5% pure Al powder and pure ethylene glycol that was painted on to AZ91D prior to it being packed in dry Al powder and heat treated. The Al/ethylene glycol paste was used to achieve better surface contact with the Mg alloy substrate, compared to dry powder alone, and evaporated once heated above 200°C. Heat treatments were carried out for 1.5 h at temperatures of 200, 300, 360, 400, 410, and 420°C, with visible but non-uniform coatings first forming at 400°C, and uniform ones at 410°C. At 420°C some localised melting began to occur, and an example of a coating formed at this temperature is shown in Figure 2-7. XRD revealed α-Mg and $Mg_{17}Al_{12}$ as the main phases, which optical analysis showed to be in the form of equiaxed grains and dendrites. The corrosion behaviour of coated and uncoated samples was assessed by anodic/cathodic polarisation and EIS measurements. These yielded an OCP of −1.627 V_{SCE} and I_{corr} of 381 μA/cm^2 for AZ91D, compared values of −1.512 V_{SCE} and 4.1 μA/cm^2 for the coating, which is a two order of magnitude improvement.

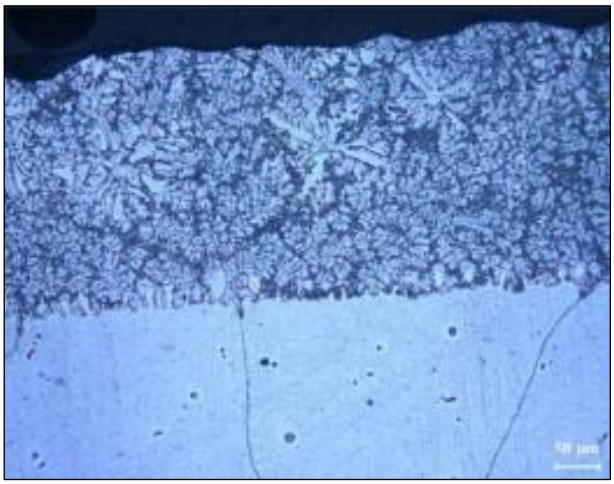

Figure 2-7 – Example of an engineered Mg-Al intermetallic layer produced by Zhu & Song 2006 [60] through the heat treatment of AZ91D in contact with a mixture of Al and Zn powder at 420°C for 1.5 h.

Liu *et al.* 2008 [61] produced a coating on a pure Mg substrate by embedding it in 99.5 wt% pure Al powder held in an iron container and heat treating at 420°C for 1.5 h. Optical microscopy, SEM, and EDX were used to determine structure and composition and the coating was described as being homogenous, dense, and free from cracks and pores. As shown in Figure 2-8 three regions were identified, and these are described as outer, inner, and transition layers. The outer layer was 50 μm deep and consisted mainly of α-Al, with a small amount of Mg_2Al_3. The inner layer had a thickness of

500 µm and a structure of mainly $Mg_{17}Al_{12}$ with precipitates of α-Mg, as well as some Mg_2Al_3. The transition layer adjacent to the Mg substrate was 20 μm thick, with greater penetration into the substrate at grain boundaries, and contained mainly α-Mg and quantities of Mg_2Al_3 but no $Mg_{17}Al_{12}$.

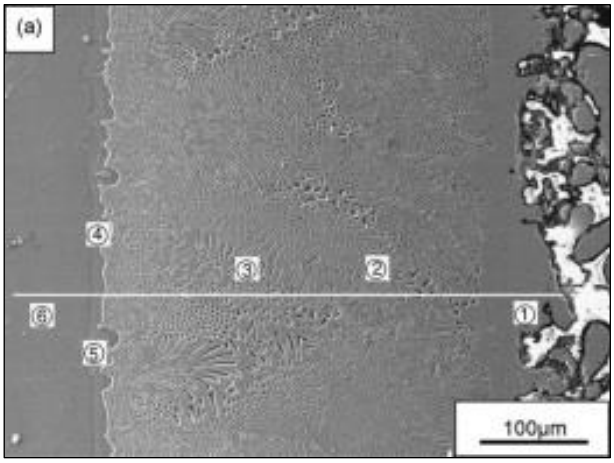

Figure 2-8 – Example of an engineered Mg-Al intermetallic layer produced by Liu *et al.* 2008 [61] through the heat treatment of pure Mg in contact with Al powder at 420°C for 1.5 h.

Corrosion properties of coated and un-coated pure Mg, as well as an AZ91 alloy for comparison, in 5% NaCl solution were all assessed using anodic/cathodic polarisation measurements. Pure Mg and AZ91 exhibited OCPs of −1.250 V_{SCE} and −1.214 V_{SCE} respectively, and I_{corr} values of 430 µA/cm^2 and 144 µA/cm^2. The coating had a more positive OCP of −0.866 V_{SCE} and an I_{corr} that was one order of magnitude lower at 51 µA/cm^2.

In a further modification Sun *et al.* 2008 [62] produced a 100-200 µm thick layer on an AZ91D substrate using a combination of surface mechanical attrition treatment (SMAT) and powder diffusion. The SMAT process involved placing an alloy sample in a room temperature chamber containing Al balls, and then vibrating it ultrasonically for 20 min. This created what was described as a nanocrystalline layer that should improve diffusion at the surface. After SMAT the alloy was buried in a powder mixture of 70 wt% Al, 25 wt% Al_2O_3, and 5 wt% Zn. The container was then topped up with a blend of foundry sand and coke to reduce oxidation during subsequent heat treatment at 400°C for 24 h. Al_2O_3 was included in the powder mixture to prevent the Al and Zn from consolidating while at temperature. The resulting surface layer was examined by optical microscopy, SEM, TEM, EDX, and XRD and, as shown in Figure 2-9, three

areas were identified. The AZ91D substrate was observed as being a single phase α-Mg solid solution, and adjacent to this was an Mg-rich region consisting of α-Mg with lamella precipitates of $Mg_{17}Al_{12}$. At the surface there was a thin Al-rich layer of $Mg_{17}Al_{12}$ with α-Mg 'island' type precipitates. The differences in structure and composition were explained by the diffusion processes that occurred during heat treatment. The presence of Zn is mentioned but was not detected by the methods used. The corrosion performance of this coating was not measured.

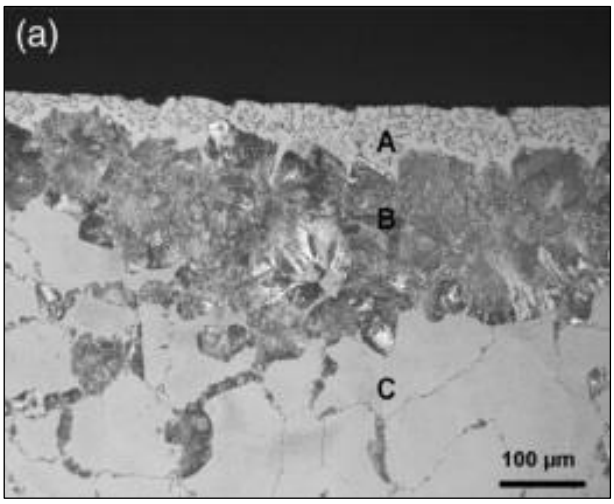

Figure 2-9 – Example of an engineered Mg-Al intermetallic layer produced by Sun *et al.* 2008 [62] through the heat treatment of pure Mg in contact with Al powder at 400°C for 24 h.

2.2.3 Sputtering

Huo *et al.* 2007 [63] used heat treatment of an AZ91D Mg alloy coated with Al by magnetron sputtering to create an Al diffusion coating. Specimens were examined using SEM, EDX, and XRD. Sputter deposition was carried out for 1.5 h in a 0.2 Pa argon atmosphere at a power of 1500 W, which created an 8 µm coating of cylindrical Al crystals. The authors concluded that a sputtered coating alone, especially considering the reactivity of Mg alloys, did not provide good enough protection. As such vacuum heat treatment at 450°C for 2 h was performed to create a diffusion coating. Post heat treatment the surface was described as being smooth and dense, and free from defects, such as holes and interstices, that had previously been visible. The cross-section in Figure 2-10 reveals a 30 µm coating consisting of a continuous matrix $Mg_{17}Al_{12}$ light phase, with darker α-Mg precipitates.

Anodic/cathodic polarisation in 3.5% NaCl solution was used to assess corrosion performance, and this showed that the OCP of the coating was −1.238 V_{SCE} compared to a more active −1.576 V_{SCE} for the AZ91D substrate. The change in I_{corr} followed the same trend of an order of magnitude improvement but the values recorded — 39.55 µA/cm^2 for the coating and 569.1 µA/cm^2 for AZ91D — are both two orders greater than seen previously. The behaviour of the as sputtered Al coating was also measured and this exhibited an OCP of −1.483 V_{SCE} and I_{corr} of 6250 µA/cm^2. The surprisingly high I_{corr} value was explained by poor adhesion of the sputtered layer, which was observed to scale off and accelerate corrosion by acting as a cathode. This finding indicates the magnitude of the galvanic couples that can develop between coatings and substrates, and further supports the benefits of creating diffused Mg-Al layers.

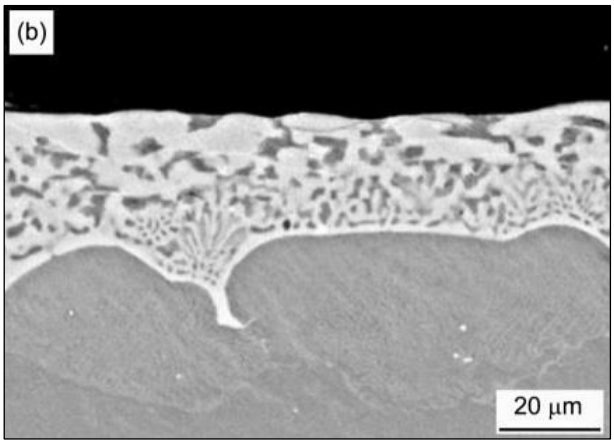

Figure 2-10 – Example of an engineered Mg-Al intermetallic layer produced by Huo *et al.* 2007 [63] through the heat treatment of AZ91D with a sputtered Al coating at 450°C for 2 h.

A similar method was also used by Zhu & Gao 2009 [64] to produce a coating on AZ91E. The substrate was coated with Al by magnetron sputtering for 6 h in a pure argon atmosphere at 1.33 Pa to produce a 7-10 µm thick layer. Examination by SEM and EDX showed that following heat treatment at 450°C for 1 min the original Al coating was completely consumed and a 30 µm layer with a eutectic structure of α-Mg and $Mg_{17}Al_{12}$ had formed, as shown in Figure 2-11. This was explained by extensive local melting of the sputtered coating and part of substrate due to heating above the eutectic point (437°C), which increased the ratio of Mg to Al in the surface liquid to below that of $Mg_{17}Al_{12}$ causing it to solidify with a eutectic morphology.

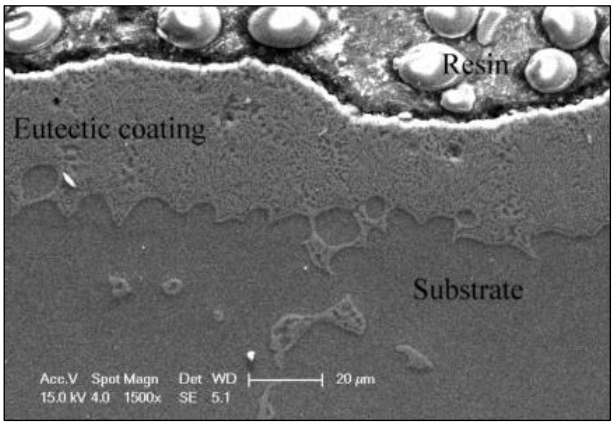

Figure 2-11 – Example of an engineered Mg-Al intermetallic layer produced by Zhu & Gao 2009 [64] through the heat treatment of AZ91E with a sputtered Al coating at 450°C for 1 min.

Following heat treatment at 435°C for 5 min a 10 µm $Mg_{17}Al_{12}$ region, with some Al at its surface, had formed and this was interconnected to areas of the same phase in the AZ91E substrate. This structure in shown in Figure 2-12, and the authors argue that it may have a pinning effect that could enhance coating adhesion. Possible structural changes to the AZ91E alloy as a result of heat treatment were also discussed and it was highlighted that the short duration had little effect on the eutectic $Mg_{17}Al_{12}$ but caused the dissolution of fine the $Mg_{17}Al_{12}$ lamellae, which could affect creep resistance at elevated temperatures. No electrochemical corrosion measurements were recorded for either layer.

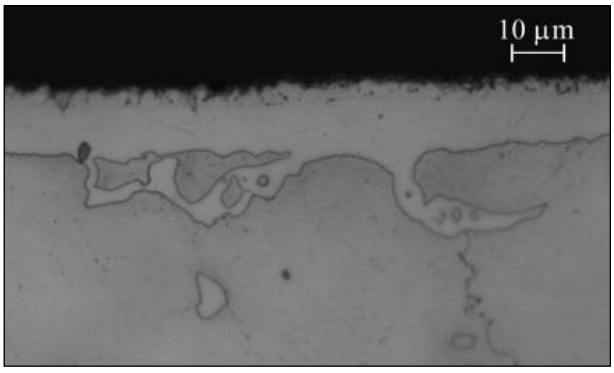

Figure 2-12 – Example of an engineered Mg-Al intermetallic layer produced by Zhu & Gao 2009 [64] through the heat treatment of AZ91E with a sputtered Al coating at 435°C for 5 min.

2.2.4 Thermal Spray

Two examples of the formation of intermetallic surface layers using the heat treatment of thermally sprayed coatings are described by Spencer & Zhang 2009 [65] and Zhang *et al.* 2009 [69], who formed layers on AZ91E and pure Mg substrates respectively. Both employed a cold spray kinetic metallisation system, which uses helium gas to accelerate Al powder of 15 µm average diameter to subsonic speeds. This high velocity Al powder was targeted at the substrate to form a dense and well bonded coating. Heat treatment was then carried out at 400°C for 20 h by Spencer & Zhang 2009 [65] and at 413°C for 24 h by Zhang *et al.* 2009 [69] and, as shown in Figure 2-13 and Figure 2-14, despite the different substrate materials near identical diffusion layers were produced, with both exhibiting a characteristic $Mg_{17}Al_{12}$ layer adjacent to the substrate and consistently thicker region of Mg_2Al_3 above. It was also observed that altering the heat treatment temperature changed the thickness of these phase layers. Further work by Spencer & Zhang 2009 [139] has also shown that composite Ni/Al coatings can be produced using a similar technique.

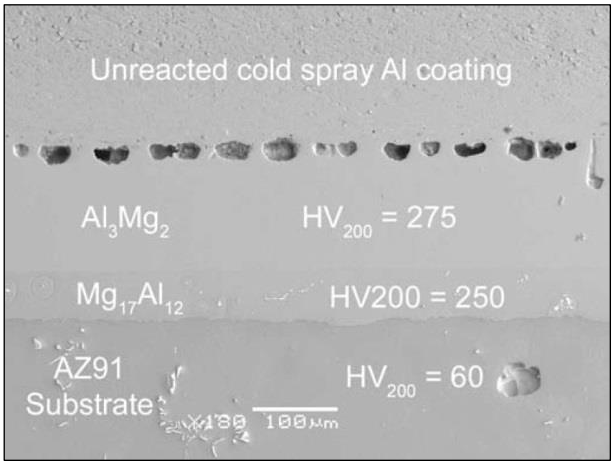

Figure 2-13 – Example of an engineered Mg-Al intermetallic layer produced by Spencer & Zhang 2009 [65] through the heat treatment of AZ91E with a thermally sprayed Al coating at 400°C for 20 h.

As was also reported in the work on contact diffusion by Yang *et al.* 2011 [57], a layer of the original Al coating remained at the surface. This was separated from the intermetallic by Kirkendall voids, which formed as a result of Al diffusing into the substrate faster than the substrate material diffused in the Al coating. These voids meant the residual Al layer could easily be removed.

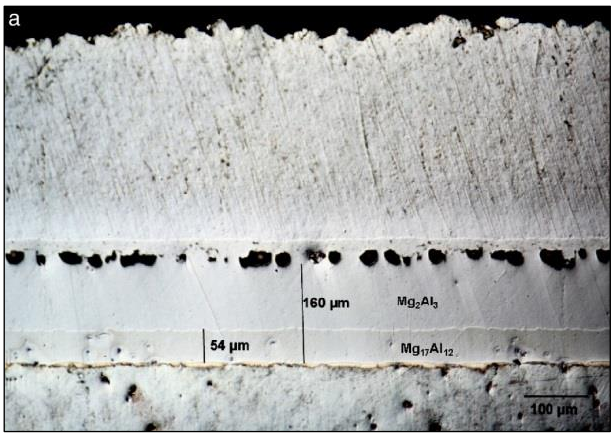

Figure 2-14 – Example of an engineered Mg-Al intermetallic layer produced by Zhang *et al.* 2009 [69] through the heat treatment of pure Mg with a thermally sprayed Al coating at 413°C for 6 h.

A comprehensive set of anodic/cathodic polarisation results are given by Spencer & Zhang 2009 [65], and these showed that the substrate materials exhibited the most active OCPs (−2.133 V_{SCE} for pure Mg and −1.980 V_{SCE} for AZ91E) and the largest I_{corr} values (11 µA/cm^2 for pure Mg and 5.2 µA/cm^2 for AZ91E). The corrosion behaviour of a pure Al sample was also recorded and this produced an OCP of −1.442 V_{SCE} and I_{corr} of 0.21 µA/cm^2. Given these results it is interesting to find that the OCP and I_{corr} of the cold sprayed coating, which is also pure Al, were −1.576 V_{SCE} and 4.0 µA/cm^2 respectively. The similarity of these values to both substrate materials might be explained by porosity in the coating, which could expose areas of the substrate leading to galvanic effects and an increase in corrosion rate [76].

The self-corrosion behaviour of both Mg-Al intermetallics was also measured and this showed that $Mg_{17}Al_{12}$ had an OCP of −1.667 V_{SCE} and I_{corr} of 0.05 µA/cm^2, while Mg_2Al_3 exhibited a more active OCP (−1.724 V_{SCE}) and a larger I_{corr} (0.51 µA/cm^2). This is another unusual result, firstly because it is the Mg-rich intermetallic that has the most noble OCP and the smallest I_{corr}, and secondly because this I_{corr} value is an order of magnitude less than those reported for an intermetallic layer in the other work

discussed here. The disparity between the magnitudes of the OCP results given by Spencer & Zhang 2009 [65] and those reported elsewhere is discussed in Section 4.3.4.2.

2.2.5 Molten Salts

Both Meifeng *et al.* 2008 [66] and Zhong *et al.* 2010 [67] demonstrate the use of molten $AlCl_3$-NaCl salts as a way of forming intermetallic surface coatings on an AZ91D substrate. Diffusion at temperature of 250, 300, 350, and 400°C was investigated by Meifeng *et al.* 2008 [66], with samples being dipped and held in the molten salt for 8 h. The resulting surface layers are shown in Figure 2-15. At 250°C the layer consisted of α-Al and $Mg_{17}Al_{12}$, while at higher temperatures they contained $Mg_{17}Al_{12}$ and Mg_2Al_3.

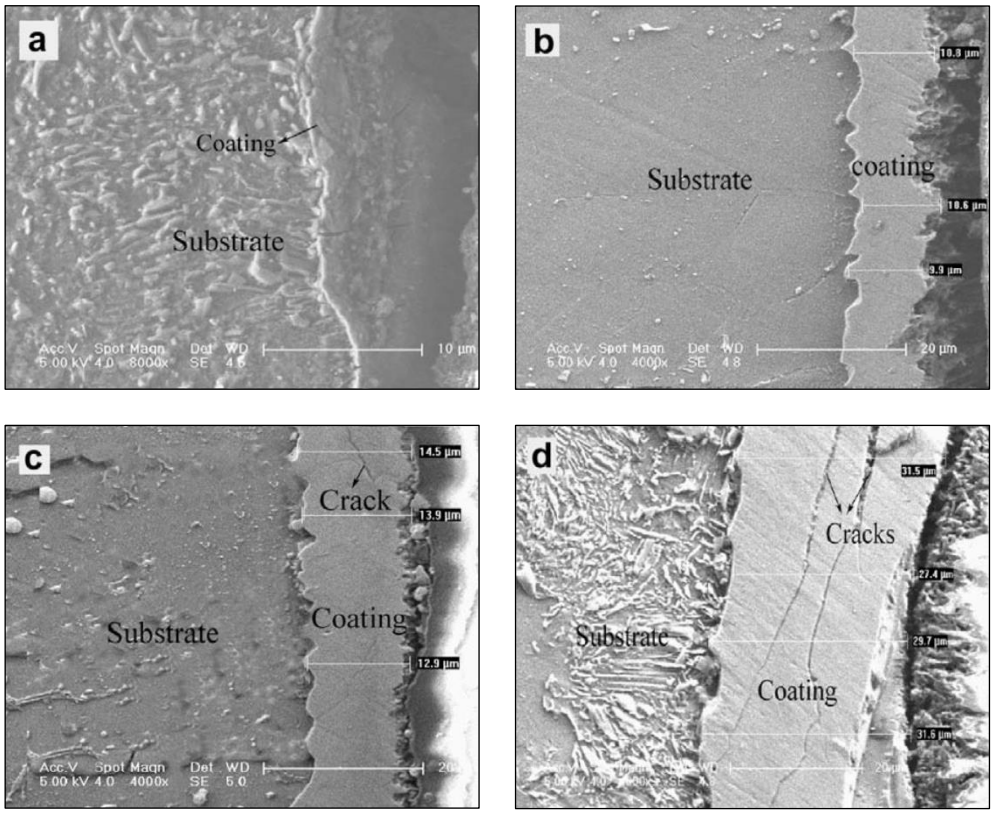

Figure 2-15 – Examples of engineered Mg-Al intermetallic layers produced by Meifeng *et al.* 2008 [66] on pure Mg by submerging in molten Al salts for 8 h at (a) 250°C, (b) 300°C, (c) 350°C, and (d) 400°C.

The structures described by Zhong *et al.* 2010 [67] are shown in Figure 2-16, and were formed at 300, 350, and 400°C with a holding time of 6 h. At 300°C an $Mg_{17}Al_{12}$ layer developed but above this temperature a two layer structure was observed, consisting of an outer region of Mg_2Al_3 and an inner region of $Mg_{17}Al_{12}$.

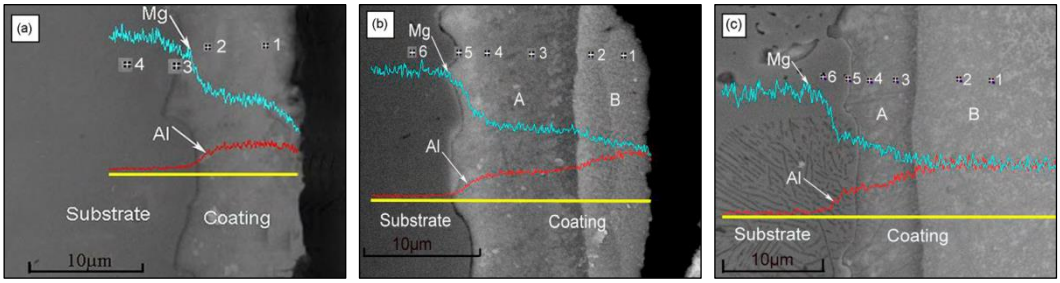

Figure 2-16 – Examples of engineered Mg-Al intermetallic layers produced by Zhong *et al.* 2010 [67] on AZ91D by submerging in molten Al salts for 6 h at (a) 300°C, (b) 350°C, and (d) 400°C.

Meifeng *et al.* 2008 [66] studied corrosion behaviour using anodic/cathodic polarisation and EIS, and recorded OCP and I_{corr} values of −1.593 V_{SCE} and 36.5 µA/cm^2 for the AZ91D substrate. The coatings produced at 250, 300, 350, and 400 exhibited OCPs of −1.700, −1.526, −1.681, and −1.493 V_{SCE} respectively, and I_{corr} values of 23.7, 3.9, 4.7 and 11.5 µA/cm^2. The anodic/cathodic polarisation results produced by Zhong *et al.* 2010 [67] showed that AZ91D had an OCP of −1.52 V_{SCE} and I_{corr} of 400 µA/cm^2, while the layer produced at 400°C exhibited OCP and I_{corr} values of −1.42 V_{SCE} and 14 µA/cm^2 respectively, which is an order of magnitude reduction.

2.2.6 Electrodeposition

As discussed in Section 2.1.1.1 the electrodeposition of Al on to an Mg substrate was first reported by Chang *et al.* 2007 [83] as a way of improving the corrosion properties of AZ91D. The acidic ionic liquid aluminium chloride 1-ethyl-3methyllimidazolium chloride ($AlCl_3$-EMIC), with a molar ratio of 1.5:1, was used as the electrolyte and electrodeposition was performed with a three electrode system under potentiostatically controlled conditions. The AZ91D was used as the working electrode (WE) and pure Al for both the counter (CE) and reference (RE) electrodes. Potentials of −0.2 V and −0.4 V (versus the RE) were applied to yield a total passed charge of 50 C/cm^2. The surface morphologies of both Al deposits were examined by SEM and showed that those produced at −0.2 V were dense and uniform. The deposit formed at −0.4 V did not appear as compact and also exhibited several small cracks. The thickness of both

deposits was approximately 20 µm, which is consistent with that expected from the total charge passed. XRD and EDX confirmed that only pure Al was deposited and no residual $AlCl_3$-EMIC had been incorporated.

Yang *et al.* 2011 [68] subsequently investigated the corrosion properties of an AZ91D Mg alloy with an electrodeposited and heat treated Al coating. This work used the same acidic ionic liquid employed by Chang *et al.* 2007 [83], with an identical three-electrode set up but under galvanic, rather than potentiostatic, control. After coating for 1 h at a current density of 1500 µA/cm^2 the Al coatings were described as continuous, uniform (18 µm thick and consistent with Faraday), and dense, with complete surface coverage. XRD and EDX confirmed the layer was pure Al, with EDX also revealing an amount of oxygen at the substrate/coating interface. The presence of oxygen at the interface was given as a possible reason for the poor coating adhesion exhibited during tape tests. Two heat treatments were subsequently completed in a vacuum furnace to develop intermetallic layers with difference microstructures, as shown in Figure 2-17.

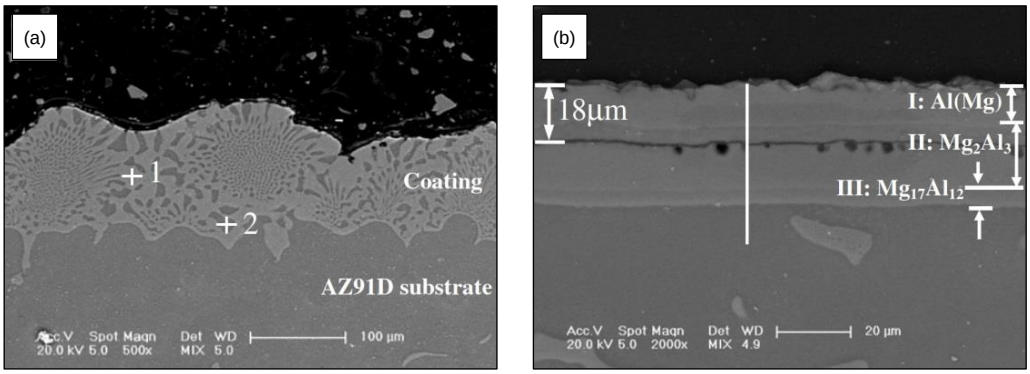

Figure 2-17 – Examples of engineered Mg-Al intermetallic layer produced by Yang *et al.* 2011 [68] through the heat treatment of AZ91D with an electrodeposited Al coating at (a) 420°C for 2 h, and (b) 200°C for 12 h.

Heating to 420°C for 2 h produced a two-phase coating structure with a thickness of 100-140 µm. This consisted of a continuous network light phase (identified as $Mg_{17}Al_{12}$) interspersed with a dark phase (identified as α-Mg). No Al-rich phases appeared to be present. Heat treatment at 200°C for 12 h resulted in the development of a layered structure consisting of three different phases. These phases were estimated to be α-Al solid solution (top layer), Mg_2Al_3 intermetallic (middle layer), and $Mg_{17}Al_{12}$ intermetallic (bottom layer). The top layer was found to be weakly attached and easily removed.

Corrosion performance in 3.5% NaCl solution was evaluated using anodic/cathodic polarisation and this showed that AZ91D had an OCP of −1.638 V_{SCE} and I_{corr} of 5.57 µA/cm^2. The coating formed at 420°C for 2 h exhibited an OCP of −1.535 V_{SCE} and I_{corr} of 0.54 µA/cm^2, while the values for the layer produced at 200°C for 12 h were −1.271 V_{SCE} and 0.14 µA/cm^2 respectively. The properties for as plated Al were also measured and gave an OCP of −1.242 V_{SCE} and I_{corr} of 0.12 µA/cm^2, which is only marginally lower than the post heat treatment I_{corr} value.

2.2.7 Summary of Intermetallic Surface Layers

Table 2-7 summarises the processes used to produce Mg-Al intermetallic surface layers that have been discussed here, and briefly describes the structures that were formed. A comparison of these diffusion layers suggests that their final appearance is more strongly linked to heating temperature and duration, rather than the method used to provide the Al source. At temperatures above approximately 300°C, with the exception of those produced using a thermal spray process, the diffused coatings tend to have microstructures of mixed compositions containing solid solution and intermetallic phases. Below around 300°C, it is more common to find discrete layers of the $Mg_{17}Al_{12}$ and Mg_2Al_3 intermetallics.

The electrochemical corrosion characteristics of the intermetallic layers discussed here are summarised in Table 2-8, and compared in the plots in Figure 2-18 and Figure 2-19. In all cases the OCP of the diffused layers is more noble than the substrate material or the alloy it is intended to protect. This comparison also shows that there is always at least an order of magnitude reduction in corrosion rate between the Mg-Al intermetallic layer and the substrate.

Table 2-7 – Table summarising the Mg-Al intermetallic layers formed using the methods described here.

Method	Substrate	Coating Material	Heat Treatment			Layer Structure	Reference
			Conditions	Temp.	Duration		
Contact diffusion	Pure Mg	Pure Al foil + Mg-Al eutectic powder solder	80 MPa lowering to 30 MPa as temperature rises	450°C	2 h	Layered structure of α-Mg + $Mg_{17}Al_{12}$, $Mg_{17}Al_{12}$, Mg_2Al_3 and α-Al	Li *et al.* 2009 [56]
Contact diffusion	AZ91D	Thin Al plate	20 MPa and 10^{-3} Pa vacuum	300°C	2-18 h	Layered structure of $Mg_{17}Al_{12}$, Mg_2Al_3 and α-Al separated by voids	Yang *et al.* 2011 [57]
Powder diffusion	AZ91D	Al powder	Pure argon atmosphere	450°C	1 h	$Mg_{17}Al_{12}$ with lamellae of α-Mg + $Mg_{17}Al_{12}$	Shigematsu *et al.* 2000 [58]
Powder diffusion	AZ91D	Mixture of Al and Zn powder	Protective gas	430°C	12 h	Three component, single layer. α-Mg + Zn, $Mg_{17}Al_{12}$ + Zn, $Mg_{17}Al_{12}$ + $Al_5Mg_{11}Zn_4$	Zhang *et al.* 2002 [59]
Powder diffusion	AZ91D	Mixture of Al and Zn powder	Protective gas	420°C	1.5 h	Equiaxed grains and dendrites of $Mg_{17}Al_{12}$ + α-Mg	Zhu & Song 2006 [60]
Powder diffusion	Pure Mg	Al powder	10^{-2} Pa vacuum	420°C	1.5 h	Outer layer of α-Mg + Mg_2Al_3. Inner layer enriched with $Mg_{17}Al_{12}$ + some α-Mg and Mg_2Al_3. Transition layer of α-Mg + some Mg_2Al_3	Liu *et al.* 2008 [61]
Powder diffusion	AZ91D	Al powder	Covered with foundry coke and sand to reduce oxidation	400°C	24 h	α-Mg + $Mg_{17}Al_{12}$ lamellae. Surface rich in $Mg_{17}Al_{12}$ + α-Mg precipitates	Sun *et al.* 2008 [62]
Sputtering	AZ91D	Al coating	Vacuum annealing	450°C	2 h	$Mg_{17}Al_{12}$ + α-Mg precipitates	Huo *et al.* 2007 [63]
Sputtering	AZ91E	Al coating	Vacuum annealing	450°C	1 min	Eutectic structure of α-Mg and $Mg_{17}Al_{12}$	Zhu & Gao 2009 [64]
	AZ91E	Al coating	Vacuum annealing	435°C	5 min	$Mg_{17}Al_{12}$ layer pinned into the substrate	
Thermal spray	AZ91E	Cold sprayed Al coating	Argon atmosphere	400°C	20 h	Layered structure of $Mg_{17}Al_{12}$, Mg_2Al_3 and α-Al separated by voids	Spencer & Zhang 2009 [65]
Thermal spray	Pure Mg	Cold sprayed Al coating	Argon atmosphere	413°C	6 h	Layered structure of $Mg_{17}Al_{12}$, Mg_2Al_3 and α-Al separated by voids	Zhang *et al.* 2009 [69]
Molten salts	AZ91D	Diffused Al	Argon atmosphere	250°C	8 h	Layer of $Mg_{17}Al_{12}$ + α-Al	Meifeng *et al.* 2008 [66]
	AZ91D	Diffused Al	Argon atmosphere	300-400°C	8 h	Layer of $Mg_{17}Al_{12}$ + Mg_2Al_3	
Molten salts	AZ91D	Diffused Al	Argon atmosphere	300°C	6 h	Layered structure of $Mg_{17}Al_{12}$ and α-Al	Zhong *et al.* 2010 [67]
	AZ91D	Diffused Al	Argon atmosphere	350-400°C	6 h	Layered structure of $Mg_{17}Al_{12}$ and Mg_2Al_3	
Electro-deposition	AZ91D	Pure Al coating	10^{-3} Pa vacuum	420°C	2 h	$Mg_{17}Al_{12}$ + α-Mg precipitates	Yang *et al.* 2011 [68]
	AZ91D	Pure Al coating	10^{-3} Pa vacuum	200°C	12 h	Layered structure of $Mg_{17}Al_{12}$ and Mg_2Al_3	

Table 2-8 – Table listing OCP and I_{corr} values for pure Mg, AZ91D/E, $Mg_{17}Al_{12}$, Mg_2Al_3, and Mg-Al intermetallic layers in the work discussed here.

Method	Substrate	Electrolyte	Open Circuit Potential[A] (V_{SCE})	Corrosion Rate		Reference
				Technique	Current Density[A] ($\mu A/cm^2$)	
Contact diffusion	Pure Mg	5% NaCl	−1.250	Tafel	1	Li *et al.* 2009 [56]
	Pure Al	5% NaCl	−0.760	Tafel	0.2	
	IM layer	5% NaCl	−0.887	Tafel	0.2	
Contact diffusion	AZ91D	3.5% NaCl	−1.66	Tafel	5.57	Yang *et al.* 2011 [57]
	IM layer	3.5% NaCl	−1.29	Tafel	0.21	
Powder diffusion	AZ91D	5% NaCl	−1.627	Tafel	381	Zhu & Song 2006 [60]
	IM layer	5% NaCl	−1.512	Tafel	4.1	
Powder diffusion	Pure Mg	5% NaCl	−1.250	Tafel	430	Liu *et al.* 2008 [61]
	AZ91	5% NaCl	−1.214	Tafel	144	
	IM layer	5% NaCl	−0.866	Tafel	51	
Sputtering	AZ91D	3.5% NaCl	−1.576	Tafel	569.1	Huo *et al.* 2007 [63]
	Sputtered Al	3.5% NaCl	−1.483	Tafel	6250	
	IM layer	3.5% NaCl	−1.238	Tafel	39.55	
Thermal spray	Pure Mg	5% NaCl	−2.133	Tafel	11	Spencer & Zhang 2009 [65].
	AZ91E	5% NaCl	−1.980	Tafel	5.2	
	Pure Al	5% NaCl	−1.442	Tafel	0.21	
	Cold sprayed Al	5% NaCl	−1.576	Tafel	4.0	
	$Mg_{17}Al_{12}$	5% NaCl	−1.667	Tafel	0.05	
	Mg_2Al_3	5% NaCl	−1.724	Tafel	0.51	
Molten salts	AZ91D	3.5% NaCl	−1.593	EIS	36.5[B]	Meifeng *et al.* 2008 [66]
	IM layer (250°C)	3.5% NaCl	−1.700	EIS	23.7[B]	
	IM layer (300°C)	3.5% NaCl	−1.526	EIS	3.9[B]	
	IM layer (350°C)	3.5% NaCl	−1.681	EIS	4.7[B]	
	IM layer (400°C)	3.5% NaCl	−1.493	EIS	11.5[B]	
Molten salts	AZ91D	3.5% NaCl	−1.532	Tafel	400	Zhong *et al.* 2010 [67]
	IM layer (400°C)	3.5% NaCl	−1.424	Tafel	14	
Electrodeposition	AZ91D	3.5% NaCl	−1.638	Tafel	5.57	Yang *et al.* 2011 [68]
	Electroplated Al	3.5% NaCl	−1.242	Tafel	0.12	
	IM layer (420°C, 2 h)	3.5% NaCl	−1.535	Tafel	0.54	
	IM layer (200°C, 12 h)	3.5% NaCl	−1.271	Tafel	0.14	

A – Where listed the value from the reference is given. Where none were available the plots from the reference were digitised and a value extrapolated.
B – Value converted from R_{ct} to I_{corr} as described in Section 4.3.2.2.

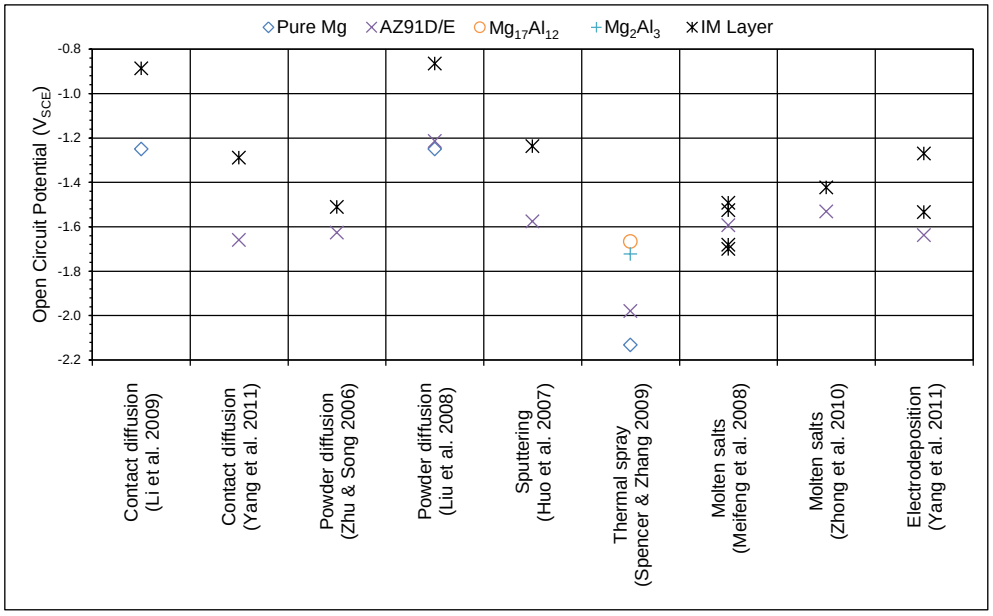

Figure 2-18 – Comparison of OCP values for the substrates and associated Mg-Al intermetallic layers listed in Table 2-8.

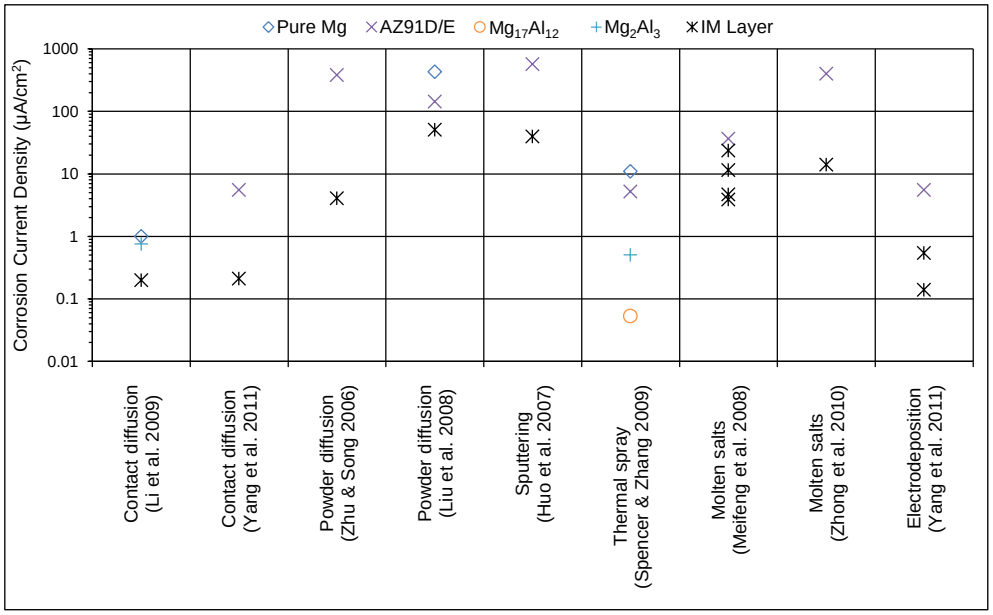

Figure 2-19 – Comparison of I_{corr} values for the substrates and associated Mg-Al intermetallic layers listed in Table 2-8.

2.3 Literature Review Summary

The plots in Figure 2-20 and Figure 2-21 compare the electrochemical corrosion properties of the substrates, the conventional surface treatments, and the Mg-Al intermetallic surface layers that have been discussed in this review. Possibly the most apparent feature of this comparison is the spread of results that have been published. While each author has demonstrated that a protective treatment offers a corrosion performance improvement, evaluation against other work can often prove difficult as it is not possible to easily define what a 'good' or 'bad' corrosion rate is.

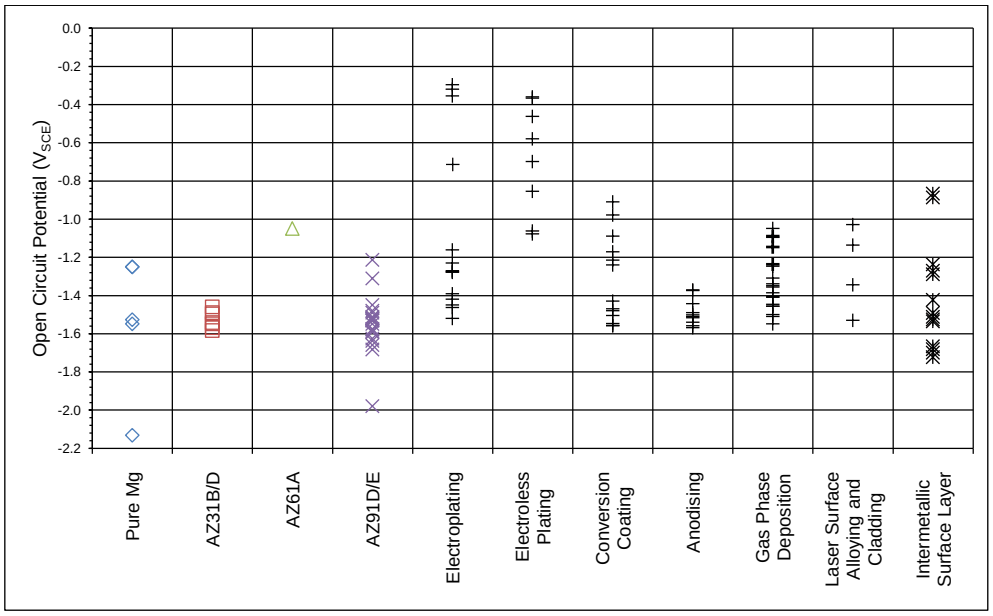

Figure 2-20 – Comparison of OCP values for the substrates and associated conventional surface treatments listed in Table 2-1, Table 2-2, Table 2-3, Table 2-4, Table 2-5, and Table 2-6, and the substrates and associated Mg-Al intermetallic layers listed in Table 2-8.

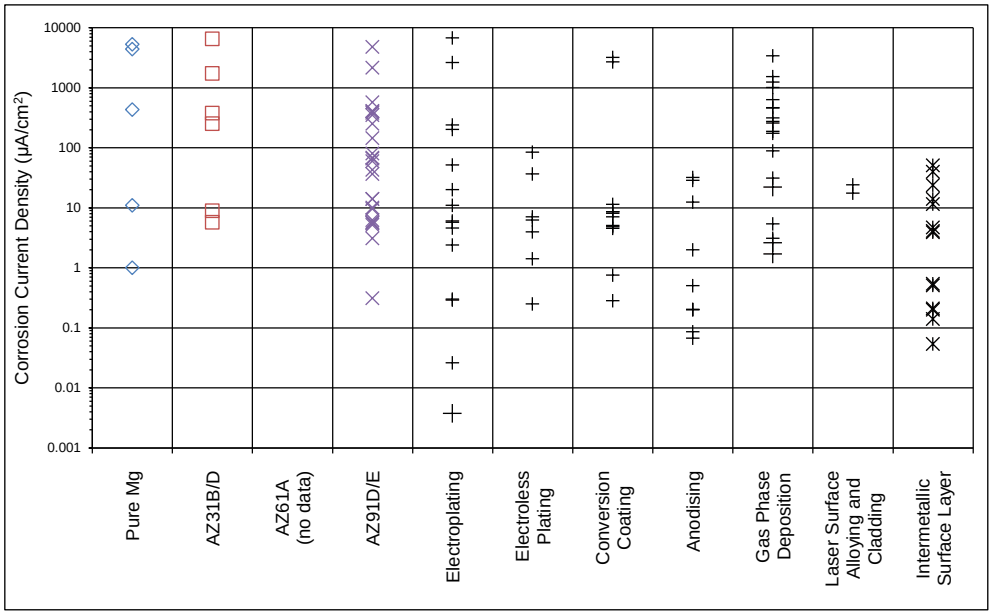

Figure 2-21 – Comparison of I_{corr} values for the substrates and associated conventional surface treatments listed in Table 2-1, Table 2-2, Table 2-3, Table 2-4, Table 2-5, and Table 2-6, and the substrates and associated Mg-Al intermetallic layers listed in Table 2-8.

Despite the reductions in corrosion rate for Mg-Al intermetallic layers not being as large as some of those recorded for some conventional surface treatments, they could still hold an advantage if the message from Murray and Hillis 1991 [140] is considered. Because of the way they are produced, and the corrosion performance they can offer, Mg-Al intermetallic layers could be considered as a single step technique that combines pretreatment, primer, and top coat. This may apply to situations when they are bonded directly to other components, and where their inherent robustness — being part of the material and not just a surface coating — is likely to be a particular strength.

An Mg-Al intermetallic layer is also less likely to have a strong galvanic interaction with the substrate when compared to other more noble conventional treatments, and its similarity to Al, which it is likely to come into contact with in large assemblies, should also reduce any galvanic effects from coupling dissimilar components. While these types of galvanic interactions have been discussed for conventional surface treatments in the literature reviewed here, no research has been found on how an Mg-Al intermetallic layer would perform.

3 METHODOLOGY

3.1 Thesis Structure

The methodology behind the research discussed here is described by the flow diagram in Figure 3-1. This shows how an initial proposal — the idea of forming protective Mg-Al intermetallic layers by heat treating an Mg substrate with an electrodeposited Al coating — has led to the development of a substantial body of research.

At each stage a key question has evolved into one of the objectives listed in Section 1.4. Objectives 1 to 5 involve experimental work and these are addressed in turn in Section 4, with each package of research building knowledge that is used in the next. Section 5 deals with the final objective, and brings together the experimental findings and discusses what they mean for the future of Mg-Al intermetallic layers.

3.2 Examination and Analysis Equipment

Optical images were taken using Nikon Prism Acquisition and Nikon Eclipse ME600 microscopes, and Synoptics Ltd. AcQuis V4.0.1.10 image capture software. Image analysis to calculate sample surface areas and phase proportions was conducted using Matlab R2007b (V7.5). Scanning electron microscope (SEM) images, energy dispersive X-ray (EDX) data, and electron backscatter diffraction (EBSD) data were obtained using an FEI XL30 scanning field emission gun (SFEG) and Oxford Instruments AztecEnergy V2.2, and AztecHKL V2.2 software. An error of ±5% can be assumed for all EDX measurements [141]. X-ray diffraction was conducted with a Siemens D5005 X-Ray Diffractometer, and Bruker DIFFRAC^{plus} XRD Commander V2.4.1 and EVA V5.0 software. The focused ion beam (FIB) system was an FEI FIB 200 Focused Ion Beam Workstation.

3.3 Electrochemical Corrosion Measurements

3.3.1 Equipment and Software

All corrosion measurements were conducted in 3.5% NaCl solution made up using laboratory reagent grade NaCl powder and de-ionised water. Self-corrosion was recorded using a Solartron 1280 Electrochemical Measurement Unit connected to a Solartron 1281 Multiplexer, and Scribner Associates, Inc. CorrWare V2.8d1, CorrView V2.8d, ZPlot V2.8d1, and ZView V2.8d software. The limit of error for this equipment is

0.1% [142]. Galvanic corrosion was measured by zero resistance ammetry (ZRA) with an ACM Instruments GalvoGill 12 and GalvoGill 12 logging software V1.01.03. The resistance box technique also used the ACM Instruments GalvoGill 12, as well as an ACM Instruments GillAC and Sequencer V5 software. Both the GalvoGill 12 and the GillAC have measurement resolutions of 1 µV [143,144]. In each case a saturated calomel electrode (SCE) and a platinum electrode were used as the reference (RE) and the counter (CE) electrodes respectively.

3.3.2 Error Assessment

The equipment errors listed above lead to corresponding errors in the values given in Section 4.3, Section 4.4, and Section 4.5. As a result of the 0.1% limit of error the listed self-corrosion measurements has a maximum potential error of ±2 mV, and a maximum current error of ±0.1 µA/cm^2. The galvanic equipment's resolution of 1 µV leads to a maximum current error of ±0.2 µA/cm^2, or 1.8%. It should be noted that the magnitudes of these errors are small enough such that they do not affect the subsequent discussion of the relative corrosion behaviours of the materials.

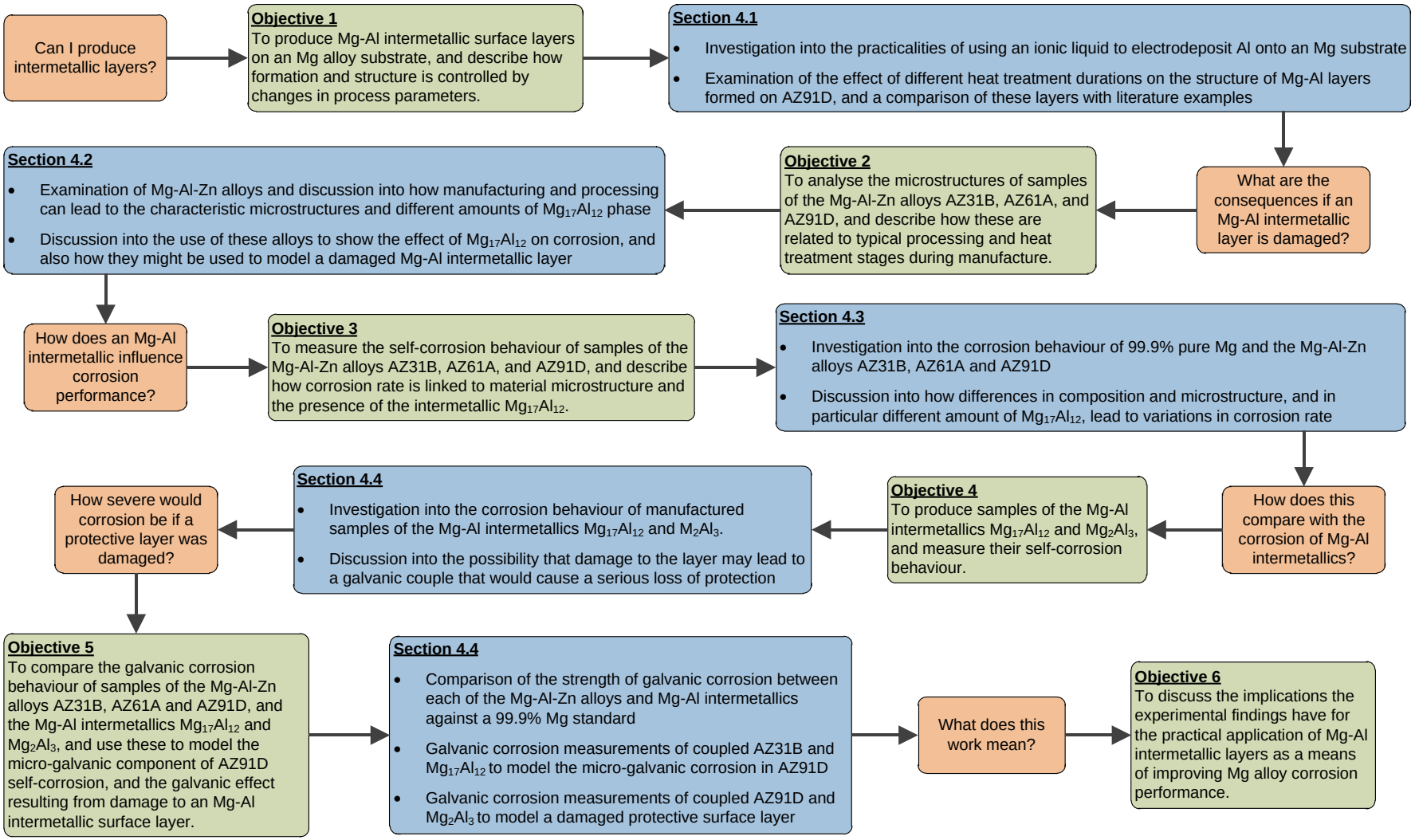

Figure 3-1 – Flow diagram outlining the methodology behind this body of research.

4 EXPERIMENTAL WORK

4.1 Formation of Intermetallic Surface Layers

4.1.1 Introduction

This section addresses the first objective and describes how protective Mg-Al intermetallic surface layers can be formed through the heat treatment of Mg substrates with an electrodeposited Al coating. The practicalities of using this novel ionic liquid electroplating process for Mg are assessed, and the structures formed as a result of different heat treatment durations are examined. These Mg-Al layers are then compared with literature examples produced using different techniques, before the implications they might have for subsequent corrosion performance are highlighted.

4.1.2 Materials and Methods

4.1.2.1 Pure Mg and Mg Alloy Substrates

The materials used in this work were 98% and 99.9% pure Mg, and ASTM standard Mg-Al-Zn alloy AZ91D. Both the 98% and 99.9% pure Mg were cut from 0.25 mm thick rolled sheets, while the AZ91D was sectioned from a 5 mm thick cast bar. The processing and heat treatment condition of these materials was not known.

The EDX analysis results in Table 4-1 list the major elements present in these materials, and shows that the 98% and 99.9% Mg are of the expected purities. The analysis also confirms that the primary constituents of the AZ91D alloy, which should contain a nominal 9 wt% Al and 1 wt% Zn, fall within the ASTM specifications given previously in Table 1-3.

Table 4-1 – Analysed compositions of 98% and 99.9% pure Mg, and AZ91D.

Material[A]	Al	Cu[B]	Fe[B]	Mn	Ni[B]	Zn	Mg
98% Mg	-	-	-	1.47	-	-	98.53
99.9% Mg	-	-	-	-	-	-	100.00
AZ91D	8.43	-	-	0.13	-	0.81	90.63

A - All values in weight %. Only elements that were identified by analysis are shown.
B - 'Impurity' elements included in table but not picked up by this analysis.

4.1.2.2 Ionic Liquid Electroplating

A layer of Al was deposited on to the Mg substrates by electroplating from the ionic liquid (IL) 1-butyl-3-methyl-imidazolium heptachloroaluminate, or [BMIm] Al_2Cl_7, using a two electrode system as shown schematically in Figure 4-1. Because this is a water intolerant IL the equipment was set up in a sealed glove box containing argon at 1-20 mbar positive pressure and <2 ppm water. Equipment and samples were transferred to and from the glove box via an air-lock chamber to ensure the inert atmosphere was maintained. The IL was contained in a glass laboratory beaker with a length of 99.9% Al wire coiled around its inner wall. A measured area of the sample being electroplated was suspended in the IL using a crocodile clip held in a clamp stand. The electroplating current was supplied by a galvanostat outside the glove box, with wires fed inside through a sealed penetration. The Al wire anode and Mg cathode were connected to the positive and negative terminals respectively, and the current was set such that a 10 mA/cm^2 current density was maintained for 1.5 h.

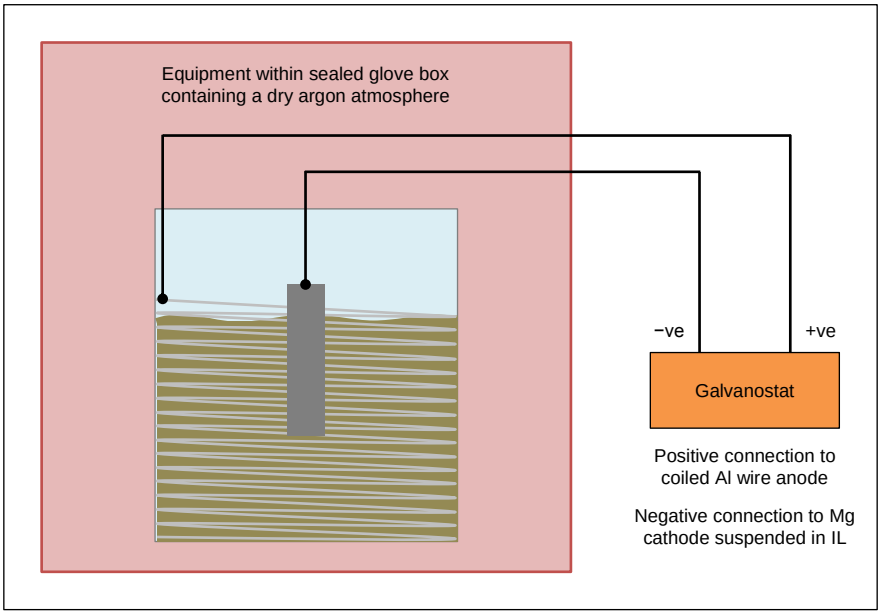

Figure 4-1 – Schematic representation of the equipment arrangement used to electroplate Al onto Mg from an ionic liquid.

During the resulting electrochemical reaction Al is deposited at the Mg cathode according to the following equations [145].

Reduction at cathode $$4Al_2Cl_7^- + 3e^- \rightarrow Al + 7AlCl_4^-$$ 4-1

Oxidation at anode $$4AlCl_4^- \rightarrow 2Al_2Cl_7^- + Cl_2 + 2e^-$$ 4-2

Overall $$8Al_2Cl_7^- + 12AlCl_4^- \rightarrow 2Al + 14AlCl_4^- + 6Al_2Cl_7^- + 3Cl_2$$ 4-3

The mass of metal deposited, m (g), during electrodeposition can be determined as follows.

$$m = \frac{QM}{Fz}$$ 4-4

Where Q (coulombs, C) is the total electric charge passed, M (g/mol) is the molar mass of the metal being deposited, z is the valence number of its ions, and F is the Faraday constant (96485 C/mol). The total electric charge passed depends on the rate of current flow, I (C/s), and the duration for which it is applied, t (s).

$$Q = It$$ 4-5

Combining Equation 4-4 and Equation 4-5 allows the mass deposition rate, $\dot{m}$ (g/s) to be calculated.

$$\dot{m} = \frac{IM}{Fz}$$ 4-6

The mass rate is independent of the size of the specimen being electroplated and so it is generally more useful to think in terms of a depth rate, $\dot{s}$ (cm/s). This is achieved by introducing current density, J (C/s/cm^2), instead of current, and adding a term for the metal density, ρ (g/cm^3).

$$\dot{s} = \frac{JM}{\rho F z} \qquad 4\text{-}7$$

Aluminium has a molar mass of 26.98 g/mol, density of 2.70 g/cm^3, and valence number of 3. At a 10 mA/cm^2 current density this yields a deposition rate of 3.5×10^{-7} cm/s, which corresponds to a theoretical deposit depth of 18.6 µm over 1.5 h

4.1.2.3 Heat Treatment

Heat treatments were conducted in an electric horizontal tube furnace and under an inert argon atmosphere. The furnace was profiled and the hot zone defined such that the temperature of the samples was within ±5°C. Prior to beginning treatment the furnace was purged for at least 30 minutes, before being heated at a ramp rate of 6°C per minute. After holding at temperature for the desired duration the furnace was cooled at a rate of 6°C per minute to ambient.

4.1.3 Results and Discussion

4.1.3.1 Initial Process Refinements using Pure Mg

The optical image in Figure 4-2 shows a 98% Mg substrate with an electrodeposited Al coating prior to any heat treatment. The Al layer has a thickness of around 18 µm, which is consistent with that calculated in Section 0. This image confirms that Al can be successfully deposited on to Mg using IL electroplating.

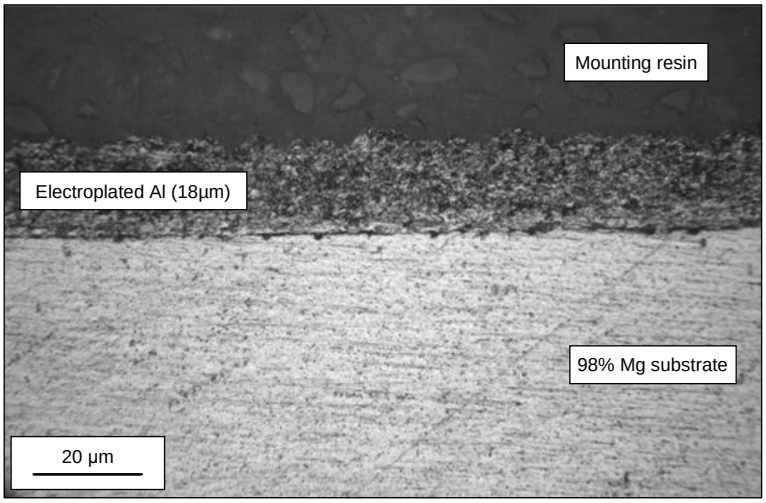

Figure 4-2 – Optical image of a 98% Mg substrate with an approximately 18 µm thick electrodeposited Al coating, and without heat treatment.

Identical Al coated samples were subsequently heat treated at a series of temperatures between 200 and 420°C for durations ranging from 2 to 20 h. These parameters were chosen because they encompass the ranges used by Yang *et al.* 2011 [68], whose work was described in Section 2.2.6 and who successfully formed Mg-Al intermetallic layers on AZ91D by the same method. Subsequent examination of the surfaces and of cross-sections of the heat treated samples by optical microscope showed that no obvious changes had taken place, and revealed that they were almost identical in appearance to the un-treated sample that was shown in Figure 4-2. Further examination by SEM and analysis using EDX and XRD also did not uncover any evidence of diffusion between the substrate and coating.

Scrutiny of the process steps led to the theory that an oxide film on the substrate could be impeding diffusion. To confirm this supposition the 98% Mg was abraded with P4000 SiC paper in two stages prior to electroplating. Any substantial surface oxide was first removed by abrading in air. A second abrasion was then conducted in the electroplating chamber just prior to deposition, the idea being that the dry argon atmosphere would substantially slow oxide reformation.

A series of samples electroplated in this way were subsequently heat treated over a range of temperatures and durations as before. The temperatures were all kept below the eutectic temperature of 437°C — as shown on the phase diagram in Figure 4-20 — to prevent melting, with lower temperatures being preferred as they would allow more control over subsequent diffusion and phase formation. The sample treated at 390°C for 4 h was the only one to undergo any changes, and the SEM image in Figure 4-3 shows an area of the top of this sample. The three distinct regions seen here are typical of those that were visible across the surface.

Analysis by EDX showed that the lower region in this image had a composition of 0.1 at% Mg, 99.8 at% Al, and 0.1 at% Cl, which is consistent with that of an electroplated Al layer. The coating here was weakly attached and had visibly separated from the substrate beneath. Prior to imaging the upper region also had a separated Al coating that was removed to allow the underlying surface to be analysed. This gave a composition of 94.7 at% Mg, 1.3 at% Al, 3.4 at% Cl and 0.6 at% Mn, and confirms that the area was the 98% Mg substrate. The presence of Cl is likely to be from residual IL that, on removal from the electroplating chamber, will react with moisture in the atmosphere to produce hydrochloric acid. Subsequent attack of the Mg substrate would result in separation of the Al coating and consequently prevent diffusion.

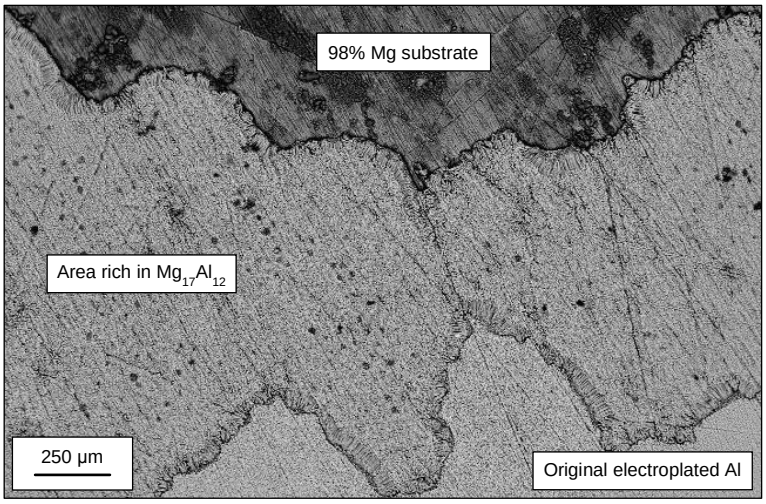

Figure 4-3 – SEM image showing three distinct regions on the top surface of a 98% Mg substrate with an electrodeposited Al coating following heat treatment at 390°C for 4 h.

The central region shows an area where diffusion between the Mg substrate and Al coating has taken place, and analysis reveals a composition of 65.1 at% Mg, 34.3 at% Al, and 0.6 at% Cl. This ratio of Mg and Al is near that of the intermetallic $Mg_{17}Al_{12,}$ and the presence of this phase is also supported by the XRD spectra in Figure 4-4. Before heat treatment only peaks for Al and Mg are identified but afterwards additional peaks that corresponding to the intermetallic phase are visible.

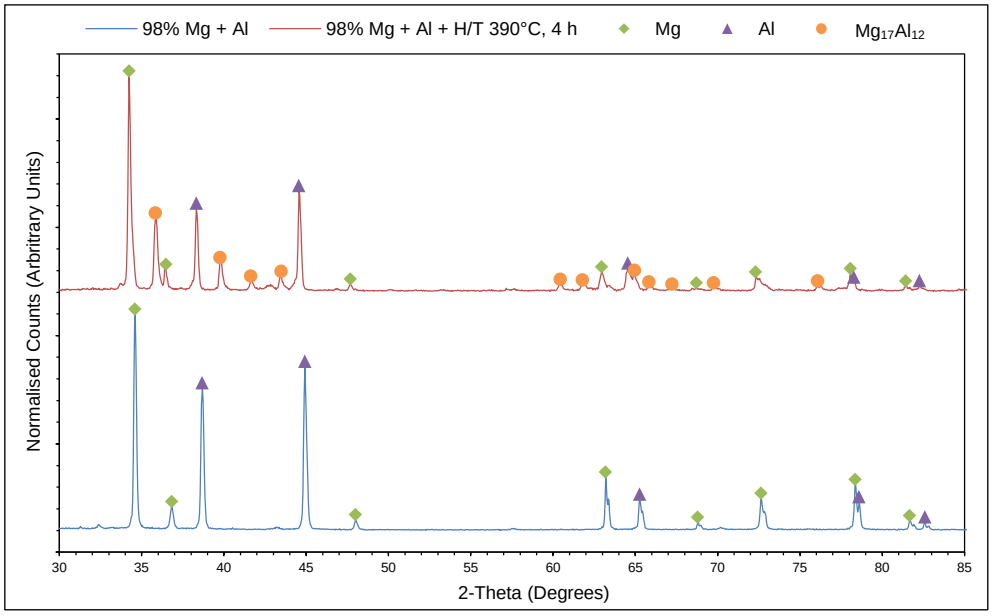

Figure 4-4 – XRD spectra for Al coated 98% Mg before (bottom) and after (top) heat treatment at 390°C for 4 h. Before heat treatment only peaks for Al and Mg are identified but afterwards additional peaks that corresponding to the $Mg_{17}Al_{12}$ intermetallic phase are visible.

The SEM image in Figure 4-5 shows a cross-section of the same sample following heat treatment. The backscatter contrast indicates that diffusion has taken place between the 98% Mg substrate and electroplated Al coating, and this is confirmed by EDX analysis. The top layer varies slightly in depth but its thickness of approximately 18 µm is the same as that expected for the original electroplated Al. It has a mean composition of 65.6 at% Mg, 33.9 at% Al and 0.5 at% Cl, which places it near the $Mg_{17}Al_{12}$ region of the Mg-Al phase diagram (Figure 4-20) and indicates that the layer is rich in the intermetallic phase.

Below the top layer there is a distinct line and the composition at this point is 72.1 at% Mg, 24.9 at% Al, 0.4 at% Si, 2.2 at% Cl and 0.4 at% Mn. The presence of Si and Mn — which are components of the 98% Mg and are not seen in the top layer — as well the location of the line, supports the suggestion that this is the original substrate/coating interface. The higher percentage of Cl also back this up as the interface is where residual IL is most likely to be trapped.

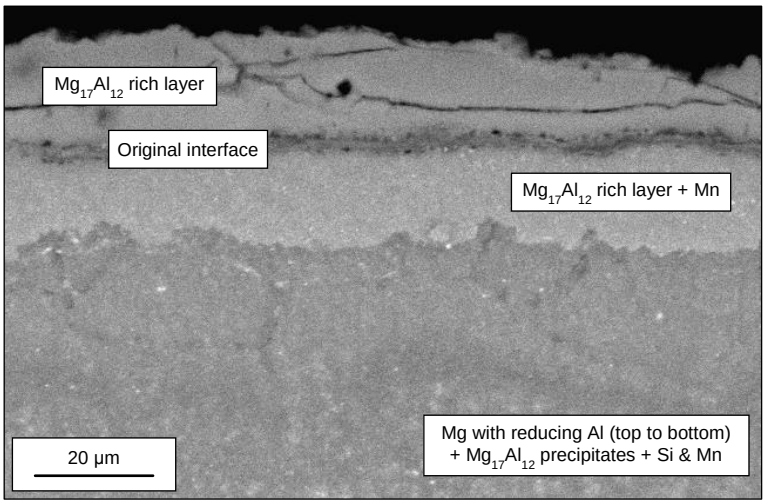

Figure 4-5 – SEM image showing a cross-section through a 98% Mg substrate with an electrodeposited Al coating following heat treatment at 390°C for 4 h.

A second layer, below the original interface, is of comparable depth to the top one and has a composition of 66.0 at% Mg, 32.9 at% Al, 0.4 at% Cl, and 0.7 at% Mn. This is almost identical to the top layer, indicating that it is also rich in the $Mg_{17}Al_{12}$ intermetallic phase. The Mn picked up here is from the 98% Mg substrate and explains the brighter appearance under backscatter contrast.

The interdiffusion of components in a binary system, like that shown here, can be described by Fick's law as follows [146].

$$\tilde{J}_i = -\tilde{D}\frac{\partial C_i}{\partial x} \qquad 4\text{-}8$$

Where $\tilde{J}_i$ (mol/m^2/s) is the interdiffusion flux of a component i, $\tilde{D}$ (m^2/s) is the interdiffusion coefficient, C_i (mol/m^3) is the concentration of component i, and x (m) is the position. The interdiffusion coefficient will vary according to the composition at a given position, and is the same for both components [146]. The work of Kulkarni & Luo 2013 [146] extensively discusses the complexity of interdiffusion in an Mg-Al system, and also lists experimentally obtained coefficients for different compositions at different temperatures.

A temperature of 390°C was used in the work presented here, and Kulkarni & Luo 2013 [146] provide interdiffusion coefficients at 380 and 400°C. In an Mg-rich area, with 2 at% Al, these are 8.3×10^{-16} m^2/s and 3.5×10^{-15} m^2/s

respectively, and in an Al-rich area, with 2 at% Mg, they are 9.5×10^{-15} m^2/s and 1.5×10^{-14} m^2/s respectively. These values show that diffusion in an Mg-rich area is around ten times slower than in an Al-rich area.

For the sample described here this means that, in the initial stages of diffusion between the Mg substrate and electroplated Al coating, the Al would migrate into the Mg slower than the Mg migrates into the Al; and indeed this is what is shown. To achieve two similarly sized Mg-rich layers the respective rates of diffusion must be different. Note that the larger Mn atoms are not seen in the top layer because their lower mobility means they are not able to diffuse into the Al coating.

Below these two layers is a third region with a graded composition. Near the interface with the second layer the composition is 84.6 at% Mg, 13.8 at% Al, 0.6 at% Si, 0.3 at% Cl and 0.7 at% Mn. Moving away from this interface in equal steps the amount of Mg gradually increases from 87.6 at%, to 91.6 at%, and finally 93.8 at%, with the amount of Al reducing correspondingly from 11.1 at%, to 6.8 at%, then 4.8 at%. The levels of Si, Cl, and Mn remain relatively consistent throughout the layer. At these quantities of Al it is likely that precipitates of $Mg_{17}Al_{12}$ intermetallic have formed. This, along with the presence of heavier elements, could explain the mottled appearance under backscatter contrast.

Abrasion of the Mg substrate prior to electroplating with Al has resulted in diffusion being able to proceed during subsequent heat treatment, and this supports the idea that a thin oxide had previously been acting as a barrier. The environmental controls needed for the IL are therefore advantageous for the formation of IM layers by this method as they also reduce the rate of native oxide reformation. It is also conceivable that an electropolishing technique could be used instead of physical abrasion, although this has not been explored.

4.1.3.2 Further Process Refinements

The initial premise for using pure Mg was to examine the diffusion processes in the absence of other elements. Some success was achieved with 98% Mg but the layers were not consistently uniform. Subsequent attempts with 99.9% Mg resulted in lower quality Al coatings and heat treatment did not yield any intermetallic layers. However, further refinement of the methodology in an attempt to overcome the problem was invaluable in understanding the critical parts of the process. Examination has shown that the IL will react with the Mg substrate at two key steps in such a way as to prevent a well adhered Al coating from forming.

Key Step 1 – Exposure to the Ionic Liquid

The first detrimental reaction occurs when the Mg substrate is submerged in the IL. At this point the IL is stable and the Mg has no appreciable protective oxide film, this having been removed by abrasion. Despite no current actively being passed through the system a surface layer was observed to develop, and subsequent EDX analysis showed that this was an Al deposit. The deposit generated by this mechanism is weakly adhered to the substrate and its thickness appears to be self-limiting. Consequently when the current is switched on Al is deposited on top of this weak layer.

Measurements of potential for Mg, Al and steel against the coiled Al wire, which is connected as the anode during electroplating, yields values of −105 mV, −8.7 mV, and +800 mV respectively. These confirm that Al is neutral against an Al reference, while steel is slightly more noble and Mg is significantly more active. Thin Al layers do not form on Al or steel if left submerged in the IL and therefore the deposition seen with Mg is thought to be linked to a displacement reaction caused by its electrochemical activity in the IL.

When Mg is exposed to the IL it begins to self-corrode according to the anodic partial reaction in Equation 4-9. This results in the dissolution of Mg^{2+} ions into the IL and makes electrons available to react at cathodic sights and deposit Al according to Equation 4-10, as would normally happen when a current is passed.

Anodic partial reaction

$$3Mg \rightarrow 3Mg^{2+} + 6e^{-} \quad \text{4-9}$$

Cathodic partial reaction

$$8Al_2Cl_7^{-} + 6e^{-} \rightarrow 2Al + 14AlCl_4^{-} \quad \text{4-10}$$

This effect is self-limiting because once a uniform layer of Al has built up the Mg is isolated from the IL and there is no longer a potential difference driving the reaction. Turning on the power prior to exposure of the Mg to the IL should ensure that the desired Al electrodeposition reaction occurs in preference. A further proof of this theory would be to check for Mg contamination in the IL but this has not been possible.

Key Step 2 – Removal from the Environmental Chamber

A second detrimental reaction occurs when an Al electroplated Mg sample is removed from the environmental chamber. At this point any residual IL reacts with moisture in the atmosphere to form hydrochloric acid that in turn reacts vigorously with the Mg substrate. In severe cases this can lead to an Al coating, which previously appeared well formed, becoming entirely detached from the Mg substrate. It is therefore important to remove as much residual IL as possible while the sample is in the chamber. This reaction appears to be worse if the weak Al layer has been allowed to form suggesting that it can more easily retain residual IL compared the electrodeposited Al.

4.1.3.3 Intermetallic Layers on AZ91D

Aluminium was electrodeposited on to a series of AZ91D specimens using the methodology that was developed during the work with pure Mg. These samples were subsequently heat treated at 390°C for 1, 2, 4, 6, 8, and 12 h to produce coatings with varying degrees of diffusion and the resulting microstructures are examined in this section.

Electrodeposition of Al on to AZ91D

The first step in preparing an AZ91D sample for electroplating was to abrade it with P4000 SiC paper and then ultrasonically clean in isopropyl alcohol (IPA). Once abraded and cleaned for the first time each sample was kept in IPA and transferred to the environmental chamber where it was abraded with P4000 SiC paper for a second

time before being rinsed in IPA and allowed to dry. The sample was then submerged in the IL and electroplated by applying a 10 mA/cm^2 current density for 1.5 h, after which time it was lifted out and allowed to drip dry in the chamber for at least 12 h. A further rinse with IPA was then carried out before it was removed from the chamber and dried thoroughly with a stream of warm air.

Characteristics of an Al Coating Prior to Heat Treatment

The SEM images in Figure 4-6 show typical examples of the surface of an AZ91D specimen following electrodeposition. These reveal the granular nature of the deposit and illustrate how the Al crystals, which are all less than 10 µm across, grow with a characteristic facetted structure.

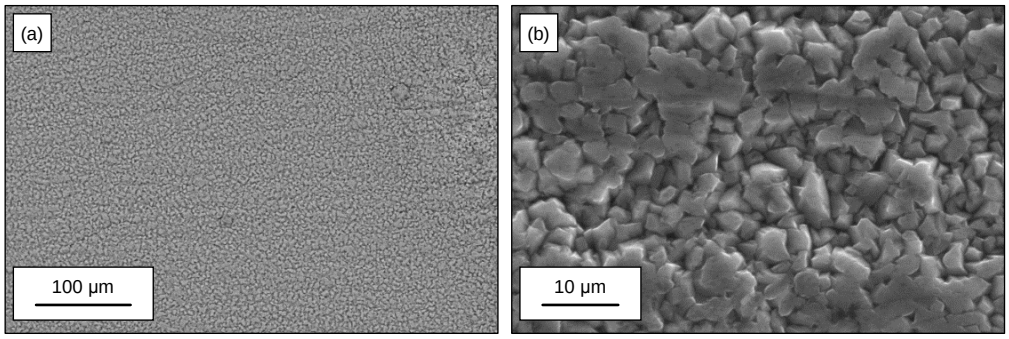

Figure 4-6 – SEM images showing the top surface of an AZ91D substrate with electroplated Al at (a) 250× magnification and (b) 2000× magnification. Characteristic faceted Al crystals are visible and these all less than 10 µm across.

The thickness of the Al deposited on to AZ91D was confirmed by examining a cross-section (Figure 4-7). This SEM image shows that the layer produced by electrodeposition was not of a uniform depth and in this example it ranges from 10 to 38 µm, with a mean depth of 30 µm. The non-uniformity of the coating compared to that produced on 98% Mg could be as result of variations in microstructure due to their differing compositions.

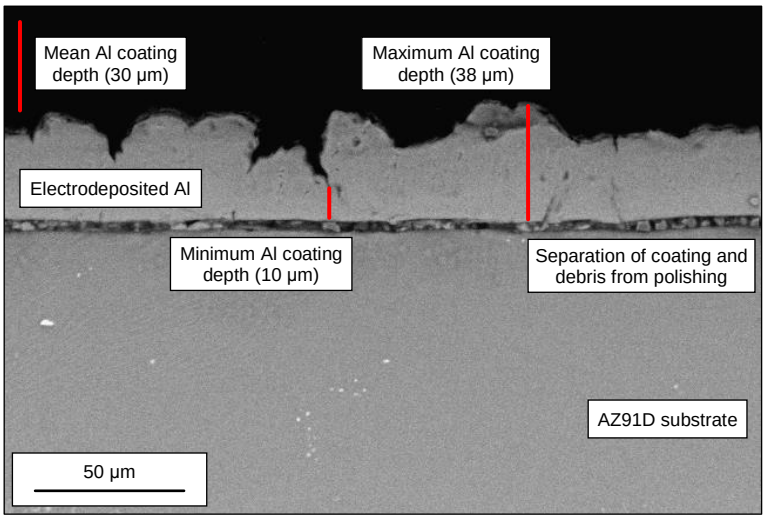

Figure 4-7 – SEM image showing a cross-section through an AZ91D substrate with an electrodeposited Al coating and no heat treatment.

The separation of the coating and substrate seen here has been caused by shrinkage of the mounting resin while curing. This has pulled away the Al layer and the resulting gap has subsequently filled with polishing debris. If separation of this magnitude was a characteristic feature of the coating then diffusion would not have occurred during the heat treatment of other AZ91D samples.

Post Heat Treatment Characteristics

The optical image in Figure 4-8 is typical of a sample following heat treatment and shows four characteristic features. At the far left is a portion of the original AZ91D substrate that, because the sample was not fully immersed, would have been just above the IL surface during electroplating. Adjacent to this is an area of electrodeposited Al that did not diffuse during heat treatment. Some regions of non-diffused Al are seen on every sample but the location of this one — at a point just below the surface of the IL during electroplating — is common to all of them.

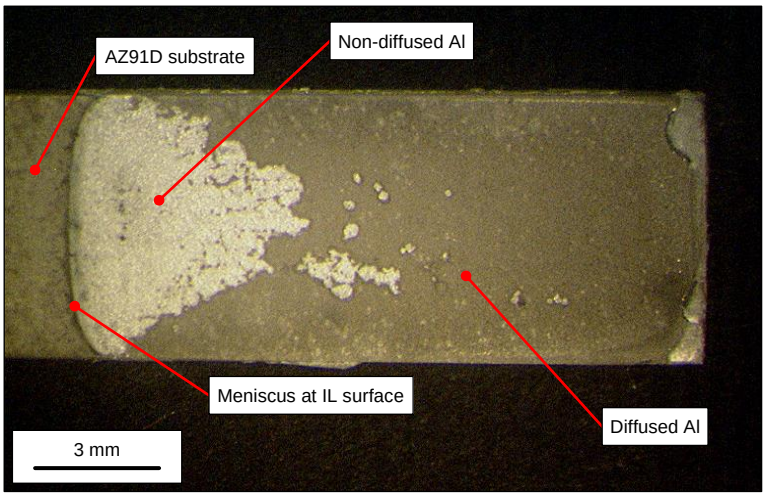

Figure 4-8 – Optical image showing an AZ91D substrate with an electrodeposited Al coating following heat treatment at 390°C for 6 h. The labelled features are typical of those seen for every heat treatment during. Note that the sample was not fully immersed in the IL, so an area of substrate and an associated meniscus line can be seen.

The lack of diffusion here shows that the substrate and coating were not in good contact during heat treatment. Their separation is thought to have been caused by capillary action drawing in residual IL, and/or IPA used to rinse the sample, at the boundary between the electroplated and non-electroplated parts of the substrate. To the right of the non-diffused region is a darker area where diffusion has taken place.

Examination of Non-Diffused Surface Regions

Each of the six samples heat treated for 1, 2, 4, 6, 8 and 12 h respectively was analysed by EDX at three locations of non-diffusion spread out across the surface, with ten analysis points selected randomly per area. The SEM image in Figure 4-9 shows a representative one of these areas and confirms that the appearance of the facetted Al crystals, which were seen in Figure 4-6 prior to heat treatment, has not been altered.

Of the 180 surface points examined across all of the samples 135 exhibited only Al and the rest had no less than 97 at% Al. The remainder was either all, or a combination of, Mg or Cl with no more than 3 at% and 2 at% of each respectively. As described previously the presence of Cl indicates that residual IL has remained in some of these regions, with its subsequent reaction on contact with moisture in atmospheric air having a detrimental effect on the coating.

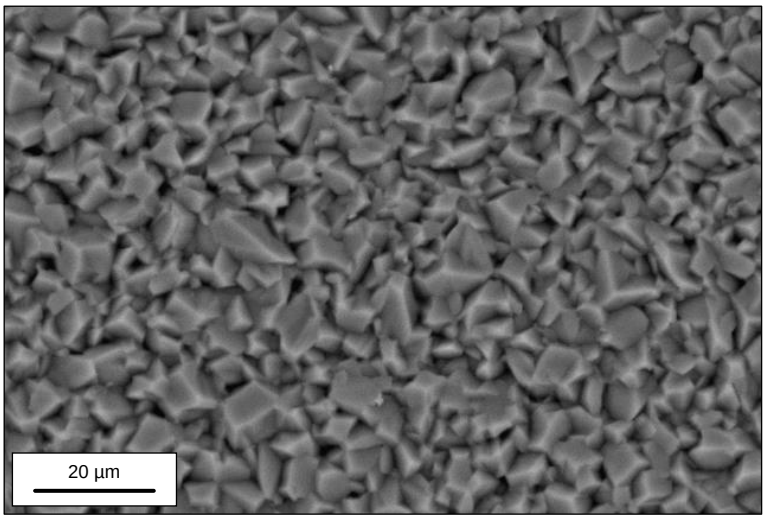

Figure 4-9 – SEM image showing a non-diffused area on the top surface of an AZ91D substrate with an electrodeposited Al coating following heat treatment at 390°C for 6 h. The appearance of the Al crystals is the same as those seen in Figure 4-6 prior to heat treatment.

The small percentages of Mg seen in the analysis could have come from any of three sources. Firstly the EDX may have picked up the AZ91D substrate although, with a minimum coating depth of 10 µm (Figure 4-7) and an electron penetration depth in Al of around 3 µm at an acceleration voltage of 20 kV, this is unlikely. Secondly small particles of Mg could have been left on the surface following the second abrasion step in the electroplating chamber. During subsequent electrodeposition these may have become trapped by the growing Al crystals and transported outwards to a point where they are close enough to the surface to be captured by EDX. Finally it is also possible that some diffusion may have occurred at localised areas despite there being no clear visual signs of this on the surface.

Examination of Diffused Surface Regions

The SEM image in Figure 4-10 shows the distinctive surface appearance at a region where the Al coating and AZ91D substrate have diffused together during heat treatment. The crystalline structure of the electrodeposited Al is still visible, and the dimensions of the crystals are of a similar size (up to 10 µm), but they are now less sharply defined.

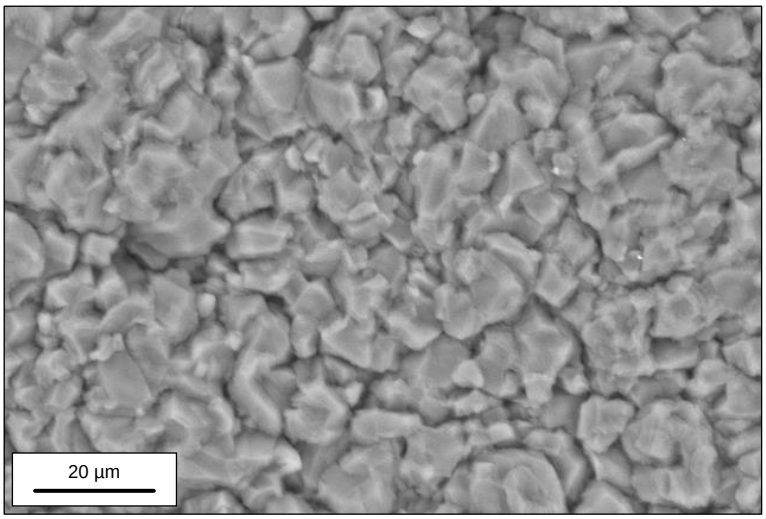

Figure 4-10 – SEM image of an area of diffusion on the top surface of an AZ91D substrate with an electrodeposited Al coating following heat treatment at 390°C for 6 h. The Al crystals are less sharply defined compared to a non-diffused region.

Analysis by EDX of the diffused regions on each sample was carried out in the same manner as with the non-diffused areas, with three locations and ten points selected at random giving thirty points per heat treatment duration. This information has been summarised in Figure 4-11 where each bar represents the composition at a single point. The horizontal lines indicate the quantities of Mg that would be expected for the intermetallic phases $Mg_{17}Al_{12}$ and Mg_2Al_3.

As the heat treatment duration increases there is a trend towards a greater quantity of Mg at the surface, with a mean of 41 at% after 1 h and 70 at% at 12 h. There is also variation in the amount of Mg at the surface of each sample, and the degree of spread appears to be influenced by heat treatment as it becomes larger as the duration increases.

The analysis points on the sample heat treated for 1 h have compositions of around 41 at% Mg, which is in line with that of the Al-rich intermetallic Mg_2Al_3 (40 at% Mg). Following a 2 h treatment the surface was further enriched with Mg and the majority of the analysis points exhibited compositions at or below that of $Mg_{17}Al_{12}$ (59 at% Mg) with the lowest being 49 at% Mg. At heat treatments of 4, 6 and 8 h the mean surface composition sits around that of $Mg_{17}Al_{12}$ with some spread either side. After 12 h the compositions tend to be richer in Mg and above the $Mg_{17}Al_{12}$ line.

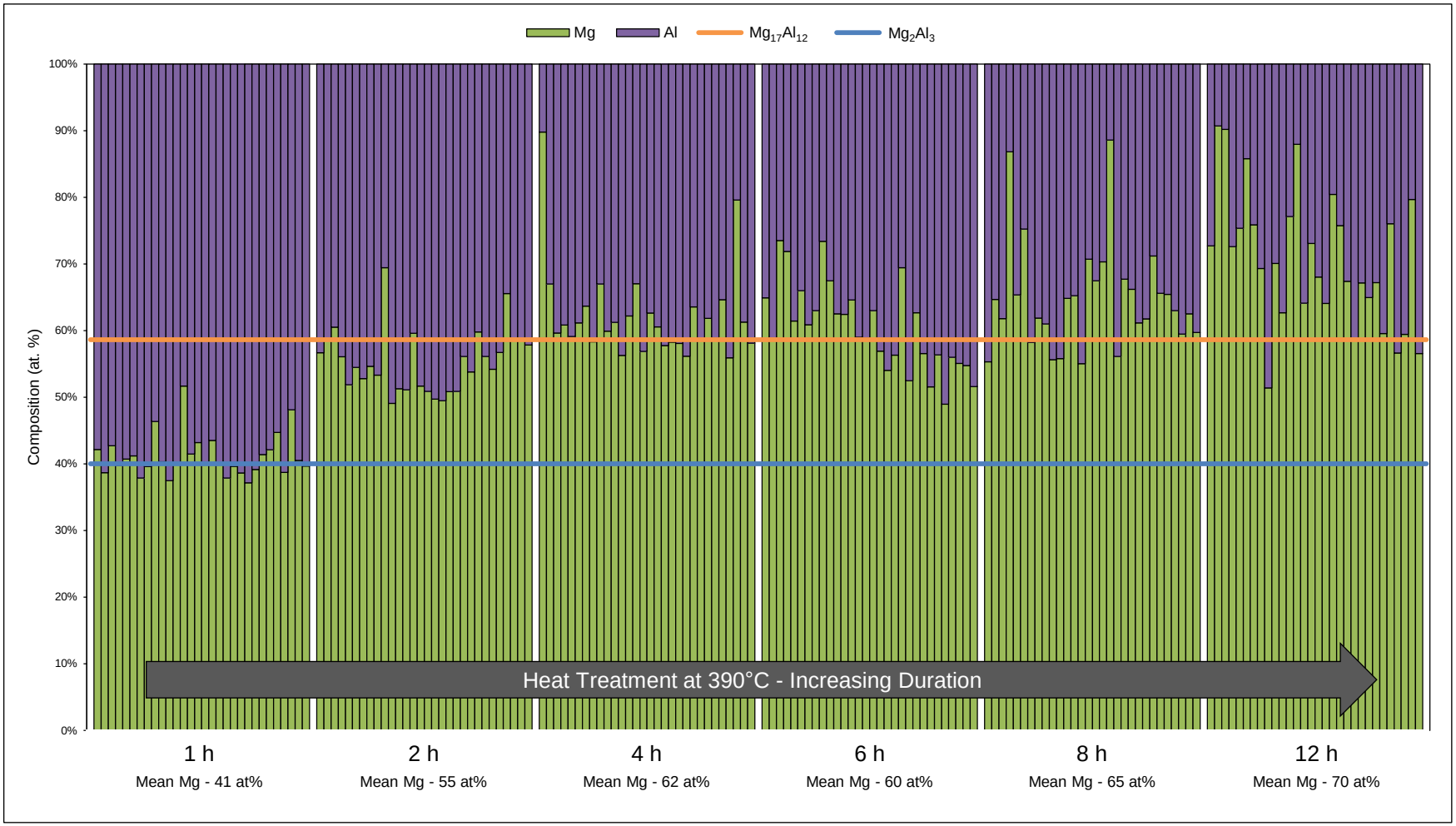

Figure 4-11 – Summary of the surface analysis data collected for each of the heat treated samples. Each bar represents the composition at an analysis point and the horizontal lines indicate the quantities of Mg that would be expected for the intermetallics $Mg_{17}Al_{12}$ and Mg_2Al_3.

The presence of intermetallic phases is also supported XRD and Figure 4-12 gives example before and after spectra for the 1 h heat treatment. Although the AZ91D alloy used here contains the $Mg_{17}Al_{12}$ intermetallic, as shown in Section 4.2.3.3, it is not visible in the before spectra as the peaks are suppressed by the Al coating. Peaks for both intermetallic phases can be identified for the 1 h and 2 h heat treatments, but only $Mg_{17}Al_{12}$ appears after the 4, 6, 8, and 12 h cycles.

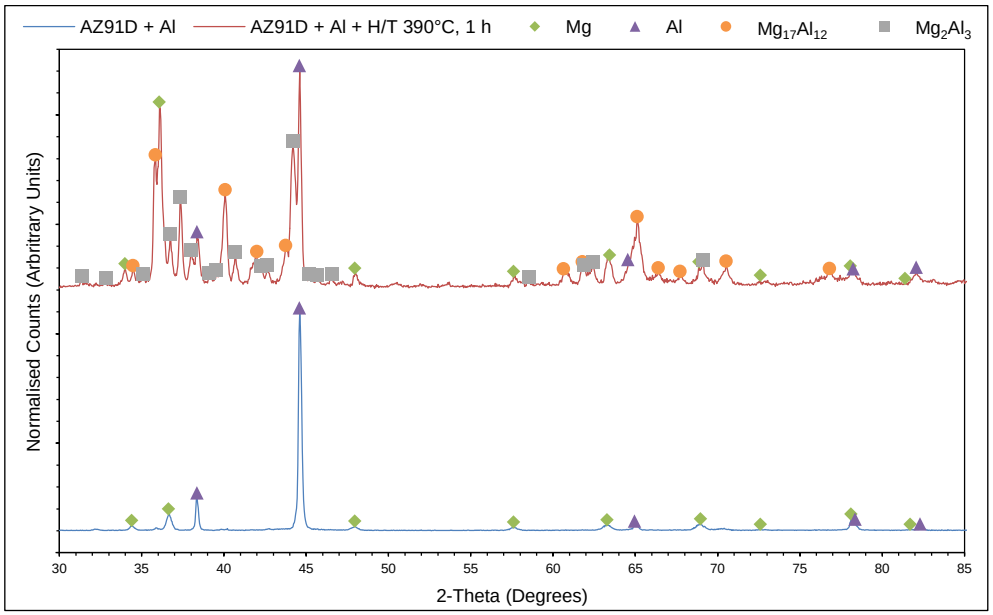

Figure 4-12 – XRD spectra for Al coated AZ91D before (bottom) and after (top) heat treatment at 390°C for 1 h. Before heat treatment only peaks for Al and Mg are identified but afterwards additional peaks that corresponding to the $Mg_{17}Al_{12}$ and Mg_2Al_3 intermetallic phases are visible.

Examination of Diffusion Cross-Sections

Examination of cross-sections of each sample reveals more about what has happened during heat treatment, and confirms that the $Mg_{17}Al_{12}$ seen in the XRD spectra is not just from the substrate. Three areas were selected for EDX analysis on each sample and the information gathered is summarised in Figure 4-13. The SEM images show areas representative of each sample and the adjacent bars are mean compositions from three corresponding analysis points, which are labelled Spectrum 1-10. Horizontal lines indicate the quantities of Mg that would be expected for AZ91D, $Mg_{17}Al_{12,}$ and Mg_2Al_3. It should be noted that small quantities of Si, Cl, Mn, and Zn were also detected but have been removed for clarity. The images in Figure 4-13 are also shown separately in Figure 4-14 to Figure 4-19.

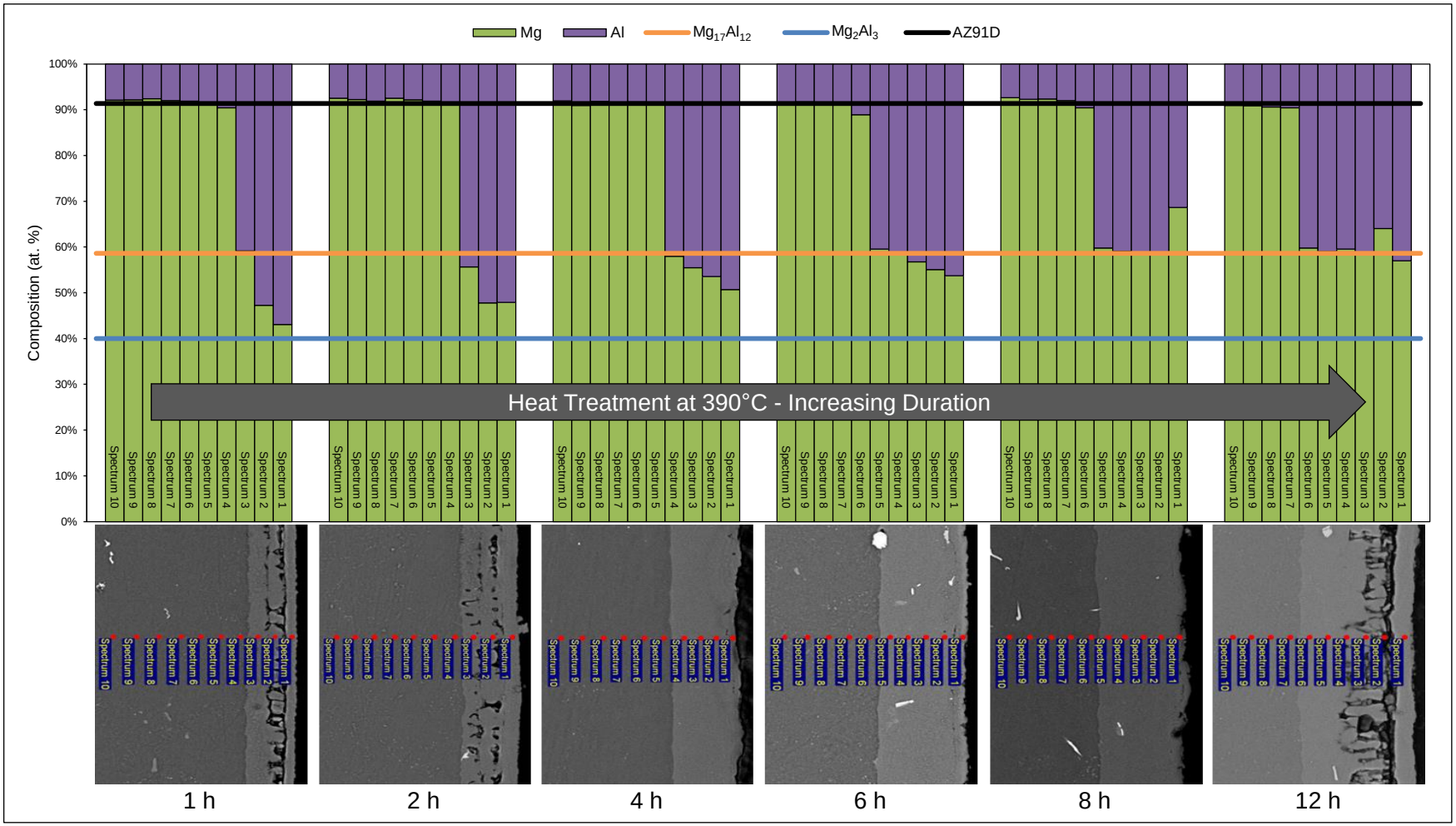

Figure 4-13 – Summary of cross-section analysis data collected for the heat treated samples. Each bar represents the composition at a point on the adjacent image and the horizontal lines indicate the quantities of Mg that would be expected for AZ91D, $Mg_{17}Al_{12,}$ and Mg_2Al_3.

Varying the heat treatment time has led to diffusion and graded layers that exhibit a distribution of phases. Comparison of the structures formed over different heat treatment durations suggests that the rate of diffusion is such that any Mg_2Al_3 intermetallic, formed of by Mg enrichment of the Al coating, is quickly transformed into a solid solution and ultimately $Mg_{17}Al_{12}$. At the 1 h and 2 h heat treatments three distinct layers are seen above the substrate material. Analysis shows that the layer adjacent to the substrate consists mainly of the $Mg_{17}Al_{12}$ intermetallic. In both cases it is not possible to prescribe a particular phase to the top and middle layers although they appear to be a combination of $Mg_{17}Al_{12}$, Mg_2Al_3 and solid solution. An increasingly $Mg_{17}Al_{12}$ rich composition is seen in the layers produced at 4 h and 6 h respectively with some solid solution and very little, if any, Mg_2Al_3. At the 8 h and 12 h heat treatments the diffusion layer appears to be mainly $Mg_{17}Al_{12}$.

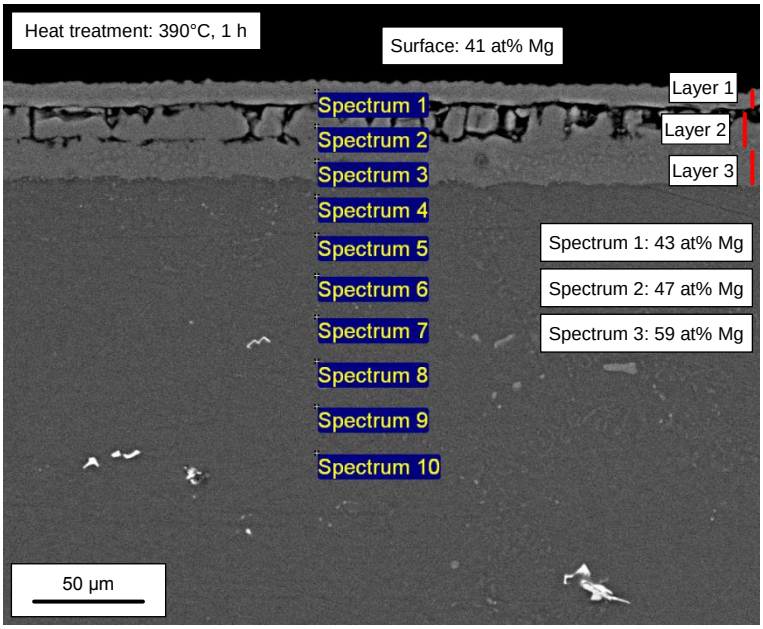

Figure 4-14 – SEM image and EDX analysis points of a cross-section of an AZ91D substrate with an electroplated Al coating heat treated at 390°C for 1 h. Listed compositions are mean values from three similar sites with Al as the remainder.

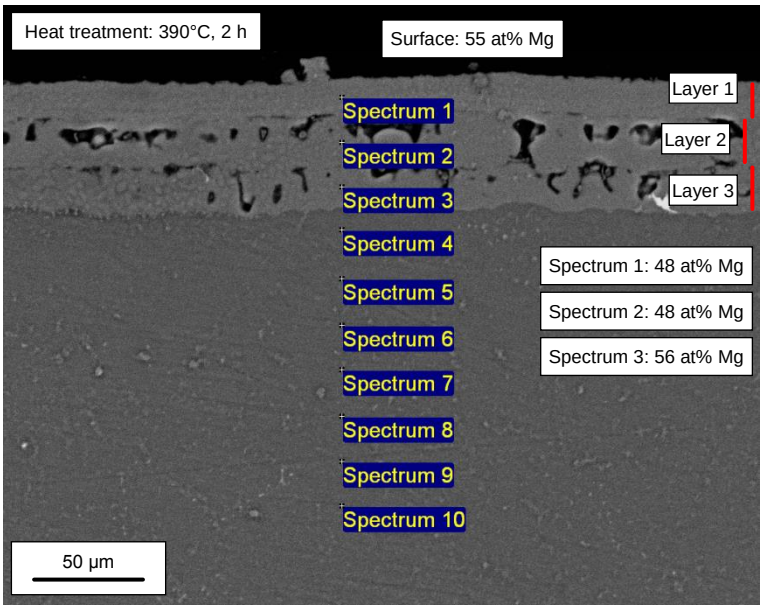

Figure 4-15 – SEM image and EDX analysis points of a cross-section of an AZ91D substrate with an electroplated Al coating heat treated at 390°C for 2 h. Listed compositions are mean values from three similar sites with Al as the remainder.

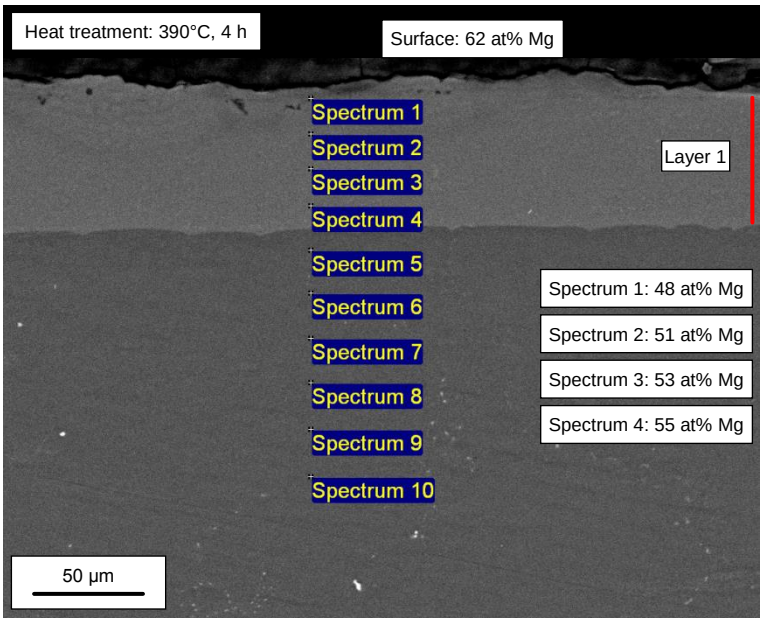

Figure 4-16 – SEM image and EDX analysis points of a cross-section of an AZ91D substrate with an electroplated Al coating heat treated at 390°C for 4 h. Listed compositions are mean values from three similar sites with Al as the remainder.

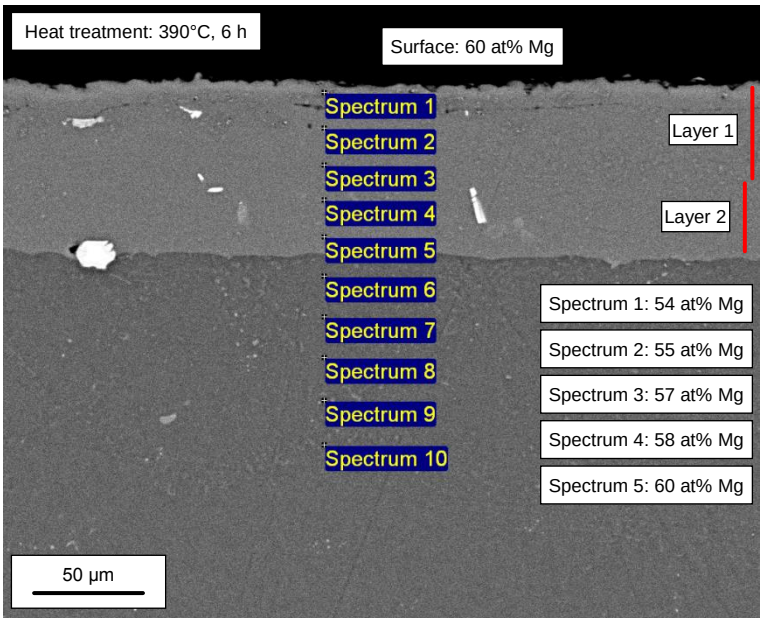

Figure 4-17 – SEM image and EDX analysis points of a cross-section of an AZ91D substrate with an electroplated Al coating heat treated at 390°C for 6 h. Listed compositions are mean values from three similar sites with Al as the remainder.

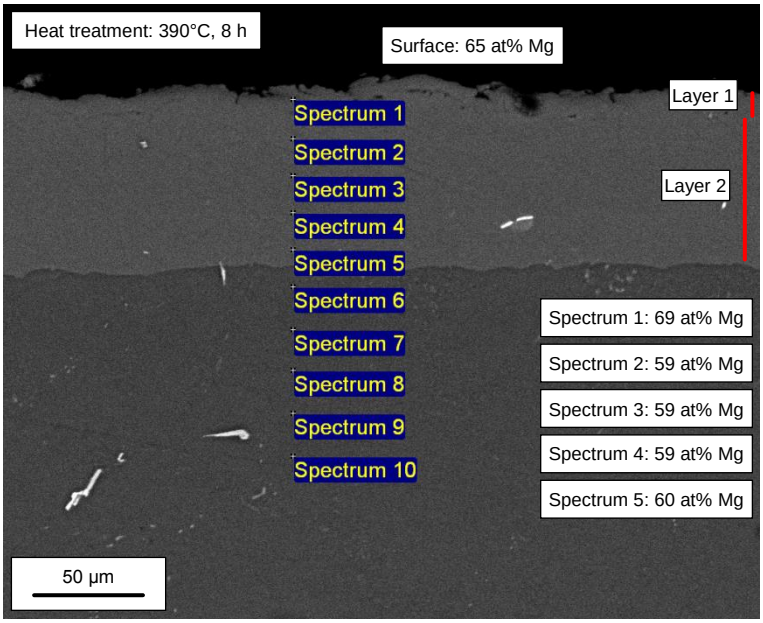

Figure 4-18 – SEM image and EDX analysis points of a cross-section of an AZ91D substrate with an electroplated Al coating heat treated at 390°C for 8 h. Listed compositions are mean values from three similar sites with Al as the remainder.

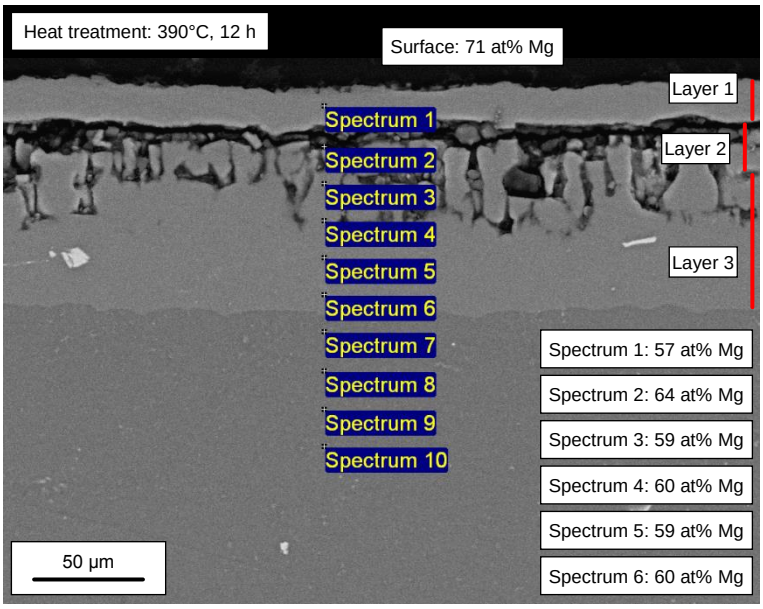

Figure 4-19 – SEM image and EDX analysis points of a cross-section of an AZ91D substrate with an electroplated Al coating heat treated at 390°C for 12 h. Listed compositions are mean values from three similar sites with Al as the remainder.

4.1.4 Further Discussion

A review of the literature in Section 2.2 highlighted that intermetallic layers can be produced using a number of Al sources, including contact diffusion, powder diffusion, sputtering, thermal spray, molten salts, and electrodeposition. As with this work the structure of the layers was dependent on the duration of diffusion, as well as the temperature at which it occurred. Yang *et al.* 2011 [68] used the same electrodeposition process that has been employed in this work, and the diffusion layers that were produced on an AZ91D substrate were shown previously in Figure 2-17.

Although the heat treatments used by Yang *et al.* 2011 [68] are different to those used here, similar characteristics are observed. At the higher temperature (420°C) for a shorter duration (2 h), the layer is similar to those produced in this work at 390°C for between 4 and 8 h. When a lower temperature (200°C) longer duration (12 h) treatment is applied the layer is comparable to those formed at 390°C for between 1 and 2 h.

Section 1.3 described the role that intermetallic phases play in the self-corrosion of certain Mg-Al-Zn alloys. The presence of $Mg_{17}Al_{12}$ in the microstructure is understood to result in the formation of micro-galvanic couples between other phases and accelerate their corrosion. This mechanism could have consequences for the addition of an Mg-Al intermetallic layer to an Mg substrate, as it is conceivable that a similar galvanic couple could develop if the protective surface is damaged. The subsequent experimental work was conceived with this in mind.

4.1.5 Summary

This investigation into the practicalities of forming a protective intermetallic surface layer through the heat treatment of an Al coated Mg substrate has shown that the quality of the electrodeposited Al is fundamental to achieving subsequent diffusion. It is essential that any protective surface oxide film is removed from the substrate prior to electroplating, and care must be taken at two critical stages during the process.

The main results of this work are summarised in Figure 4-13, which shows that different layer structures can be formed on an AZ91D substrate by altering the heat treatment duration. Analysis of the graded diffusion layers revealed that the $Mg_{17}Al_{12}$ and Mg_2Al_3 intermetallic phases will form as diffusion proceeds, with discreet layers developing if conditions are correct. When this occurs the Mg-rich $Mg_{17}Al_{12}$ is seen adjacent to the substrate while Al-rich Mg_2Al_3 forms at surface.

4.2 Mg-Al-Zn Alloy Microstructures

4.2.1 Introduction

This section examines the as received microstructures of samples of the Mg alloys AZ31B, AZ61A, and AZ91D. Optical microscopy has been used in combination with EDX, XRD and EBSD to provide a comprehensive evaluation of the alloys and the findings are discussed with reference to the Mg-Al binary phase diagram with the aim of understanding how manufacturing and processing can deliver their characteristic structures.

4.2.2 Materials and Methods

4.2.2.1 Mg-Al-Zn Alloys

The materials used in this work were ASTM standard Mg-Al-Zn alloys AZ31B, AZ61A, and AZ91D. Both the AZ31B and AZ61A were cut from 1 mm thick rolled sheets, while the AZ91D was sectioned from a 5 mm thick cast bar. The processing and heat treatment condition of these materials was not known.

Preparation of the samples prior to examination involved mounting in epoxy resin, followed by an initial grinding down to P4000 SiC paper with water to achieve a flat and uniform surface. A further grinding was then carried out using P4000 SiC paper coated in wax, with a glycerol/IPA mix for lubrication. This was done to remove any oxide that may have developed during grinding with water. A series of polishing steps were then conducted using oil based diamond pastes ranging from 6 to 1 µm, and IPA as a lubricant. Samples being examined optically were given a final short polish (maximum of 2 minutes) with colloidal silica, before being etched with dilute acetic picral. Those being examined by SEM and EDX were given the same short final polish but were not etched. For the EBSD analysis the duration of the final polish with colloidal silica was a minimum of 20 minutes, and no etch was used.

The EDX analysis results in Table 4-2 list the major elements present in these materials. AZ31B, AZ61A, and AZ91D should contain a nominal 3, 6, and 9 wt% Al respectively, as well as a nominal 1 wt% Zn. The analysis confirms that the primary constituents of these alloys fall within the ASTM specifications given previously in Table 1-3. The impurity elements — Fe, Ni, and Cu — discussed in Section 1.3.1 were not detected, which shows that they were significantly below the levels that might affect corrosion behaviour.

Table 4-2 – Analysed compositions of AZ31B, AZ61A, and AZ91D.

Material[A]	Al	Cu[B]	Fe[B]	Mn	Ni[B]	Zn	Mg
AZ31B	2.69	-	-	0.38	-	1.30	95.63
AZ61A	5.86	-	-	0.28	-	0.99	92.87
AZ91D	8.43	-	-	0.13	-	0.81	90.63

A - All values in weight %. Only elements that were identified by analysis are shown.
B - 'Impurity' elements included in table but not picked up by this analysis.

4.2.2.2 The Mg-Al Binary Phase Diagram

The Mg-Al-Zn group of Mg alloys have microstructures that are dominated by the Mg-Al system and the constraints of the associated binary phase diagram in Figure 4-20. The nominal Al content of the AZ31B, AZ61A, and AZ91D alloys examined here is 3, 6, and 9 wt % Al respectively, and composition lines representing these are marked on the phase diagram. The variation in Al content results in each alloy crossing the liquidus, solidus and solvus lines at different temperatures under equilibrium cooling. These points are marked *a* to *i* on the phase diagram and the associated temperature and composition values are listed in Table 4-3.

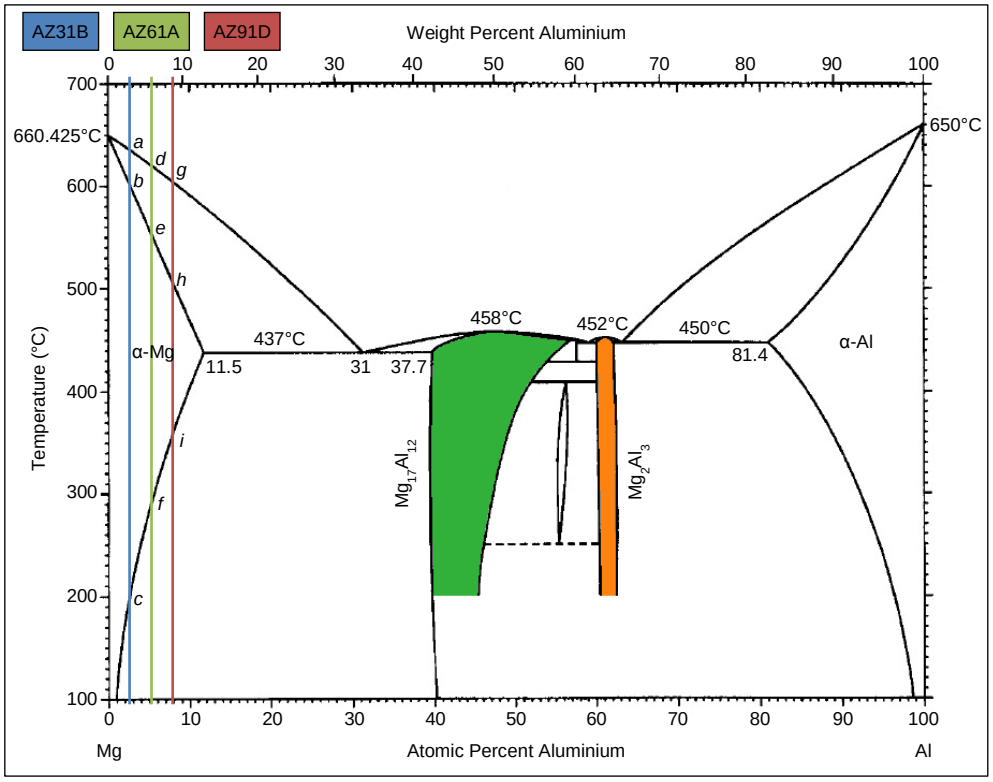

Figure 4-20 – Mg-Al binary phase diagram showing the $Mg_{17}Al_{12}$ and Mg_2Al_3 intermetallic phases, and equilibrium cooling composition lines for the Mg alloys AZ31B, AZ61A and AZ91D [147]. The points at which these cross the liquidus, solidus and solvus lines are marked and the associated temperature and composition values are listed in Table 4-3.

Table 4-3 – Temperature and composition values for the alloys AZ31B, AZ61A, and AZ91D at the points marked on the binary phase diagram in Figure 4-20.

Alloy	Liquidus				Solidus				Solvus	
	Point	Temp.	First solid (% Al)	Liquid (% Al)	Point	Temp.	Solid (% Al)	Last liquid (% Al)	Point	Temp.
AZ31B	*a*	635°C	1 wt%	3 wt%	*b*	600°C	3 wt%	9.5 wt%	*c*	210°C
AZ61A	*d*	620°C	1.8 wt%	6 wt%	*e*	550°C	6 wt%	18 wt%	*f*	300°C
AZ91D	*g*	604°C	2.9 wt%	9 wt%	*h*	502°C	9 wt%	26 wt%	*i*	370°C

4.2.3 Results and Discussion

4.2.3.1 AZ31B

Microstructure Examination

The optical image in Figure 4-2 shows that the AZ31B alloy has a microstructure consisting of equiaxed grains. There is no evidence of Mg-Al second phases within the grains or at grain boundaries, but some dark inclusion particles are distributed throughout the matrix. EDX analysis of the same sample gave an average Al content of 2.69 wt%, which is within the ASTM standard composition range (2.5 to 3.5 wt% Al), and also revealed that the inclusions contained combinations of Mg (1.9 to 18.0 wt%), Al (47.0 to 52.8 wt%) and Mn (33.2 to 47.3 wt%). Additions of Mn in AZ31B can range from 0.2 to 1.0 wt% (Table 1-3) and it has the combined benefits of increasing creep resistance and improving corrosion resistance by controlling Fe content through the formation of Fe-Al-Mn precipitates at the melting and casting stage as described in Section 1.3.1.

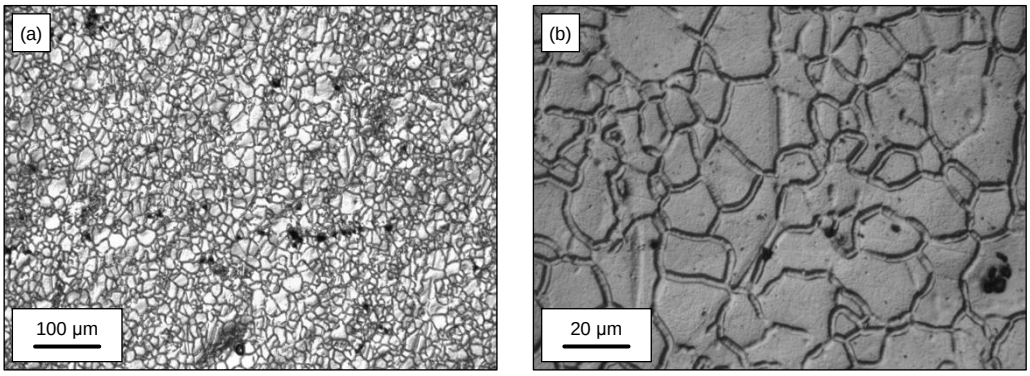

Figure 4-21 – Optical images of AZ31B at (a) 10× magnification and (b) 50× magnification showing equiaxed grains and dark inclusions.

The microstructure of the AZ31B can also be seen in the EBSD image in Figure 4-22, which confirms that the grains are single phase and have a hexagonal close packed (HCP) Mg crystal structure. Aluminium is not seen as it is either in the α-Mg solid solution, or within second phase particles in the grains that are too small to be detect by this method. The EBSD response from the inclusion particles was not of sufficient quality to allow their structure to be fully characterised, although the $Mg_{17}Al_{12}$ phase was identified in some cases.

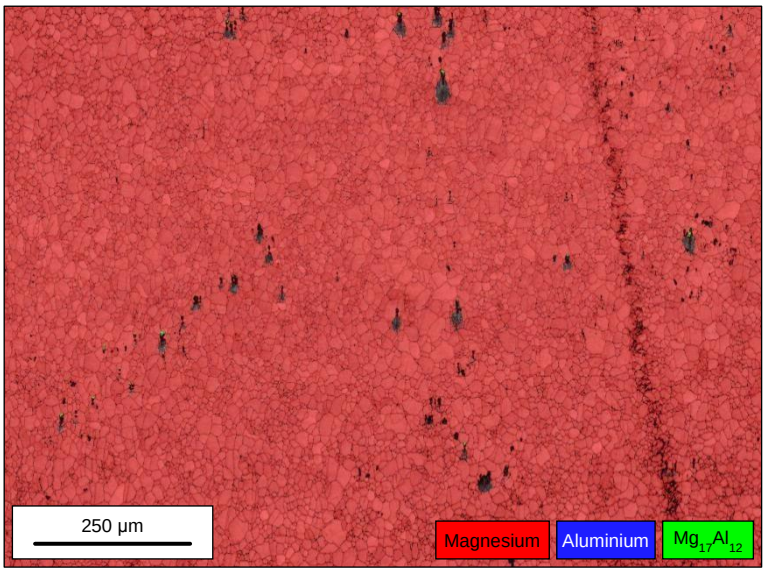

Figure 4-22 – EBSD image of AZ31B showing equiaxed grains and dark inclusions. Grains are single phase and have an HCP Mg crystal structure. Aluminium is held in solid solution, and some of the inclusion particles are shown to contain the $Mg_{17}Al_{12}$ intermetallic.

Microstructure Formation

The Mg-Al binary phase diagram in Figure 4-20 is marked with a composition line for AZ31B with 3 wt% Al. Because the treatment of the alloy is not known the subsequent discussion proposes how the observed structure may have formed. Following the composition line from the liquid phase shows that once the melt reaches the liquidus line at point *a* (635°C) solidification will begin with the precipitation of primary α-Mg grains containing 1 wt% Al. If cooling proceeds under equilibrium conditions these grains will grow and their composition will follow the solidus line until complete solidification at 600°C (point *b*) as a primary α-Mg solid solution with 3 wt% Al. Continued cooling of the solid solution will bring it to the solvus line at 210°C (point *c*) at which point the intermetallic second phase $Mg_{17}Al_{12}$ can begin to precipitate.

Under non-equilibrium cooling, which is a more likely case, solidification will happen at a rate such that there is insufficient diffusion within the α-Mg grains to allow them to equilibrate to the composition line defined by the solidus. Instead a cored structure of α-Mg layers will develop with the centre having a lower fraction of Al compared to the outside. The average composition of the cored structure defines a new α-Mg solidus, thus lowering the final freezing temperature and allowing a liquid with a greater concentration of Al to exist than would be expected [1]. Enrichment of the liquid by this

mechanism could be sufficient to enable eutectic structures of α-Mg and $Mg_{17}Al_{12}$ to develop directly from the liquid in alloys where equilibrium would prohibit their formation.

The AZ31B alloy examined here does not show evidence of any second phases and the relatively low Al content means enrichment of the liquid is not likely to have been sufficient to allow a eutectic to form. The equiaxed grains in this rolled material also indicate that it has undergone heat treatment [148–152]. The ASTM stress-relieving treatment for wrought Mg alloys gives an annealing procedure, which involves heating to 343°C for 2 h [153]. This brings the alloy into the single phase primary α-Mg region and would have resulted in the dissolution of any second phases that may have formed during initial processing. On cooling following heat treatment the alloy would again cross the solvus line at point *c* where the intermetallic phase $Mg_{17}Al_{12}$ could begin to precipitate.

4.2.3.2 AZ61A

Microstructure Examination

The optical images in Figure 4-23 show the structure of AZ61A, and reveal that there are a variety of grain sizes and number of distinct inclusion particles. EDX analysis of several areas of the same sample showed that these inclusions are rich in Al (29 to 51 wt%) and Mn (26 to 42 wt%) with Mg as the remainder (7 to 44 wt%). Additions of Mn in AZ61A can range from 0.15 to 0.5 wt% (Table 1-3).

At the higher optical magnification it is possible to see structures at the grain boundaries and possibly a fine precipitate evenly distributed throughout the matrix. EDX analysis of these area showed that only Mg and Al were present and it is therefore conceivable that the $Mg_{17}Al_{12}$ intermetallic has formed. The composition of the grains was consistently 4.9 wt% Al (95.1 wt% Mg), which is below the ASTM standard range of 5.8 to 7.2 wt% (Table 1-3). This depletion of Al also supports the proposal that some second phases were present.

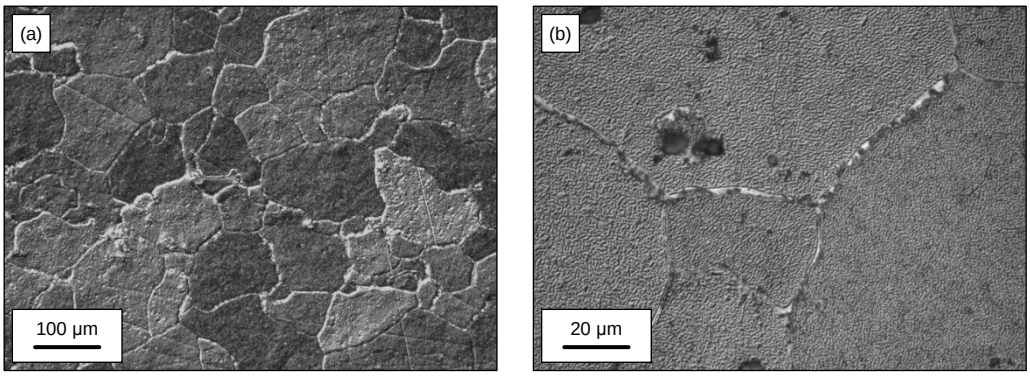

Figure 4-23 – Optical images of AZ61A at (a) 10× magnification and (b) 50× magnification showing a variety of grain sizes and dark inclusions. A higher magnification reveals structures at the grain boundaries and evidence of a fine precipitate evenly distributed throughout the matrix.

The EBSD image in Figure 4-24 confirms that the bulk of the material has an HCP Mg crystal structure, and also shows that $Mg_{17}Al_{12}$ is present in some of the inclusion particles. No Al is seen as it is held in solid solution within the α-Mg grains, and although second phases may have been visible in the optical images their existence was not apparent under EBSD.

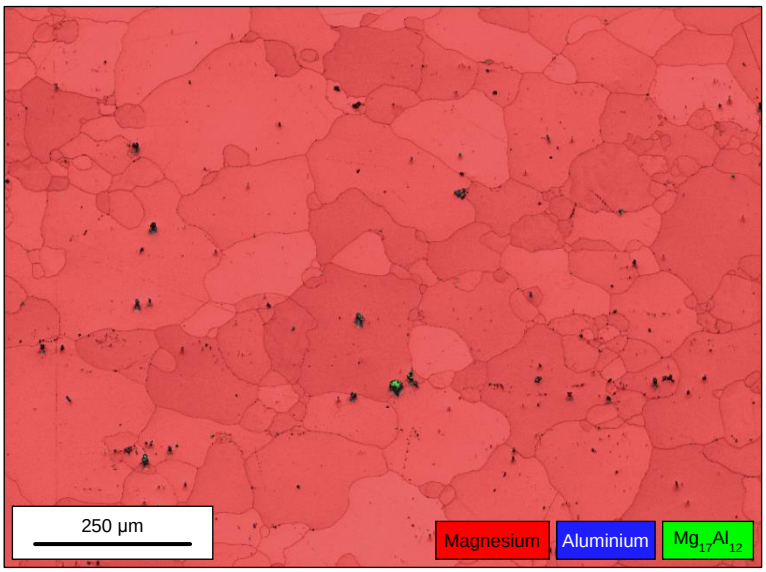

Figure 4-24 – EBSD image of the top surface of an AZ61A alloy showing a variety of grain sizes and large inclusions. Grains have an HCP Mg crystal structure and EDX indicates that 4.9 wt % Al is in solid solution. The $Mg_{17}Al_{12}$ intermetallic is seen in some of the inclusion particles and EDX shows that Al-Mn and Mg-Al-Mn phases may also be present within these.

Microstructure Formation

The Mg-Al binary phase diagram in Figure 4-20 is marked with a composition line for an AZ61A alloy with 6 wt% Al. Because the treatment of the alloy is not known the subsequent discussion proposes how the observed structure may have formed. Following this line from the liquid phase shows that once the melt reaches the liquidus line at point *d* (620°C) solidification begins with the precipitation of primary α-Mg grains containing 1.8 wt% Al. Under equilibrium conditions the composition will follow the solidus line until complete solidification at point *e* (550°C) as a primary α-Mg solid solution with 6 wt% Al. Under non-equilibrium conditions, which are more likely, some Al enrichment of the liquid phase would have occurred, although the lack of a eutectic structure indicates that this was not substantial. The solvus line is reached at point *f* (300°C) after which the alloy is within the two phase region where $Mg_{17}Al_{12}$ can begin to precipitate.

The rounded grains of this rolled material suggest that it has been heat treated and so any phases formed during initial cooling of the melt would have been modified [154]. If the ASTM annealing procedure for wrought Mg alloys was employed (343°C for 2 h) this would take the alloy into the single phase α-Mg solid solution region [153]. The higher Al content of this alloy means that it will enter the two phase region at a higher temperature of 300°C, compared to 210°C for AZ31B. This means there is a greater likelihood of an $Mg_{17}Al_{12}$ precipitate forming, and explains why this may have occurred in AZ61A and not AZ31B.

4.2.3.3 AZ91D

Microstructure Examination

The optical images in Figure 4-25 show that two distinct microstructures are present in cast AZ91D. At the higher magnification it is possible to differentiate a region of continuous and discontinuous precipitates dominated by a lamellar, eutectic type, morphology with some globular structures. Adjacent to this is a region that appears to be largely single phase and has some precipitates at grain boundaries, and possibly within the grains.

The SEM image in Figure 4-26 shows the region of AZ91D that exhibits continuous and discontinuous precipitates in greater detail. EDX analysis confirms that the globular continuous precipitates are the intermetallic phase $Mg_{17}Al_{12}$, with spectra 1 and 3 both having 64 at% Mg and 36 at% Al. Spectrum 4, which is across one of the discontinuous lamella precipitates, is not as rich in Al (85 at% Mg and 15 at% Al) but it still thought the be the $Mg_{17}Al_{12}$ phase. The lower Al content can be explained by the volume activated by the electron beam being larger than the precipitate, meaning some of the surrounding phase has also been picked up. Spectrum 2 is in an area of α-Mg solid solution and contains 96 wt% Mg and 4 wt% Al (97 at% Mg, 3 at% Al). This is leaner than the ASTM specification range of 8.3 to 9.7 wt% Al, and would be expected as some of the Al has been consumed in forming the intermetallic precipitates.

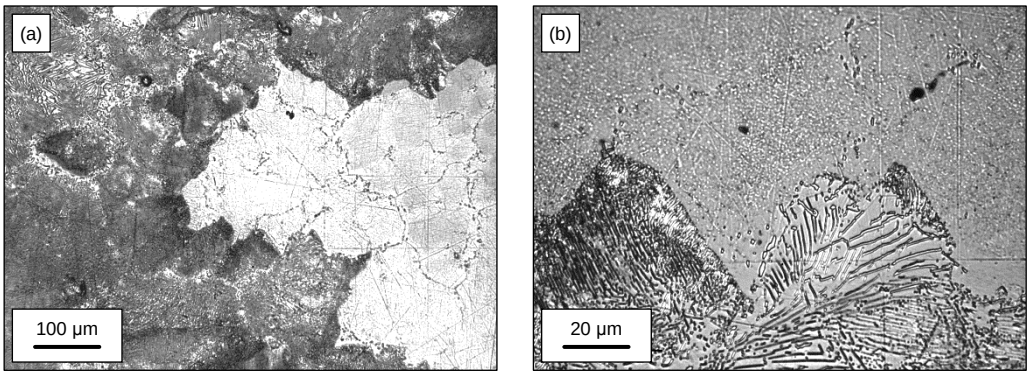

Figure 4-25 – Optical images of AZ91D at (a) 10× magnification and (b) 50× magnification showing two distinct microstructures regions. One has a two phase structure of continuous and discontinuous precipitates; the other is largely single phase with grain boundary precipitates.

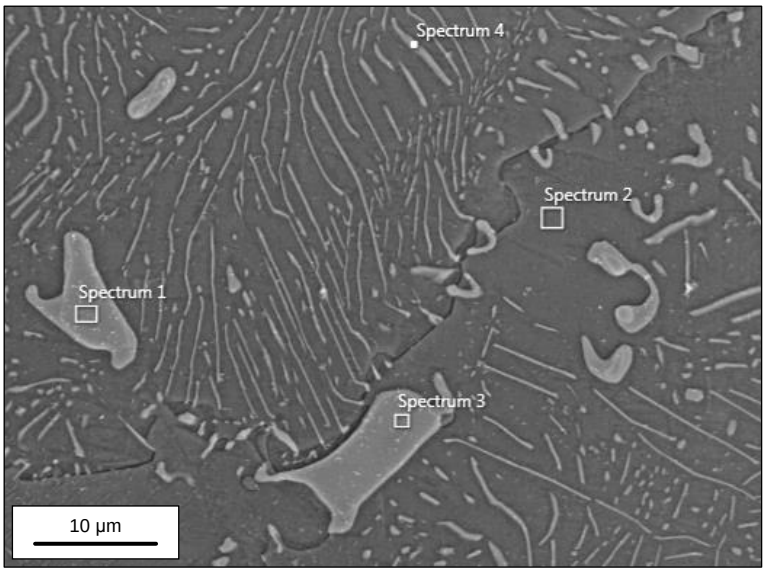

Figure 4-26 – SEM image of the top surface of an AZ91D alloy. EDX analysis shows that the precipitates are the intermetallic phase $Mg_{17}Al_{12}$ and the single phase area in leaner in Mg that that specified by the ASTM standard.

The EBSD image in Figure 4-27 highlights the different grain structure of this cast alloy compared to rolled AZ31B and AZ61A. This image was produced at an area that exhibited both types of morphology — one of continuous and discontinuous precipitates, and one single phase with grain boundaries precipitates — and, although EBSD has not identified the phase, some of the grains show evidence of having a lamellar structure. The bulk of the material has an HCP Mg crystal structure and some continuous $Mg_{17}Al_{12}$ precipitates can be seen in grains and at grain boundaries. EDX showed that the larger inclusion particles comprise of Mg, Al, and Mn and so could, as with AZ31B and AZ61A, contain Al-Mn and Mg-Al-Mn phases, although EBSD only confirms that $Mg_{17}Al_{12}$ has also formed.

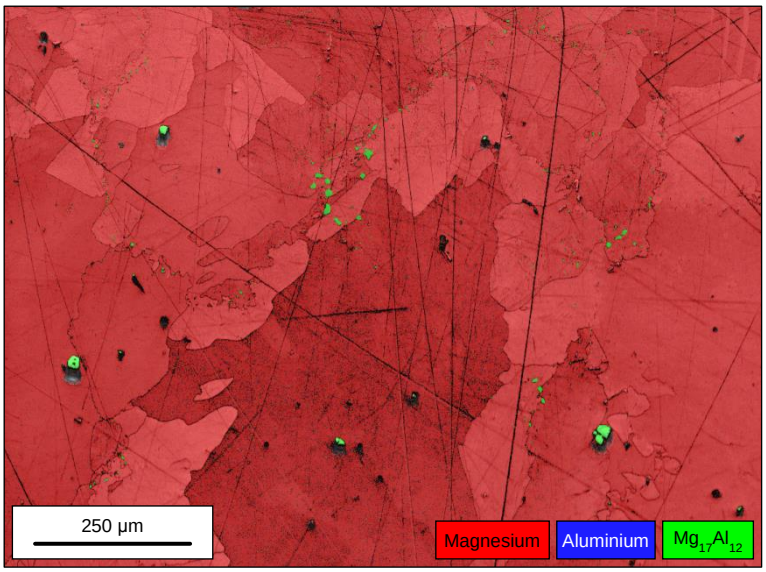

Figure 4-27 – EBSD image of the top surface of an AZ91D alloy showing grains and large inclusions. Grains have an HCP Mg crystal structure and the $Mg_{17}Al_{12}$ intermetallic is seen as a continuous precipitate both within the grains and at grain boundaries. $Mg_{17}Al_{12}$ is seen in the larger inclusion particles, and EDX shows that they may also contain Al-Mn and Mg-Al-Mn phases.

Microstructure Formation

The Mg-Al binary phase diagram in Figure 4-20 is marked with a composition line for AZ91D at 9 wt% Al. Because the treatment of the alloy is not known the subsequent discussion proposes how the observed structure may have formed. Following this from the liquid phase shows that once the melt reaches the liquidus at point *g* (604°C) solidification begins with the precipitation of primary α-Mg grains containing 2.9 wt% Al. Under equilibrium conditions the composition will follow the solidus line until complete solidification at point *h* (502°C) as a primary α-Mg solid solution with 9 wt% Al. The solvus line is reached at point *i* (370°C) after which the alloy is within the two phase region where $Mg_{17}Al_{12}$ can begin to precipitate.

As AZ91D has a higher Al content the degree of Al enrichment of the liquid needed from non-equilibrium cooling to result in the development of a eutectic structure is less. A eutectic type structure is visible in the specimen examined here but the large amount, and its widespread distribution throughout the material, suggests it has formed by precipitation from the solid phase rather than during solidification of the liquid.

The ASTM standard for AZ91D alloys describes T4 and T6 heat treatment schedules, and the application of these can explain the microstructure seen here [153,155]. Both

the T4 and T6 schedules involve solution heat treatment at 413°C for between 16 and 24 h [153]. This takes the alloy to a temperature within the single phase region, the consequence of this being the dissolution of any second phases back into solution. The T6 schedule specifies subsequent aging in two cycles by heating to 168°C for 16 h and then 216°C for 5 to 6 h [153]. Materials with a T4 schedule require no further treatment and undergo natural aging at room temperature [153]. Any subsequent aging takes place within the two phase region and will result in the precipitation of second phases of the type seen here [16].

4.2.4 Further Discussion

Optical images of AZ31B, AZ61A, and AZ91D from this work are compared with literature examples in Figure 4-28, Figure 4-29 and Figure 4-30 respectively. In all cases the grain morphologies are similar to those seen in the literature, although there is disparity in grain sizes between the AZ31B and AZ61A comparisons that is likely to be the result of differences in manufacturing and heat treatment processes. These similarities confirm that the alloys used here have microstructures that are typical of their type, and the variation in phase distribution between them, and in particular the different amounts of $Mg_{17}Al_{12}$, means they are ideal for assessing the effect of the intermetallic on corrosion rate.

This is relevant to the use of protective Mg-Al intermetallic surface layers because, as described in Section 1.3, a damaged layer might result in corrosion involving similar phases and the same galvanic mechanisms. The analysis also shows that AZ31B is comparable in composition to the solid solution phase in AZ91D. This allows the micro-galvanic component of AZ91D corrosion to be modelled by coupling AZ31B with a manufactured sample of $Mg_{17}Al_{12}$.

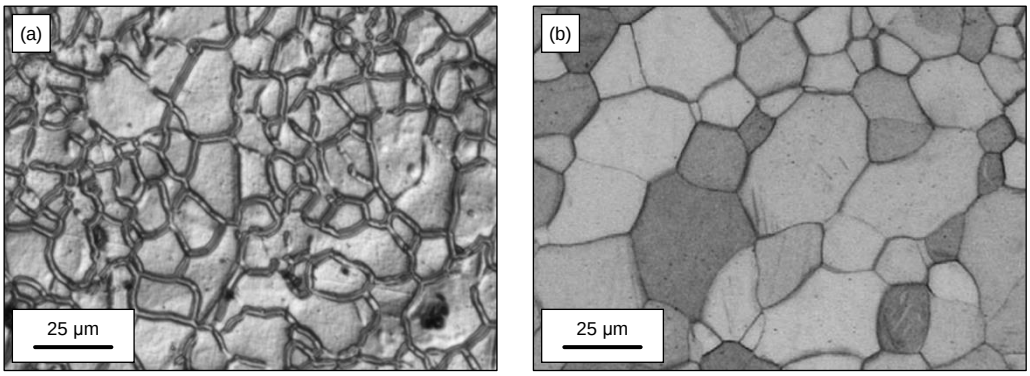

Figure 4-28 – Comparison of optical images of AZ31B from (a) this work, and (b) Jäger *et al*. 2006 [151].

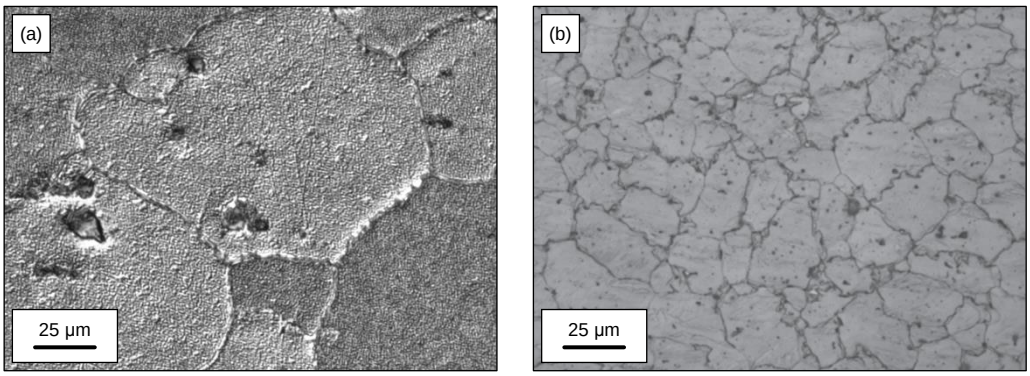

Figure 4-29 – Comparison of optical images of AZ61A from (a) this work, and (b) Kim & Kim 2013 [154].

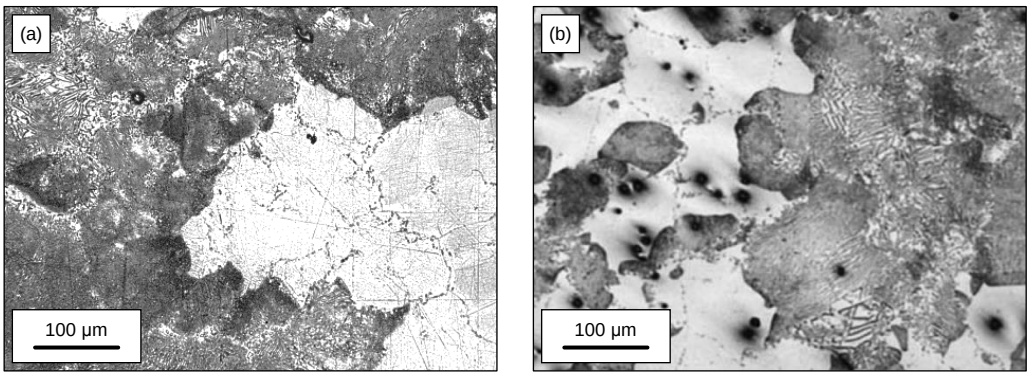

Figure 4-30 – Comparison of optical images of AZ91D from (a) this work, and (b) Čížek *et al*. 2004 [156].

4.2.5 Summary

The metallurgy of Mg-Al-Zn alloys is dominated by the Mg-Al system and the microstructures that develop are linked to Al content, processing during manufacture, and any subsequent heat treatment. The AZ31B, AZ61A and AZ91D alloys, which contain 3, 6 and 9 wt% Al respectively, were examined so that the distribution of Al — either in solid solution with Mg or as $Mg_{17}Al_{12}$ — could be determined. This showed that AZ31B had a largely single phase α-Mg microstructure and some inclusion particles containing $Mg_{17}Al_{12}$. The AZ61A had a similar appearance to AZ31B, but the α-Mg solid solution was richer in Al and there was a greater proportion of the $Mg_{17}Al_{12}$ phase. The appearance of AZ91D was markedly different and exhibited a eutectic type microstructure with lamellae of $Mg_{17}Al_{12}$ separated by α-Mg solid solution.

4.3 Mg-Al-Zn Alloy Self-Corrosion

4.3.1 Introduction

This section examines the corrosion behaviour of 99.9% pure Mg and the Mg-Al-Zn alloys AZ31B, AZ61A, and AZ91D. This is achieved by exposing the materials to 3.5% NaCl solution, recording their open circuit potentials, and measuring their corrosion rates using electrochemical impedance spectroscopy. Reasoned explanations for the differences in corrosion behaviour are given based on material compositions and microstructures, and the implications these have for the use of Mg-Al intermetallic surface layers for improving corrosion performance are highlighted.

4.3.2 Materials and Methods

4.3.2.1 Pure Mg and Mg-Al-Zn Alloys

The materials selected for corrosion testing were 99.9% pure Mg and ASTM standard Mg-Al-Zn alloys AZ31B, AZ61A, and AZ91D. The 99.9 Mg was 0.25 mm rolled sheet and the alloys were 1 mm rolled AZ31B and AZ61A, and a 5 mm section of cast AZ91D. The elemental composition of the 99.9% pure Mg was examined previously in Section 4.1.2.1 and that of the Mg-Al-Zn alloys was confirmed in Section 4.2.2.1, and the quantities of the impurity elements — Fe, Ni, and Cu — discussed in Section 1.3.1 were shown to be below levels that might affect corrosion behaviour. The microstructure of each of the alloys was also discussed in Section 0.

The corrosion behaviour of each material was measured five times, and immediately prior a test they were abraded with P4000 SiC paper and then rinsed in IPA and dried. This ensured that any substantial oxide surface layer was removed, and gave a visually consistent surface roughness.

4.3.2.2 Self-Corrosion Theory

Exposure of any metal to an aqueous environment has the potential to lead to corrosion. The nature of the resulting behaviour is governed by the electrochemical system that is established and to control corrosion it is important to understand the mechanisms by which it occurs. The units given in the following sections are those chosen for consistency and ease of comparison.

The Electrochemistry of Self-Corrosion

The corrosion of Mg in pH neutral 3.5% NaCl solution proceeds according to the following reaction to produce magnesium hydroxide and hydrogen gas [157].

$$Mg + 2H_2O \rightarrow Mg(OH)_2 + H_2 \qquad 4\text{-}11$$

The reaction in Equation 4-11 involves separate oxidation (anodic) and reduction (cathodic) steps and can therefore be split into partial reactions, with Mg oxidised to Mg^{2+} (Equation 4-12) and water reduced to H_2 and OH^- (Equation 4-13) [48,157–159]. This process is insensitive to oxygen concentration [70].

Oxidation (anodic reaction)
$$Mg \rightarrow Mg^{2+} + 2e^- \qquad 4\text{-}12$$

Reduction (cathodic reaction)
$$2H_2O + 2e^- \rightarrow H_2 + 2OH^- \qquad 4\text{-}13$$

During self-corrosion the oxidation and reduction reactions take place together on the metal's surface at anodic and cathodic sites respectively. Electrons that are liberated through the oxidation reaction at anodic sites flow to cathodic sites where the reduction reaction occurs. This is illustrated for Mg corrosion in Figure 4-31. The location and distribution of anodic and cathodic sites is dependent on surface conditions at the time and, as corrosion proceeds and the surface changes, these can move or switch.

The anodic and cathodic partial reactions are two halves of an electrochemical cell, and their interdependence means the rate of oxidation always equals the rate of reduction. The flow of electrons generated by these reactions is directly proportional to the rate of metal loss, and determining this corrosion current (I_{corr}) is the key to understanding how fast a metal is corroding in a particular environment.

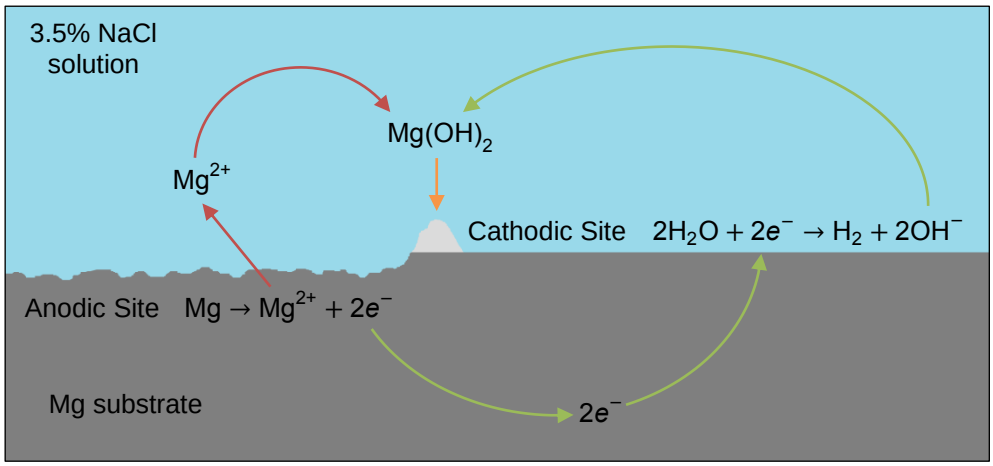

Figure 4-31 – Schematic representation of the electrochemical processes that take place during the self-corrosion of Mg in 3.5% NaCl solution. Electrons are liberated by the oxidation reaction at anodic sites and flow to cathodic sites where the reduction reaction occurs. The location and distribution of sites is dependent on surface conditions, and as corrosion proceeds these can move or switch.

It is essential to appreciate that the current which flows during corrosion is contained entirely within the metal and so the net magnitude across the surface is zero, meaning it is not possible to measure directly by conventional methods i.e. using a simple ammeter. Therefore to establish the corrosion current, which is more commonly expressed as a current per unit area, or current density, for a particular system it must be calculated from other measureable parameters.

The Evans Diagram

The research of Dr Ulick Richardson Evans in the early twentieth century established the foundations of modern corrosion science and his work is fundamental to the techniques used to determine the corrosion current. Evans illustrated the relationship between the oxidation and reduction processes on a simple plot that became known as the Evans diagram [160]. This displays the anodic and cathodic components of the corrosion reaction as separate curves on an electrode potential versus log current density graph, and an example of an Evans diagram for Mg in 3.5% NaCl solution is given in Figure 4-32.

During corrosion the flow of electrons within the metal is driven by the difference in the electrode potential of anodic and cathodic sites, E_{anode} and $E_{cathode}$ respectively. At the corrosion current (I_{corr}), where the rates of the two reactions are equal, these potentials coincide at an intermediate value known as the open circuit potential (OCP).

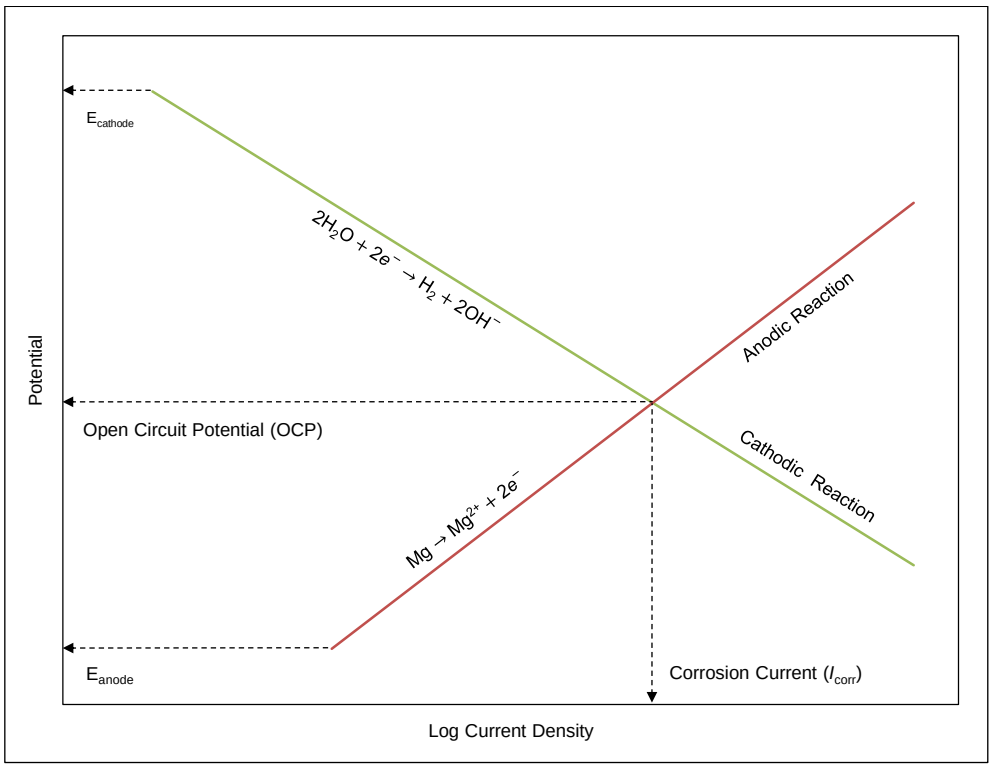

Figure 4-32 – Schematic Evans diagrams illustrating the self-corrosion of Mg in 3.5% NaCl solution [161]. Electron flow within the metal is driven by the difference in the electrode potential of anodic and cathodic sites, E_{anode} and $E_{cathode}$ respectively. The point at which the rates of the two reactions are equal (the corrosion current, I_{corr}) occurs at an intermediate value known as the open circuit potential (OCP).

The Evans diagram describes how the open circuit potential and corrosion rate are linked to the anodic and cathodic reactions. It also demonstrates how the corrosion current can be determined from the behaviour of the system at potentials away from the open circuit value, where the net measureable current is zero. By applying a controlled voltage or current to a system it is possible to change its corrosion behaviour. Anodic polarisation — the removal of electrons through the application of a positive current — increases the rate of the anodic reaction, by providing another path for electron consumption, and supresses the cathodic reaction. This causes the potential of the system to shift to a more positive, or noble, value. Conversely, cathodic

polarisation — the supply of electrons through the application of a negative current — increases the rate of the cathodic reaction, by making more electrons available, and suppresses the anodic reaction resulting in a negative, or active, shift in potential. This behaviour is governed by the kinetics of the corrosion reactions.

Corrosion Kinetics

The kinetics of corrosion relates to the net transfer of charge at anode sites and, on the condition that these reactions are controlled by electrical charge transfer and not diffusion processes, this is described by the Butler-Volmer equation as follows [162].

$$i = i_0 \left(\exp\left[\frac{\alpha_a z \eta F}{RT}\right] - \exp\left[-\frac{\alpha_c z \eta F}{RT}\right] \right) \quad \text{4-14}$$

Where i (A) is the applied current density, i_0 (A) is the exchange current density, α_a and α_c are the dimensionless anodic and cathodic charge transfer coefficients respectively, z is the number of electrons involved in the reaction, η (V) is the overpotential, F (C/mol) is the Faraday constant, R (J/mol/K) is the universal gas constant, and T (K) is the absolute temperature.

The two limiting cases for the Butler-Volmer equation — high overpotential, and low overpotential — allow it to be simplified. At high anodic or cathodic overpotentials, where η is large, the Butler-Volmer equation simplifies to the following [162].

Anodic $$i = i_0 . \exp\left[\frac{\alpha_a z \eta F}{RT}\right] \quad \text{4-15}$$

Cathodic $$i = i_0 . \exp\left[-\frac{\alpha_c z \eta F}{RT}\right] \quad \text{4-16}$$

This can be rearranged to give an expression for η as follows.

Anodic $$\eta = 2.3 \frac{RT}{\alpha_a z F} (\log i - \log i_0) \quad \text{4-17}$$

Cathodic $$\eta = -2.3 \frac{RT}{\alpha_c z F} (\log i - \log i_0) \quad \text{4-18}$$

These expressions for the anodic and cathodic overpotentials are often given as the Tafel equations.

Anodic $$\eta = a + b_a \log i$$ 4-19

Cathodic $$\eta = a - b_c \log i$$ 4-20

Where a is,

Anodic $$a = -2.3\frac{RT}{\alpha_a zF}\log i_0$$ 4-21

Cathodic $$a = -2.3\frac{RT}{\alpha_c zF}\log i_0$$ 4-22

The factors b_a and b_c are the Tafel constants as follows, and are used in Tafel extrapolation as described later.

Anodic $$b_a = -2.3\frac{RT}{\alpha_a zF}$$ 4-23

Cathodic $$b_c = -2.3\frac{RT}{\alpha_c zF}$$ 4-24

At low overpotentials, where η is small, the Butler-Volmer equation simplifies to the following, and shows that the applied current is directly proportional to the overpotential [162]. This limiting case is employed in linear polarisation resistance (LPR), which is described later.

$$i = i_0\left[\frac{z\eta F}{RT}\right]$$ 4-25

When corrosion behaviour is controlled by diffusion processes, rather than electrical charge transfer, the overpotential can be expressed as follows [162].

$$\eta = 2.3\frac{RT}{zF}\log\frac{i_L - i_0}{i_L} \qquad 4\text{-}26$$

Where i_L is the limiting current density.

Tafel Extrapolation

The schematic polarisation plot in Figure 4-33 shows anodic and cathodic polarisation curves that might be obtained experimentally for Mg in 3.5% NaCl solution by applying an external current to shift the OCP to more noble (positive) or more active (negative) values.

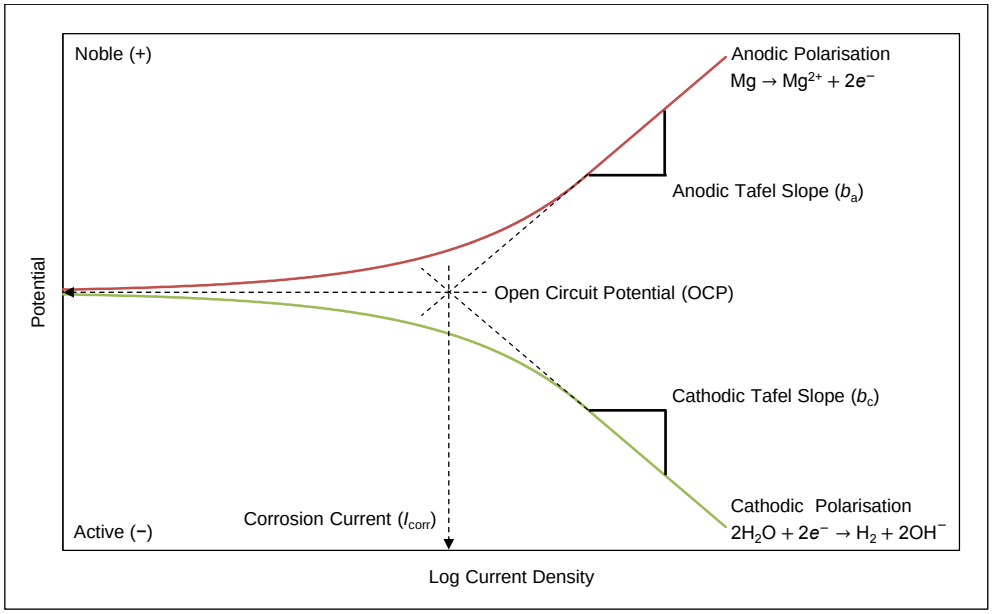

Figure 4-33 – Schematic polarisation plot showing anodic and cathodic curves that might be obtained experimentally for Mg in 3.5% NaCl solution by applying an external current to shift the OCP to more noble (positive) and more active (negative) values. At potentials somewhat more noble or more active than the OCP the reaction rate is directly proportional to current flow. Extrapolating the linear regions back to the OCP allows the corrosion current to be determined [163].

At potentials at or near to the OCP both reactions proceed and the total current flowing through the system is a net of the anodic and cathodic currents, and any external current involved in actively shifting the potential. This causes the anodic and cathodic curves to deflect, and tend towards zero, as the magnitude of the polarisation reduces and the balance of the two reactions becomes equal.

Polarisation of the system to potentials somewhat more noble or more active than the OCP will halt the respective cathodic or anodic reactions. At this point the rate of the reaction that continues is directly proportional to the current flow, and the curves become linear on a semi-logarithmic scale. Tafel extrapolation exploits this property by using the Tafel slopes, which are the gradients of these parts of the curves, to extend the linear regions back to the OCP where they intersect at the corrosion current.

Tafel extrapolation can be conducted using either or both of the polarisation curves, but in shifting the potential by the amounts required to get into the linear region on a semi-logarithmic scale the system can be significantly altered. During anodic polarisation the rate of the anodic reaction increases and the surface of the metal can be physically changed. As well as damaging the sample being tested these changes, which can include particle undermining, gross oxide formation, and severe gas bubble nucleation, can alter the exposed surface area, and may cause an indeterminable increase, or decrease, in the corrosion current density. This can be a particular problem for metals at the active end of the galvanic series, such as Zn or Mg, and as a result Tafel extrapolation should be used with some caution.

Linear Polarisation Resistance

Linear polarisation resistance (LPR) is a modification to Tafel extrapolation which helps to overcome some of its inherent problems. At potentials close to the OCP the anodic and cathodic curves are linearly related to corrosion current i.e. potential is directly proportional to current [161]. By shifting the potential in the noble and active directions by an amount that is still within the linear region (Figure 4-34) a value for electrical resistance to corrosion, known as the polarisation resistance, can be calculated (Equation 4-27).

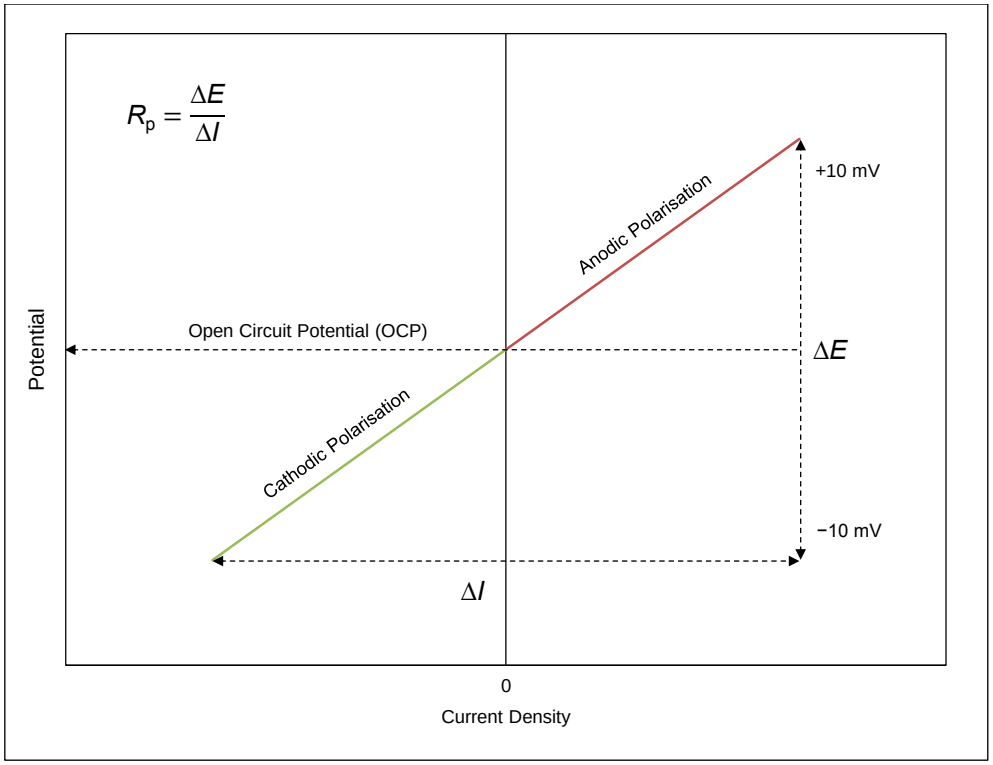

Figure 4-34 – Diagram illustrating the changes in potential that are applied during linear polarisation resistance. The potential is shifted in the noble and active directions by an amount small enough such that the system still behaves linearly. This allows a value for electrical resistance to corrosion, known as the polarisation resistance, to be calculated according to Equation 4-27.

$$R_p = \frac{\Delta E}{\Delta I} \qquad 4\text{-}27$$

Where R_p is the polarisation resistance ($\Omega.cm^2$), ΔE is the change in potential (mV) and ΔI is the change in current density ($\mu A/cm^2$). The advantage of the LPR technique is that the small changes in potential (±10 mV) do not have any significant effect on the behaviour of the corroding surface [161].

Conversion of the polarisation resistance to corrosion current is conducted using the Stearn-Geary equation (Equation 4-29), which is discussed later, and requires values for the Tafel slopes that are used in the Tafel extrapolation method. This means the problems with surface changes that were highlighted for the Tafel method can still cause some uncertainty when determining the corrosion current by LPR. Despite this the LPR technique holds an advantage over Tafel extrapolation as the Tafel slopes can be derived in separate experiments, and the sample undergoing corrosion testing can remain undamaged.

Electrochemical Impedance Spectroscopy

Electrochemical impedance spectroscopy (EIS) uses the same principles as LPR but enables more information about the surface to be inferred and eliminates a factor that can cause error in LPR results.

During corrosion the oxidation process liberates electrons within the metal and releases positive ions into the surrounding electrolyte, as was shown in Figure 4-31. The resulting excess of electrons gives the metal a net negative charge and attracts positive ions to its surface to form an adsorbed fixed layer. The fixed positive layer then attracts negative ions from the electrolyte to form a second diffuse mobile layer in which the ions are free to move around. The proximity of the negative mobile layer is controlled by the degree of repulsion exerted by electrons in the metal. These two ion layers, one fixed and one mobile, are called an electrical double layer [164].

The behaviour of the double layer changes with the type of electrical current being supplied, either direct current (DC) or alternating current (AC). Under anodic polarisation with a DC supply electrons are removed at a fixed rate and the metal becomes more positive. This has the effect of speeding up the dissolution of metal ions (the corrosion rate) by repelling them from the fixed layer and into the electrolyte,

thereby exposing more surface atoms that can subsequently ionise. With DC cathodic polarisation the opposite is true and the fixed layer is held more tightly and the rate of metal ion dissolution is reduced. During anodic and cathodic DC polarisation the mobile layer is held at a fixed distance that is related to the magnitude of the current and the associated electron charge within the metal. The net current flow with a DC supply means the double layer acts like a resistor, the magnitude of which is termed the charge transfer resistance (R_{ct}) [164].

With an alternating current (AC) supply the double layer behaves like a capacitor and can be charged and discharged. During anodic polarisation electrons are drawn out of the metal, making it more positive and allowing the mobile layer to be held closer and more strongly; the double layer is charged. Under cathodic polarisation electrons are pushed into the metal, causing it to become more negative and repel the mobile layer; the double layer is discharged. The magnitude of the capacitive effect is known as the double layer capacitance (C_{dl}).

The resistive response to DC and capacitive response to AC means a corroding metal can be modelled as an equivalent electrical circuit, like that shown in Figure 4-35. The behaviour of the electrical double layer can be equated to a capacitor (C_{dl}) and resistor (R_{ct}) in parallel. Resistor R_0 is introduced to represent the resistance of the electrolyte [164].

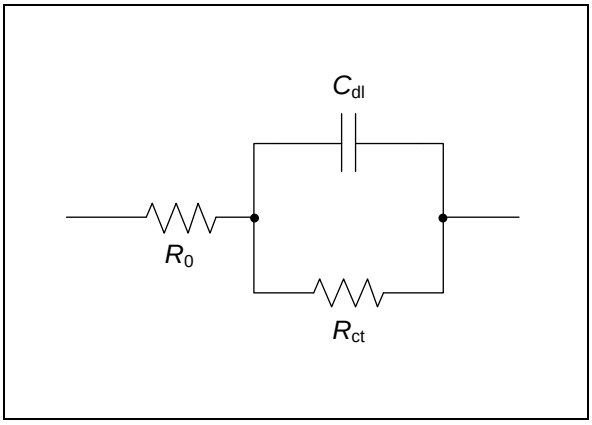

Figure 4-35 – Example of an equivalent circuit used to model a corroding system. The parallel capacitor and resistor (C_{dl} and R_{ct} respectively) simulates the behaviour of the electrical double layer. Resistor R_0 corresponds to the resistance of the electrolyte [165].

Modelling the corrosion process as an electrical circuit highlights two flaws with the LPR technique. Firstly, the equivalent circuit shows that there is more than one resistive component but with LPR only a single resistance (R_p) is obtained. Secondly, the behaviour of the system changes with the type of current supplied (DC or AC). The single voltage sweep for LPR is typically conducted at a rate of 10 mV per minute and although this is a slow change the response of the parallel resistive and capacitive components, R_{ct} and C_{dl} respectively, is unknown. With EIS instead of single voltage sweep a spectrum of identical magnitude sweeps (±10 mV) are conducted over a range of frequencies. This enables the response of the system to both DC and AC to be quantified, and also allows the electrical resistance of the solution to be accounted for.

The response obtained from EIS is commonly displayed on a Nyquist plot and an example of this is given in Figure 4-36 for a system that can be modelling by the equivalent circuit in Figure 4-35. The resistance of R_{ct} and the AC equivalent of impedance for C_{dl} are measured in response to different frequencies, and plotted against the *x* and *y* axes respectively. High frequency behaviour is seen to the left of the plot, while low frequencies are to the right. When a high frequency voltage change is applied (equivalent to an AC supply) the impedance of C_{dl} is low and the current bypasses R_{ct}. The high frequency response therefore provides a value for the electrolyte resistance, R_0. On a Nyquist plot this means the data sits on the *x* axis at R_0 until the frequency is sufficiently low such that the impedance of C_{dl} starts to increase.

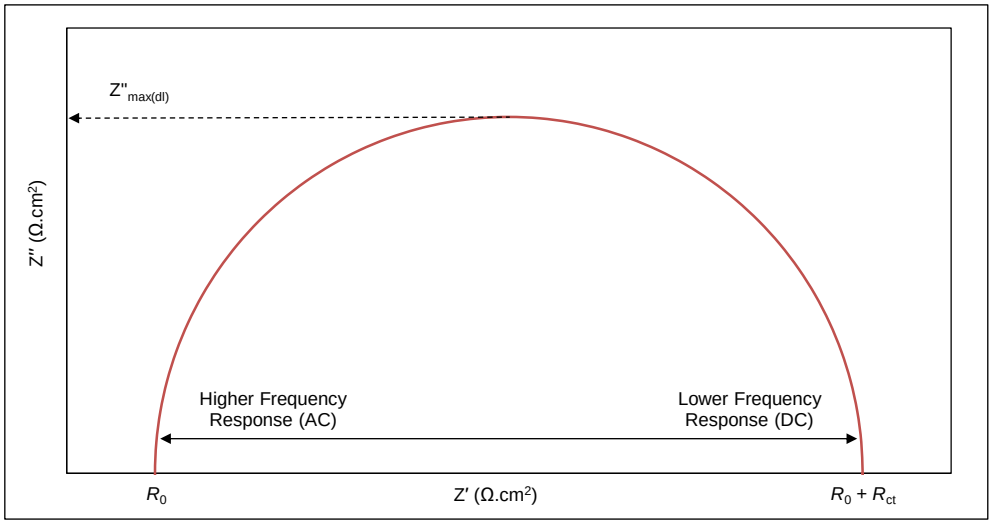

Figure 4-36 – Nyquist plot showing the electrical response of the equivalent circuit model in Figure 4-35 to different voltage frequencies. With a high frequency voltage change (equivalent to an AC supply) the impedance of C_{dl} is low and the current bypasses R_{ct}. This provides a value for the electrolyte resistance, R_0. As the frequency is reduced further C_{dl} reaches a maximum beyond which the DC response begins to dominate, and most of the current flows through R_{ct}. At very low frequencies, equivalent to a DC supply, the current bypasses C_{dl} and flows through R_0 and R_{ct}.

The impedance of C_{dl} increases as the frequency is lowered until it reaches a maximum ($Z''_{max(dl)}$), where it is equal to the resistance of R_{ct}. After this point the DC response of the system begins to dominate and, as the frequency drops further, the impedance of C_{dl} increases so that most of the current flows through R_{ct}. At very low frequencies, which are equivalent to a DC supply, no current flows through C_{dl} and this point marks the sum of R_0 and R_{ct}. The magnitude of R_{ct} can then be calculated by subtracting the value for R_0 that was obtained from the high frequency response.

The presence of a surface layer, like an oxide, paint film or other treatment, alters the electrical response and necessitates a more complex equivalent circuit model like that shown in Figure 4-37. The components R_{pf} and C_{pf} represent the resistive and capacitive behaviours of the surface layer. The associated Nyquist plot in Figure 4-38 now exhibits a different response that corresponds to the summation of two curves, one related to corrosion as before and a second representing the surface layer. In the example given here the smaller curve is the surface layer and the larger curve is the corroding metal, although this is not always the case.

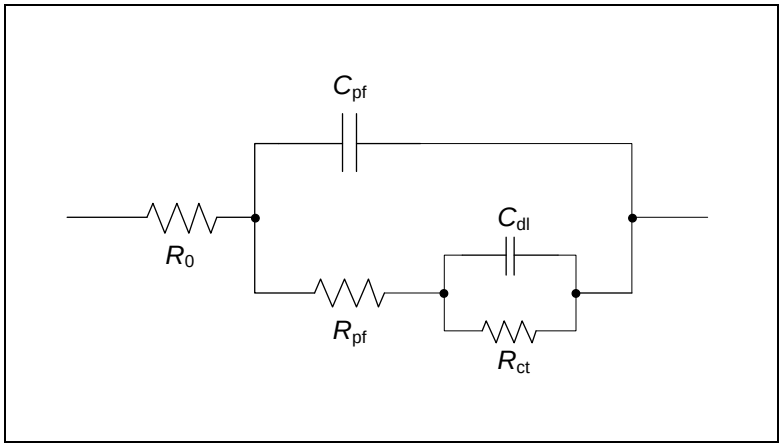

Figure 4-37 – Example of an equivalent circuit model for a coated material [165].

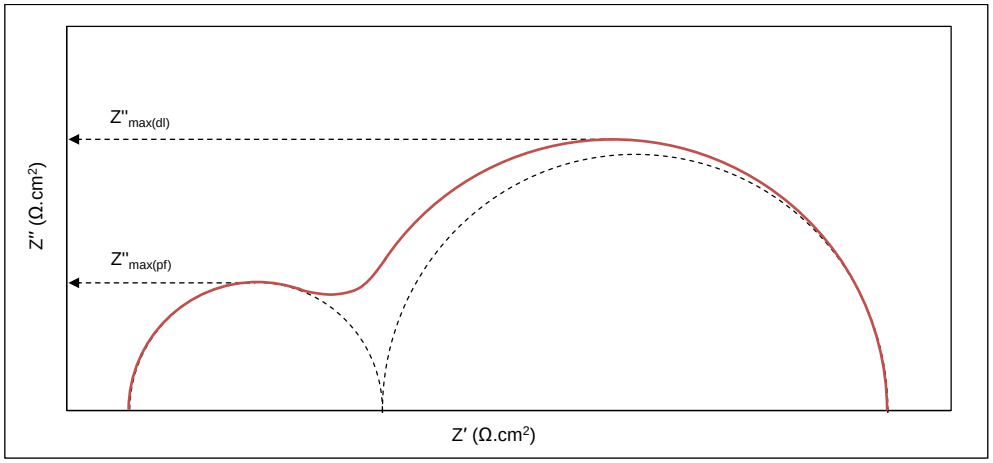

Figure 4-38 – Nyquist plot showing the electrical response of the equivalent circuit model in Figure 4-37 to different voltage frequencies [165].

A further modification to the equivalent circuit can be made through the addition of a Warburg diffusion impedance term (Z_ω) that accounts for diffusion processes in the environment near the corroding surface (Figure 4-39). The magnitude of this effect is dependent on the frequency of the voltage change being applied and is directly linked to the behaviour of the electrical double layer. The Nyquist plot in Figure 4-40 shows the resulting electrical response. At high frequencies, equivalent to an AC supply, the diffusion distance is small and the magnitude of the Warburg impedance is insignificant. At low frequencies, equivalent to a DC supply, the diffusion distance is larger and the Warburg impedance is great, thereby causing the characteristic 45° diffusion tail [165].

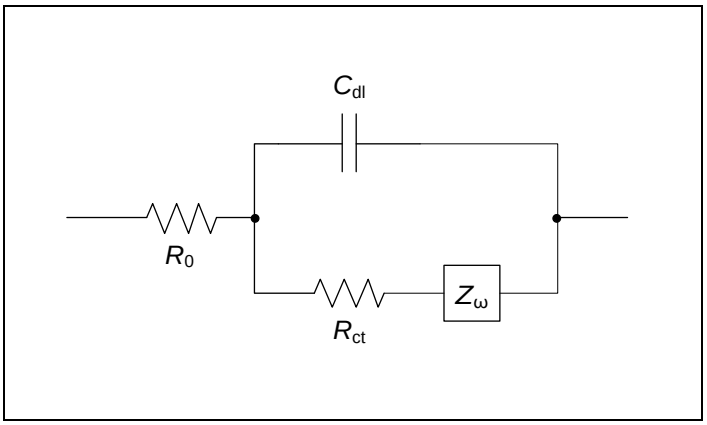

Figure 4-39 – Example of an equivalent circuit model with a Warburg diffusion impedance to account for diffusion processes [165].

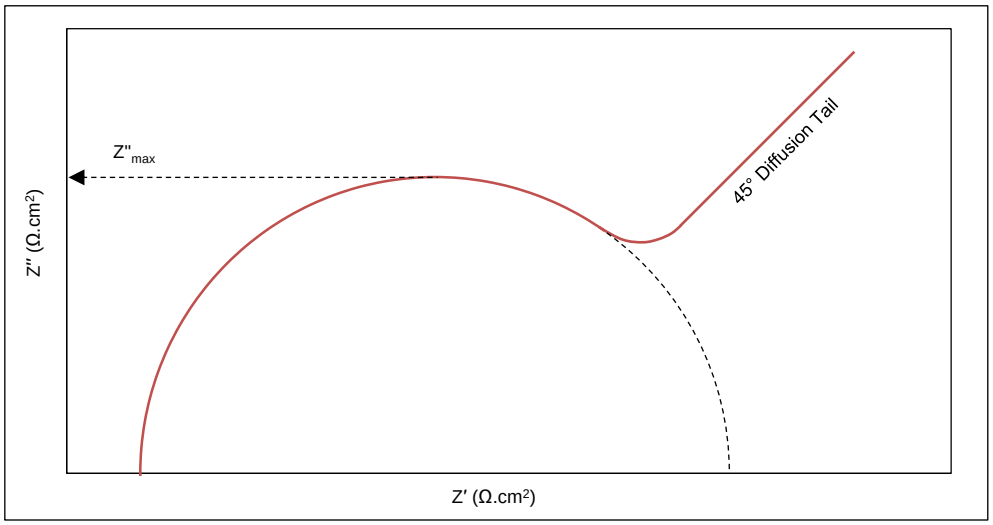

Figure 4-40 – Nyquist plot showing the electrical response of the equivalent circuit model in Figure 4-39 to different voltage frequencies [165].

As with LPR the conversion of EIS results to corrosion current requires values for the Tafel slopes, which means it is still open to the same error. The power of EIS though is its ability to distinguish between the individual parts that make up a corrosion system. By doing this the component specifically related to corrosion rate (R_{ct}) can be singled out and consequently quantified more accurately.

Quantifying Corrosion

A convenient way to define the corrosion resistance of a material is in terms of the thickness that is removed over a period of time. This corrosion penetration rate is commonly expressed in millimetres per year and is easily relatable to real world scenarios.

The corrosion penetration rate for a metal can be found empirically by conducting weight loss experiments. The mass of metal lost when a sample is exposed to a particular environment can then be converted into a corrosion penetration rate using the following expression.

$$\text{corrosion rate (mm/y)} = 3.1536 \times 10^8 \frac{m}{\rho A T} \qquad 4\text{-}28$$

Where m is the weight loss (g), ρ is the density (g/cm^3), A is the surface area (cm^2), and T is the time of exposure (s). The numerical factor is there to scale to the correct units.

When using electrochemical techniques, such as LPR or EIS, the corrosion rate tends to be expressed in terms of a current density. This is obtained by converting the measured resistances, R_p for LPR or R_{ct} for EIS, using the Stern-Geary equation below.

$$I_{corr} = \frac{B}{R_p \text{ or } R_{ct}} \qquad 4\text{-}29$$

Where B is the Stern-Geary constant (mV) and is calculated according to the following equation.

$$B = \frac{b_a . b_c}{2.3(b_a + b_c)} \qquad 4\text{-}30$$

Identifying the Stern-Geary constant is a pivotal part of determining corrosion rate, and values are found experimentally using the principles of Tafel extrapolation that were previously outlined. For many materials it is well defined but, due to damaging accelerated corrosion that was also described earlier, the identification of a value for

Mg is a difficult task [163,166]. It is also important to acknowledge that for any material the Stern-Geary constant will change over time as surface films and corrosion products form. The difficulties in defining a Stern-Geary constant for Mg are discussed by Pardo *et al.* 2010 [166], who compared gravimetric and electrochemical corrosion measurements of some Mg-Al-Zn alloys in 3.5% NaCl.

In the work described here a Stern-Geary constant was calculated from the information given by Yang *et al.* 2011 [57], who conducted similar work and examined the corrosion behaviour of AZ91D using both anodic/cathodic polarisation and EIS. This yielded an I_{corr} of 5.57 μA/cm^2 and R_{ct} of 2087 Ω.cm^2 respectively that, by rearrangement of Equation 4-29, gives a *B* value of 12 mV.

Once the corrosion current has been determined it can be converted into a corrosion penetration rate, on the condition that it is uniform across the surface, using the principles of Faraday's law, which states:

$$m = \left(\frac{It}{F}\right)\left(\frac{M}{z}\right) \qquad 4\text{-}31$$

Where *m* is the mass of substance corroded (g), *I* is the applied constant current (A), *t* is the total time the current is applied for (s), *F* is the Faraday constant (96,485 C/mol), *M* is the molar mass (g/mol) and *z* is the valence number of the ions produced during corrosion.

Combining equations 4-28 and 4-31 and translating molar mass to atomic weight yields a corrosion penetration rate in millimetres per year derived from the corrosion current density as follows.

$$\text{corrosion penetration rate (mm/y)} = 0.00327\frac{Ia}{\rho z} \qquad 4\text{-}32$$

Where *I* is the current density (μA/cm^2) and *a* is the atomic weight.

For Mg this gives the following identity.

$$1\ \mu A/cm^2 \equiv 0.023\ mm/y \qquad 4\text{-}33$$

4.3.2.3 Self-Corrosion Measurements

A measured area of each sample was exposed to 3.5% NaCl using the arrangement shown in Figure 4-41, and electrochemical data was then recorded with the equipment and software given in Section 3.3. The RE was positioned approximately 20 mm from the surface of the sample, and the CE was kept at least 60 mm away. The OCP measurements were started immediately following exposure of a sample to the solution. This was recorded for ten minutes so the corroding system could settle to a relatively steady OCP. Immediately following this an EIS run was started from a frequency of 20 kHz reducing on a log scale with 10 readings taken per decade at an amplitude of 10 mV on potentiostat bandwidth F. Once a satisfactory semicircle had been recorded and no meaningful data was being gathered the run was stopped. The circle fit function built into the ZPlot software was then used to obtain values for R_{ct}.

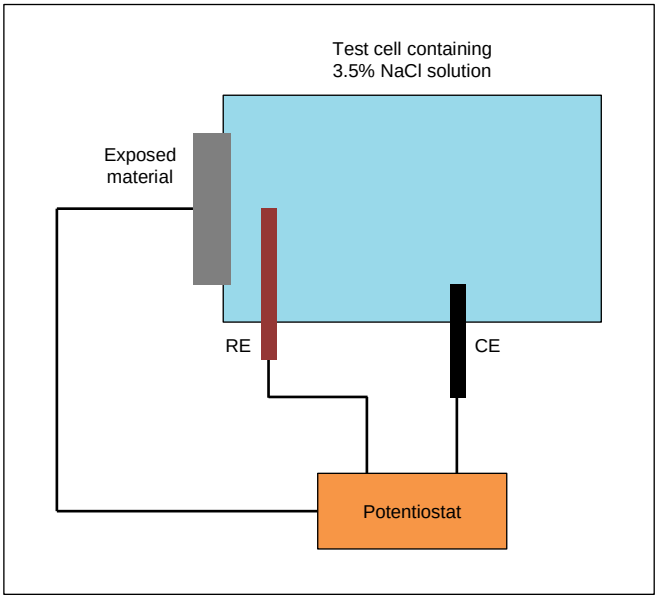

Figure 4-41 – Schematic representation of the equipment arrangement used to conduct OCP and EIS measurements.

4.3.3 Results and Discussion

4.3.3.1 Open Circuit Potentials

A series of OCP measurements were conducted for 99.9% Mg and the Mg alloys AZ31B, AZ61A, and AZ91D in 3.5% NaCl solution. The characteristics of a typical OCP plot are described first using 99.9% Mg as an example, before the OCPs recorded for each of the materials are compared.

99.9% Mg Example

An example of an OCP measurement for 99.9% Mg is given in Figure 4-42, and this shows the changes in potential that occurred during the first 600 s after exposure. In this case the OCP had an initial value of −1.721 V_{SCE} (point *a)* and over the following 9 s this dropped to a minimum of −1.723 V_{SCE} (point *b*). During the next 143 s the potential rose steadily to a maximum of −1.632 V_{SCE} (point *c*) before reducing to settle at a mean, which was calculated over the last 100 s, of −1.646 V_{SCE} (range *d*).

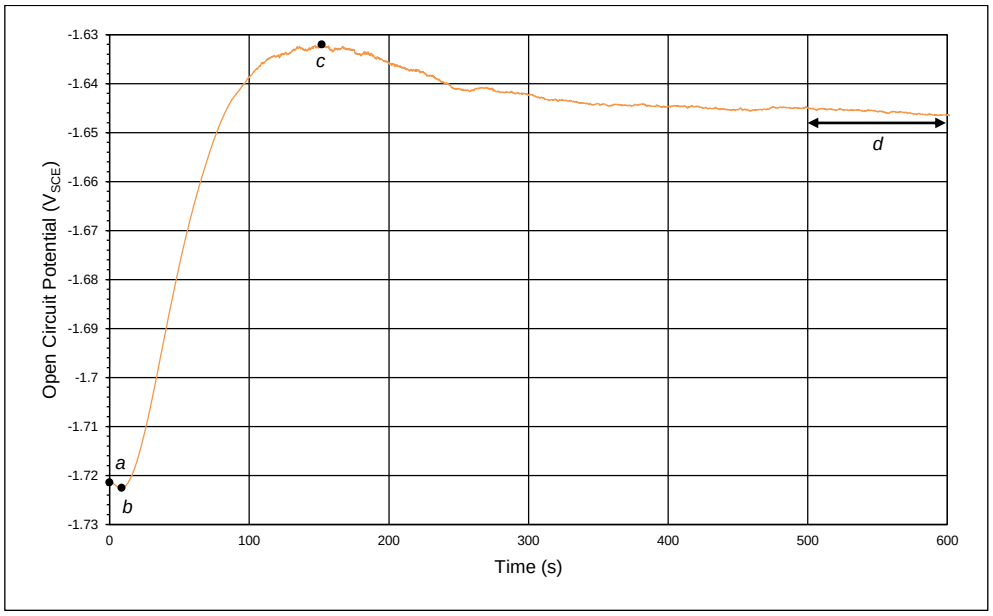

Figure 4-42 – Potential versus time plot showing the OCP recorded for 99.9% Mg over the first 600 s of exposure to 3.5% NaCl solution. Initial potential (point *a*) is −1.721 V_{SCE}. The minimum potential (point *b*) is −1.723 V_{SCE} and the maximum (point *c*) is −1.632 V_{SCE}. The mean potential calculated over the last 100 s is −1.646 V_{SCE} (range *d*).

The OCP measured when Mg is exposed to 3.5% NaCl solution is controlled by the rates of the co-dependent anodic and cathodic reactions. In this case the cathodic reaction (water reduction) is thought to be fairly consistent and it is proposed that the observed variations in OCP can be explained in terms of changes to the anodic reaction, which is related the condition of the metals surface. A series of Evans diagrams are given in Figure 4-43 to illustrate how the balance of the corrosion reactions differs between the key points, *a*, *b*, *c* and *d*, in Figure 4-42.

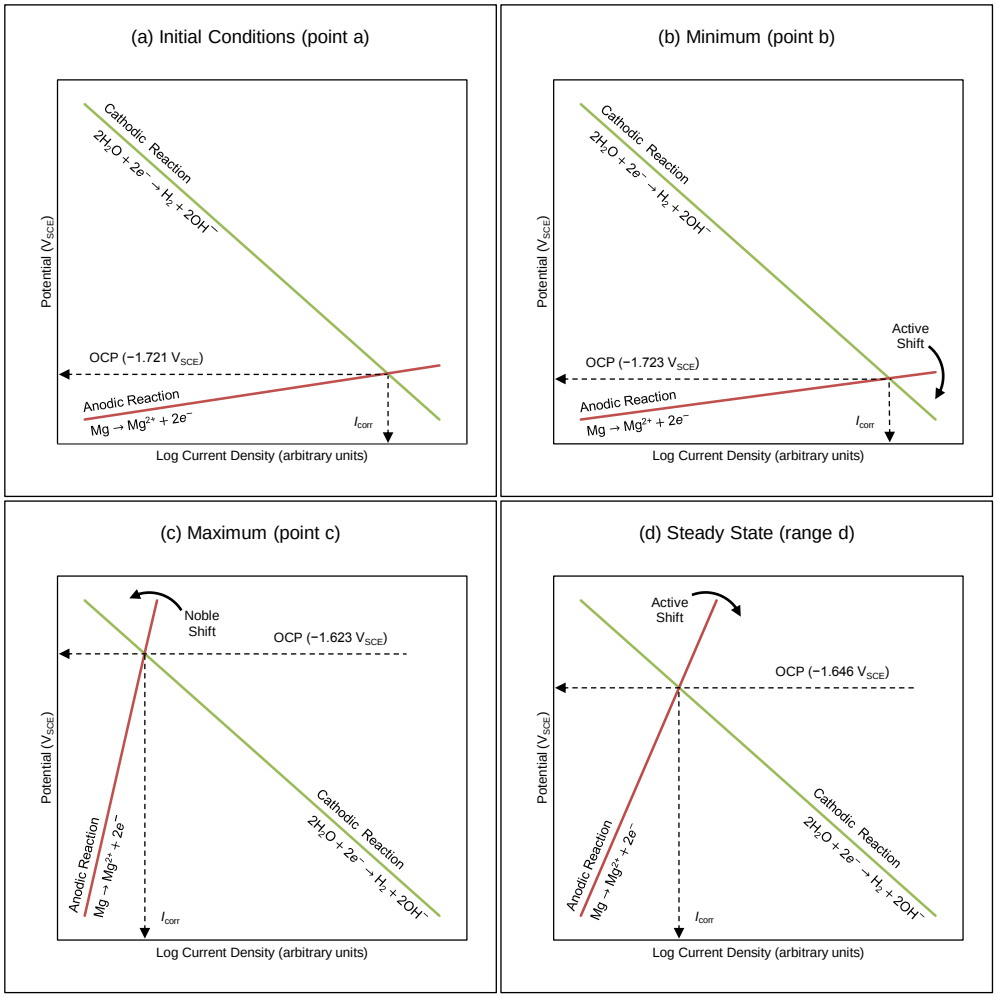

Figure 4-43 – Evans diagrams illustrating the balance of the corrosion reactions at key points, *a*, *b*, *c* and *d*, in Figure 4-42. (a) Initial conditions at point *a*. Anodic and cathodic curves intersect at −1.721 V_{SCE}. (b) Minimum OCP at point *b*. Corrosion current increases due to breakdown of air-formed oxide layer. Gradient of anodic curve reduces and intersects the cathodic curve at −1.723 V_{SCE}. (c) Maximum OCP at point *c*. More robust protective oxide forms and reduces the corrosion current. Gradient of anodic curve increases and intersects the cathodic curve at −1.632 V_{SCE}. (d) Steady state OCP over range *d*. Instability of oxide limits the protection it can offer and equilibrium position between film formation and breakdown has a higher corrosion current. Gradient of the anodic curve is reduced and intersects the cathodic curve at −1.646 V_{SCE}.

The diagram in Figure 4-43 (a) represents the initial conditions, and the anodic and cathodic curves intersect at −1.721 V_{SCE} (point *a* in Figure 4-42) and at a particular corrosion current. Over the following 9 s there is a small active shift to −1.723 V_{SCE} (point *b* in Figure 4-42) due to the breakdown of an air-formed $Mg(OH)_2$ film and this is

represented by the Evans diagram in Figure 4-43 (b). While abrasion of the surface immediately before the experiment meant that any substantial oxides, which had formed during prior handling and storage, would have been removed a native air-formed $Mg(OH)_2$ layer, with a thickness in the order of 2 nm, will rapidly develop [167]. This thin oxide was initially providing some protection to the Mg but its breakdown in the 3.5% NaCl solution exposes the underlying substrate and consequently causes an increase in corrosion current, and active shift in potential, that is associated with the anodic reaction and a reduction in the gradient of the anodic curve.

As corrosion proceeds a more robust $Mg(OH)_2$ layer develops and thickens, consequently offering a greater amount of protection and reducing the corrosion current by slowing the anodic reaction. This increases the gradient of the anodic curve and causes a corresponding noble shift in potential over the next 143 s, to a maximum of −1.632 V_{SCE} (point *c* in Figure 4-42), as represented by the Evans diagram given in Figure 4-43 (c). However, the more protective film that forms is not very stable and after some time areas begin to break off and fresh substrate is exposed [168]. This limits its protective ability and further film breakdown causes an overall increase in corrosion rate and a corresponding active shift in potential. Once equilibrium between film formation and breakdown is reached the corrosion rate stabilises at a steady state and the potential settles to a mean of −1.632 V_{SCE} (range *d* in Figure 4-42) as shown by the Evans diagram in Figure 4-43 (d). Continuous formation and breakdown of the $Mg(OH)_2$ film can be observed as noise on the curve in Figure 4-42.

Comparison of 99.9% Mg and Mg-Al-Zn Alloys

Figure 4-44 shows the changes in OCP that occurred when five freshly abraded samples of 99.9% Mg, AZ31B, AZ61A, and AZ91D were exposed to 3.5% NaCl solution. In every case a relatively active OCP was seen immediately following exposure to the solution which then, over a period of around ten minutes, settled to values that are approximately 100 mV more noble. The observed changes in OCP can be explained in a similar manner to the single 99.9% Mg sample discussed above, and are again caused by variations to the rate of the anodic reaction during corrosion as a result of the formation and breakdown of surface films.

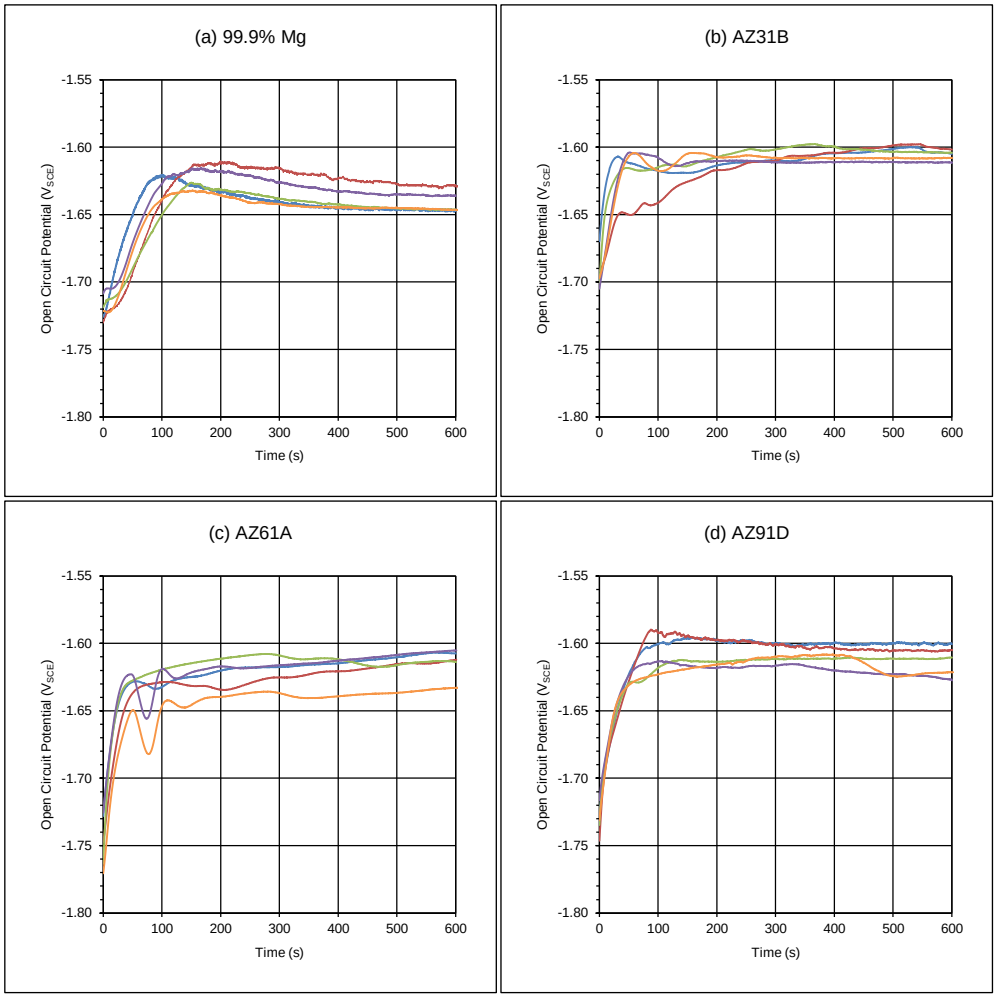

Figure 4-44 – Plots showing the OCPs of five freshly abraded samples of: (a) 99.9% Mg, (b) AZ31B, (c) AZ61A, and (d) AZ91D, over the first 600 s of exposure to 3.5% NaCl solution.

The points plotted in Figure 4-45 are mean OCP values calculated from the last 100 s of data for each measurement seen in Figure 4-44. The five OCPs for 99.9% Mg are spread over a range of 18 mV, with a minimum of −1.646 V_{SCE}, a maximum of −1.626 V_{SCE} and an overall mean of −1.640 V_{SCE}. The alloys AZ31B, AZ61A, and AZ91D have overall mean OCPs of −1.605 V_{SCE}, −1.610 V_{SCE} and −1.613 V_{SCE} respectively. AZ91D exhibited the largest spread of values at 24 mV (minimum −1.625 V_{SCE}, maximum −1.600 V_{SCE}) followed by 12 mV for AZ31B (minimum −1.611 V_{SCE}, maximum −1.599 V_{SCE}) and 7 mV for AZ61A (minimum −1.614 V_{SCE}, maximum −1.607 V_{SCE}).

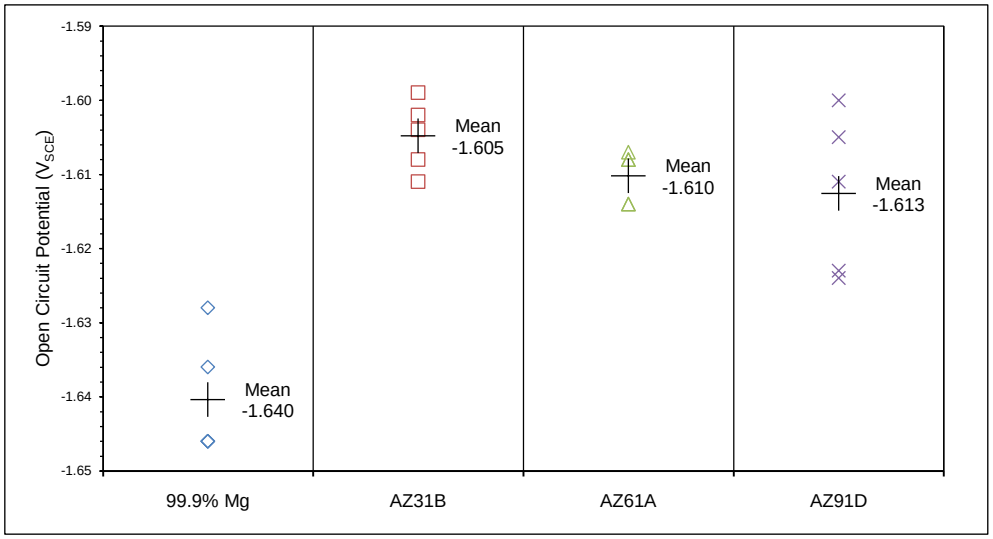

Figure 4-45 – Mean OCP values for five samples each of 99.9% Mg, AZ31B, AZ61A, and AZ91D exposed to 3.5% NaCl solution. The mean was calculated from the last 100 s of data recorded over 600 s from initial exposure of a freshly abraded sample.

The range of OCP values obtained for 99.9% Mg, AZ31B, AZ61A and AZ91D shows that no precise potential can be considered representative of a particular material. The spread across the alloys also highlights that despite their differences in composition and microstructure they cannot be distinguished by their surface activities, although compared to 99.9% Mg they are consistently more noble.

4.3.3.2 Self-Corrosion Rates

A series of self-corrosion rate measurements were conducted for 99.9% Mg and the Mg-Al-Zn alloys AZ31B, AZ61A, and AZ91D in 3.5% NaCl solution using electrochemical impedance spectroscopy. Each of these was completed immediately following one of the OCP measurements described above. Charge transfer resistances were obtained assuming that the system could be modelled by the simple equivalent circuit in Figure 4-46. These were subsequently converted into corrosion current densities and corrosion penetration rates for comparison.

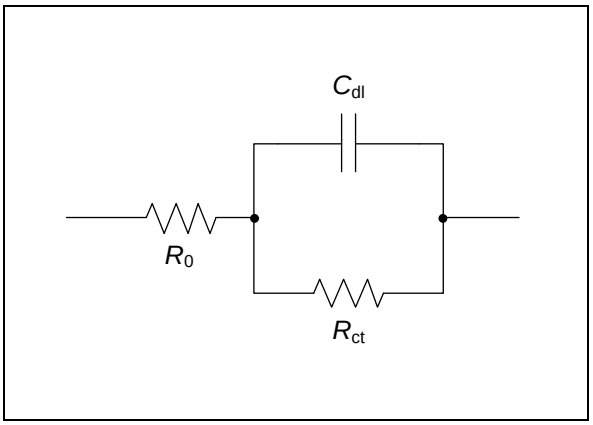

Figure 4-46 – Assumed equivalent circuit model used to obtain R_{ct} values from EIS results for 99.9% Mg and the Mg-Al-Zn alloys (AZ31B, AZ61A and AZ91D) in 3.5% NaCl solution [165].

Charge Transfer Resistance

The Nyquist plot in Figure 4-47 shows an example of one of the electrochemical impedance spectroscopy experiments for AZ31B. The data points follow a single clear semicircle from low impedance (high frequencies) to high impedance (low frequencies) and there are no diffusion effects in the environment near the corroding surface, which would have produced a 45° diffusion tail at the lower frequencies as illustrated earlier in Figure 4-40. Overlaid on to this is a curve representing the circle fit function in ZPlot, which applies a true semicircle (not just a line of best fit) that best matches the data between two chosen points. The points of intersection of the fitted semicircle with the x-axis correspond to the magnitudes of R_0 (solution resistance) and $R_0 + R_{ct}$ (solution resistance plus charge transfer resistance) in the equivalent circuit model (Figure 4-46), which in this case gives an R_0 of 61.5 Ω.cm^2 and an R_{ct} of 789 Ω.cm^2.

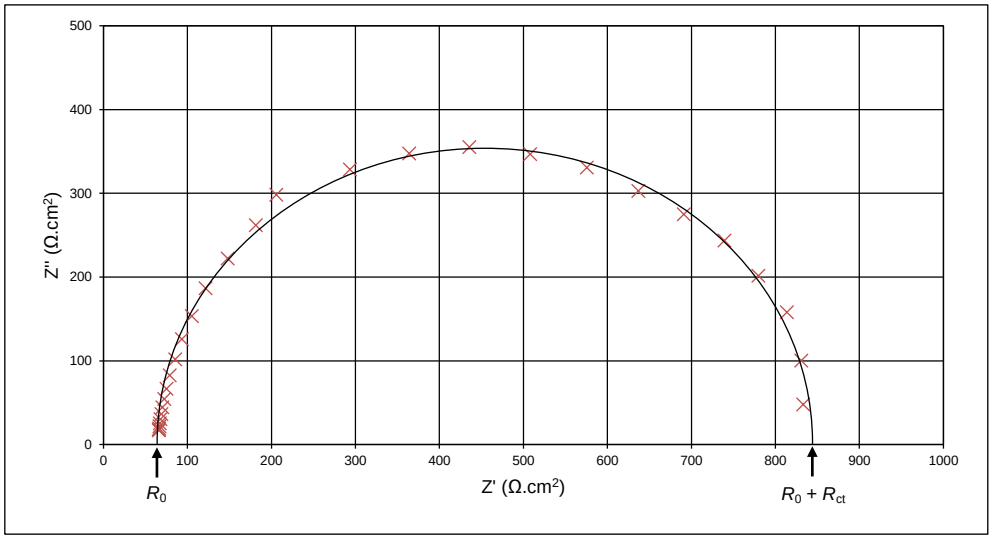

Figure 4-47 – Nyquist plot showing the result of an EIS experiment for AZ31B in 3.5% NaCl solution taken immediately following a ten minute settling period after exposure to 3.5% NaCl solution. Overlaid is a curve representing the circle fit function in ZPlot and values for R_0 (61.5 Ω.cm^2) and R_{ct} (789 Ω.cm^2) are found from the points of intersection with the x-axis as marked.

This methodology was applied to each of the five EIS runs for 99.9% Mg and the Mg alloys AZ31B, AZ61A, and AZ91D, and the corresponding Nyquist plots are given in Figure 4-48, Figure 4-49, Figure 4-50 and Figure 4-51 respectively. In every case a single clear semicircle is produced and no 45° diffusion tail is evident. The slight flattening evident for some of the curves is likely to be the result of a distribution of time constants [169]. That is to say the curve is not in fact one single semicircle, but a series of overlapping semicircles each with its own time constant. A combined Nyquist plot is shown in Figure 4-52 alongside the associated R_{ct} values in Table 4-4.

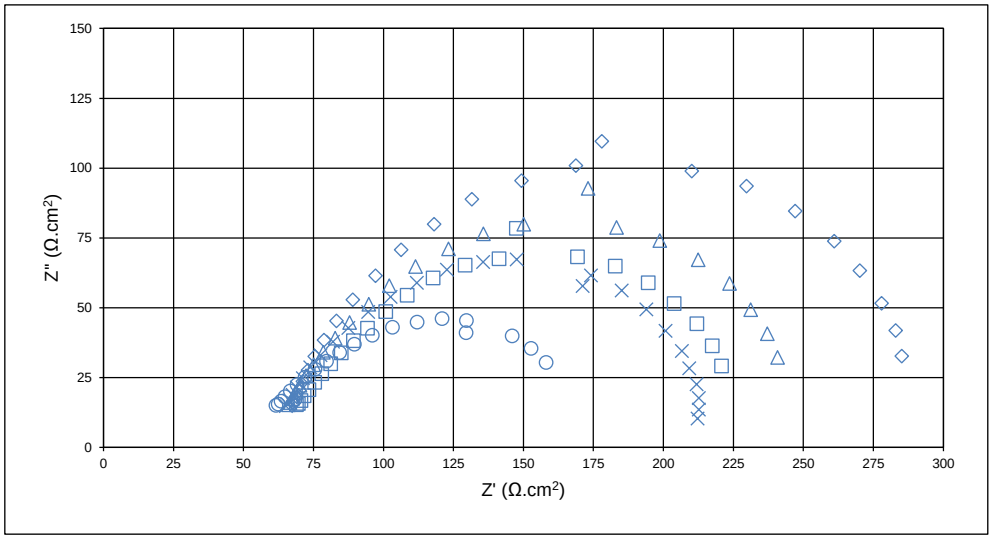

Figure 4-48 – Nyquist plot showing the results of five EIS experiments each for 99.9% Mg in 3.5% NaCl solution taken immediately following the OCP measurements seen in Figure 4-44 (a).

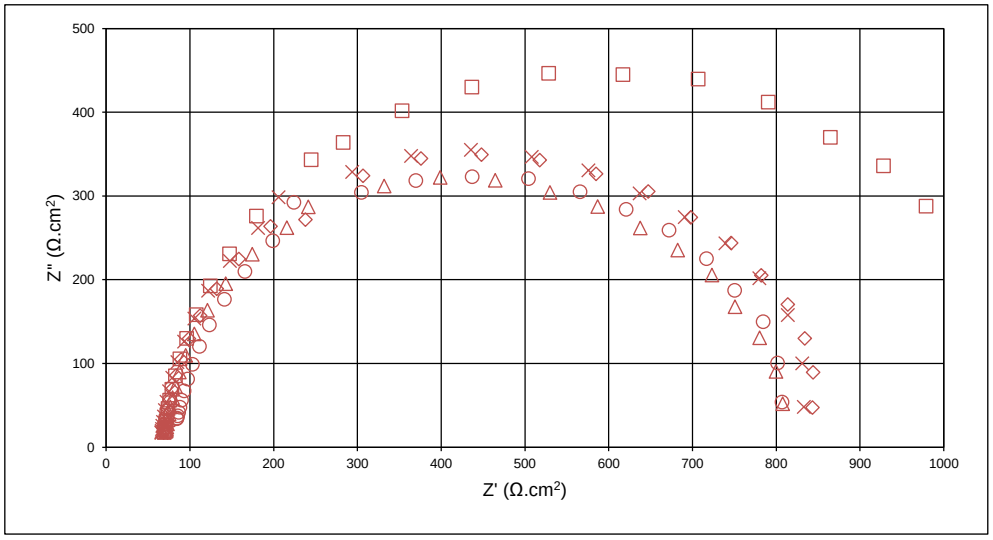

Figure 4-49 – Nyquist plot showing the results of five EIS experiments each for AZ31B in 3.5% NaCl solution taken immediately following the OCP measurements seen in Figure 4-44 (b).

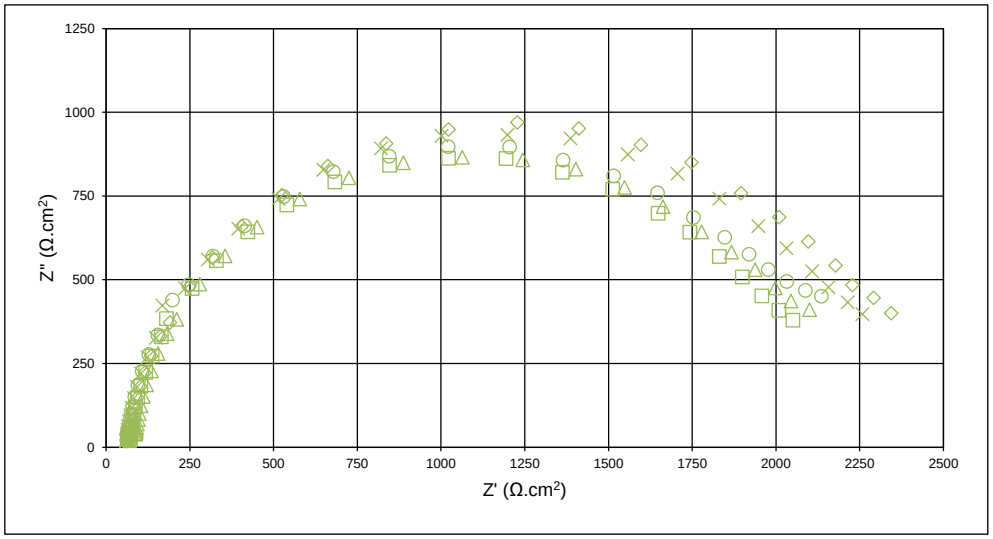

Figure 4-50 – Nyquist plot showing the results of five EIS experiments each for AZ61A in 3.5% NaCl solution taken immediately following the OCP measurements seen in Figure 4-44 (c).

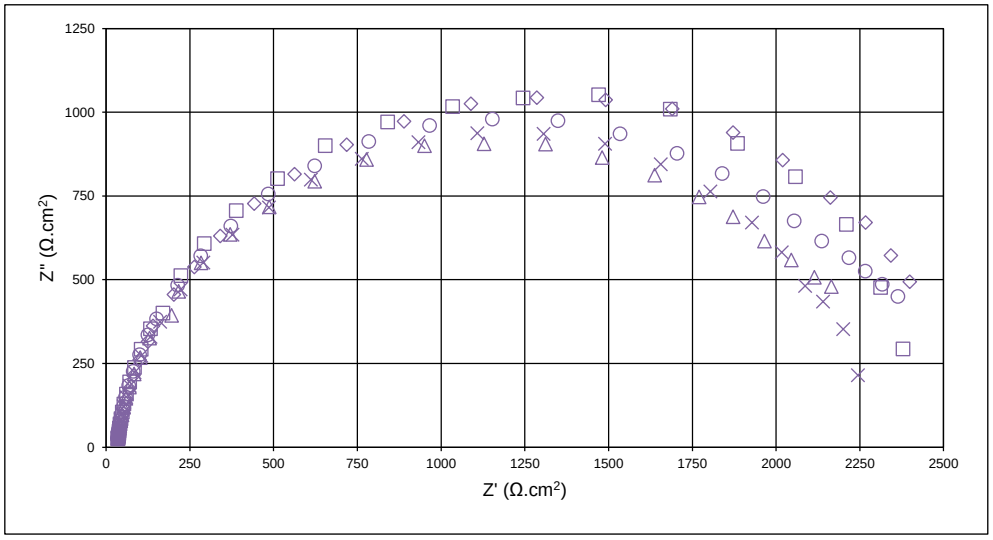

Figure 4-51 – Nyquist plot showing the results of five EIS experiments each for AZ91D in 3.5% NaCl solution taken immediately following the OCP measurements seen in Figure 4-44 (d).

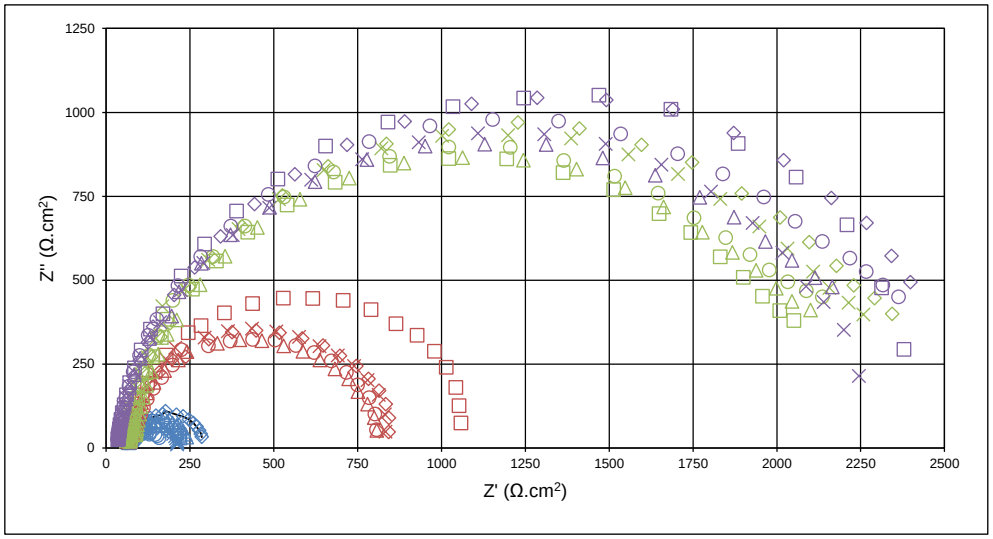

Figure 4-52 – Nyquist plot showing the results of five EIS experiments each for 99.9% Mg, AZ31B, AZ61A and AZ91D in 3.5% NaCl solution taken immediately following the OCP measurements seen in Figure 4-44.

Table 4-4 – Values for R_{ct} obtained from the Nyquist plots in Figure 4-52.

Charge Transfer Resistance (Ω.cm²)							
99.9% Mg		AZ31B		AZ61A		AZ91D	
□	161	□	1040	□	2090	□	2470
◇	228	◇	808	◇	2350	◇	2600
△	184	△	751	△	2130	△	2310
×	154	×	789	×	2310	×	2290
○	120	○	748	○	2160	○	2410
Mean	169	Mean	828	Mean	2160	Mean	2420

The charge transfer resistances are plotted for comparison in Figure 4-53. The lowest R_{ct} values are seen for 99.9% Mg, which has a mean of 169 Ω.cm^2 over a 108 Ω.cm^2 range (minimum 120 Ω.cm^2, maximum 228 Ω.cm^2. AZ31B has the next highest mean R_{ct} at 828 Ω.cm^2 and a range of 292 Ω.cm^2 (minimum 748 Ω.cm^2, maximum 1040 Ω.cm^2). The largest mean R_{ct} is seen for AZ91D at 2420 Ω.cm^2 with AZ61A slightly lower at 2160 Ω.cm^2. The spread of data for AZ61A and AZ91D (ranges 260 Ω.cm^2 and 310 Ω.cm^2 respectively) results in some overlap between the alloys, with a maximum of 2350 Ω.cm^2 for AZ61A and a minimum of 2290 Ω.cm^2 for AZ91D.

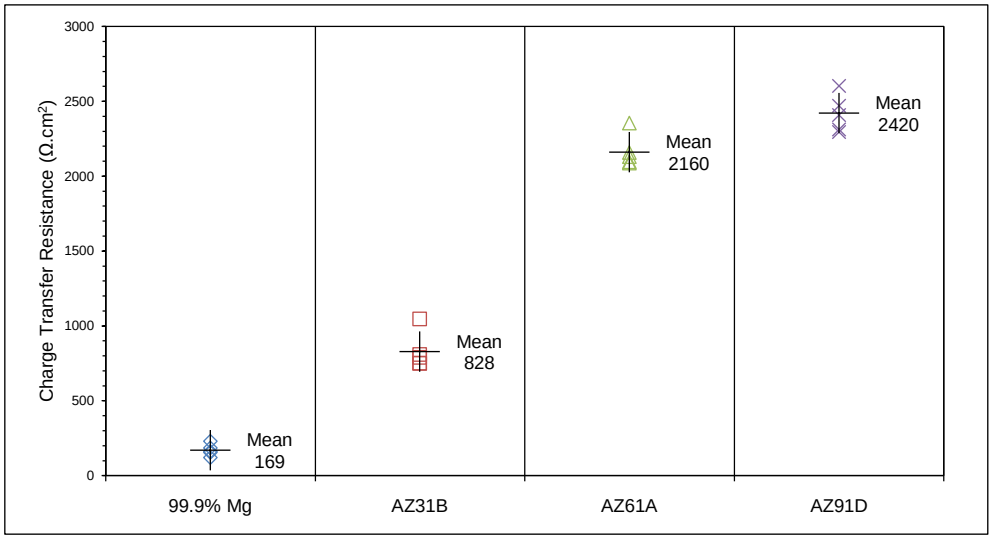

Figure 4-53 – Plot showing the charge transfer resistances from five EIS experiments each for 99.9% Mg, AZ31B, AZ61A and AZ91D in 3.5% NaCl solution taken immediately following the OCP measurements seen in Figure 4-44.

Corrosion Current Density

The R_{ct} were translated into corrosion current densities using Equation 4-29, and these are compared in Figure 4-54. The mean corrosion current densities for 99.9% Mg, AZ31B, and AZ61A were 71.9 µA/cm^2, 14.2 µA/cm^2 and 5.38 µA/cm^2 respectively and, although some variation was seen for each material, there is a clear reduction in corrosion rate as the Al content increases.

AZ91D, with 9 wt% Al, exhibited a mean corrosion current density of 4.82 µA/cm^2. While this is a further reduction compared to the other materials, the previously highlighted ranges also showed that there was a crossover between results for AZ61A and AZ91D, meaning it is not possible to conclude that one will always corrode faster than the other. This also indicates that the reduction in corrosion has begun to plateau at 6 wt% Al, with the addition of more Al not having such a large effect.

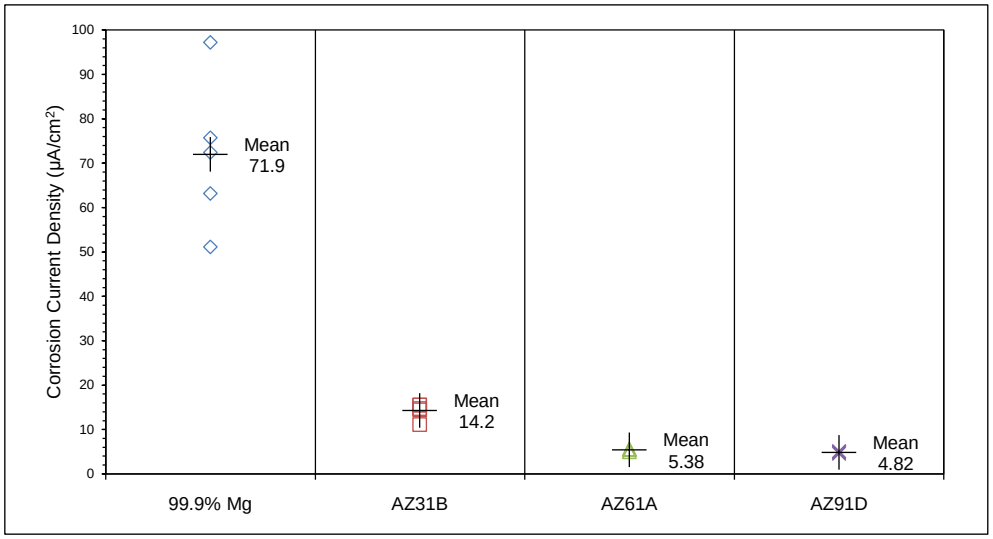

Figure 4-54 – Plot showing the corrosion current densities calculated from five EIS experiments each for 99.9% Mg, AZ31B, AZ61A and AZ91D in 3.5% NaCl solution taken immediately following the OCP measurements seen in Figure 4-44.

Corrosion Penetration Rate

The conversion of corrosion current density to corrosion penetration rate can be achieved using the identity given by Equation 4-33, which states that 1 µA/cm^2 is equivalent to a 0.023 mm/y loss, on the condition that corrosion is uniform. This yields mean corrosion penetration rates for 99.9% Mg, AZ31B, AZ61A, and AZ91D of 1.65 mm/y, 0.328 mm/y, 0.124 mm/y, and 0.111 mm/y respectively. These are plotted alongside all of the measured results in Figure 4-55.

It should be noted that over the relatively short duration of these tests — a maximum of 15 minutes for the combined OCP and EIS measurements — the corrosion was observed to be largely uniform, with only a couple of areas of localised attack being apparent on the samples. Over a longer period the uniform corrosion assumption would likely no longer apply. This does not affect the presented assessment and discussion of the influence Al content on the relative behaviours of the alloys.

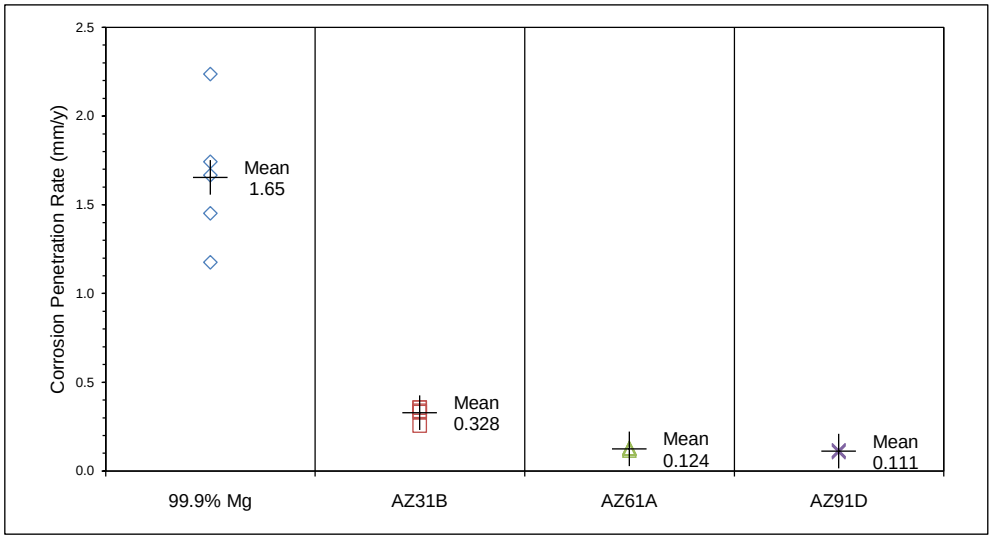

Figure 4-55 – Plot showing the corrosion penetration rates from five EIS experiments each for 99.9% Mg, AZ31B, AZ61A and AZ91D in 3.5% NaCl solution taken immediately following the OCP measurements seen in Figure 4-44.

4.3.4 Further Discussion

4.3.4.1 Corrosion Rate and Mg-Al-Zn Alloy Microstructures

The Mg examined here was 99.9% pure and for the purposes of this comparative study can be considered to behave as a single element. It has been shown to have the most active OCP of the materials tested and also has the highest corrosion rate. This gives a baseline by which the influence of alloying can be evaluated, and allows the corrosion behaviours of the Mg-Al-Zn alloys to be examined in terms of their Al content and characteristic microstructures.

AZ31B had a single phase microstructure consisting of α-Mg grains with Al held in solid solution. Adding Al as an alloying element, which is less active, has yielded a more noble OCP and reduced the corrosion rate compared to 99.9% Mg. The microstructure of AZ61A was made up of α-Mg with Al in solid solution and evidence of intermetallic $Mg_{17}Al_{12}$ precipitates within the grains and at grain boundaries. Some separate larger particles of $Mg_{17}Al_{12}$ were also distributed throughout the matrix. The greater concentration of noble Al lowers the corrosion rate even further, although the presence of a second phase introduces micro-galvanic couples into the corrosion system which may modify this effect. The OCP and corrosion rate of AZ91D are similar to AZ61A despite it having a greater Al concentration. The composition and processing of AZ91D has created a microstructure of α-Mg with continuous and discontinuous precipitates of

$Mg_{17}Al_{12,}$ which is very different to that of the other alloys. The large amount of intermetallic suggests that corrosion might now be dominated by micro-galvanic couples between phases, rather than self-corrosion of a single phase. A change in corrosion mechanism could explain why the benefits that might be expected from having more Al are not observed. This is relevant for the use of Mg-Al layers as it demonstrates how the presence of an intermetallic can influence corrosion behaviour.

4.3.4.2 Comparison with Literature Results

The results of this work are compared against a series of OCP measurements for pure Mg and AZ91D/E taken from the literature in Figure 4-56, with more detail given in Table 4-5. In each literature example the OCP of a material is given as a specific value, although it is likely that some variation would have been observed by the respective authors. The most noble OCP for AZ91D/E was −1.214 V_{SCE} (Liu *et al.* 2008 [61]), whereas the most active was −1.980 V_{SCE} (Spencer & Zhang 2009 [65]). These outlying values are not consistent with the work conducted here, and the extremes of OCP for pure Mg (−1.250 V_{SCE} and −2.133 V_{SCE}) also appear in the same respective works, with one further publication by Li *et al.* 2009 [56] also giving an OCP of −1.250 V_{SCE}. These publications are the only two where a comparison of the activity change between pure Mg and AZ91D/E can be made, and AZ91D/E is more noble than pure Mg in both. Liu *et al.* 2008 [61] shows a difference of 36 mV and Spencer & Zhang 2009 [65] records a 15 mV change, while in this work a shift of 27 mV is observed. Given the magnitude of the OCP shift, and the commonality between the authors listed by Liu *et al.* 2008 [61] and Li *et al.* 2009 [56], it is deemed reasonable to conclude that these OCPs are caused by an error in scaling, rather than an error with the measurements themselves. The OCP values for AZ91D/E given in the other references are all of the same order as those recorded here.

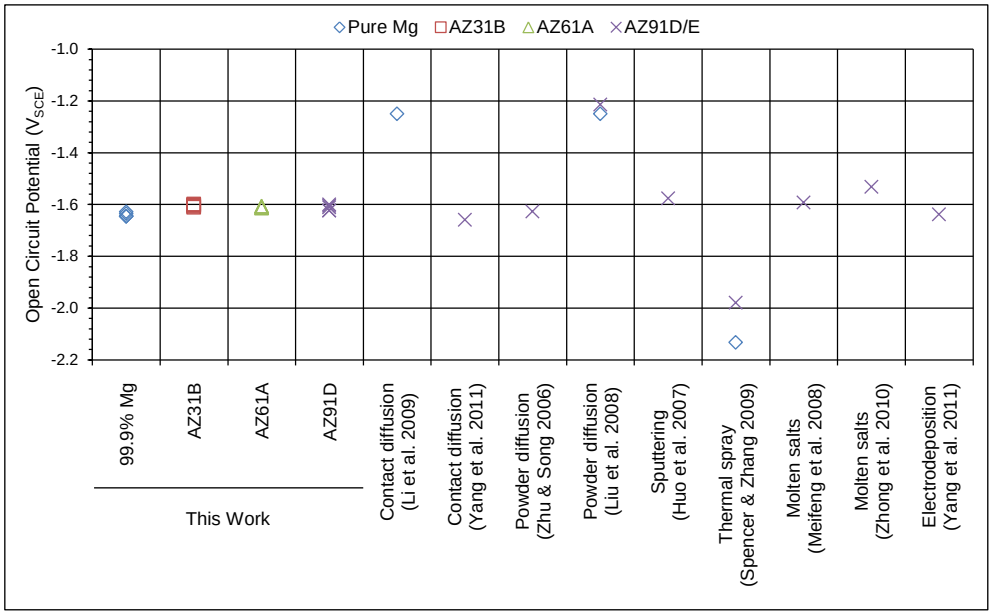

Figure 4-56 – Comparison of OCP values from this work for 99.9% Mg and Mg-Al-Zn alloys given in Figure 4-45, against measurements for pure Mg and AZ91D/E listed in Table 2-8.

The corrosion current density from this work and values for pure Mg and AZ91D/E from the literature are compared in Figure 4-57, and further detail is given in Table 4-5. The three literature values for pure Mg are between one and two orders of magnitude lower than those recorded here. Seven results for AZ91D/E are available for comparison and four of these are between one and two orders of magnitude greater. The remaining three compare well with the findings in this work. It is only possible to compare the difference in corrosion rate between pure Mg and AZ91D/E in two cases, and neither of these is consistent with that seen here. The repeatability of the results obtained in this work shows that the method used is robust. Similar standards would most likely have been applied in the literature, and so the variability in results between works shows how important material preparation and experimental setup is to the outcome.

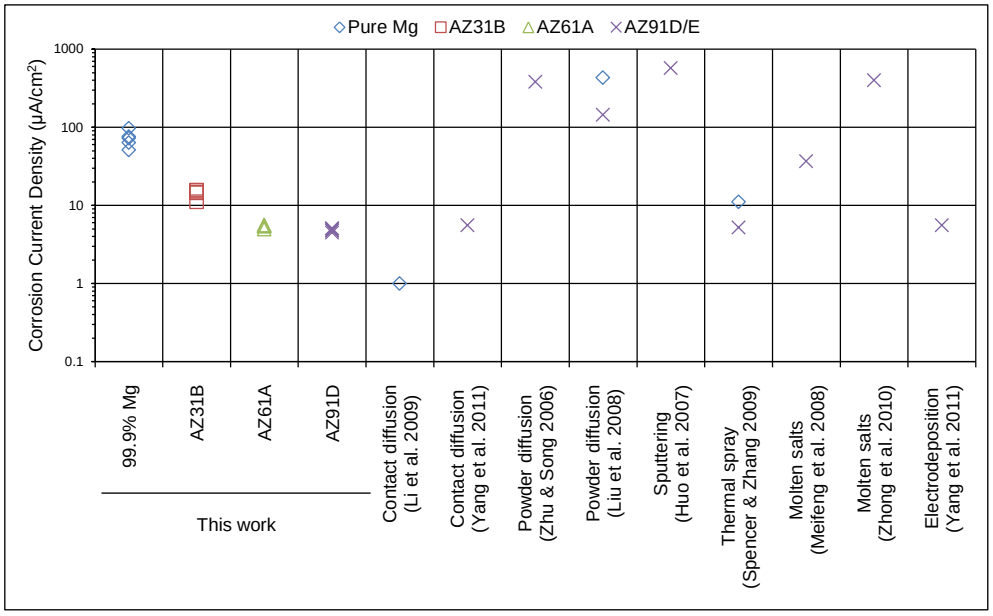

Figure 4-57 – Comparison of I_{corr} values from this work for 99.9% Mg and Mg-Al-Zn alloys given in Figure 4-54, against measurements for pure Mg and AZ91D/E listed in Table 2-8.

Table 4-5 – Values for OCP and I_{corr} from this work for 99.9% Mg and the Mg-Al-Zn alloys given in Figure 4-54, and for pure Mg and AZ91D/E listed in Table 2-8.

Material	Electrolyte	Open Circuit Potential[A] (V_{SCE})	Current Density[A] ($\mu A/cm^2$)	Reference
99.9% Mg	3.5% NaCl	−1.640	71.9	This work
AZ31B	3.5% NaCl	−1.605	14.2	This work
AZ61A	3.5% NaCl	−1.610	5.38	This work
AZ91D	3.5% NaCl	−1.613	4.82	This work
Pure Mg	5% NaCl	−1.250	1.0	Li *et al.* 2009 [56]
AZ91D	3.5% NaCl	−1.66	5.57	Yang *et al.* 2011 [57]
AZ91D	5% NaCl	−1.627	381	Zhu & Song 2006 [60]
Pure Mg	5% NaCl	-1.250	430	Liu *et al.* 2008 [61]
AZ91D	5% NaCl	−1.214	144	Liu *et al.* 2008 [61]
AZ91D	3.5% NaCl	−1.576	569.1	Huo *et al.* 2007 [63]
Pure Mg	5% NaCl	−2.133	11	Spencer & Zhang 2009 [65]
AZ91E	5% NaCl	−1.980	5.2	Spencer & Zhang 2009 [65]
AZ91D	3.5% NaCl	−1.593	36.5	Meifeng *et al.* 2008 [66]
AZ91D	3.5% NaCl	−1.532	400	Zhong *et al.* 2010 [67]
AZ91D	3.5% NaCl	−1.638	5.57	Yang *et al.* 2011 [68]

A – Where listed the value from the reference is given. Where none were available the plots from the reference were digitised and a value extrapolated.

4.3.5 Summary

The self-corrosion behaviours of 99.9% Mg and the alloys AZ31B, AZ61A, and AZ91D in 3.5% NaCl solution were compared using electrochemical techniques. Table 4-6 summarises these results, which show that 99.9% Mg has the most active OCP and the highest corrosion rate of the materials examined. The addition of 3% Al in AZ31B resulted in a corrosion current density which was 20% of that measured for 99.9% Mg and an OCP that was 35 mV more noble. For AZ61A, with 6 wt% Al, the corrosion rate reduced further to 7.4% of that of 99.9% Mg but the OCP shift was slightly less at 30 mV more noble. The results for AZ91D were similar to AZ61A with a corrosion rate of 6.7% of the value for 99.9% Mg and an OCP that was 27 mV more noble. The overlap between results for AZ61A and AZ91D shows that more Al does not necessarily lead to a lower corrosion rate, and in this case also means it is not possible to confirm that one has better self-corrosion properties than the other.

The spread of OCP and corrosion rate results observed between this work and the literature also highlights that the electrochemical behaviour of a material, especially one as active at Mg, is very dependent on test conditions, which includes the way it is stored and prepared beforehand. Provided there is consistency in the experimental method then good comparisons can be drawn.

Table 4-6 – Summary of the OCP and I_{corr} values recorded in this work for 99.9% Mg and the Mg-Al-Zn alloys.

Substrate	Open Circuit Potential (V_{SCE})	Corrosion Rate		
		Charge Transfer Resistance ($\Omega.cm^2$)	Corrosion Current Density ($\mu A/cm^2$)	Corrosion Penetration Rate (mm/y)
99.9% Mg	−1.640	169	71.9	1.65
AZ31B	−1.605	828	14.2	0.328
AZ61A	−1.610	2160	5.38	0.124
AZ91D	−1.613	2420	4.82	0.111

4.4 Mg-Al Intermetallic Self-Corrosion

4.4.1 Introduction

This section investigates the corrosion behaviour of the Mg-Al intermetallics $Mg_{17}Al_{12}$ and M_2Al_3 by exposing samples to 3.5% NaCl solution and measuring their electrochemical characteristics. The recorded OCPs and corrosion rates are compared with those of the Mg-Al-Zn alloys, and the implications these results may have for the use of Mg-Al intermetallic surface layers for improving corrosion performance are discussed.

4.4.2 Materials and Methods

4.4.2.1 Manufacturing of Mg-Al Intermetallics

The two intermetallics used for corrosion testing were manufactured by melting 99.9% pure Mg ribbon and 99.9% pure Al wire at 750°C (1023 K) in a sealed stainless steel vessel in weight proportions equivalent to their respective atomic compositions. For the intermetallic $Mg_{17}Al_{12}$ this corresponds to 56 wt% Mg and 44 wt% Al, while for Mg_2Al_3 it is 38 wt% Mg and 62 wt% Al. The regions where the two intermetallics can form are highlighted in the binary phase diagram in Figure 4-20. Immediately before being added to the melt vessel the raw Mg and Al were abraded with P4000 SiC paper and ultrasonically cleaned in IPA to ensure the amount of surface oxide and other contaminants was minimised.

Stainless Steel Melt Vessel

To prevent gross oxidation of Mg at high temperatures the Mg and Al were melted together in a sealed stainless steel vessel so that oxygen availability was limited. This was constructed from 1″ NB schedule 40 SS304 welded pipe (26.6 mm ID, 3.38 mm wall thickness) with 6 mm thick SS304 welded end caps. Material was added to the vessel through a central filler tube made from a 150 mm length of SS316 seamless pipe (6 mm OD, 1 mm wall thickness) welded into one end cap, which was then crimped and seal welded. A diagram of the vessel is shown in Figure 4-58.

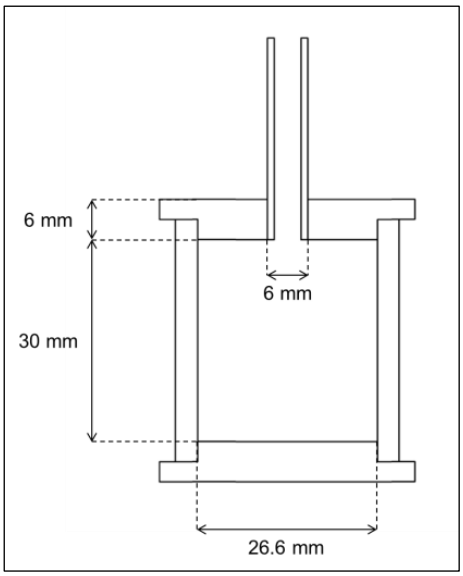

Figure 4-58 – Diagram showing the stainless steel vessel in which Mg and Al were melted to produce $Mg_{17}Al_{12}$ and Mg_2Al_3 intermetallics.

The sealed vessel contains air that will cause the internal pressure to increase when it is heated to 750°C (1023 K). To ensure the vessel could be safely heated to this temperature the mechanical properties were assessed assuming it was filled entirely with atmospheric air.

The combined gas law in Equation 4-34 describes the relationship between pressure (P), volume (V) and temperature (T) of the vessel system at room temperature (P_1, V_1, T_1) and at high temperature (P_2, V_2, T_2).

$$\frac{P_1.V_1}{T_1} = \frac{P_2.V_2}{T_2} \qquad 4\text{-}34$$

As the volume of the vessel is fixed ($V_1 = V_2$) this can be simplified, and rearranged, to give the following.

$$P_2 = P_1.\frac{T_2}{T_1} \qquad 4\text{-}35$$

Where P_1 is the internal pressure at room temperature (assumed 100 kPa), T_1 is room temperature (assumed 298 K) and T_2 is the temperature the sealed vessel is heated to

(1023 K). This yields an absolute internal pressure at melt temperature (P_2) of 343 kPa and a net pressure (absolute internal pressure minus outside air pressure) of 243 kPa.

Barlow's formula (Equation 4-36) relates the internal pressure (P) that a pipe can withstand (its burst pressure) to its outside diameter (D), wall thickness (t) and the strength of the material (S) [170]. The resulting pressure has been multiplied by a safety factor of 0.5 to account for the use of welded pipe and joints.

$$P = \frac{2St}{D} \qquad 4\text{-}36$$

The room temperature tensile strength of SS304 and SS316 is 579 MPa, and these correspond to burst pressures of 59 MPa for the vessel body and 97 MPa for the filler tube. At 1089 K (66 K above the melt temperature) the tensile strengths drop to 124 MPa and 186 MPa for the vessel body and filler tube respectively, which yields burst pressures of 13 MPa and 19 MPa. In all cases the burst pressure is significantly greater than the internal pressure due the heating of air sealed within the vessel.

At a melt temperature of 1023 K creep rupture is also a possible failure mechanism. The stress for rupture in 1000 h at 1033 K is 53 MPa for SS304 and 71 MPa for SS316, although the vessel will be at temperature for no more than 10 h at a time. These stresses correspond to internal pressures of 5 MPa and 12 MPa respectively, which are also significantly higher than the maximum internal pressure that could be achieved by heating.

In-Vessel Oxide Formation

Any oxygen that remains in the vessel once it is sealed will react to form oxides when the temperature is raised. Assuming that this will occur preferentially with Mg, the mass of oxide that could form was calculated to make sure it would not compromise the quality of the melt.

As this is a sealed vessel the volume of air is fixed and will not change with temperature. The amount of oxygen it contains can be calculated according to the ideal gas law in Equation 4-37.

$$PV = nRT \qquad 4\text{-}37$$

The absolute internal pressure (P) and temperature (T) are assumed to be 100 kPa and 298 K respectively. The volume of the vessel (V) is 1.96×10^{-5} m^3 and the ideal gas constant (R) is 8.315 $Pa.m^3/K$, yielding 7.91 x 10^{-4} moles (n) of air. Only 21% of this, or 1.66×10^{-4} moles, is oxygen that will react according to Equation 4-38.

$$2Mg + 2O_2 \rightarrow 2MgO \qquad 4\text{-}38$$

As such the maximum amount of Mg that could react due to oxygen in the vessel would be 1.66×10^{-4} moles, or 0.004 g (24.3 g/mol), which is 0.07% of the Mg used to manufacture the Mg-rich intermetallic.

Melt Procedure

An electric vertical tube furnace was used to melt the mix of Mg and Al, and this was pre-heated to 750°C prior to lowering in the sealed stainless steel vessel. Once the temperature had returned back up to 750°C it was left for 30 min, before being vigorously shaken to break up surface oxides that can prevent proper mixing of the melt. This was carried out two more times, with the temperature allowed to return to 750°C in between. The vessel was then left at temperature for a further 1 h, after which time it was removed from the furnace and allowed to cool to ambient temperature in still air.

Preparation for Corrosion Testing

A precision saw was subsequently used to cut open the vessel, and the resulting intermetallics are shown in Figure 4-59 following an initial grinding with SiC paper to create a flat and uniform surface. The compositions of the melts and the presence of the relevant Mg-Al intermetallics were confirmed using EDX and XRD.

To ensure that a known area of intermetallic was exposed the voids caused by porosity were masked with epoxy resin; as was the outer ring of the stainless steel melt vessel, to which the samples were fused. The exposed area of intermetallic was then calculated by image analysis. Immediately prior to testing the samples were abraded with P4000 SiC paper and then rinsed in IPA and dried.

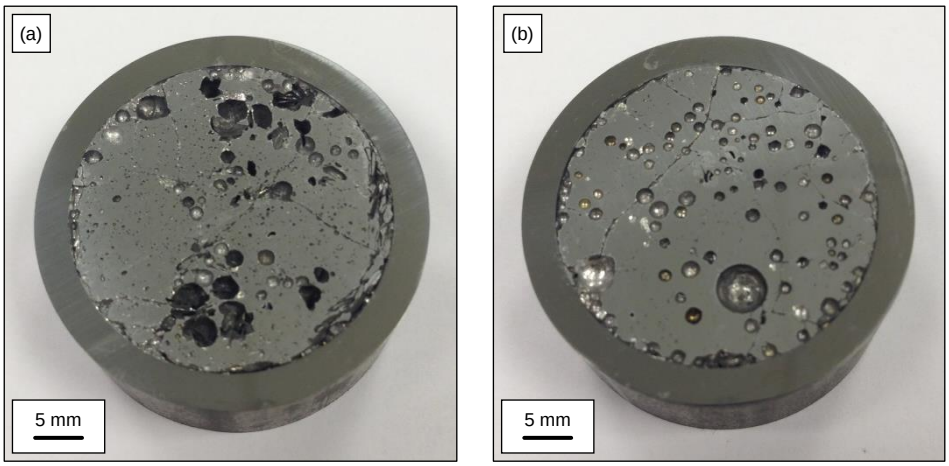

Figure 4-59 – Manufactured samples of a) $Mg_{17}Al_{12}$, and b) Mg_2Al_3, after sectioning and prior to masking. The wall of the stainless steel vessel can be seen surrounding the intermetallics.

4.4.2.2 Self-Corrosion Measurements

Following preparation each sample was exposed to 3.5% NaCl a single time and electrochemical data was recorded using the equipment and software given in Section 3.3. The OCP measurements were begun immediately following exposure of a sample, and continued until the corroding system had settled to a relatively steady OCP. An EIS run was then started from a frequency of 20 kHz reducing on a log scale with 10 readings taken per decade at an amplitude of 10 mV on potentiostat bandwidth F. Once a satisfactory semicircle had been recorded and no meaningful data was being gathered the run was stopped. The circle fit function built into the ZPlot software was then used to obtain values for R_{ct}.

4.4.3 Results and Discussion

4.4.3.1 Open Circuit Potentials

Mg-Al Intermetallics

Open circuit potential measurements were conducted for the Mg-Al intermetallics $Mg_{17}Al_{12}$ and Mg_2Al_3 in 3.5% NaCl solution, and the plot in Figure 4-60 shows the changes that occurred during the first 10 h after exposure. Mean OCPs were calculated over the last 1 h and gave values of −1.058 V_{SCE} for $Mg_{17}Al_{12}$ (range *a*), and −1.115 V_{SCE} for Mg_2Al_3 (range *b*). These OCPs sit between those of Mg (−1.640 V_{SCE} for the 99.9% Mg measured here) and Al (−1.02 V_{SCE} as given in Section 2.1.1.1), which indicates that the intermetallics have mixed potentials that are the result of the combined behaviour of local anodes (Mg) and cathodes (Al) on their surfaces.

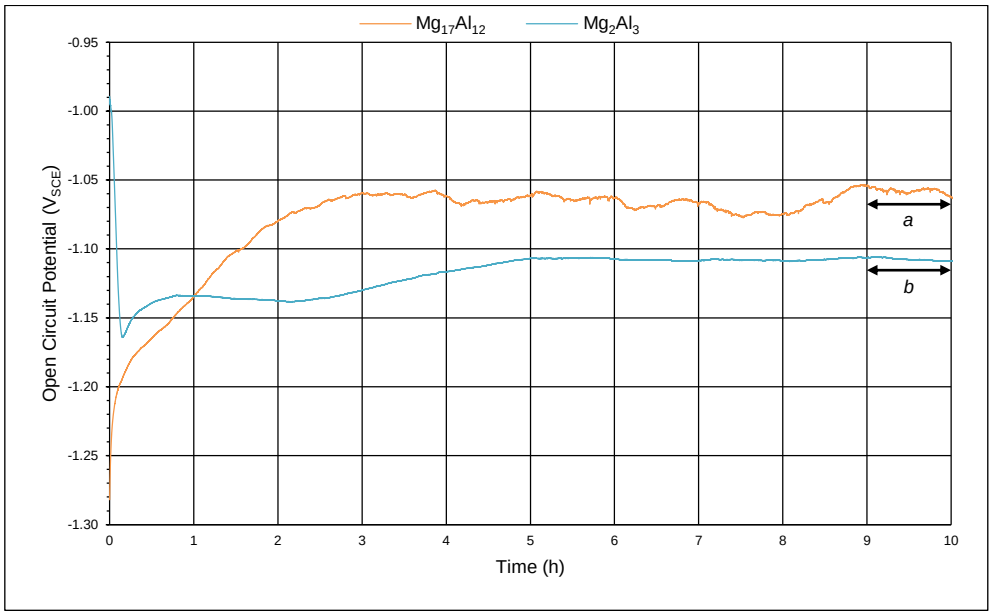

Figure 4-60 – Potential versus time plot showing the OCPs recorded for the Mg-Al intermetallics $Mg_{17}Al_{12}$ and Mg_2Al_3 over the first 10 h of exposure to 3.5% NaCl solution. The mean potentials calculated over the last 1 h are −1.058 V_{SCE} for $Mg_{17}Al_{12}$ (range *a*), and −1.115 V_{SCE} for Mg_2Al_3 (range *b*).

A series of Evans diagrams (Figure 4-43) were used in Section 4.3.3.1 to describe how variations in OCP observed for 99.9% Mg and the Mg-Al-Zn alloys can be explained by anodic reaction rate changes, and the same arguments apply to those recorded for $Mg_{17}Al_{12}$ and Mg_2Al_3. The Mg-Al intermetallics are thought to take longer to reach relatively settled OCPs (approximately 6 h compared to around 10 min for 99.9% Mg

and the Mg-Al-Zn alloys) because their more noble surfaces slow down the rate at which a protective oxide layer develops. It should also be noted that the intermetallics are single phase, and so there will be no micro-galvanic corrosion effects.

Comparison of 99.9% Mg, Mg-Al-Zn Alloys and Mg-Al Intermetallics

Figure 4-45 shows the OCP values for 99.9% Mg and the Mg-Al-Zn alloys (AZ31B, AZ61A and AZ91D) described in Section 4.3.3.1, alongside those of the Mg-Al intermetallics ($Mg_{17}Al_{12}$ and Mg_2Al_3) recorded here. This shows that the intermetallics have potentials that are at least 498 mV more noble than the other materials, with the greatest difference (582 mV) seen between 99.9% Mg and $Mg_{17}Al_{12}$. Perhaps counter to what might be expected, due the relative proportions of more active Mg and more noble Al, the Mg-rich $Mg_{17}Al_{12}$ is 57 mV more noble than Al-rich Mg_2Al_3.

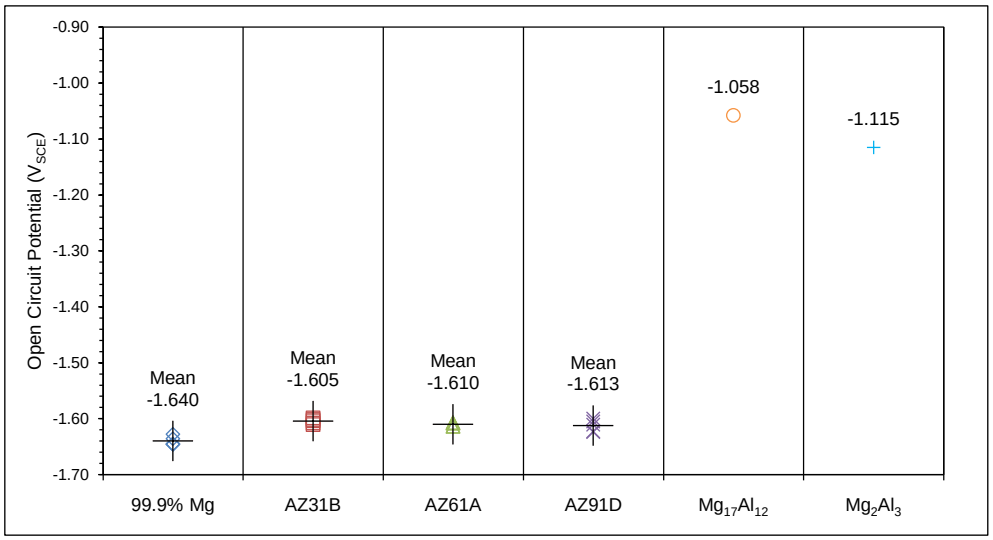

Figure 4-61 – Plot showing the OCP values for 99.9% Mg, the Mg-Al-Zn alloys (AZ31B, AZ61A, and AZ91D) and the Mg-Al intermetallics ($Mg_{17}Al_{12}$ and Mg_2Al_3) exposed to 3.5% NaCl solution.

4.4.3.2 Self-Corrosion Rates

Self-corrosion rate measurements were conducted for the Mg-Al intermetallics $Mg_{17}Al_{12}$ and Mg_2Al_3 in 3.5% NaCl solution using electrochemical impedance spectroscopy. Charge transfer resistances were obtained assuming that the system could be modelled by the simple equivalent circuit model in Figure 4-62. These were subsequently converted into corrosion current densities and corrosion penetration rates for comparison.

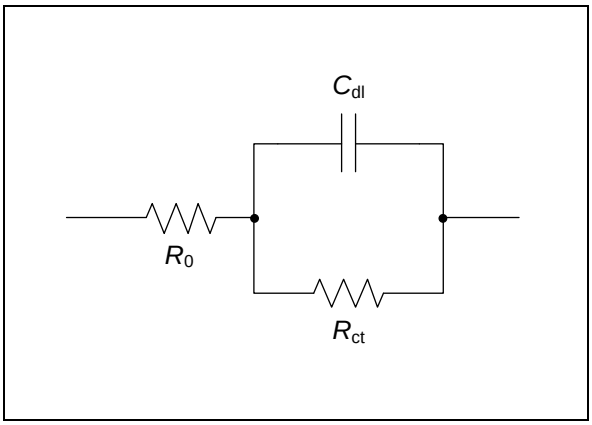

Figure 4-62 – Assumed equivalent circuit model used to obtain R_{ct} values from EIS results for the Mg-Al intermetallics ($Mg_{17}Al_{12}$ and Mg_2Al_3) in 3.5% NaCl solution [165].

Charge Transfer Resistance

The Nyquist plot in Figure 4-63 shows the EIS results for the intermetallics $Mg_{17}Al_{12}$ and Mg_2Al_3. The data points follow single semicircles from low impedance (high frequencies) to high impedance (low frequencies) and, although they are not as complete as those recorded for 99.9% Mg and the Mg-Al-Zn alloys (Figure 4-52), there is no evidence of a 45° diffusion tail relating to a Warburg impedance at lower frequencies as was illustrated earlier in Figure 4-40.

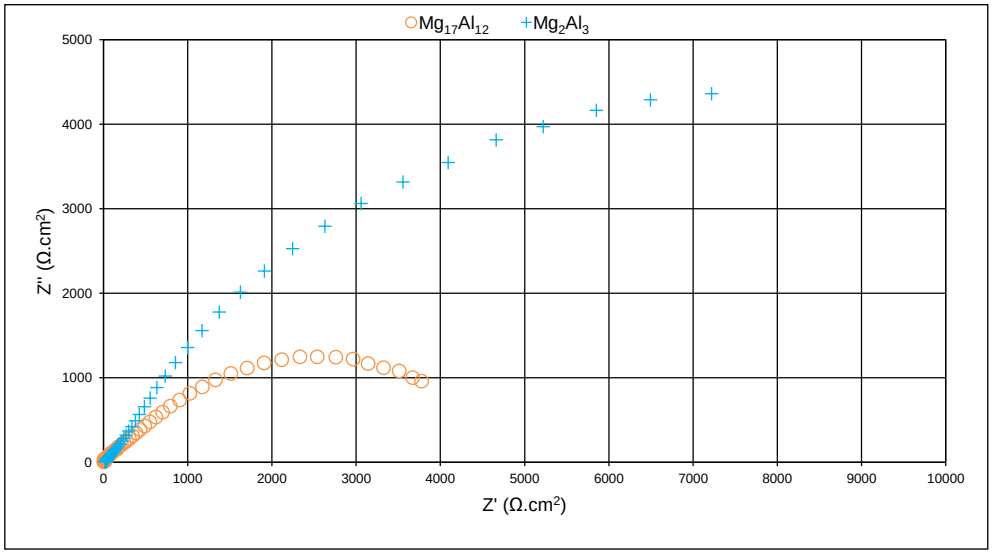

Figure 4-63 – Nyquist plot showing the results of EIS experiments for the Mg-Al intermetallics $Mg_{17}Al_{12}$ and Mg_2Al_3 in 3.5% NaCl solution. The associated charge transfer resistances are 4770 $\Omega.cm^2$ for $Mg_{17}Al_{12}$, and 15400 $\Omega.cm^2$ for Mg_2Al_3.

The circle fit function in ZPlot yielded charge transfer resistances of 4770 Ω.cm^2 for $Mg_{17}Al_{12}$ and 15400 Ω.cm^2 for Mg_2Al_3 and these are plotted for comparison with those of 99.9% Mg and the Mg-Al-Zn alloys in Figure 4-64. This shows that $Mg_{17}Al_{12}$ has an R_{ct} almost twice that of AZ91D (the greatest for the alloys), while the R_{ct} of Mg_2Al_3 is over six times larger than AZ91D.

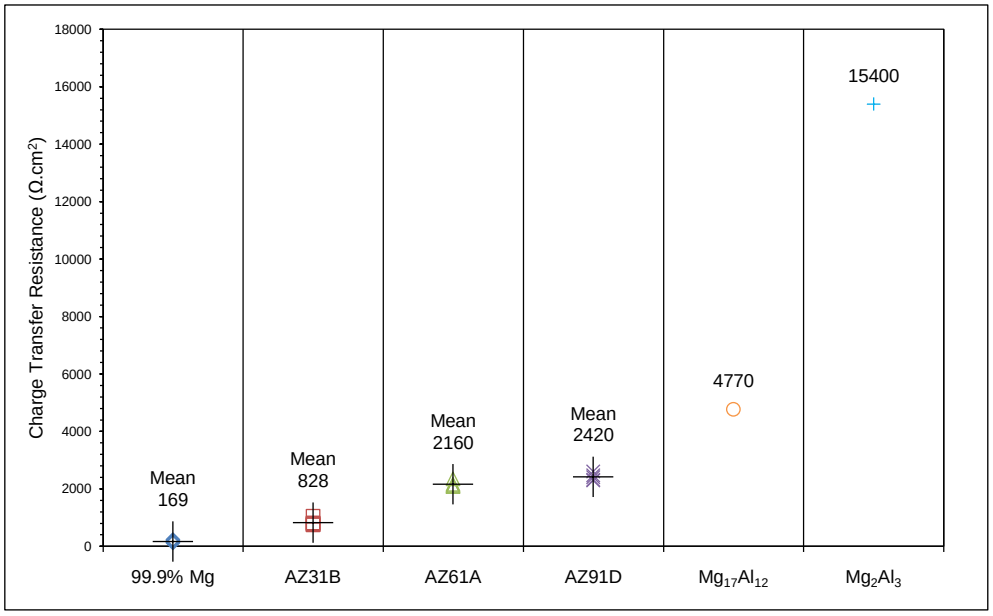

Figure 4-64 – Plot showing the charge transfer resistances for 99.9% Mg, the Mg-Al-Zn alloys (AZ31B, AZ61A, and AZ91D) and the Mg-Al intermetallics ($Mg_{17}Al_{12}$ and Mg_2Al_3) exposed to 3.5% NaCl solution.

Corrosion Current Density

The R_{ct} values in Figure 4-64 were translated into corrosion current densities using Equation 4-29, and these are compared in Figure 4-65. The I_{corr} values for 99.9% Mg, AZ31B, AZ61A, and AZ91D were 71.9 µA/cm^2, 14.2 µA/cm^2, 5.38 µA/cm^2 and 4.82 µA/cm^2 respectively, and Section 4.3.3.1 highlighted how reducing corrosion rates were related to an increase in the amount of $Mg_{17}Al_{12}$ within the microstructure. It is logical therefore that a sample of $Mg_{17}Al_{12}$ displays an even lower I_{corr} of 2.44 µA/cm^2. With a further increase in Al content an even lower corrosion rate is recorded, with the Mg_2Al_3 intermetallic exhibiting an I_{corr} value of 0.75 µA/cm^2.

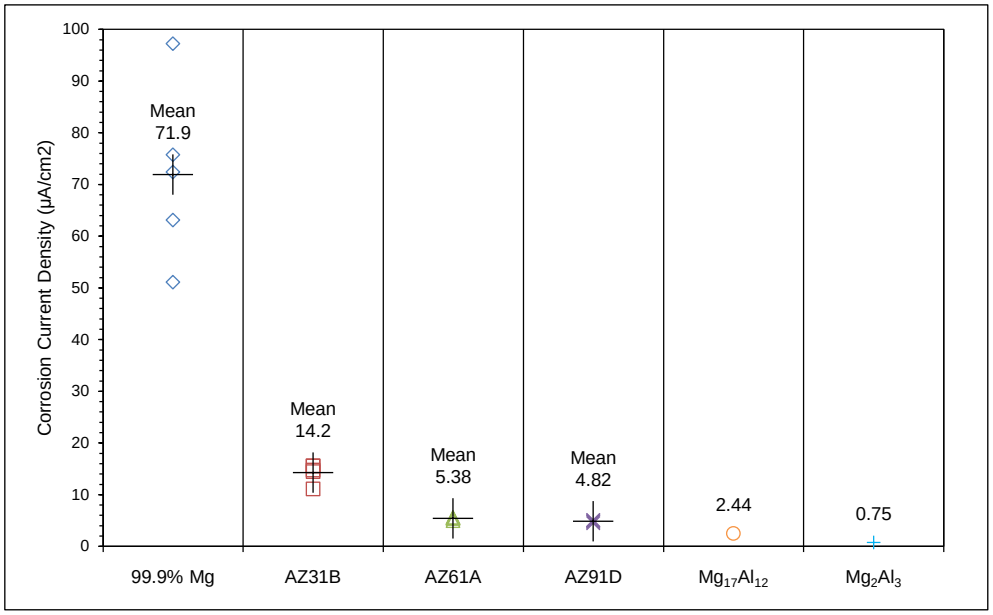

Figure 4-65 – Plot showing the I_{corr} values for 99.9% Mg, the Mg-Al-Zn alloys (AZ31B, AZ61A, and AZ91D) and the Mg-Al intermetallics ($Mg_{17}Al_{12}$ and Mg_2Al_3) exposed to 3.5% NaCl solution.

It is perhaps intuitive that of the two intermetallics the Al-rich one has the lowest I_{corr}, but it is maybe not so instinctive to find that it also has the most active OCP. So far any changes in OCP and I_{corr} have been discussed in terms of variations to the anodic curve on the Evans diagram. However, as illustrated in Figure 4-66, it is also possible for the slope of the cathodic curve to change if the rate of the cathodic reaction is altered. This does not preclude fluctuations in the anodic reaction, but does illustrate how changes to the cathodic reaction can lead to the result found here.

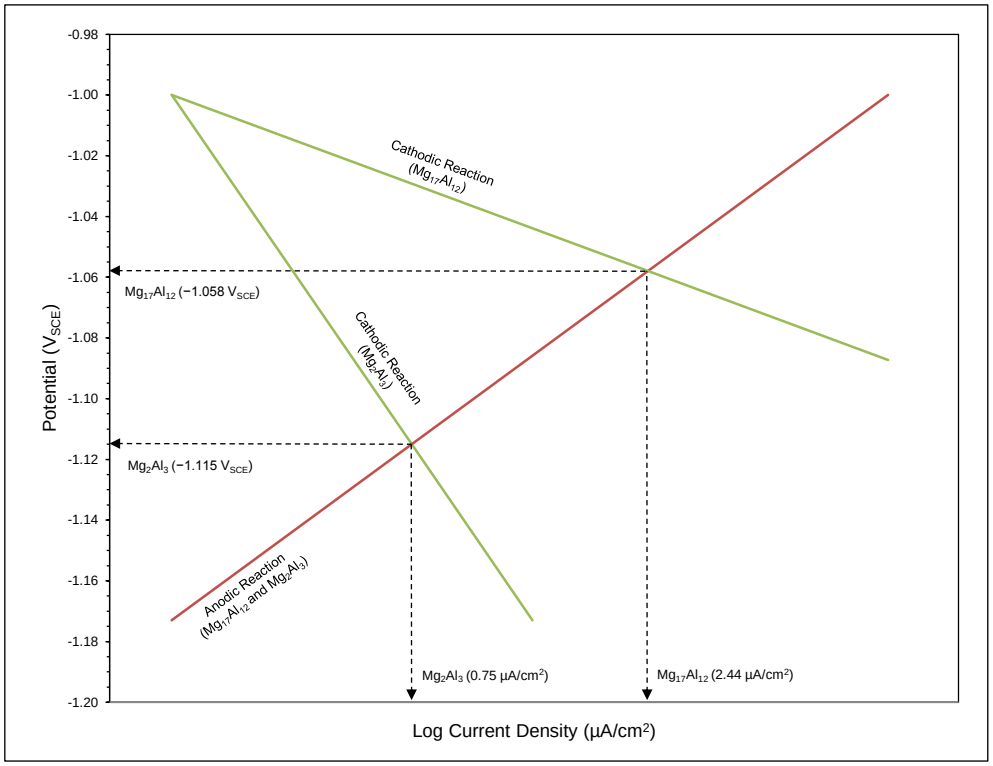

Figure 4-66 – Evans diagrams for corroding $Mg_{17}Al_{12}$ and Mg_2Al_3 illustrating how changes to the slope of the cathodic reaction can lead to a lower I_{corr} and more active OCP.

Corrosion Penetration Rate

The conversion of I_{corr} to corrosion penetration rate can be achieved using the identity given by Equation 4-33, which states that 1 µA/cm^2 is equivalent to a 0.023 mm/y loss, on the condition that corrosion is uniform. This translates to mean corrosion penetration rates of 0.056 mm/y for $Mg_{17}Al_{12}$, and 0.017 mm/y for Mg_2Al_3. These are plotted in Figure 4-67 alongside the results for 99.9% Mg, AZ31B, AZ61A, and AZ91D.

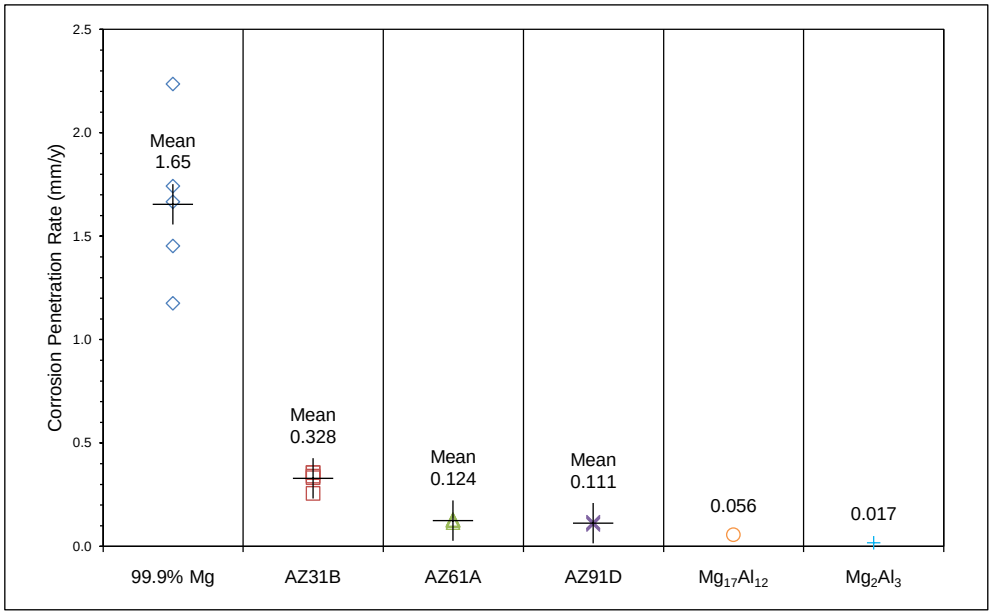

Figure 4-67 – Plot showing the corrosion penetration rates for 99.9% Mg, the Mg-Al-Zn alloys (AZ31B, AZ61A, and AZ91D) and the Mg-Al intermetallics ($Mg_{17}Al_{12}$ and Mg_2Al_3) exposed to 3.5% NaCl solution.

4.4.4 Further Discussion

Only one literature example specifically examining the corrosion behaviour of the Mg-Al intermetallics could be found, and as such the comparisons of OCP and I_{corr} in Figure 4-68 and Figure 4-69 respectively include examples of intermetallic surface layers produced by different methods. Where available, results for pure Mg and AZ91D/E are also shown. Further details, including the concentrations of NaCl in the electrolytes and the electrochemical techniques used, are given in Table 4-7.

The OCPs of the Mg-Al intermetallics measured here were more noble than 99.9% Mg and the Mg-Al-Zn alloys and this was also shown in the work of Spencer & Zhang 2009 [65], albeit with an offset that was explained as a scaling error in Section 4.3.4.2. Also reflected in this work was the fact that, perhaps counterintuitively, the Mg-rich intermetallic $Mg_{17}Al_{12}$ is more noble than the Al-rich Mg_2Al_3. In each case where the OCP of an IM layer and the substrate material can be compared, the substrate is always more active.

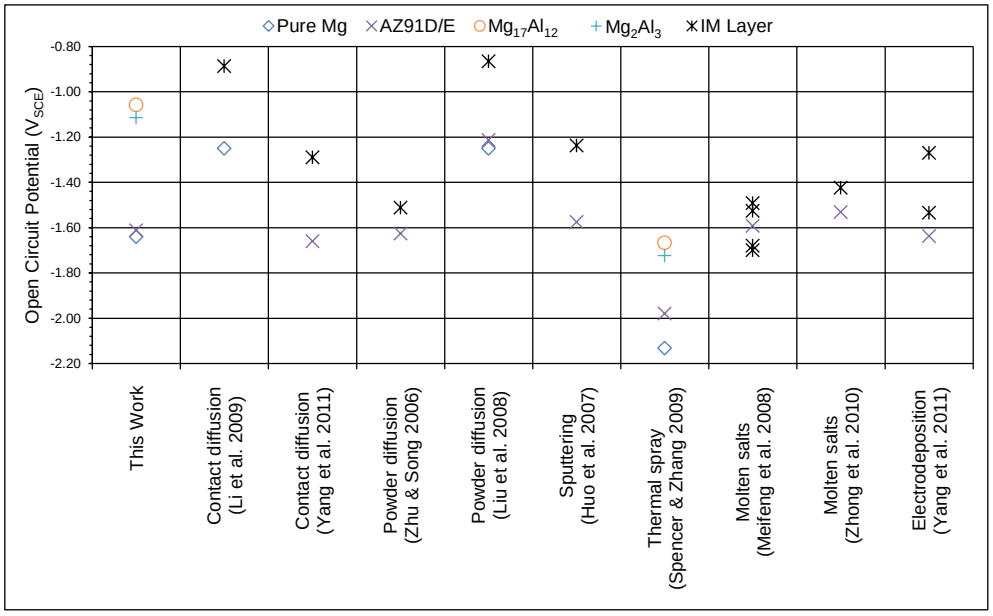

Figure 4-68 – Comparison of OCP values from this work for 99.9% Mg, AZ91D, $Mg_{17}Al_{12}$, and Mg_2Al_3 given in Figure 4-45 and Figure 4-61, against measurements for pure Mg, AZ91D/E, $Mg_{17}Al_{12}$, Mg_2Al_3, and Mg-Al intermetallic layers listed in Table 2-8.

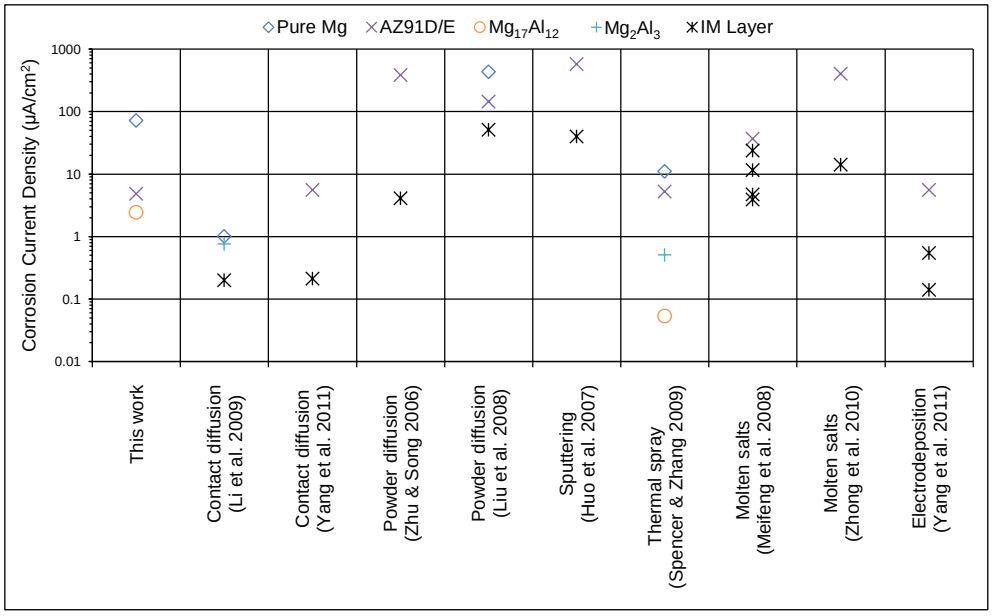

Figure 4-69 – Comparison of I_{corr} values from this work for 99.9% Mg, AZ91D, $Mg_{17}Al_{12}$, and Mg_2Al_3 given in Figure 4-54 and Figure 4-65, against measurements for pure Mg, AZ91D/E, $Mg_{17}Al_{12}$, Mg_2Al_3, and Mg-Al intermetallic layers listed in Table 2-8.

Table 4-7 – Values for OCP and I_{corr} from this work for $Mg_{17}Al_{12}$, and Mg_2Al_3 given in Figure 4-65, and for $Mg_{17}Al_{12,}$ $Mg_2Al_{3,}$ and Mg-Al intermetallic layers listed in Table 2-8.

Material	Electrolyte	Open Circuit Potential[A] (V_{SCE})	Current Density[A] ($\mu A/cm^2$)	Reference
$Mg_{17}Al_{12}$	3.5% NaCl	−1.058	2.44	This work
Mg_2Al_3	3.5% NaCl	−1.115	0.75	This work
IM Layer	5% NaCl	−0.887	0.2	Li *et al.* 2009 [56]
IM Layer	3.5% NaCl	−1.29	0.21	Yang *et al.* 2011 [57]
IM Layer	5% NaCl	−1.512	4.1	Zhu & Song 2006 [60]
IM Layer	5% NaCl	−0.866	51	Liu *et al.* 2008 [61]
IM Layer	3.5% NaCl	−1.238	39.55	Huo *et al.* 2007 [63]
$Mg_{17}Al_{12}$	5% NaCl	−1.667	0.05	Spencer & Zhang 2009 [65]
Mg_2Al_3	5% NaCl	−1.724	0.51	Spencer & Zhang 2009 [65]
IM Layer	3.5% NaCl	−1.700	23.7	Meifeng *et al.* 2008 [66]
IM Layer	3.5% NaCl	−1.526	3.9	Meifeng *et al.* 2008 [66]
IM Layer	3.5% NaCl	−1.681	4.7	Meifeng *et al.* 2008 [66]
IM Layer	3.5% NaCl	−1.493	11.5	Meifeng *et al.* 2008 [66]
IM Layer	3.5% NaCl	−1.424	14	Zhong *et al.* 2010 [67]
IM Layer	3.5% NaCl	−1.535	0.54	Yang *et al.* 2011 [68]
IM Layer	3.5% NaCl	−1.271	0.14	Yang *et al.* 2011 [68]

A – Where listed the value from the reference is given. Where none were available the plots from the reference were digitised and a value extrapolated.

The I_{corr} values for the manufactured samples of $Mg_{17}Al_{12}$ and Mg_2Al_3 examined here were lower than those of the Mg-Al-Zn alloys and this is also seen in the work by Spencer & Zhang 2009 [65]. The magnitudes of the differences in not consistent however, with this work showing AZ91D corroding at twice the rate of $Mg_{17}Al_{12}$ and over six times the rate of Mg_2Al_3, and Spencer & Zhang 2009 [65] recording an opposite, and more pronounced, difference where the corrosion rate of Mg_2Al_3 was one order of magnitude lower than AZ91D and $Mg_{17}Al_{12}$ was two orders of magnitude lower. These order of magnitude reductions in corrosion rate are also seen in the examples where an IM layer and the associated substrate can be compared.

The experimental work conducted here and the examples shown from the literature confirm that an Mg-Al intermetallic surface layer would corrode at a slower rate than the Mg substrate. The relative OCPs of the possible substrates and surface layers also confirm that there would be a driver for galvanic corrosion if the layer was damaged.

4.4.5 Summary

The self-corrosion behaviours of $Mg_{17}Al_{12}$ and Mg_2Al_3 in 3.5% NaCl solution were compared using electrochemical techniques, and Table 4-8 summarises these results alongside those for 99.9% Mg and the Mg-Al-Zn alloys. These show that an Mg-Al intermetallic engineered as a surface layer would reduce the corrosion rate of the alloys examined here. However, their relatively noble nature also means they have the potential to become strong cathodes in a galvanic couple.

Table 4-8 – Summary of the OCP and I_{corr} values recorded in this work for 99.9% Mg, Mg-Al-Zn alloys, and Mg-Al intermetallics.

Substrate	Open Circuit Potential (V_{SCE})	Corrosion Rate		
		Charge Transfer Resistance ($\Omega.cm^2$)	Corrosion Current Density ($\mu A/cm^2$)	Corrosion Penetration Rate (mm/y)
99.9% Mg	−1.640	169	71.9	1.65
AZ31B	−1.605	828	14.2	0.328
AZ61A	−1.610	2160	5.38	0.124
AZ91D	−1.613	2420	4.82	0.111
$Mg_{17}Al_{12}$	−1.058	4470	2.44	0.056
Mg_2Al_3	−1.115	15400	0.75	0.017

4.5 Galvanic Corrosion

4.5.1 Introduction

Galvanic corrosion could be a problem for Mg-Al intermetallic layers, as any flaws, surface damage, or wear that penetrates through to the substrate might initiate a couple that leads to a serious loss of corrosion performance.

The importance of the role of intermetallic phases in controlling corrosion was demonstrated in Section 4.3, which showed how composition and microstructure influences the self-corrosion behaviour of Mg-Al-Zn alloys. The results for 99.9% Mg, AZ31B (3 wt% Al), and AZ61A (6 wt% Al) exhibited a trend of reducing self-corrosion rate with increasing Al content, and each had microstructures that were largely single phase α-Mg solid solution with increasing amounts of $Mg_{17}Al_{12}$ intermetallic. For AZ91D, which contains 9 wt% Al and had a two-phase eutectic type structure of α-Mg and $Mg_{17}Al_{12}$, this trend did not continue in such a pronounced fashion. Instead the corrosion rate was only marginally lower than AZ61A, and it was proposed that a change in the dominant corrosion mechanism was responsible, with self-corrosion of a single phase being replaced by micro-galvanic corrosion between two phases.

Given the apparent significance of galvanic couples involving intermetallics this section makes use of a zero resistance ammeter (ZRA) and the resistance box (R-box) technique to further investigate the role of micro-galvanic couples in Mg-Al-Zn alloy self-corrosion, and examines the implications for the use of protective intermetallic surface layers on Mg alloys.

A series of measurements between the alloys AZ31B, AZ61A, and AZ91D, and the intermetallics $Mg_{17}Al_{12}$ and Mg_2Al_3 are conducted against 99.9% Mg to provide a standard by which they can be compared. The microstructural analysis in Section 4.2 also revealed that the α-Mg solid solution phase in AZ91D was similar to AZ31B, and so a simulation of micro-galvanic corrosion in AZ91D is conducted by coupling AZ31B with the intermetallic $Mg_{17}Al_{12}$. A damaged protective surface layer is also simulated using a couple of AZ91D and the intermetallic Mg_2Al_3, representing the substrate and the surface layer respectively. These experiments are summarised in Table 4-9.

Table 4-9 – Summary of the galvanic experiments discussed here.

Galvanic Couple		Experiment Aim
Assumed Anode	Assumed Cathode	
99.9% Mg	AZ31B	Standard against pure Mg for comparison
99.9% Mg	AZ61A	Standard against pure Mg for comparison
99.9% Mg	AZ91D	Standard against pure Mg for comparison
99.9% Mg	$Mg_{17}Al_{12}$	Standard against pure Mg for comparison
99.9% Mg	Mg_2Al_3	Standard against pure Mg for comparison
AZ31B	$Mg_{17}Al_{12}$	Simulation of the micro-galvanic couples involved in AZ91D self-corrosion. The two phases are represented by AZ31B (α-Mg solid solution) and $Mg_{17}Al_{12}$ (intermetallic).
AZ91D	Mg_2Al_3	Simulation of corrosion resulting from a damaged intermetallic surface layer (Mg_2Al_3) on an AZ91D substrate.

4.5.2 Materials and Methods

4.5.2.1 Pure Mg, Mg-Al-Zn Alloys, and Mg-Al Intermetallics

The materials used for galvanic corrosion testing were 99.9% pure Mg, ASTM standard Mg-Al-Zn alloys AZ31B, AZ61A, and AZ91D, and the Mg-Al intermetallics $Mg_{17}Al_{12}$ and Mg_2Al_3. The 99.9 Mg was 0.25 mm rolled sheet and the alloys were 1 mm rolled AZ31B and AZ61A, and a 5 mm section of cast AZ91D. The elemental composition of the 99.9% pure Mg was examined previously in Section 4.1.2.1 and that of the Mg-Al-Zn alloys was confirmed in Section 4.2.2.1. The microstructures of the alloys were also discussed in Section 0. The manufacture and preparation of the intermetallics was described in Section 4.4.2.1.

The behaviours of the examined galvanic couples, which are listed in Table 4-9, were recorded once using each of the two measurement methods described in Section 4.5.2.3. Immediately prior to testing the samples were abraded with P4000 SiC paper then rinsed in IPA and dried.

4.5.2.2 Galvanic Corrosion Theory

The electrochemistry of self-corrosion, and the techniques that can be used to measure it, were discussed in Section 4.3.2.2. This described how the electrical current generated within a material during self-corrosion is fundamentally linked to its dissolution rate, and illustrated how the current flows from anodic (more negative) sites to cathodic (more positive) sites on its surface.

Galvanic corrosion occurs when two or more dissimilar metals are electrically connected and exposed to an electrolyte. This allows electrons, which would normally flow within a material during self-corrosion, to pass between materials. The movement of electrons — the galvanic current — is driven by the difference in their OCPs, and the greater this is the stronger the current will be. The direction of the galvanic current is determined by the relative activities of the materials involved. In a simple galvanic couple involving only two metals, as illustrated in Figure 4-70, the more active (negative) material becomes the anode and electrons will flow away from it to the more noble (positive) cathode, with the result being a change in the overall corrosion rate of each.

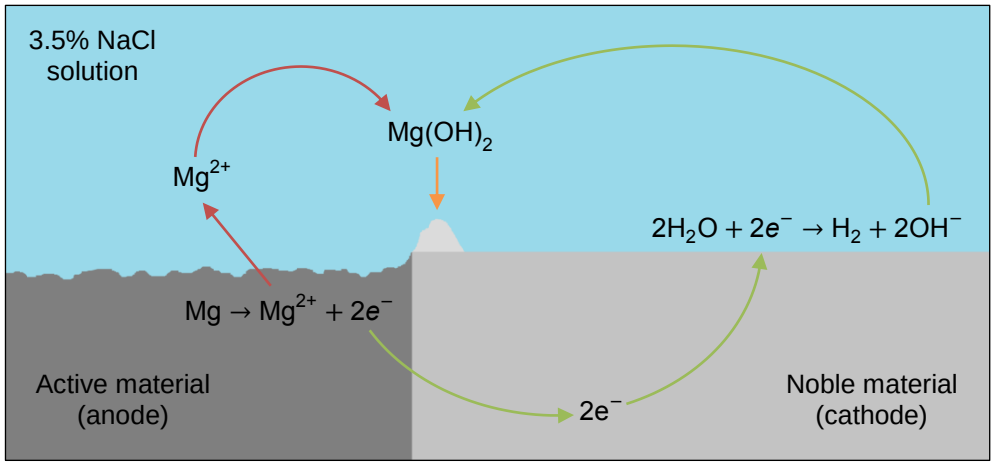

Figure 4-70 – Schematic representation of the electrochemical processes that take place during the galvanic corrosion of Mg in 3.5% NaCl solution when coupled to a more noble material. It is important to note that, depending on the strength of the galvanic current, self-corrosion may still be occurring independently on each metal.

For the anode in a galvanic couple the current flow means electrons are removed faster than they otherwise would be during self-corrosion, and the anodic reaction rate is able to increase (it corrodes more rapidly). The opposite is true for the cathode, which sees a corresponding reduction in the anodic reaction rate (it corrodes more slowly). These changes to the anodic reaction on each material are balanced by changes to the cathodic reaction, with it reducing on the anode and increasing on the cathode.

Although the galvanic current is driven by a potential difference, it cannot be measured when the metals are coupled. Instead they exhibit a unique mixed potential that lies at or between their individual open circuit potentials, the magnitude of which depends on the behaviour of each material. The balance of reaction rates on the anode and cathode in galvanic corrosion can be displayed on an Evans diagram (Figure 4-71) in a similar manner to self-corrosion, as described in Section 4.3.2.2.

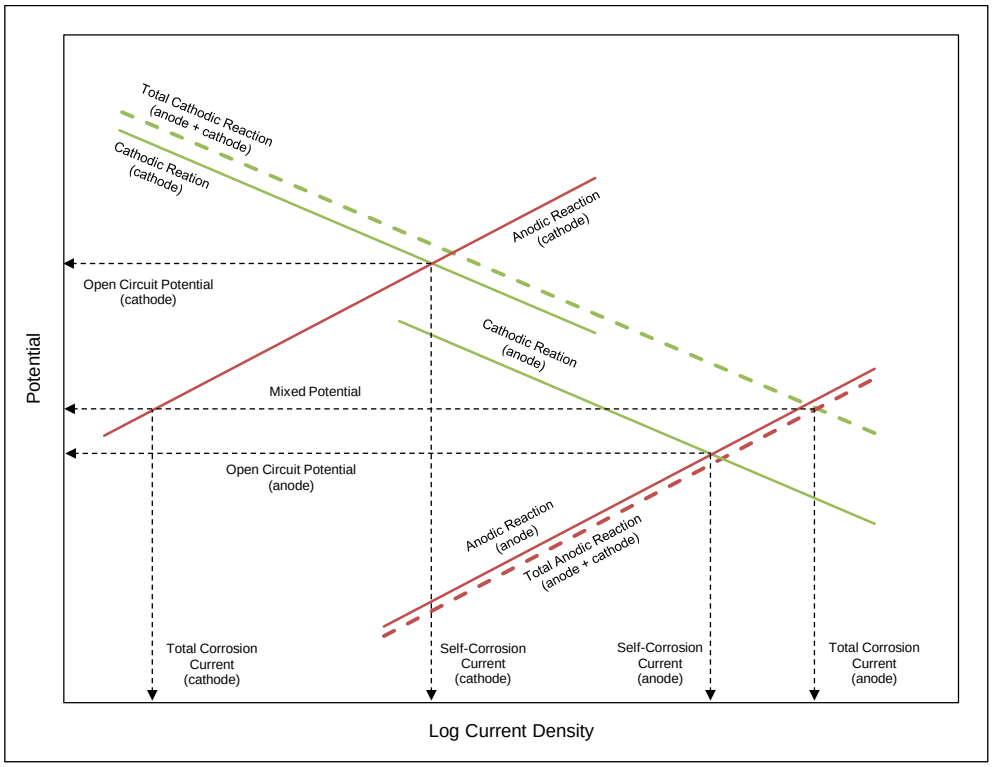

Figure 4-71 – Evans diagrams illustrating the galvanic corrosion of two coupled metals [161]. Corrosion now occurs at some intermediate mixed potential that sits between the OCPs of the individual materials. The galvanic current causes the overall corrosion rate of the anode to be increased, while the corrosion rate of the cathode is reduced.

The Evans diagram for galvanic corrosion shows how the open circuit potentials and self-corrosion currents of two metals coincide at some mixed potential and a greater current density. For the anode this current corresponds to the magnitude of the increase in corrosion rate, while for the cathode it is the magnitude of the decrease in corrosion rate.

4.5.2.3 Galvanic Corrosion Measurements

Zero Resistance Ammetry

The diagram in Figure 4-70 illustrated how an electrical current flows between coupled dissimilar metals, and this can be measured using zero resistance ammetry (ZRA). The advantage of ZRA is that it allows the magnitude of an electrical current to be determined without affecting the circuit by increasing its resistance. This is particularly relevant for small currents like those generated during galvanic corrosion. ZRA equipment that is designed for measuring electrochemical activity may also allow the mixed potential of a galvanic couple to be recorded. A schematic of the ZRA arrangement that has been used to monitor galvanic current and mixed potential is shown in Figure 4-72. The distance between the surfaces of the samples in the test cell was 50 mm, and the RE was placed centrally between them.

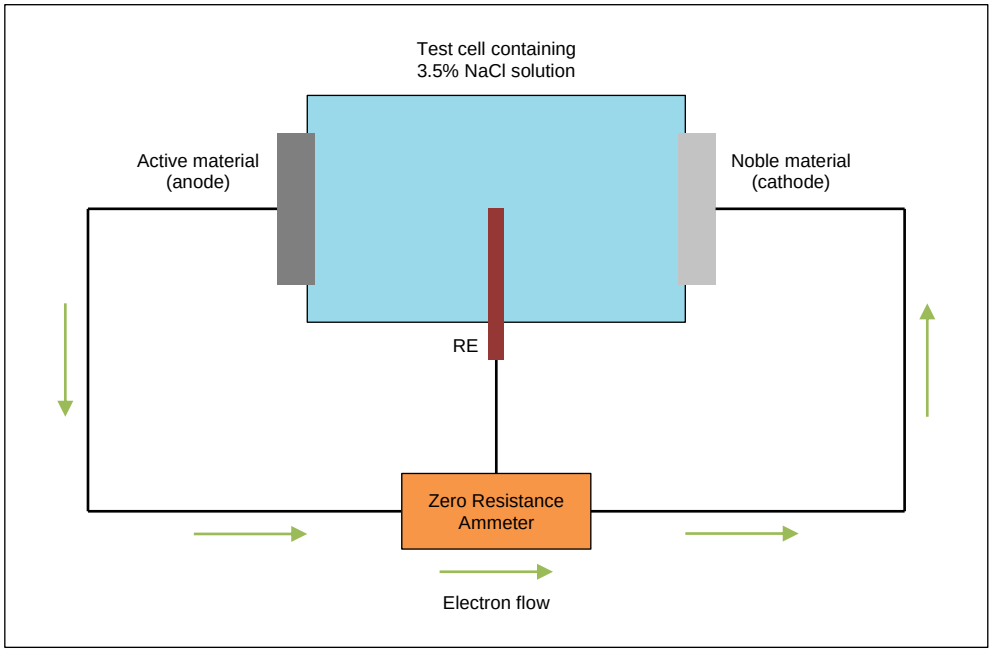

Figure 4-72 – Schematic representation of the ZRA equipment arrangement used to measure the galvanic current between two materials. Electrochemical data was recorded using the equipment and software given in Section 3.3.

The Resistance Box Technique

The resistance box (R-box) technique can be used to separate the anodic and cathodic polarisation behaviours of metals in a galvanic couple, and is described in the work of Ross and Hitchen 1961 [171]. The is a valuable tool as it enables the behaviours of the anode and cathode to be observed independently, and shows how each one is involved in controlling galvanic behaviour. The equipment arrangement used here is given in Figure 4-73. As before the distance between the surfaces of the samples in the test cell was 50 mm, and the RE was placed centrally between them.

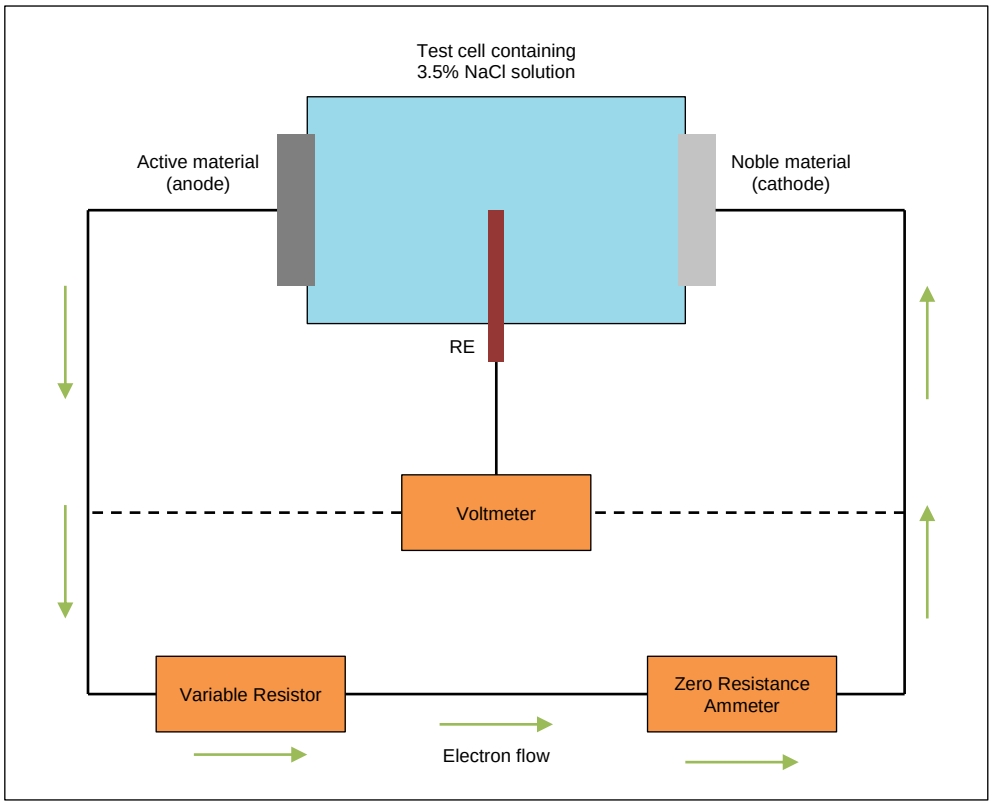

Figure 4-73 – Schematic representation of the equipment arrangement used to conduct R-box measurements. Electrochemical data was recorded using the equipment and software given in Section 3.3.

Section 4.5.2.2 explained that when two metals are coupled they both corrode at some mixed potential and not at their individual open circuit potentials. The R-box technique allows the transition from self-corrosion to galvanic corrosion to be examined, and shows how the individual potentials develop into a single mixed potential.

The R-box resistance is initially set to a relatively high value — 1000 Ω has been use here — meaning little current flows and dissolution is mainly due to self-corrosion. The galvanic current and the potential of each metal against a reference are then recorded while the resistance is systematically reduced to zero. This allows the galvanic effect to increase, and when plotted the result is a characteristic Evans diagram similar to that given Figure 4-71.

IR Drop

In conducting these experiments it must be acknowledged that there will be some error in the results due to the resistance of the 3.5% NaCl solution between the samples. This resistance will cause the potentials recorded for ZRA and the R-box to be lower than the actual values by an amount proportional to the galvanic current. This potential — the IR drop — can be calculated according to the following equation.

$$V = IR \tag{4-39}$$

Where V (V) is the voltage drop, I (A) is the ionic current, and R (Ω) is the resistance of the solution, which is determined as follows.

$$R = \frac{\rho L}{A} \tag{4-40}$$

Where ρ (Ω.cm) is the solution resistivity, L (cm) is the distance between the samples and the RE (2.5 cm), and A (cm^2) is the area of the samples. For 3.5% NaCl solution the resistivity is 20 Ω.cm, meaning the maximum solution resistance will be 22 Ω. A value of this order is also reflected in the EIS results for self-corrosion that were given in Section 4.3.3.2 and Section 4.4.3.2.

The magnitude of the galvanic current generated between the samples determines the size of the IR drop, and so this is discussed alongside the ZRA and R-box results presented later in Section 4.5.3.1, Section 4.5.3.2, and Section 4.5.3.4.

4.5.3 Results and Discussion

4.5.3.1 Mg-Al-Zn Alloys

Table 4-10 summarises the experiments that have been conducted to compare the galvanic behaviour of the Mg-Al-Zn alloys AZ31B, AZ61A and AZ91D against a standard of 99.9% pure Mg.

Table 4-10 – Summary of the galvanic experiments discussed in this section.

Galvanic Couple		Experiment Aim
Assumed Anode	Assumed Cathode	
99.9% Mg	AZ31B	Standard against pure Mg for comparison
99.9% Mg	AZ61A	Standard against pure Mg for comparison
99.9% Mg	AZ91D	Standard against pure Mg for comparison

AZ31B

The plot in Figure 4-74 shows the fluctuations in galvanic current density and mixed potential, recorded using ZRA, for a 99.9% Mg and AZ31B couple over 20 h after first exposure. The galvanic current densities and mixed potentials at the labelled points, along with the previously recorded OCP and I_{corr} values for each material, are given in Table 4-11. A positive current is observed throughout, meaning 99.9% Mg is the anode, and AZ31B is the cathode. This is consistent with the expected behaviour based on their open circuit potentials and the system is therefore acting in a similar manner to the example in Figure 4-70.

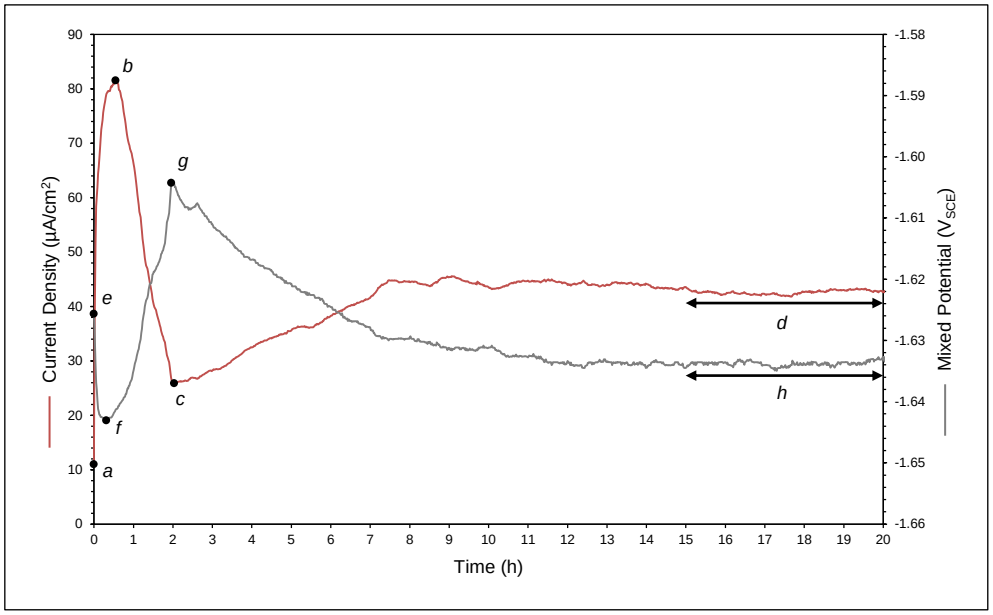

Figure 4-74 – Plot showing the galvanic current density and mixed potential produced by a galvanic couple between 99.9% Mg and AZ31B in 3.5% NaCl solution. The positive galvanic current indicates that 99.9% Mg is the anode and AZ31B is the cathode. The current densities (points *a* to *d*) and mixed potentials (points *e* to *h*) are given in Table 4-11.

Table 4-11 – Table listing the galvanic current densities and mixed potentials at the labelled points in Figure 4-74. The previously recorded OCP and I_{corr} values for each material are also given.

Self-Corrosion of Galvanic Couple Components			Zero Resistance Ammetry						Resistance Box at Zero Resistance	
			Galvanic Current			Mixed Potential				
Material	Current Density (µA/cm²)	Open Circuit Potential (V_{SCE})	Point	Time (min)	Current Density (µA/cm²)	Point	Time (min)	Mixed Potential (V_{SCE})	Current Density (µA/cm²)	Mixed Potential (V_{SCE})
99.9% Mg	71.9	−1.640	*a*	0	11.0	*e*	0	−1.626	95.4	−1.637
			b	28	81.5	*f*	19	−1.643		
AZ31B	14.2	−1.605	*c*	102	25.8	*g*	118	−1.604		
			d	900-1200	42.6	*h*	900-1200	−1.634		

The R-box results in Figure 4-75, and current and potential values in Table 4-11, provide greater detail about this galvanic couple. At a high resistance very little current flows between the materials and self-corrosion can be considered the main dissolution mechanism. This is reflected by a small current density and respective anode and cathode potentials that are of a similar order to the individual OCPs. As the R-box

resistance is reduced the potential of the anode remains stable, but the cathode is polarised such that the mixed potential recorded at zero resistance (−1.637 V_{SCE}) is almost identical to the previously recorded OCP for 99.9% Mg (−1.640 V_{SCE}).

According to Equation 4-39 the IR drop associated with a galvanic current density of 42.6 µA/cm^2 is 0.004 V. This means that the potentials recorded for ZRA and R-box are all 0.004 V lower than they would have been in the absence of the solution resistance.

The gradients of the anodic and cathodic curves allow the sensitivity of the system to these reactions to be inferred. A change to the rate of one of these reactions will lead to a corresponding change to the gradient of the associated curve, thereby moving the point of intersection that determines the current density. Because the gradient of the anodic curve is relatively shallow a variation in this will not change the intersection point as much compared to a shift in the steeper cathodic curve. As such the couple can be described as being under cathodic control.

When comparing ZRA and R-box results, it should be noted that the durations for which the couples have been made do not correspond. With R-box a complete galvanic couple (zero resistance) was not achieved for approximately 30 min, whereas it is immediate with ZRA. Also, as discussed in Section 4.3.3.1, when freshly prepared materials are exposed to the electrolyte they have an OCP that is more active relative to the OCP once the surface has formed a thicker oxide film. These initially active potentials will also be exhibited when materials are exposed in a galvanic couple. Therefore, because the R-box technique gradually introduces the galvanic couple, it is conceivable that the behaviour of the materials will differ slightly in comparison to ZRA. Nevertheless in this case the R-box result at zero resistance (95.4 µA/cm^2) reflects that of ZRA after a similar duration of exposure.

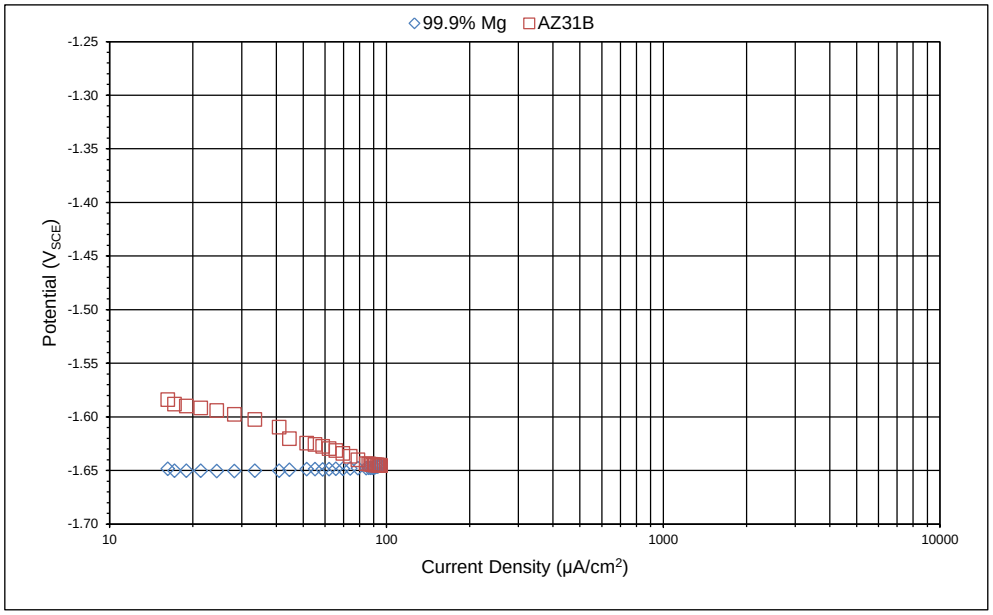

Figure 4-75 – Plot showing R-box results for a galvanic couple between 99.9% Mg and AZ31B in 3.5% NaCl solution. Strong polarisation of the cathode shows that the couple is under cathodic control. The current density and mixed potential at zero R-box resistance are given in Table 4-11. Note that the plot is scaled for comparison with other results.

The fluctuations in galvanic current and mixed potential seen for ZRA (Figure 4-74) can be described in terms of the changes occurring on the material surfaces. An initial galvanic current density of 11.0 μA/cm^2 (point *a*) and mixed potential of −1.626 V_{SCE} (point *e*) were measured between 99.9% Mg and AZ31B, with 99.9% Mg as the anode and AZ31B as the cathode. This means the overall corrosion rate of 99.9% Mg has increased and that of AZ31B has reduced. The magnitude of the galvanic current subsequently increases to 81.5 μA/cm^2 (point *b*), which can be explained by the breakdown of an air-formed oxide on 99.9% Mg. This leads to a more active surface, reflected at point *f* (−1.643 V_{SCE}), and therefore a larger potential difference between the materials and a greater driver for the galvanic current.

As corrosion continues the oxide film on 99.9% Mg grows and thickness — accelerated by the galvanic couple — and the protection it offers increases. The thickening of the oxide shifts the potential to a more noble value (−1.643 V_{SCE} at point *g*), reducing the difference between it and AZ31B, and consequently causing the galvanic current to drop to 25.8 µA/cm^2 at point *c*. However, because the oxide is not very stable its protective ability is limited and areas can subsequently break off to expose fresh substrate, leading to an increase in surface activity and a corresponding rise in galvanic current. Eventually equilibrium between film formation and breakdown is reached and the galvanic current and mixed potential stabilise at mean steady state values of 42.6 µA/cm^2 (range *d*) and −1.634 V_{SCE} (range *h*) respectively.

AZ61A

A plot showing the results of ZRA for the galvanic couple between 99.9% Mg and AZ61A is given in Figure 4-76, and the positive current illustrates that 99.9% Mg is again the anode and the alloy is the cathode. The values at the labelled points are given in Table 4-12 alongside the previously recorded OCP and I_{corr} values. According to Equation 4-39 the IR drop associated with a galvanic current density of 12.5 µA/cm^2 is 0.001 V. The same trends that were seen for AZ31B are also observed, with the galvanic current initially increasing and then decreasing before stabilising, and the mixed potential mirroring this behaviour.

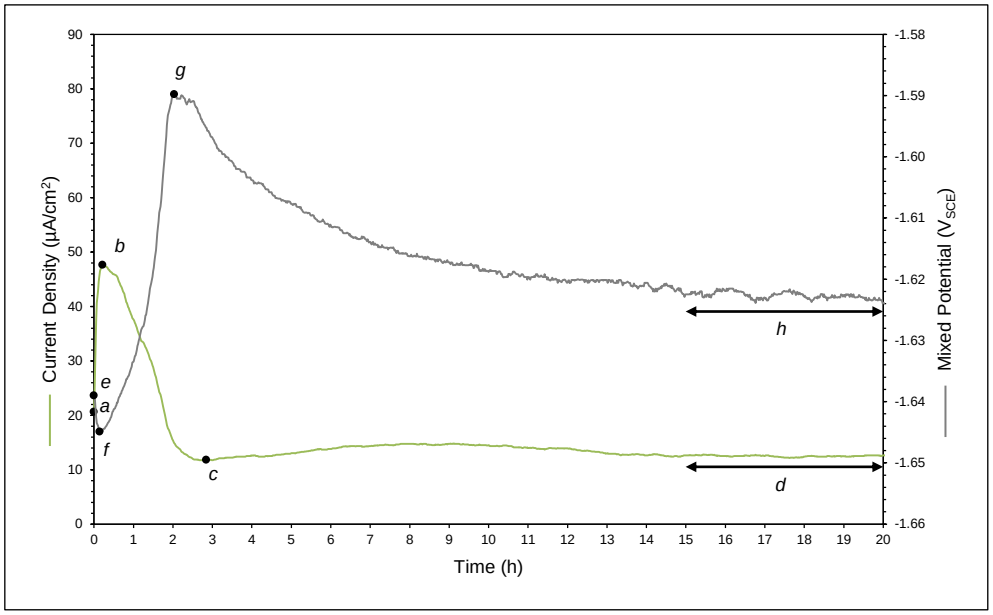

Figure 4-76 – Plot showing the galvanic current density and mixed potential produced by a galvanic couple between 99.9% Mg and AZ61A in 3.5% NaCl solution. The positive galvanic current indicates that 99.9% Mg is the anode and AZ61A is the cathode. The current densities (points *a* to *d*) and mixed potentials (points *e* to *h*) are given in Table 4-12.

Table 4-12 – Table listing the galvanic current densities and mixed potentials at the labelled points in Figure 4-76. The previously recorded OCP and I_{corr} values for each material are also given.

Self-Corrosion of Galvanic Couple Components			Zero Resistance Ammetry						Resistance Box at Zero Resistance	
			Galvanic Current			Mixed Potential				
Material	Current Density (µA/cm²)	Open Circuit Potential (V_{SCE})	Point	Time (min)	Current Density (µA/cm²)	Point	Time (min)	Mixed Potential (V_{SCE})	Current Density (µA/cm²)	Mixed Potential (V_{SCE})
99.9% Mg	71.9	−1.640	*a*	0	20.6	*e*	0	−1.639	36.9	−1.640
			b	13	47.6	*f*	9	−1.645		
AZ61A	5.38	−1.610	*c*	171	11.8	*g*	122	−1.590		
			d	900-1200	12.5	*h*	900-1200	−1.622		

The R-box results in Figure 4-77 illustrate that the couple is also under cathodic control, with the potential of 99.9% Mg remaining stable and AZ61A becoming polarised. Table 4-12 shows that at zero R-box resistance the mixed potential is −1.640 V_{SCE}, which is again similar to the OCP of 99.9% Mg, and the galvanic current is 36.9 µA/cm^2. These potential and current values also correspond to those recorded

at the initial stages of ZRA. Given the parallels between the respective couples of 99.9% Mg and either AZ31B or AZ61A, it is therefore sensible to apply the same reasoned explanations for the changes in galvanic current and mixed potential to both.

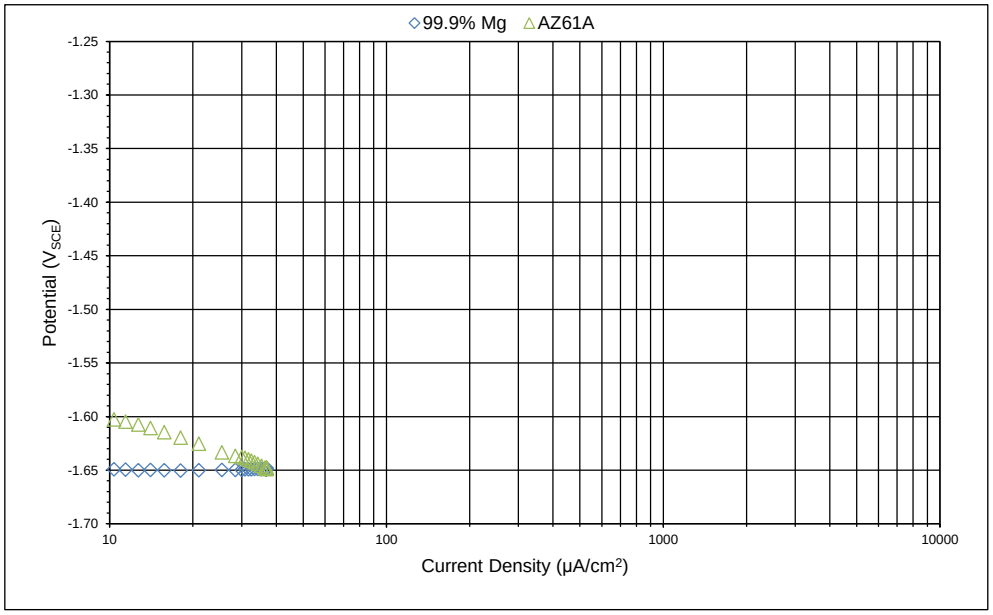

Figure 4-77 – Plot showing R-box results for a galvanic couple between 99.9% Mg and AZ61A in 3.5% NaCl solution. Strong polarisation of the cathode shows that the couple is under cathodic control. The current density and mixed potential at zero R-box resistance are given in Table 4-12. Note that the plot is scaled for comparison with other results.

AZ91D

The plot in Figure 4-78 shows the ZRA results for the 99.9% Mg and AZ91D couple over 20 h after first exposure. Table 4-13 lists the galvanic current densities and mixed potentials at the labelled points along with the previously recorded OCP and I_{corr} values. According to Equation 4-39 the IR drop associated with a galvanic current density of 12.6 μA/cm^2 is 0.001 V. The consistently positive current demonstrates that 99.9% Mg is the anode and AZ91D is the cathode, and the data follows the same pattern described for AZ31B and repeated for AZ61A.

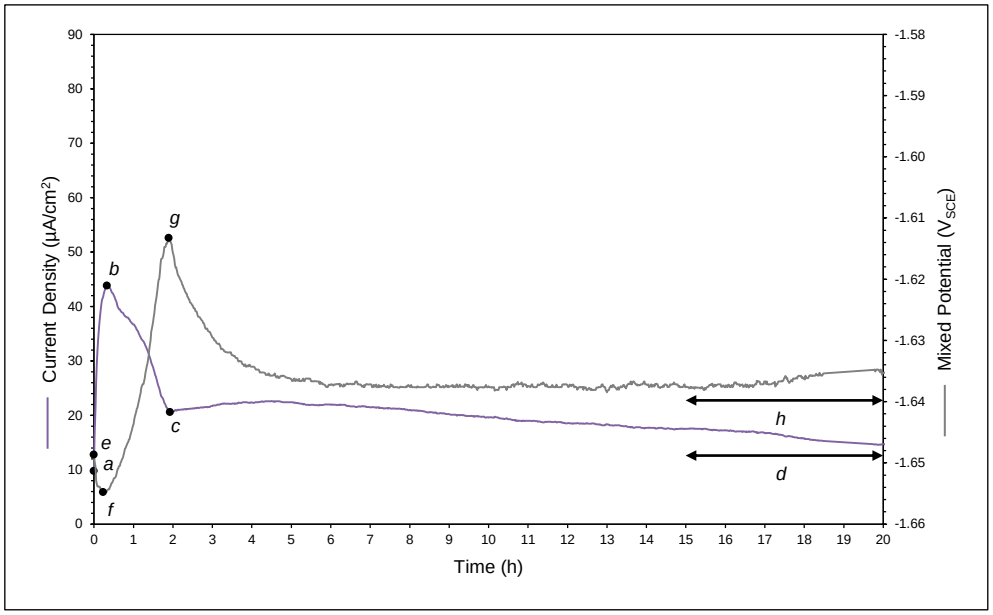

Figure 4-78 – Plot showing the galvanic current density and mixed potential produced by a galvanic couple between 99.9% Mg and AZ91D and in 3.5% NaCl solution. The positive galvanic current indicates that 99.9% Mg is the anode and AZ91D is the cathode. The current densities (points *a* to *d*) and mixed potentials (points *e* to *h*) are given in Table 4-13.

Table 4-13 – Table listing the galvanic current densities and mixed potentials at the labelled points in Figure 4-78. The previously recorded OCP and I_{corr} values for each material are also given.

Self-Corrosion of Galvanic Couple Components			Zero Resistance Ammetry						Resistance Box at Zero Resistance	
			Galvanic Current			Mixed Potential				
Material	Current Density (μA/cm²)	Open Circuit Potential (V_{SCE})	Point	Time (min)	Current Density (μA/cm²)	Point	Time (min)	Mixed Potential (V_{SCE})	Current Density (μA/cm²)	Mixed Potential (V_{SCE})
99.9% Mg	71.9	−1.640	*a*	0	9.7	*e*	0	−1.649	45.6	−1.642
			b	20	43.8	*f*	14	−1.655		
AZ91D	4.82	−1.613	*c*	116	20.5	*g*	114	−1.613		
			d	900-1200	12.6	*h*	900-1200	−1.637		

The plot in Figure 4-79 displays the R-box results for 99.9% Mg and AZ91D, with the current and potential at zero resistance listed in Table 4-13. These confirm that the couple is again under cathodic control and show how AZ91D is polarised such that the mixed potential at zero resistance is −1.637 V_{SCE}. A current of 45.6 µA/cm^2 at zero R-box resistance is again comparable to that recorded at the beginning of ZRA. The similarity in behaviour compared to the other alloys means the arguments explaining the observed trends can also be transferred.

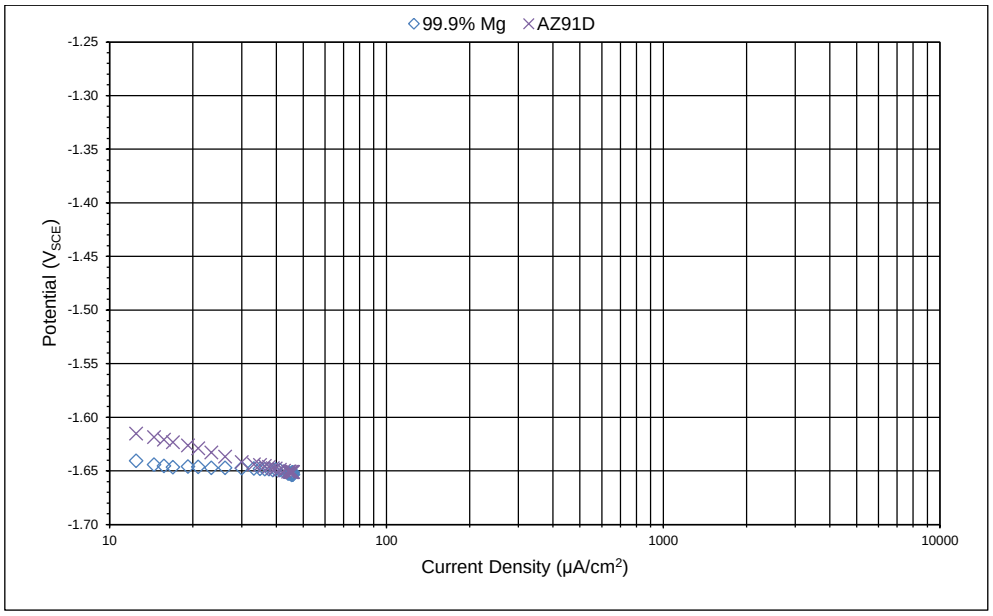

Figure 4-79 – Plot showing R-box results for a galvanic couple between 99.9% Mg and AZ91D in 3.5% NaCl solution. Strong polarisation of the cathode shows that the couple is under cathodic control. The current density and mixed potential at zero R-box resistance are given in Table 4-13. Note that the plot is scaled for comparison with other results.

4.5.3.2 Mg-Al Intermetallics

Table 4-14 summarises the experiments that have been conducted to compare the galvanic behaviour of the Mg-Al intermetallics $Mg_{17}Al_{12}$ and Mg_2Al_3 against a standard of 99.9% pure Mg.

Table 4-14 – Summary of the galvanic experiments discussed in this section.

Galvanic Couple		Experiment Aim
Assumed Anode	Assumed Cathode	
99.9% Mg	$Mg_{17}Al_{12}$	Standard against pure Mg for comparison
99.9% Mg	Mg_2Al_3	Standard against pure Mg for comparison

$Mg_{17}Al_{12}$

The plot in Figure 4-80 shows the changes in current density and mixed potential for the galvanic couple between 99.9% Mg and the intermetallic $Mg_{17}Al_{12}$ recorded over 20 h after first exposure. The values at the labelled points are given in Table 4-15, along with the previously recorded OCP and I_{corr} values of the couple components. According to Equation 4-39 the IR drop associated with a current density of 2380 µA/cm^2 is 0.117 V, which is greater than seen previously and reflects the much larger galvanic effect.

The positive galvanic current for the 99.9% Mg and $Mg_{17}Al_{12}$ couple indicates that $Mg_{17}Al_{12}$ is the cathode, and its magnitude — a mean of 2380 µA/cm^2 (range *d*) over the last 5 h — makes it is almost 56 times that of the highest mean for an Mg-Al-Zn alloy (42.6 µA/cm^2 for AZ31B). The mixed potential has a mean over the last 5 h of −1.536 V_{SCE} (range *h*) compared to −1.622 V_{SCE} for AZ61A, which was the most noble for the alloy couples. The characteristics observed here are again similar to those for the Mg-Al-Zn alloys, and therefore the same explanations for the recorded changes can be applied.

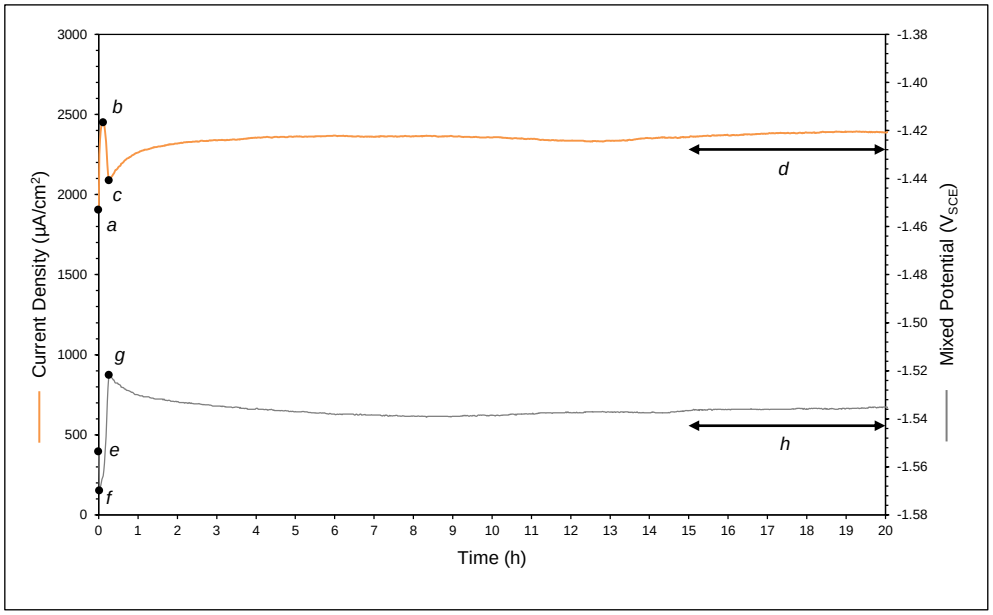

Figure 4-80 – Plot showing the galvanic current density and mixed potential produced by a galvanic couple between 99.9% Mg and $Mg_{17}Al_{12}$ and in 3.5% NaCl solution. The positive galvanic current indicates that 99.9% Mg is the anode and $Mg_{17}Al_{12}$ is the cathode. The current densities (points *a* to *d*) and mixed potentials (points *e* to *h*) are given in Table 4-15.

Table 4-15 – Table listing the galvanic current densities and mixed potentials at the labelled points in Figure 4-80. The previously recorded OCP and I_{corr} values for each material are also given.

Self-Corrosion of Galvanic Couple Components			Zero Resistance Ammetry						Resistance Box at Zero Resistance	
			Galvanic Current			Mixed Potential				
Material	Current Density (μA/cm²)	Open Circuit Potential (V_{SCE})	Point	Time (min)	Current Density (μA/cm²)	Point	Time (min)	Mixed Potential (V_{SCE})	Current Density (μA/cm²)	Mixed Potential (V_{SCE})
99.9% Mg	71.9	−1.640	*a*	0	1900	*e*	0	−1.554	2550	−1.554
			b	7	2450	*f*	1	−1.570		
$Mg_{17}Al_{12}$	2.44	−1.058	*c*	16	2090	*g*	16	−1.522		
			d	900-1200	2380	*h*	900-1200	−1.536		

The mean mixed potential is also reflected by the R-box results in Figure 4-81, which show that both the cathode ($Mg_{17}Al_{12}$) and anode (99.9% Mg) are polarised, whereas only the cathode (AZ31B, AZ61A or AZ91D) was polarised in the Mg-Al-Zn alloy couples. The couple is therefore now under mixed control — controlled by the corrosion characteristics of the cathode and the anode — rather than being under

cathodic control as seen previously. As such a change in either the rate of the anodic or cathodic reaction will affect the corrosion rate. The current density and potential at zero R-box resistance were 2550 µA/cm^2 and −1.554 V_{SCE} respectively, and are comparable to the values at the beginning of ZRA.

The greater current generated by the couple is thought to be responsible for the change to a mixed control regime. At lower galvanic currents (lower corrosion rates) like those seen for the Mg-Al-Zn alloys, the dissolution of Mg to Mg^{2+} ions at the anode surface is able to proceed at a rate determined by the magnitude of the galvanic current. At higher galvanic currents (higher corrosion rates) the dissolution of Mg becomes limited by the rate at which Mg^{2+} ions can be transported away from the anode surface, correspondingly limiting the current that can flow.

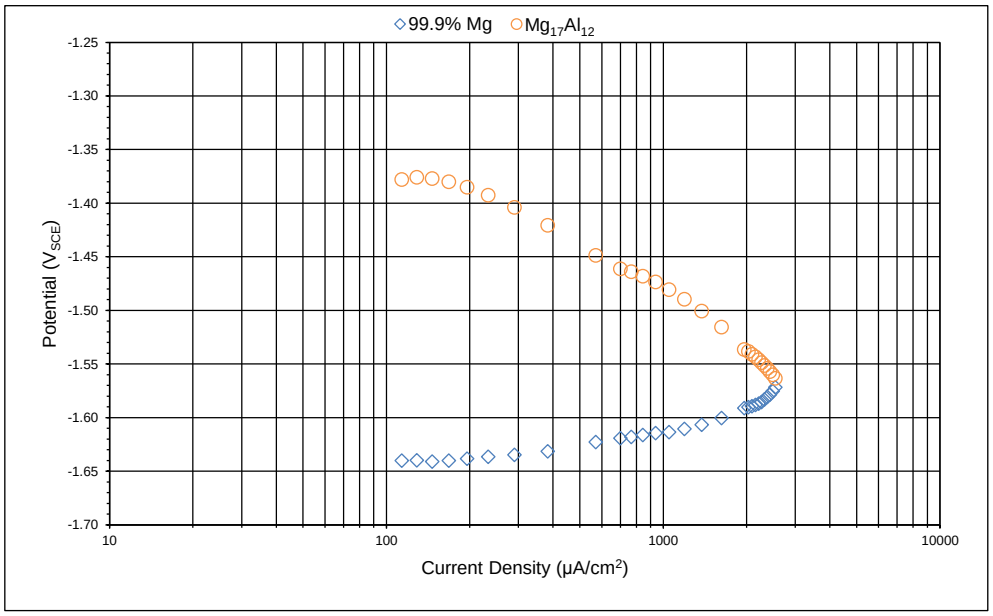

Figure 4-81 – Plot showing R-box results for a galvanic couple between 99.9% Mg and $Mg_{17}Al_{12}$ in 3.5% NaCl solution. Polarisation of the cathode and anode shows that the couple is under mixed controlled. The current density and mixed potential at zero R-box resistance are given in Table 4-15. Note that the plot is scaled for comparison with other results.

Mg_2Al_3

The plot in Figure 4-80 shows the changes in current density and mixed potential for the galvanic couple between 99.9% Mg and the intermetallic Mg_2Al_3 recorded over 20 h after first exposure. Table 4-16 lists the values at the labelled points and also gives the OCP and I_{corr} values of the couple components. According to Equation 4-39 the IR drop associated with a current density of 2740 µA/cm^2 is 0.134 V, which again reflects the much larger galvanic effect.

The galvanic current between 99.9% Mg and Mg_2Al_3 is positive and shows that they are the anode and cathode respectively. The galvanic current has a mean over the last 5 h of 2740 µA/cm^2, which is over 64 times that of any of the alloys — the greatest being AZ31B at 42.6 µA/cm^2 — and around 15% more than $Mg_{17}Al_{12}$ at 2380 µA/cm^2. The mixed potential has a mean of −1.490 V_{SCE} (range *d*), compared to −1.536 V_{SCE} for $Mg_{17}Al_{12}$ and −1.622 V_{SCE} for the most noble for the alloy couples (AZ61A). As before the trends observed here are similar to those of the other couples and the same arguments explaining the characteristic changes can be applied.

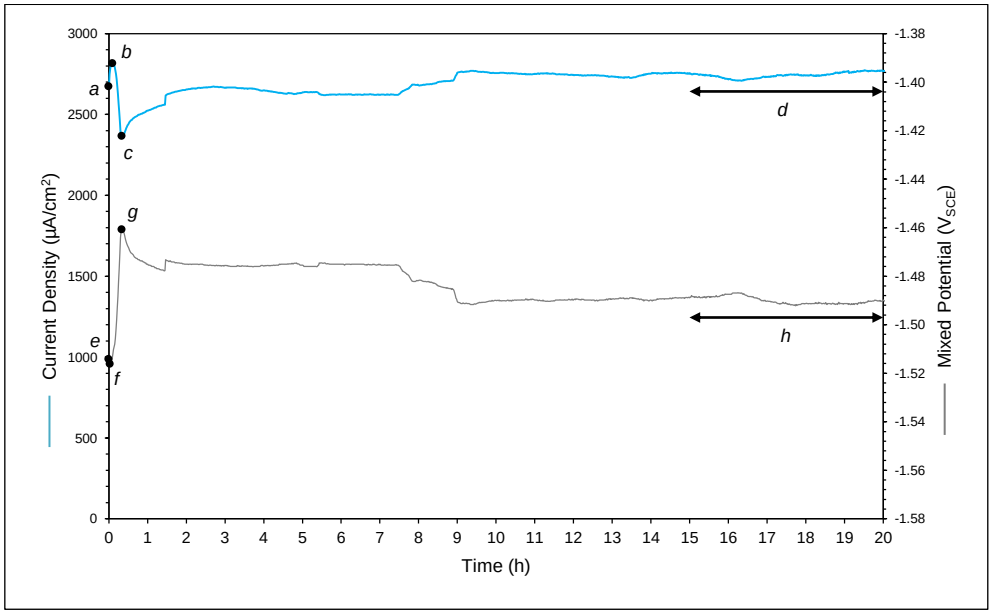

Figure 4-82 – Plot showing the galvanic current density and mixed potential produced by a galvanic couple between 99.9% Mg and Mg2Al3 and in 3.5% NaCl solution. The positive galvanic current indicates that 99.9% Mg is the anode and Mg2Al3 is the cathode. The current densities (points *a* to *d*) and mixed potentials (points *e* to *h*) are given in Table 4-16.

Table 4-16 – Table listing the galvanic current densities and mixed potentials at the labelled points in Figure 4-82. The previously recorded OCP and I_{corr} values for each material are also given.

Self-Corrosion of Galvanic Couple Components			Zero Resistance Ammetry						Resistance Box at Zero Resistance	
			Galvanic Current			Mixed Potential				
Material	Current Density ($\mu A/cm^2$)	Open Circuit Potential (V_{SCE})	Point	Time (min)	Current Density ($\mu A/cm^2$)	Point	Time (min)	Mixed Potential (V_{SCE})	Current Density ($\mu A/cm^2$)	Mixed Potential (V_{SCE})
99.9% Mg	71.9	−1.640	*a*	0	2670	*e*	0	−1.514	2660	−1.469
			b	6	2820	*f*	2	−1.516		
			c	20	2370	*g*	20	−1.461		
Mg_2Al_3	0.75	−1.115	*d*	900-1200	2740	*h*	900-1200	−1.490		

The mixed potential recorded using ZRA for the 99.9% Mg and Mg_2Al_3 couple is reflected by the R-box results in Figure 4-83, which confirm that both the anode and cathode are polarised and the system is under mixed control. Table 4-16 shows that the galvanic current at zero R-box resistance is also comparable with the results obtained during the initial stages of ZRA.

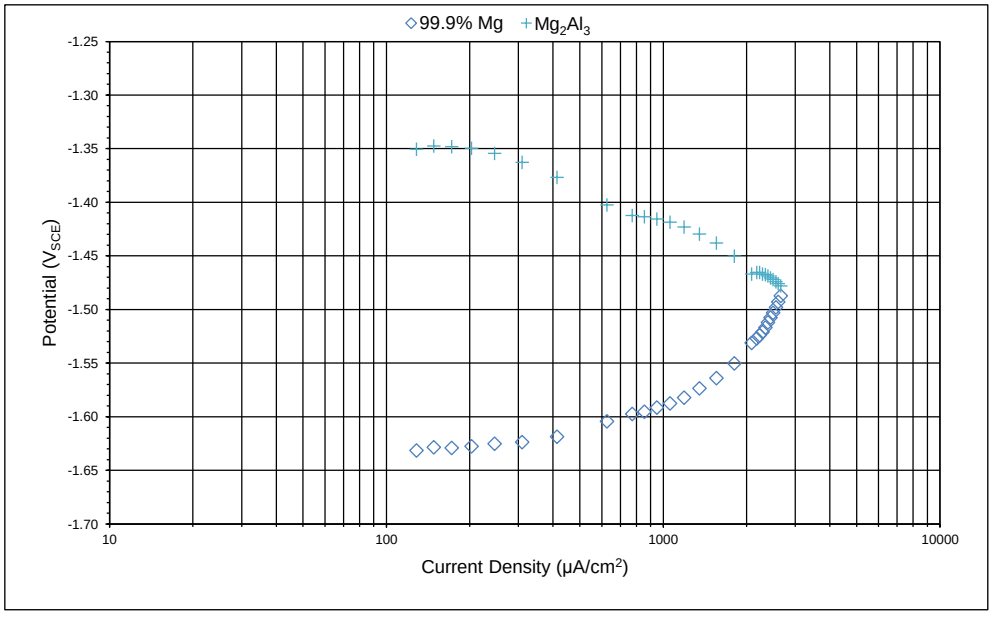

Figure 4-83 – Plot showing R-box results for a galvanic couple between 99.9% Mg and Mg2Al3 in 3.5% NaCl solution. Polarisation of the cathode and anode shows that the couple is under mixed controlled. The current density and mixed potential at zero R-box resistance are given in Table 4-16. Note that the plot is scaled for comparison with other results.

4.5.3.3 Galvanic Current Comparison

Figure 4-84 shows a plot comparing the changes in galvanic current density for each of the Mg-Al-Zn alloys — AZ31B, AZ61A, and AZ91D — and the intermetallics — $Mg_{17}Al_{12}$ and Mg_2Al_3 — when coupled with 99.9% Mg. The corresponding mean galvanic current densities and mixed potentials are summarised in Table 4-17.

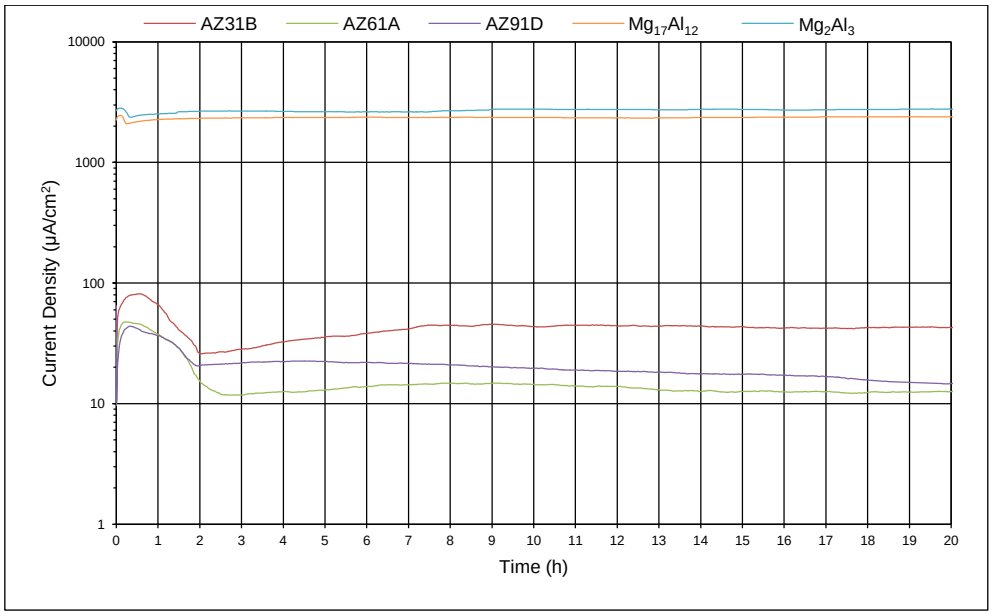

Figure 4-84 – Plot showing the current densities produced by galvanic couples between 99.9% Mg and the Mg-Al-Zn alloys AZ31B, AZ61A, and AZ91D, and the Mg-Al intermetallics, $Mg_{17}Al_{12}$ and Mg_2Al_3, in 3.5% NaCl solution. A positive galvanic current indicates that 99.9% Mg is the anode and the coupled material is the cathode.

The driver for the galvanic corrosion is the potential difference of the coupled materials and so it is useful to compare the open circuit potentials that were measured in Section 4.3 (Table 4-6) with the strength of the galvanic couples recorded here, noting that these are stabilised OCPs and not OCPs at first exposure. For the Mg-Al-Zn alloys the greatest difference (35 mV) is seen between 99.9% Mg and AZ31B, which had OCPs of −1.640 V_{SCE} and −1.605 V_{SCE} respectively, and this couple also has the largest galvanic current (42.6 µA/cm^2). AZ61A had an OCP of −1.610 V_{SCE}, giving a smaller potential difference of 30 mV against 99.9% Mg, and a galvanic current of 12.5 µA/cm^2, which is expectedly lower than the AZ31B couple. The difference between the OCPs of 99.9% Mg and AZ91D (−1.610 V_{SCE}) is even less at 27 mV, but the galvanic current is slightly higher at 12.6 µA/cm^2. Given the closeness of these

results, and taking into account the range of open circuit potentials that were seen in Section 4.3 (Figure 4-45) and the fact that there was overlap between values, it is reasonable to explain this galvanic behaviour by way of normal variability.

Table 4-17 – Summary of the galvanic current densities and mixed potentials recorded in this work for a 99.9% Mg standard coupled with the Mg-Al-Zn alloys and Mg-Al intermetallics.

Galvanic Couple		Current Density ($\mu A/cm^2$)	Mixed Potential (V_{SCE})
Anode	Cathode		
99.9% Mg	AZ31B	42.6	−1.634
99.9% Mg	AZ61A	12.5	−1.622
99.9% Mg	AZ91D	12.6	−1.637
99.9% Mg	$Mg_{17}Al_{12}$	2380	−1.536
99.9% Mg	Mg_2Al_3	2740	−1.490

The galvanic currents generated by couples between 99.9% Mg and each of the intermetallics, $Mg_{17}Al_{12}$ and Mg_2Al_3, are orders of magnitude greater than those with the Mg-Al-Zn alloys, and are driven by much larger potential differences.

4.5.3.4 AZ91D and Mg-Al Intermetallic Surface Layer Models

Table 4-18 shows the galvanic couple experiments that have been conducted to simulate the self-corrosion of an AZ91D alloy, and a damaged Al-rich Mg-Al intermetallic surface layer on an AZ91D substrate.

Table 4-18 – Summary of the galvanic experiments discussed in this section.

Galvanic Couple		Experiment Aim
Assumed Anode	Assumed Cathode	
AZ31B	$Mg_{17}Al_{12}$	Simulation of the micro-galvanic couples involved in AZ91D self-corrosion. The two phases are represented by AZ31B (α-Mg solid solution) and $Mg_{17}Al_{12}$ (intermetallic).
AZ91D	Mg_2Al_3	Simulation of corrosion resulting from a damaged intermetallic surface layer (Mg_2Al_3) on an AZ91D substrate.

AZ91D Model

Micro-galvanic couples are known to play a large part in the self-corrosion of two-phase Mg-Al-Zn alloys, but the magnitudes of the currents involved in this dissolution mechanism have not been investigated. Section 4.2.3.3 showed that AZ91D exhibited

a microstructure of α-Mg solid solution and two-phase eutectic of bands of α-Mg and $Mg_{17}Al_{12}$, with approximately equal proportions of each phase. Further analysis revealed that the quantity of Al in the α-Mg solid solution is similar to that in the single phase alloy AZ31B. By coupling AZ31B with $Mg_{17}Al_{12}$ it is therefore possible to simulate the micro-galvanic that is important in the self-corrosion of AZ91D.

The plot in Figure 4-85 shows the current density and mixed potential for the galvanic couple between AZ31B and $Mg_{17}Al_{12}$. Table 4-19 lists the mean values at the labelled points and also gives the previously recorded OCP and I_{corr} values. The positive galvanic current indicates that AZ31B is the anode and $Mg_{17}Al_{12}$ is the cathode, with a mean over the last 5 h of 2080 µA/cm^2 (range *a*). The mean mixed potential was −1.526 V_{SCE} (range *b*). According to Equation 4-39 the IR drop associated with a current density of 2080 µA/cm^2 is 0.102 V.

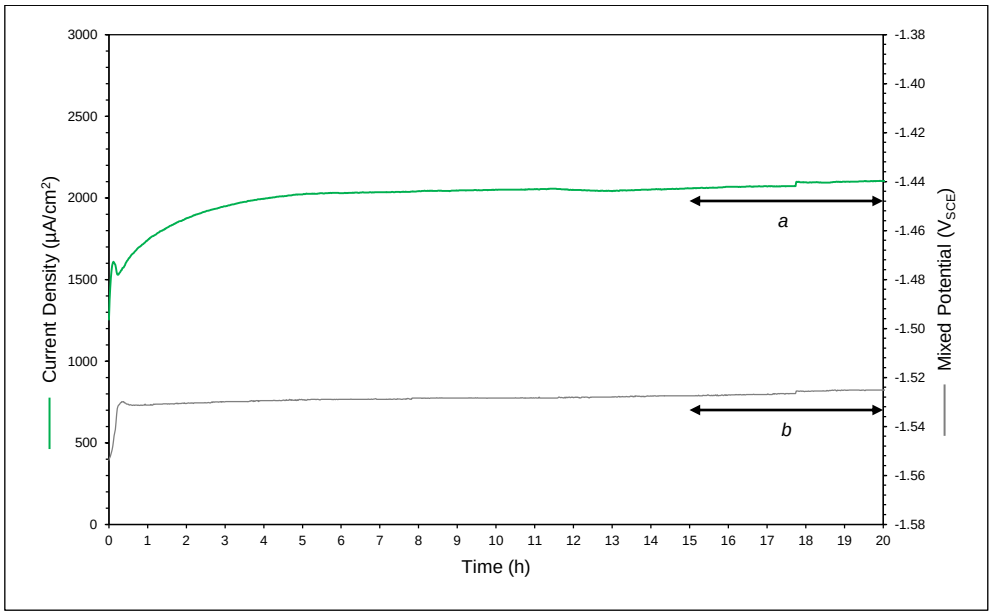

Figure 4-85 – Plot showing the current density and potential produced by a galvanic couple between AZ31B and the intermetallic $Mg_{17}Al_{12}$ to simulate the self-corrosion of AZ91D in 3.5% NaCl solution. The positive galvanic current indicates that AZ31B is the anode and $Mg_{17}Al_{12}$ is the cathode. The mean galvanic current and mixed potential over the last 5 h are 2080 µA/cm2 (range a) and −1.526 V_{SCE} (range b) respectively.

Table 4-19 – Table listing the galvanic current densities and mixed potentials at the labelled points in Figure 4-85. The previously recorded OCP and I_{corr} values for each material are also given.

Self-Corrosion of Galvanic Couple Components			Zero Resistance Ammetry						Resistance Box at Zero Resistance	
			Galvanic Current			Mixed Potential				
Material	Current Density ($\mu A/cm^2$)	Open Circuit Potential (V_{SCE})	Point	Time (min)	Current Density ($\mu A/cm^2$)	Point	Time (min)	Mixed Potential (V_{SCE})	Current Density ($\mu A/cm^2$)	Mixed Potential (V_{SCE})
AZ31B	14.2	−1.605	*a*	900-1200	2080	*b*	900-1200	−1.526	1210	−1.463
$Mg_{17}Al_{12}$	2.44	−1.058								

The R-box results given in Figure 4-86 confirm that both AZ31B and $Mg_{17}Al_{12}$ are polarised, and the system is under mixed control. The current and potential at zero R-box resistance given in Table 4-19 are comparable with the values for ZRA. The results shown here also confirm just how strong the galvanic effect in an AZ91D alloy might be.

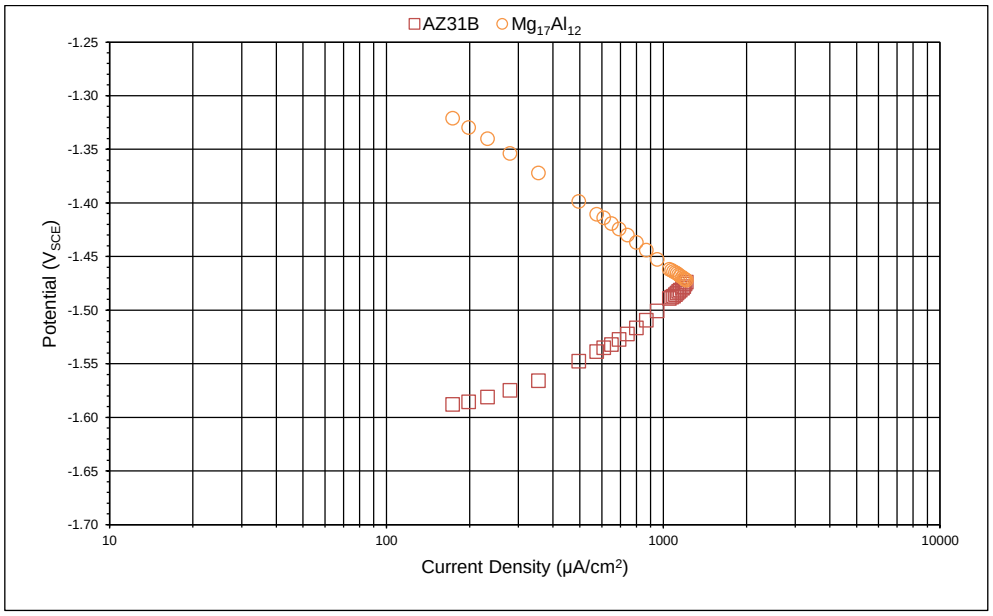

Figure 4-86 – Plot showing R-box results for a simulation of AZ91D corrosion using a galvanic couple between AZ31B and $Mg_{17}Al_{12}$ in 3.5% NaCl solution. Polarisation of the cathode and anode shows that the couple is under mixed controlled. The current density and mixed potential at zero R-box resistance are given in Table 4-19. Note that the plot is scaled for comparison with other results.

Mg-Al Intermetallic Layer Model

The galvanic corrosion currents generated by couples between 99.9% Mg and Mg-Al intermetallics have been shown to reach over 250 times those of 99.9% Mg and Mg-Al-Zn alloy couples. This is an important finding when considering the use of noble Mg-Al intermetallic surface layers as a means of protecting a less noble Mg alloy substrate. If the protective layer is damaged, and the damage penetrates through to the substrate, then it is conceivable that a galvanic couple might be set up that could severely increase corrosion.

With this in mind a galvanic couple of AZ91D and Mg_2Al_3 — to represent a substrate and an Mg-Al intermetallic surface layer respectively — has been used to assess the severity of the corrosion problem should damage occurred. The results of ZRA over 20 h after first exposure of this couple are given in the plot in Figure 4-87, and the mean values at the labelled points, as well as the previously recorded OCP and I_{corr} values, are listed in Table 4-20. According to Equation 4-39 the IR drop associated with a current density of 1920 µA/cm^2 is 0.094 V.

A positive galvanic current, with a mean of 1920 µA/cm^2 over the last 5 h, confirms that AZ91D is the anode and Mg_2Al_3 is the cathode. This is 570 µA/cm^2 greater than the current between a couple of 99.9% Mg and Mg_2Al_3 and is unexpected as the driver for galvanic corrosion (the potential different) is 500 mV for 99.9% Mg and Mg_2Al_3 compared to 473 mV for AZ91D and Mg_2Al_3. The mean mixed potential over the last 5 h of exposure was −1.481 V_{SCE} (range *b*). Figure 4-88 gives the R-box results for this galvanic couple and shows that AZ91D and Mg_2Al_3 are both polarised and the system is under mixed control. The current and potential at zero R-box resistance given in Table 4-20 are also comparable with the values for ZRA.

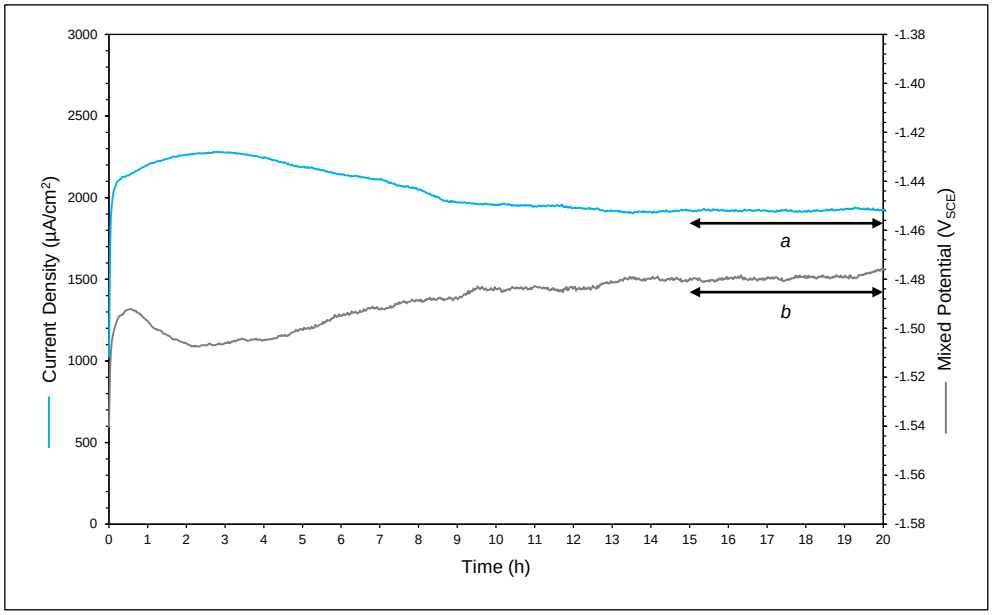

Figure 4-87 – Plot showing the current density and potential produced by a galvanic couple between AZ91D and the intermetallic Mg_2Al_3 to simulate the effect of a damaged Al-rich Mg-Al intermetallic surface layer in 3.5% NaCl solution. The positive galvanic current indicates that AZ91D is the anode and Mg_2Al_3 is the cathode. The mean galvanic current and mixed potential over the last 5 h are 1920 µA/cm2 (range a) and −1.481 V_{SCE} (range b) respectively.

Table 4-20 – Table listing the galvanic current densities and mixed potentials at the labelled points in Figure 4-87. The previously recorded OCP and I_{corr} values for each material are also given.

Self-Corrosion of Galvanic Couple Components			Zero Resistance Ammetry						Resistance Box at Zero Resistance	
			Galvanic Current			Mixed Potential				
Material	Current Density (µA/cm²)	Open Circuit Potential (V_{SCE})	Point	Time (min)	Current Density (µA/cm²)	Point	Time (min)	Mixed Potential (V_{SCE})	Current Density (µA/cm²)	Mixed Potential (V_{SCE})
AZ91D	4.82	−1.613	*a*	900-1200	1920	*b*	900-1200	−1.481	2680	−1.467
Mg_2Al_3	0.75	−1.115								

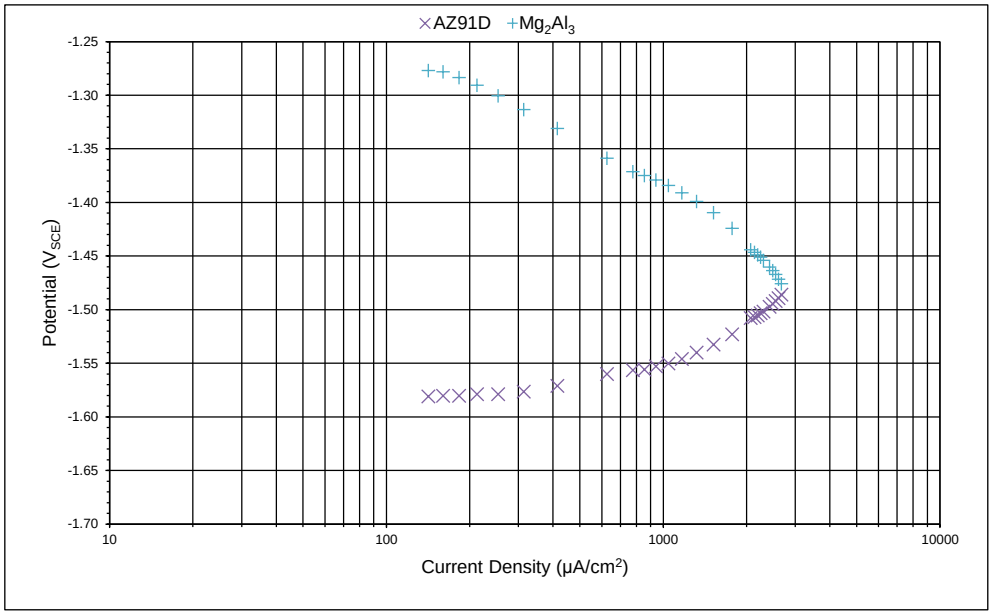

Figure 4-88 – Plot showing R-box results for a simulation of a damaged intermetallic surface layer using a galvanic couple between AZ91D and Mg_2Al_3 in 3.5% NaCl solution. Polarisation of the cathode and anode shows that the couple is under mixed controlled. The current density and mixed potential at zero R-box resistance are given in Table 4-20. Note that the plot is scaled for comparison with other results.

4.5.4 Further Discussion

The information gathered from producing Mg-Al surface layers, examining the microstructures of AZ31B, AZ61A, and AZ91D, and measuring the self-corrosion behaviour of these alloys and the two intermetallics, has provided the knowledge required to investigate how a damaged Mg-Al intermetallic surface layer might behave. The subsequent research described here has shown that the galvanic currents generated between the Mg-Al-Zn alloys and a 99.9% Mg standard reflect their similar OCPs, with each one being relatively small and of the same order of magnitude. This changes significantly when the Mg-Al intermetallics are coupled to the 99.9% Mg standard, and their more noble OCP values result in galvanic currents that are up to 250 times those seen for the alloys. This effect continues when the micro-galvanic corrosion in AZ91D and the galvanic corrosion of a damaged intermetallic layer are simulated. In both cases similarly large currents were generated, further highlighting the potential for a serious problem.

Given that the available literature consistently describes the noble nature of Mg-Al intermetallics, it is surprising that the galvanic corrosion issue investigated here has not been more widely discussed.

4.5.5 Summary

The ZRA results obtained for the series of galvanic experiments outlined in Table 4-9 are summarised in Table 4-21 alongside the self-corrosion results for the various couple components. These demonstrate how the noble nature of the Mg-Al intermetallics, compared to 99.9% Mg and the Mg-Al-Zn alloys, causes them to become strong cathodes.

Table 4-21 – Summary of the galvanic current densities and mixed potentials recorded in this work for a 99.9% Mg standard coupled with the Mg-Al-Zn alloys and Mg-Al intermetallics, as well as the AZ91D and intermetallic layer models. The previously recorded OCP and I_{corr} values for each material are also given.

Self-Corrosion of Galvanic Couple Components			Zero Resistance Ammetry	
Material	Self-Corrosion Current Density ($\mu A/cm^2$)	Open Circuit Potential (V_{SCE})	Galvanic Current Density ($\mu A/cm^2$)	Mixed Potential (V_{SCE})
99.9% Mg	71.9	−1.640	42.6	−1.634
AZ31B	14.2	−1.605		
99.9% Mg	71.9	−1.640	12.5	−1.622
AZ61A	5.38	−1.610		
99.9% Mg	71.9	−1.640	12.6	−1.637
AZ91D	4.82	−1.613		
99.9% Mg	71.9	−1.640	2380	−1.536
$Mg_{17}Al_{12}$	2.44	−1.058		
99.9% Mg	71.9	−1.640	2740	−1.490
Mg_2Al_3	0.75	−1.115		
AZ31B	14.2	−1.605	2080	−1.526
$Mg_{17}Al_{12}$	2.44	−1.058		
AZ91D	4.82	−1.613	1920	−1.481
Mg_2Al_3	0.75	−1.115		

5 GENERAL DISCUSSION

5.1 Introduction

The aim of this research was to investigate the formation of Mg-Al intermetallic surface layers on Mg substrates and provide a comprehensive understanding of how they affect the corrosion performance of an Mg-Al-Zn alloy, both as part of its microstructure and as a protective surface layer.

The experimental work in Section 4 addressed the first five objectives. This began by examining the practicalities of producing Mg-Al intermetallic surface layers on Mg substrates using electrodeposition of Al from an ionic liquid, and showed how varying the subsequent heat treatment duration changed the layer structure. It went on to investigate the effect of Mg-Al intermetallics on corrosion behaviour by firstly comparing the self-corrosion characteristics of three Mg-Al-Zn alloys (AZ31B, AZ61A and AZ91D) that contained different proportions of the $Mg_{17}Al_{12}$ phase within their microstructures. Measurements of the self-corrosion rate of manufactured samples of the intermetallics $Mg_{17}Al_{12}$ and Mg_2Al_3 then confirmed the corrosion performance benefits they could offer. Consideration of the galvanic behaviour of the alloys and intermetallics also provided an understanding of the potential drawbacks linked to using Mg-Al surface layers.

This section addresses the final objective by discussing the implications of the experimental work for the practical application of Mg-Al intermetallic surface layers and suggesting solutions to the issues raised.

5.2 Total Corrosion

5.2.1 Mg-Al-Zn Alloys

Galvanic corrosion has so far been discussed independently but, to understand if a particular galvanic couple will cause a severe problem, it must be considered alongside the self-corrosion behaviour of the coupled materials. The sum of self-corrosion and galvanic corrosion gives the total corrosion as illustrated by the plot in Figure 5-1. This shows the self-corrosion current densities for 99.9% Mg and AZ31B together with the galvanic corrosion current density that was generated when they were coupled. The 42.6 $\mu A/cm^2$ positive galvanic current associated with 99.9% Mg — which is the anode — means that electrons are being supplied by this material. These electrons are in

addition to those from the self-corrosion current of 71.9 µA/cm^2 and the effect is to increase the rate of the anodic reaction at its surface. The resulting total corrosion current of 115 µA/cm^2 is the sum of these separate self-corrosion and galvanic corrosion components.

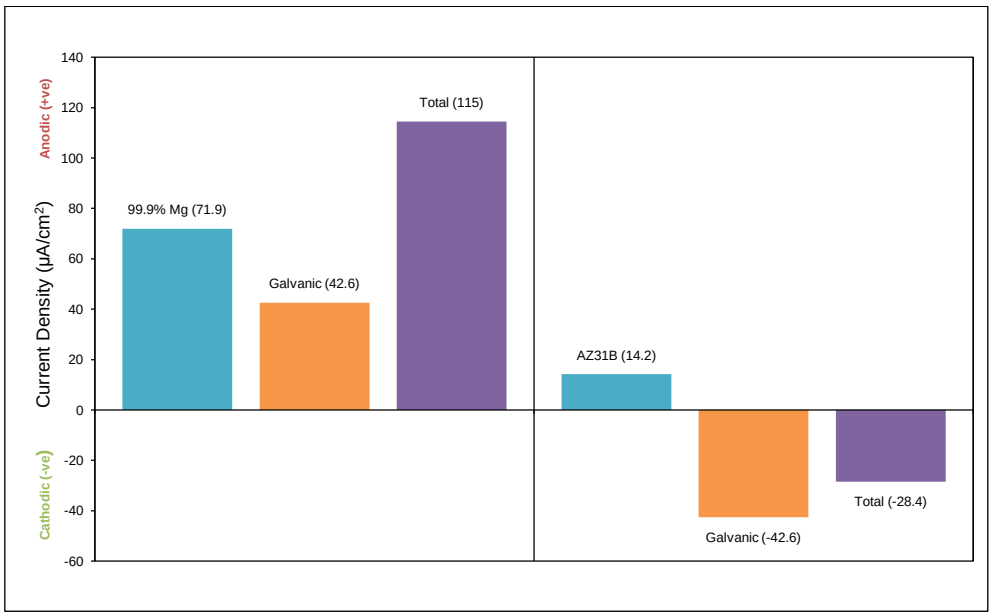

Figure 5-1 – Plot showing the self-corrosion current densities for 99.9% Mg and AZ31B together with those for galvanic and total corrosion of a couple of the same materials.

The negative galvanic current of −42.6 µA/cm^2 associated with AZ31B — which is the cathode — relates to the additional electrons supplied by the anode, and is logically equal and opposite of that for 99.9% Mg. The effect is to slow the alloy's corrosion by reducing the rate of the anodic reaction. In this case the magnitude of the opposing galvanic current is greater than the 14.2 µA/cm^2 self-corrosion current, with the consequence that AZ31B should no longer corrode. The negative total corrosion current of −28.4 µA/cm^2 for AZ31B is linked to an increase in the rate of the cathodic reaction on the surface of the alloy and not to a gain of material.

The galvanic behaviour of each of the Mg-Al-Zn alloys (AZ31B, AZ61A, and AZ91D) coupled to 99.9% Mg was discussed in Section 4.5.3.1 and showed that they were all under cathodic control i.e. controlled by the rate of the cathodic reaction. The plot in Figure 5-3 compares these galvanic current densities with the respective self-corrosion and total corrosion current densities and in all cases the Mg-Al-Zn alloy will be protected. Full protection cannot be guaranteed, however, because the potentials of the systems are not low enough to bring them into the immunity region of the most active element, which begins at –2.363 V_{SHE} (–2.607 V_{SCE}) as shown by the Mg Pourbaix diagram in Figure 5-2.

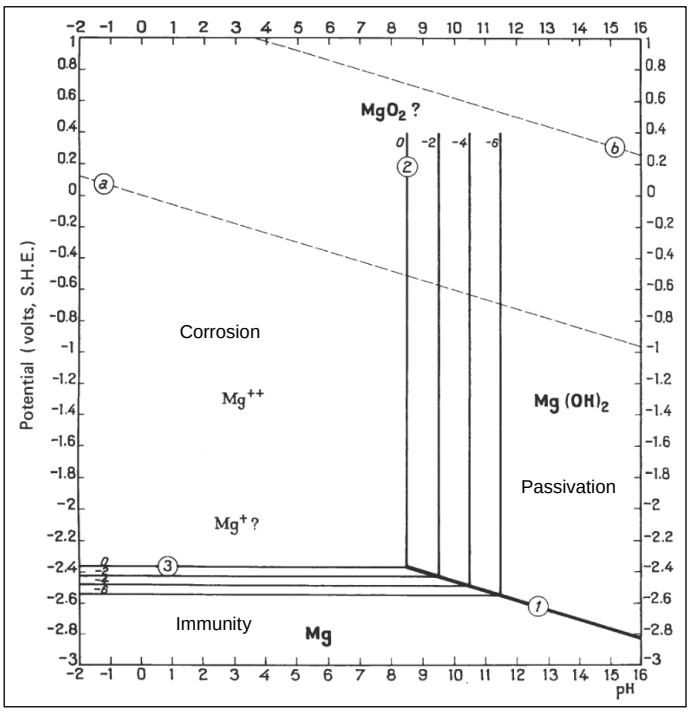

Figure 5-2 – Pourbaix diagram showing the potential-pH behaviour for an Mg and H_2O system at 25°C [172]. The lines labelled 0, −2, −4 and −6 represent log [Mg^{2+}], where Mg^{2+} is the molar concentration.

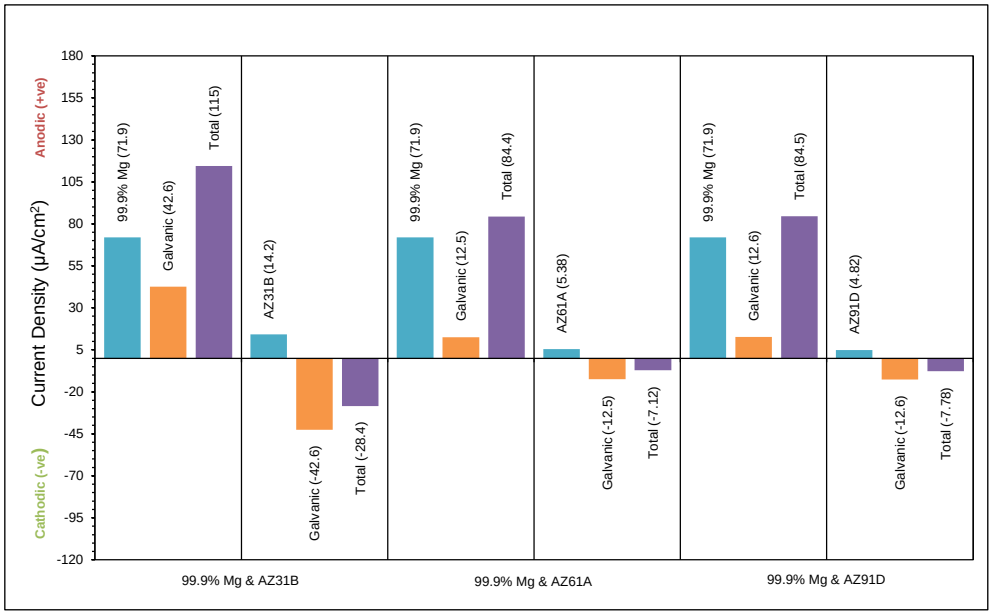

Figure 5-3 – Plot showing the self-corrosion current densities for 99.9% Mg and each of the Mg-Al-Zn alloys (AZ31B, AZ61A, and AZ91D) alongside their respective galvanic and total corrosion current densities when coupled to 99.9% Mg.

5.2.2 Mg-Al Intermetallics

Figure 5-4 shows the self-corrosion current densities for the Mg-Al intermetallics ($Mg_{17}Al_{12}$ and Mg_2Al_3) and the associated galvanic and total corrosion current densities when coupled to 99.9% Mg, alongside those seen previously for the Mg-Al-Zn alloys. Section 4.5.3.2 described how the intermetallic couples were both under mixed control, with their behaviours governed by the kinetics of the anodic and cathodic reactions. This change from cathodic control to mixed control — evident as polarisation of the R-box anode curves plotted in Figure 4-81 and Figure 4-83 — was attributed to the significant increase in the anodic reaction as a result of the greater galvanic current.

The magnitude of the galvanic effect means the intermetallics should be fully protected — again acknowledging the fact that the potentials are not within the immunity region of the Mg Pourbaix diagram — with the total corrosion currents showing that the 99.9% Mg anodes corrode over 34 and over 39 times faster when coupled to $Mg_{17}Al_{12}$ and Mg_2Al_3 respectively. These rate rises substantially exceed those associated with any of the 99.9% Mg and Mg-Al-Zn alloy couples, where the greatest increase was only 60% more than self-corrosion. This highlights just how much more damaging the intermetallics can be.

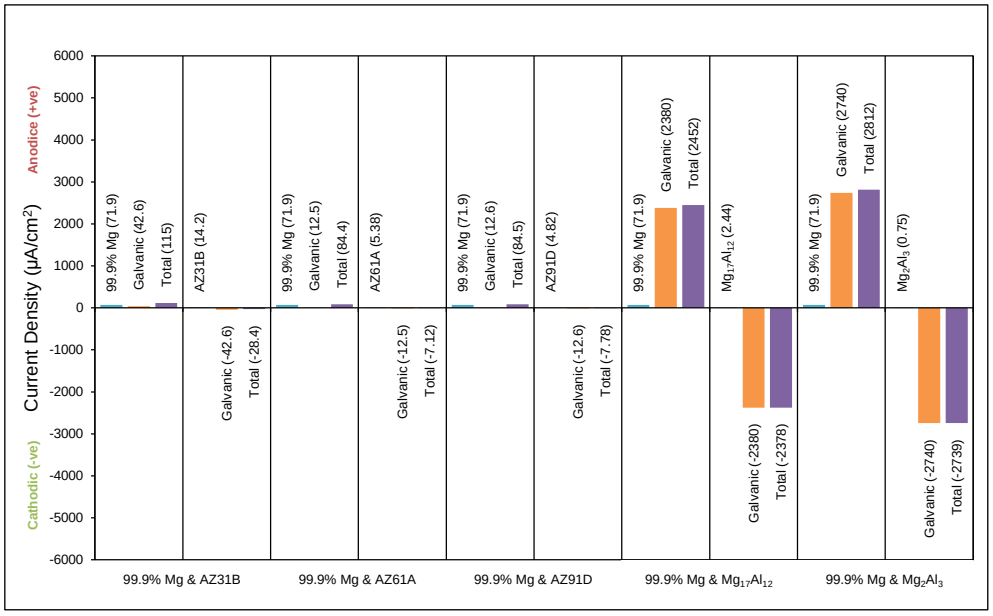

Figure 5-4 – Plot showing the self-corrosion current densities for 99.9% Mg, the Mg-Al-Zn alloys (AZ31B, AZ61A, and AZ91D) and the Mg-Al intermetallics ($Mg_{17}Al_{12}$ and Mg_2Al_3) alongside their respective galvanic and total corrosion current densities when coupled to 99.9% Mg.

Comparing the galvanic behaviours of the Mg-Al-Zn alloys and the Mg-Al intermetallics, when coupled to 99.9% Mg, shows how effective the intermetallics are as cathodes. However, although galvanic couples with 99.9% Mg highlight the significant consequences the intermetallics might have, they may not fully reflect the behaviour characteristics during practical application.

5.2.3 AZ91D and Mg-Al Intermetallic Surface Layer Models

This section discusses the total corrosion rates for the AZ91D and Mg-Al intermetallic surface layers models described in Section 4.5.3.4. These models were designed to more accurately represent real galvanic couples and enable the implications associated with Mg-Al intermetallics to be better understood.

5.2.3.1 AZ91D Model

The micro-galvanic component of AZ91D self-corrosion was modelled in Section 4.5.3.4 by coupling AZ31B (to represent the α-Mg phase) and $Mg_{17}Al_{12}$, and described how the couple was under mixed control. The plot in Figure 5-5 shows the self-corrosion current densities of the respective couple components alongside the resulting galvanic and total corrosion current densities. The direction and magnitude of

the galvanic current generated by this couple increases the corrosion rate of AZ31B by a factor of over 147 and should cause $Mg_{17}Al_{12}$ to become fully protected. As before though the potential of the system is not within the Mg immunity region, and so corrosion could still occur.

The AZ91D model used equal areas of AZ31B and $Mg_{17}Al_{12}$, which reflects the estimated 1:1 area ratio for α-Mg and $Mg_{17}Al_{12}$ that was given in Section 4.2.3.3, and therefore indicates that the $Mg_{17}Al_{12}$ phase in the alloy should not corrode. However, although the 1:1 phase ratio is reproduced by the model, the effect of phase distribution in the microstructure is not. The local phase distribution within the alloy will vary the galvanic influence of $Mg_{17}Al_{12}$ across the material's surface, with greater proportions increasing the local galvanic current and lesser proportions reducing it. Given the strength of $Mg_{17}Al_{12}$ as a cathode though it is likely to always be protected when coupled to the α-Mg phase in the AZ91D alloy examined here.

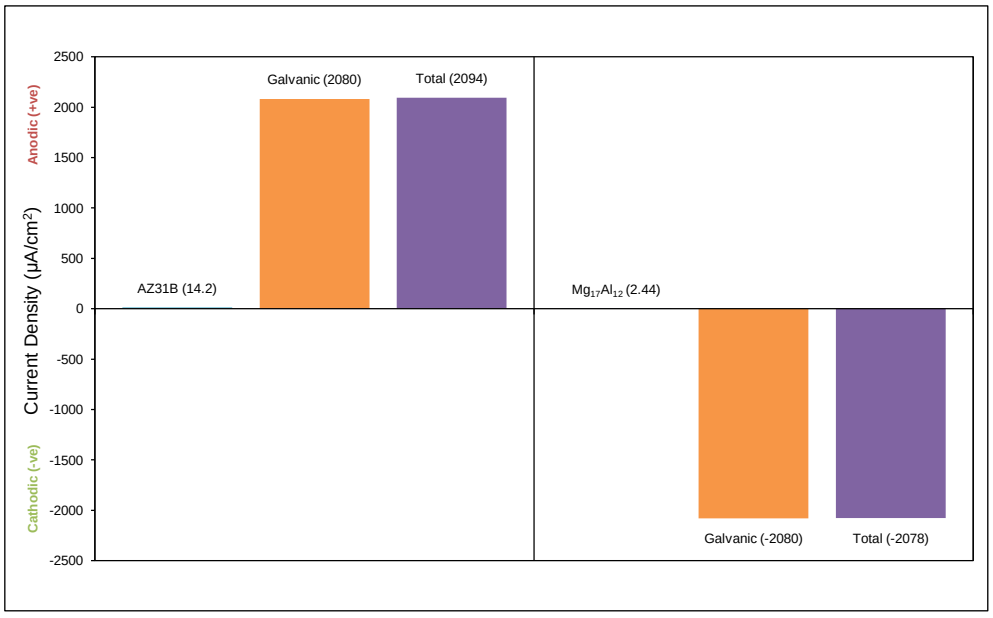

Figure 5-5 – Plot showing the self-corrosion current densities for AZ31B and $Mg_{17}Al_{12}$, together with those for galvanic and total corrosion of a couple of the same materials that was used to model the micro-galvanic component of AZ91D self-corrosion.

The AZ91D model has so far assumed the system is static but as micro-galvanic corrosion of the alloy proceeds the α-Mg phase be preferential removed. It has been argued that this effect is responsible for the improved corrosion properties associated with Mg-Al-Zn alloys containing significant proportions of $Mg_{17}Al_{12}$, as the continued dissolution of α-Mg may leave a network of $Mg_{17}Al_{12}$ that can act as a protective barrier [38,42–45,48]. The similar self-corrosion rates recorded for AZ91D and $Mg_{17}Al_{12}$ in Section 4.3.3.2 and Section 4.4.3.2 respectively suggest that this may have occurred.

The dissolution of Mg results in the formation of $Mg(OH)_2$, as shown by Equation 4-11, and it has been proposed that this corrosion product may also play a part in ensuring the integrity of a protective barrier formed through the micro-galvanic corrosion mechanism. Because it is unlikely that a continuous network of $Mg_{17}Al_{12}$ will exist there will always be gaps where α-Mg is exposed. However, if the distribution of $Mg_{17}Al_{12}$ means these gaps are narrow, it is possible for them to become blocked with corrosion product that would limit further attack [38].

5.2.3.2 Mg-Al Intermetallic Layer Model

The effect of damage to an intermetallic surface layer resulting in exposure of the substrate was modelled in Section 4.5.3.4 by coupling AZ91D and Mg_2Al_3, to represent the substrate and surface layer, and described how the couple was under mixed control. The resulting galvanic and total corrosion current densities are given alongside the respective self-corrosion current densities in Figure 5-6. This shows that Mg_2Al_3 should be fully protected — although as described previously the potential is not within the Mg immunity region — and AZ91D corrodes at nearly 400 times its normal rate.

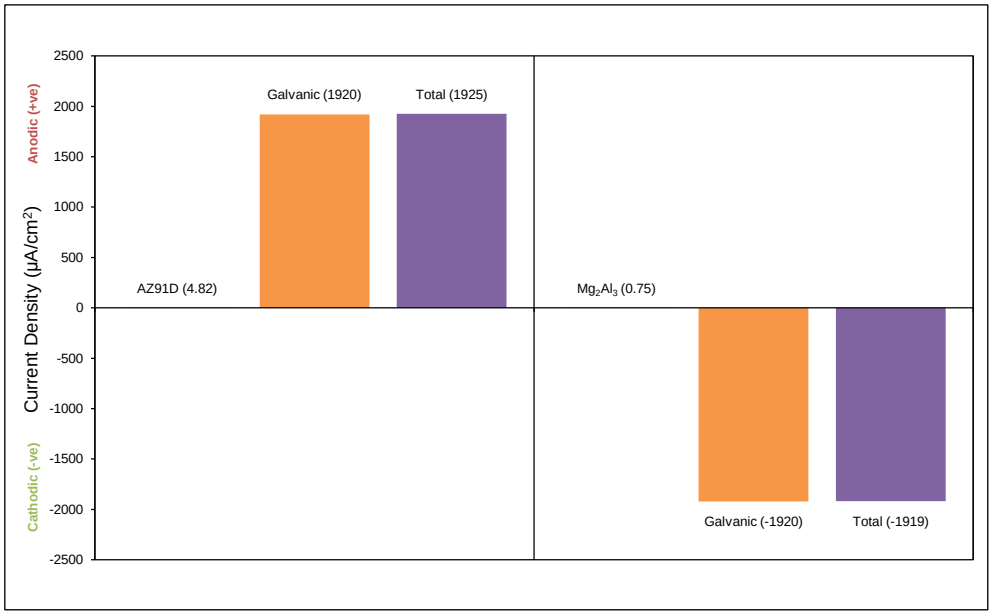

Figure 5-6 – Plot showing the self-corrosion current densities for AZ91D and Mg_2Al_3, together with those for galvanic and total corrosion of a couple of the same materials that was used to model the effect of damage to an Mg-Al intermetallic layer resulting in exposure of the substrate.

Although the rise in AZ91D corrosion rate seen here is significant, it could be even greater if a more realistic area ratio was used. The model corrosion system used equal areas of substrate and surface layer, but the area of intermetallic in an actual system — being the surface of a component — is likely to be many hundreds, or thousands, of times greater than the area of substrate exposed due to flaws, damage, or wear. Increasing the cathode area in a galvanic couple proportionally increases the galvanic current and translates to more rapid corrosion of the anode. The effect of this can be illustrated by adjusting the R-box results for the damaged intermetallic surface layer model given in Figure 4-88 to reflect a 1:1000 anode to cathode ratio as shown in Figure 5-7.

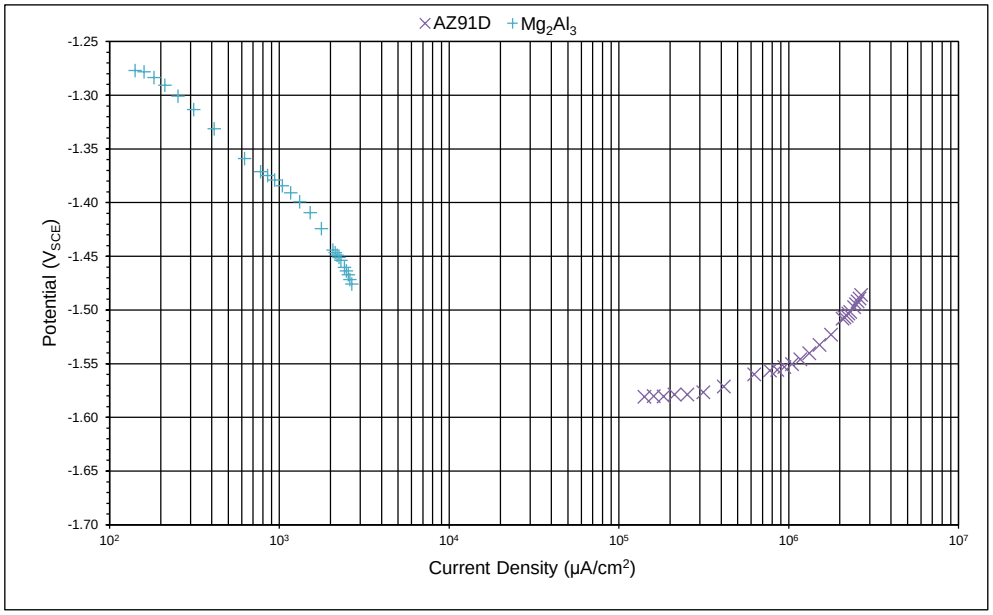

Figure 5-7 – Plot showing how the R-box results for a simulation of a damaged intermetallic surface layer would look if the area of the cathode (Mg_2Al_3) was 1000 times greater than that shown Figure 4-88. The current cathode density remains the same (2680 µA/cm^2) but the anode current density increases to 2.68 A/cm^2.

Multiplying the cathode area by 1000 times increases the galvanic current by the same factor, although the cathode current density, and therefore the position of R-box curve for Mg_2Al_3, remains the same at 2680 µA/cm^2. However, because the anode area is unchanged, the anode current density increases by 1000 times to 2.68 A/cm^2 and there is a corresponding shift in the R-box curve for AZ91D. According to Equation 4-28 this translates to a corrosion rate equivalent over 60 meters per year, which would undoubtedly cause a severe problem. Other factors are however likely to affect the actual behaviour, and these should be carefully considered before the use of Mg-Al intermetallic layers is dismissed.

Graded Mg-Al Layers

The galvanic model of a protective Mg-Al intermetallic used AZ91D and Mg_2Al_3 to represent the substrate and surface layer respectively, and demonstrated how damage may cause a severe corrosion problem. Before exploring the possible mechanisms by which this type of corrosion may become limited, it is important to address the fact that the model is a simplification of the galvanic system.

Section 4.1.3.3 described how the Mg-Al layer that develops on an Mg substrate is of a graded composition, and showed that a suitable heat treatment will generate discreet layers of $Mg_{17}Al_{12}$ and Mg_2Al_3. Damage penetrating through to the substrate will expose the edges of the layer — as illustrated by the schematic representation in Figure 5-8 — and so the resulting galvanic corrosion will involve an additional amount of $Mg_{17}Al_{12}$, as well as the Mg substrate and Mg_2Al_3 surface.

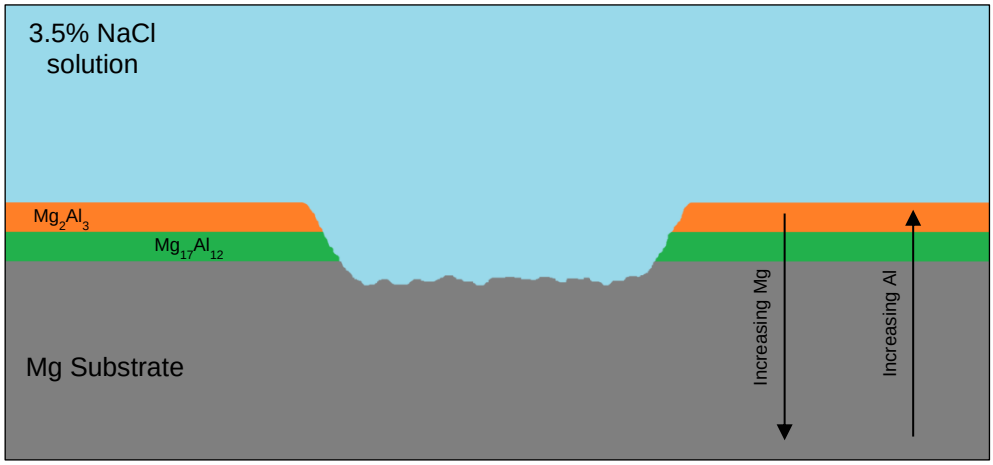

Figure 5-8 – Schematic representation of a graded Mg-Al surface layer where damage has penetrated through to the Mg substrate.

To understand if a graded layer will affect corrosion behaviour the characteristics of the system components must be considered. The OCPs of AZ91D and Mg_2Al_3 used in the surface layer model are −1.613 mV and −1.131 mV respectively, and this 482 mV difference provides a relatively large driver for the galvanic corrosion. Figure 5-7 above also showed how a greater area of Mg_2Al_3 can enhance the galvanic effect. The addition of a comparatively small area of $Mg_{17}Al_{12}$, with an OCP of −1.077 mV (54 mV more noble than Mg_2Al_3), to represent the exposed layer edges is therefore likely to have negligible influence on the overall galvanic behaviour.

Self-Limiting Damage

The AZ91D alloy used here contains approximately equal proportions of α-Mg and $Mg_{17}Al_{12}$, and its self-corrosion is known to involve the preferential attack of α-Mg due to micro-galvanic corrosion between the two phases. Coupling this alloy to Mg_2Al_3, which has an OCP similar to $Mg_{17}Al_{12}$ and more noble than α-Mg, would have the effect of increasing the rate of galvanic attack of the α-Mg phase. This would not prevent AZ91D from developing a ‘barrier’ in the same manner as described in Section 5.2.3.1

and it is therefore possible that an AZ91D substrate could act to self-limit the galvanic corrosion resulting from damage to an Mg-Al intermetallic surface layer. If this had occurred in the Mg-Al intermetallic layer model the galvanic current recorded in Section 4.5.3.4 would have dropped over time. This may not have happened because the area of AZ91D exposed in the model is relatively large, and therefore the likelihood of a suitable $Mg_{17}Al_{12}$ network being present across its surface is low. If a smaller area of substrate was exposed, either in a model or on an actual Mg-Al intermetallic layer with a chip or scratch, a barrier may be more likely to form as there is a greater chance of a suitable $Mg_{17}Al_{12}$ network being present.

Relying on $Mg_{17}Al_{12}$ to self-limit corrosion damage is not ideal though because it is conditional on the substrate having a suitable distribution of the intermetallic. However, because this mechanism does not depend solely on the existence of an $Mg_{17}Al_{12}$ network, but also on corrosion product filling any gaps in between, it leaves open the prospect of damage being able to self-repair when little or no $Mg_{17}Al_{12}$ is present in the substrate microstructure.

Self-Repairing Damage

Section 5.2.3.1 described how corrosion product may help to improve the corrosion properties of AZ91D by protecting areas of the α-Mg phase in between an $Mg_{17}Al_{12}$ network. It is therefore conceivable that a damaged Mg-Al intermetallic surface layer could ‘self-repair’ in a similar fashion, with the strong galvanic effect leading to the rapid formation of $Mg(OH)_2$ that would fill the site of exposed substrate and consequently prevent further corrosion. This effect does not rely on the existence of $Mg_{17}Al_{12}$ in the microstructure, and so would work no matter what Mg substrate was being protected.

Like the self-limiting mechanism the effect of self-repair, had it occurred, would be evident as a drop in the galvanic current recorded for the Mg-Al intermetallic layer model in Section 4.5.3.4. It was suggested that galvanic corrosion did not self-limit through the development of an $Mg_{17}Al_{12}$ network as the exposed surface area was too large. There is however, evidence to suggest a protective $Mg(OH)_2$ layer can work consistently over relatively large areas, and may even offer greater improvements in corrosion performance if suitably engineered.

5.3 Protective $Mg(OH)_2$ Layers

The $Mg(OH)_2$ surface oxide that develops during the self-corrosion of Mg is considered much less stable than the passive films that form on Al or stainless steels, and therefore does not offer the same protection [70]. It may nevertheless be possible to develop a robust $Mg(OH)_2$ layer on an Mg substrate that offers substantial improvements to corrosion performance.

5.3.1 Corrosion Performance of an $Mg(OH)_2$ Layer

During the galvanic corrosion of 99.9% Mg and AZ91D described in Section 4.5.3.1 the previously bright and shiny AZ91D sample became uniformly dull and visibly rougher across its surface. Subsequent measurements of its OCP and corrosion rate using EIS, the results of which are given in Figure 5-9 and Figure 5-10 respectively, showed that its corrosion behaviour was very different to the freshly abraded AZ91D that was examined in Section 4.3.3. Following galvanic corrosion the AZ91D sample had a mean OCP of −1.243 V_{SCE}, which is 370 mV more noble than freshly abraded AZ91D (−1.613 V_{SCE}) and 118 mV more active than Mg_2Al_3 (−1.115 V_{SCE}). The EIS results for coupled AZ91D yielded an R_{ct} of 416000 Ω.cm^2, which is nearly 172 times greater than that recorded for freshly abraded AZ91D (2420 Ω.cm^2) and almost 89 times that seen for Mg_2Al_3 (4750 Ω.cm^2). Similar results were obtained in repeats of this experiment with AZ91D, and also using AZ61A.

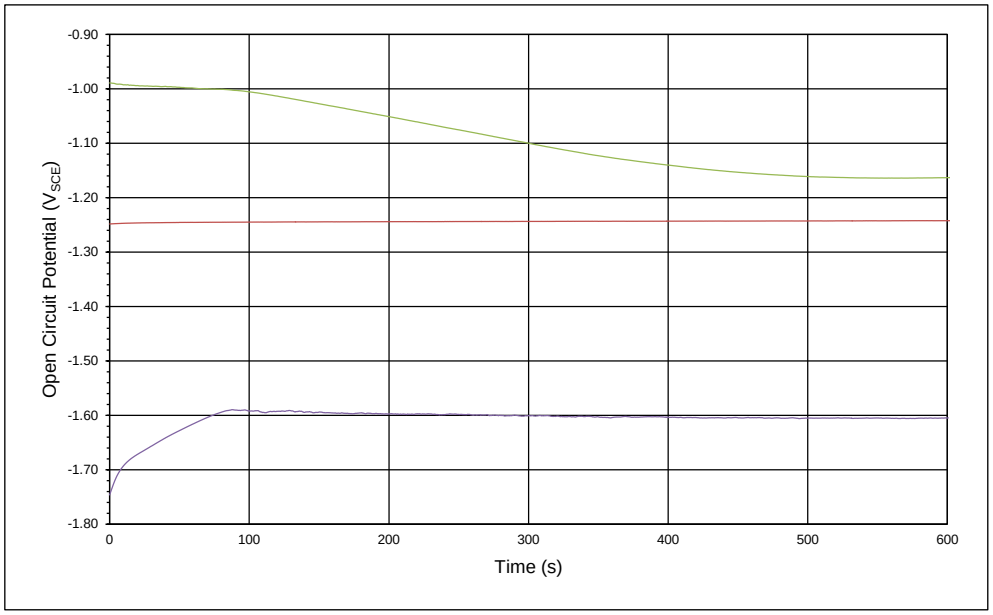

Figure 5-9 – Plot showing the OCPs recorded for freshly abraded AZ91D (purple), AZ91D after being coupled to 99.9% Mg for 20 h (red), and Mg_2Al_3 (green) over the first 600 s of exposure to 3.5% NaCl solution. The mean OCPs are −1.613 V_{SCE}, −1.243 V_{SCE} and −1.115 V_{SCE} respectively.

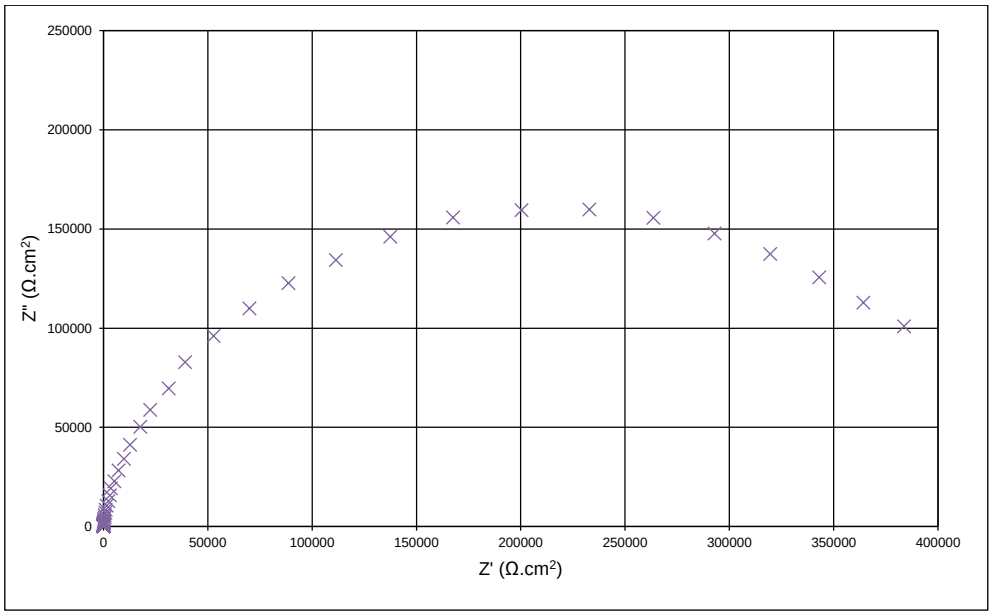

Figure 5-10 – Nyquist plot showing the EIS result for AZ91D after being coupled to 99.9% Mg for 20 h, and taken immediately following the OCP measurement in Figure 5-9. The circle fit function in ZPlot gave an R_{ct} of 416000 Ω.cm^2 to 3 s.f. The mean R_{ct} for freshly abraded AZ91D was 2420 Ω.cm^2 (Figure 4-53). The intermetallic Mg_2Al_3 had an R_{ct} of 4770 Ω.cm^2 (Figure 4-64).

5.3.2 Physical Characteristics of an $Mg(OH)_2$ Layer

The SEM images in Figure 5-11 and Figure 5-12 show the top surface of the coupled AZ91D sample that exhibited a very low corrosion rate. Analysis by EDX revealed that the filamentous surface, as well as the nodules that appear to be made of the same filaments, contain only Mg and O in 36.23 at% and 63.72 at% proportions respectively, which is very close to that of the $Mg(OH)_2$ corrosion product.

The image in Figure 5-13 was obtained using a focused ion beam (FIB) system to cut a cross-section through the surface layer. The $Mg(OH)_2$ surface filaments can be seen at the top of the image and beneath is an approximately 1 µm thick layer that appears to be part of the same structure. Below this it is possible to see lamellae in the eutectic type microstructure of the AZ91D substrate.

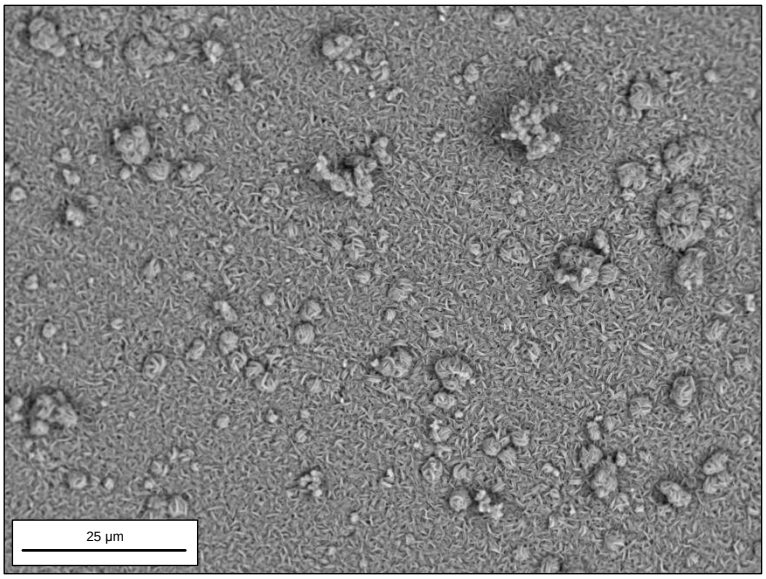

Figure 5-11 – SEM image of the top surface of AZ91D after being coupled to 99.9% Mg for 20 h. EDX shows that the filamentous surface and the nodules contain 36.23 at% Mg and 63.72 at% O.

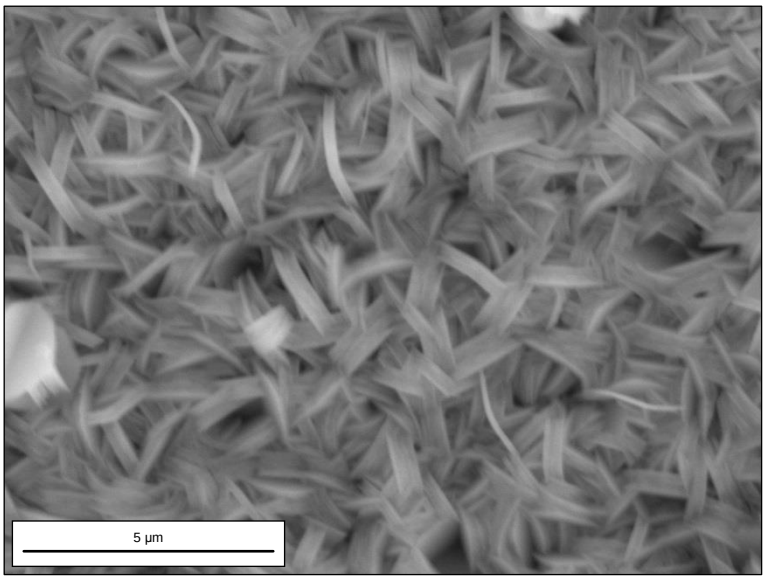

Figure 5-12 – High magnification SEM image of the top surface of AZ91D after being coupled to 99.9% Mg for 20 h.

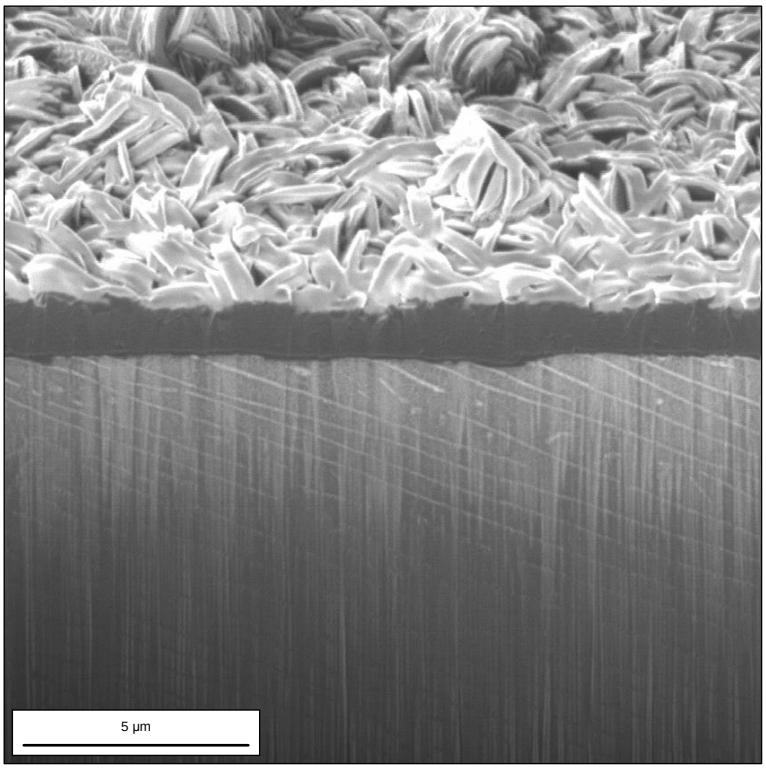

Figure 5-13 – SEM image of a cross-section of AZ91D after being coupled to 99.9% Mg for 20 h. The top of the image shows $Mg(OH)_2$ surface filaments above a 1 µm thick layer. Below is the AZ91D substrate with visible lamellae from the eutectic type microstructure.

5.3.3 Formation of an $Mg(OH)_2$ Layer

Section 4.3.2.2 described the aqueous corrosion of Mg in pH neutral conditions and showed how this involves the oxidation of Mg to Mg^{2+} (Equation 4-12) and the reduction of water to H_2 and OH^- (Equation 4-13), which leads to the formation of $Mg(OH)_2$ as the corrosion product. During self-corrosion these reactions took place at sites on the same surface, but when 99.9% Mg and AZ91D were coupled the magnitude of the galvanic current density meant the anodic and cathodic components were entirely separated such that only Mg^{2+} ions were generated at the 99.9% Mg anode and only OH^- ions formed at the AZ91D cathode. Because the electrolyte was not refreshed or disturbed during the experiment this separation would have led to an increase in the concentration of Mg^{2+} ions at the anode, and a build-up of OH^- ions and an associated rise in pH at the cathode. The Pourbaix diagram in Figure 5-2 shows the effect pH has on the behaviour of Mg in water, and defines regions of corrosion, immunity, or passivation. The lines labelled 0, −2, −4 and −6 represent log $[Mg^{2+}]$, where Mg^{2+} is the molar concentration, and demonstrate how the boundaries between corrosion, immunity, and passivation are correspondingly moved e.g. at 1 M Mg^{2+} (log $[Mg^{2+}]$ equals 0) an $Mg(OH)_2$ film will form when the pH is greater than 8.5.

The 3.5% NaCl solution used in the galvanic test cell was initially neutral and the couple had a mixed potential of −1.642 V_{SCE} (−1.398 V_{SHE}). Over time the rise in pH at the cathode, combined with the migration of Mg^{2+} ions from the anode due to a continued increase in concentration, could move the system into the passivation regime causing the AZ91D to develop a stable $Mg(OH)_2$ film [21,172,173]. This effect should become more favourable with time because, as shown by the Pourbaix diagram in Figure 5-2, the rise in pH required to generate a passive film reduces as the solution becomes more saturated with Mg^{2+} ions.

5.3.4 Further Discussion

Very little information could be found about the development and use of actively grown $Mg(OH)_2$ layers to protect Mg substrates, but the research conducted by Ishizaki *et al*. 2013 [174] described the formation of such layers on AZ31B by exposing it to steam at different temperatures for various durations. This yielded $Mg(OH)_2$ film thicknesses ranging from 2 to 68 µm and a reduction in corrosion rate of up to six orders of magnitude, which confirms the significant improvements that can be achieved. The $Mg(OH)_2$ layer produced in the work presented here was around 1 µm

and resulted in a two order of magnitude reduction in corrosion rate. Although this is not as large as that reported by Ishizaki *et al*. 2013 [174], the method of formation described here could lend itself better to industrial application.

By optimising conditions it might possible to develop thicker $Mg(OH)_2$ layers that could deliver greater improvements in corrosion performance and good long term stability. The concentration of Mg^{2+} ions and a rise in pH appear to be critical factors in the process, as a stable $Mg(OH)_2$ layer did not form when AZ91D alone was exposed to 3.5% NaCl solution and a current with the same magnitude and direction as the measured galvanic current was passed using a Pt electrode. It may be possible to develop a layer if a solution containing a suitable concentration of Mg^{2+} ions was used instead.

5.4 The Practical Application of Mg-Al Layers

The aerospace and automotive industries both aim to create products that deliver performance and efficiency, and materials selection is a key element of achieving this [4–12,14–18]. Different materials, such as steel and Al or Mg alloys, will be more suited to different applications and so it is inevitable that they will need to be joined, often using combinations of bolts, rivets, and high strength adhesives [175]. The coupling of dissimilar materials can be a particular problem for Mg or Mg alloys because its active nature means it is susceptible to severe galvanic corrosion [17,18,22–24,176]. To inhibit this it is common for multi-layer coating schemes to be employed, with the primary aim being to prevent electrical contact between materials [17,18,23]. A simple Mg-Al intermetallic layer could eliminate the need for complex systems and may even improve the mechanical robustness of such assemblies as explained below.

Section 5.2.3.2 discussed the use of an Mg-Al layer to reduce the corrosion of an Mg alloy and showed how damage could lead to significant galvanic corrosion of the substrate. This effect was caused by a favourable anode to cathode area ratio combined with a relatively large OCP difference between Mg_2Al_3 ($-1.131\ V_{SCE}$) and AZ91D ($-1.605\ V_{SCE}$). The OCP of Al ($-0.760\ V_{SCE}$) means that coupling it directly to Mg in an assembly will create even more severe galvanic corrosion [56,176]. Joining Al to Mg that has an Mg-Al layer would reduce the potential difference from 845 mV to 371 mV, therefore greatly lowering the driver for galvanic corrosion and possibly preventing substantial damage.

Unlike a paint film, which sits on the surface of material, an Mg-Al layer is a structural part of the material because it is formed by diffusion between the Mg substrate and Al coating. The resulting mechanical properties, such as improved hardness and wear resistance, also mean it is likely to offer greater pull off strength compared to other coatings [56–58,62,67]. This may translate to greater strength of adhesive joints, while still maintaining a good level of resistance to self-corrosion and galvanic corrosion.

6 CONCLUSIONS

1. The electroplating of Al on to Mg substrates showed that expert processing is required to achieve a high quality deposit. It is also essential to remove any surface oxide that might impede subsequent diffusion. Altering the duration of the heat treatment demonstrated how the structure of an Mg-Al layer can be varied to achieve the desired characteristics.

2. Examination of the alloys confirmed that the amount of intermetallic phase in their microstructures was linked to the quantity of Al they contained. Discussion relating to the Mg-Al phase diagram also showed how processing during manufacture, and any subsequent heat treatment, influences its development.

3. Self-corrosion measurements of the three alloys demonstrated that their corrosion performance was connected to the amount of intermetallic phase in their microstructures. The ratio of anodic to cathodic phases determined whether simple self-corrosion or micro-galvanic corrosion was the dominant dissolution mechanism.

4. Self-corrosion measurements of the Mg-Al intermetallics showed that they have corrosion rates lower than the alloys, and could therefore improve their performance if engineered as surface layers. Their noble nature also indicated that they would become cathodes in a galvanic couple with an Mg substrate.

5. Galvanic corrosion measurements showed the relative behaviour of the alloys and Mg-Al intermetallics, and demonstrated that the intermetallics are strong cathodes. Galvanic models also confirmed that a damaged intermetallic surface layer could lead to a serious loss of corrosion protection, although further discussion described how this might self-limit or self-repair.

6. Galvanic corrosion experiments revealed how the combination of current flow and a solution saturated with Mg^{2+} ions could lead to the formation of a highly protective $Mg(OH)_2$ film, which has the potential for future development.

7 FUTURE WORK

- Further investigation into why the quality of an Al coating electrodeposited from an ionic liquid varied with the type of Mg substrate. This appears to be directly related to the electrochemical activity of the substrate.

- Investigate the formation of intermetallic surface layers on Mg substrates at temperatures lower than 390°C to allow more control of the diffusion processes and enable processing parameters for an ‘ideal’ layer to be developed.

- Electrochemical corrosion assessments of an intermetallic layer with surface damage to investigate if there is a severe loss of protection, and determine whether the proposed self-limiting or self-repairing mechanisms transpire.

- Study into whether the behaviour of a damaged intermetallic surface layer, including any self-limiting or self-repair, is affected by the composition and microstructure of the substrate.

- Investigation into how an intermetallic layer performs in a galvanic couple with other engineering materials such as steel or aluminium in both an ‘ideal’ and ‘damaged’ condition.

- Further examination of the mechanisms involved in the formation of a protective $Mg(OH)_2$ film, and analysis of its corrosion performance and long term stability.

8 REFERENCES

[1] W.D. Callister, Materials Science and Engineering: An Introduction, 6th ed., John Wiley & Sons, Inc., 2003.

[2] M.K. Kulekci, Magnesium and its alloys applications in automotive industry, Int. J. Adv. Manuf. Technol. 39 (2007) 851–865.

[3] D. Hawke, K. Gaw, Effects of chemical surface treatments on the performance of an automotive paint system on die cast magnesium, in: SAE Int. Congr. Expo., Detroit, 1992: pp. 1–11.

[4] R. Hodkinson, J. Fenton, Lightweight electric/hybrid vehicle design, Butterworth-Heinemann, 2001.

[5] H. Friedrich, S. Schumann, Research for a "new age of magnesium" in the automotive industry, J. Mater. Process. Technol. 117 (2001) 276–281.

[6] S. Kim, H. Yoo, Y. Kim, Research strategy for AM60 magnesium steering wheel, Magnes. Technol. 2 (2002).

[7] A.A. Luo, Magnesium: Current and potential automotive applications, JOM J. Miner. Met. Mater. Soc. 54 (2002) 42–48.

[8] G.S. Cole, Issues that influence magnesium's use in the automotive industry, Mater. Sci. Forum. 419-422 (2003) 43–50.

[9] S. Schumann, H. Friedrich, Current and future use of magnesium in the automobile industry, in: Mater. Sci. Forum, 2003: pp. 51–56.

[10] C. Blawert, N. Hort, Automotive applications of magnesium and its alloys, Trans. Indian Inst. Met. 57 (2004) 397–408.

[11] S. Schumann, The paths and strategies for increased magnesium applications in vehicles, Mater. Sci. Forum. 488-489 (2005) 1–8.

[12] B. DeForce, T. Eden, J. Potter, V. Champagne, P. Leyman, D. Helfritch, Application of aluminum coatings for the corrosion protection of magnesium by cold spray, in: Tri-Service Corros. Conf., 2007.

[13] V. Truong, Corrosion protection of magnesium by electroactive polypyrrole/paint coatings, Synth. Met. 110 (2000) 7–15.

[14] I. Ostrovsky, Y. Henn, Present state and future of magnesium application in aerospace industry, in: Int. Conf. “New Challenges Aeronaut., 2007.

[15] B. Gwynne, P. Lyon, Magnesium alloys in aerospace applications, past concerns, current solutions, in: Trienn. Int. Aircr. Fire Cabin Saf. Res. Conf., 2007.

[16] I.J. Polmear, Light Alloys: From Traditional Alloys to Nanocrystals, 4th ed., Butterworth-Heinemann, 2006.

[17] H. Schreckenberger, M. Papke, S. Eisenberg, The magnesium hatchback of the 3-liter car: Processing and corrosion protection, SAE Trans. J. Mater. Manuf. 109 (2000) 606–612.

[18] G.T. Bretz, K.A. Lazarz, D.J. Hill, P.J. Blanchard, Adhesive bonding and corrosion protection of a die cast magnesium automotive door, in: Magnes. Technol., 2004: pp. 113–119.

[19] G. Wang, K. Stewart, R. Berkmortel, J.I. Skar, Corrosion prevention for external magnesium automotive components, in: Light Met. Appl. Automot. Ind. Alum. Magnes., 2001.

[20] V.K. Champagne, The repair of magnesium rotorcraft components by cold spray, J. Fail. Anal. Prev. 8 (2008) 164–175.

[21] G. Song, A. Atrens, Understanding magnesium corrosion: A framework for improved alloy performance, Adv. Eng. Mater. 5 (2003) 837–858.

[22] G. Gerstmayr, G. Mori, H. Leitner, W. Eichlseder, On the applicability of high strength self-tapping aluminium bolts in magnesium nut materials for automotive applications, Mater. Corros. 61 (2009) 379–387.

[23] C. Blawert, V. Heitmann, D. Höche, K.U. Kainer, H. Schreckenberger, P. Izquierdo, et al., Design of hybrid Mg/Al components for the automotive body - Preventing general and galvanic corrosion, in: IMA 67th Annu. World Magnes. Conf., Hong Kong, 2010: p. 9.

[24] N. LeBozec, A. LeGac, D. Thierry, Corrosion performance and mechanical properties of joined automotive materials, Mater. Corros. 62 (2011).

[25] B951-10: Standard practice for codification of unalloyed magnesium and magnesium-alloys, cast and wrought, ASTM Int. (2010).

[26] J.D. Hanawalt, C.E. Nelson, J.A. Peloubet, Corrosion studies of magnesium and its alloys, Trans. Am. Inst. Min. Metall. Eng. 147 (1942) 273–299.

[27] K.N. Reichek, K.J. Clark, J.E. Hillis, Controlling the salt water corrosion performance of magnesium AZ91 alloy, SAE Trans. 94 (1985) 318–329.

[28] B90/B90M-07: Specification for magnesium-alloy sheet and plate, ASTM Int. (2007).

[29] B91-07: Standard specification for magnesium-alloy forgings, ASTM Int. (2007).

[30] B107/B107M-07: Specification for magnesium-alloy extruded bars, rods, profiles, tubes, and wire, ASTM Int. (2007).

[31] B843-07: Standard specification for magnesium alloy anodes for cathodic protection, ASTM Int. (2007).

[32] B93/B93M-09: Specification for magnesium alloys in ingot form for sand castings, permanent mold castings, and die castings, ASTM Int. (2009).

[33] B94-07: Standard specification for magnesium-alloy die castings, ASTM Int. (2007).

[34] B80-09: Standard specification for magnesium-alloy sand castings, ASTM Int. (2009).

[35] B199-07: Standard specification for magnesium-alloy permanent mold castings, ASTM Int. (2007).

[36] B403-07: Standard specification for magnesium-alloy investment castings, ASTM Int. (2007).

[37] O. Lunder, T. Kr Aune, K. Nisancioglu, Effect of Mn additions on the corrosion behavior of mould-cast magnesium ASTM AZ91, Corrosion. 43 (1987) 291–295.

[38] G. Song, A. Atrens, M. Dargusch, Influence of microstructure on the corrosion of diecast AZ91D, Corros. Sci. 41 (1999) 249–273.

[39] A.K. Dahle, Y.C. Lee, M.D. Nave, P.L. Schaffer, D.H. StJohn, Development of the as-cast microstructure in magnesium-aluminium alloys, J. Light Met. 1 (2001) 61–72.

[40] N. Hort, Y. Huang, K.U. Kainer, Intermetallics in magnesium alloys, Adv. Eng. Mater. 8 (2006) 235–240.

[41] K.M. Braszczynska, Precipitates of γ–Mg17Al12 phase in AZ91 alloy, in: F. Czerwinski (Ed.), Magnes. Alloy. - Des. Process. Prop., InTech, 2011: pp. 95–112.

[42] O. Lunder, J.E. Lein, T.K. Aune, K. Nisancioglu, The role of Mg17Al12 phase in the corrosion of Mg alloy AZ91, Corrosion. 45 (1989) 741–748.

[43] R. Ambat, N.N. Aung, W. Zhou, Evaluation of microstructural effects on corrosion behaviour of AZ91D magnesium alloy, Corros. Sci. 42 (2000) 1433–1455.

[44] G. Song, A.L. Bowles, D.H. StJohn, Corrosion resistance of aged die cast magnesium alloy AZ91D, Mater. Sci. Eng. A. 366 (2004) 74–86.

[45] G. Ballerini, U. Bardi, R. Bignucolo, G. Ceraolo, About some corrosion mechanisms of AZ91D magnesium alloy, Corros. Sci. 47 (2005) 2173–2184.

[46] G. Song, Recent progress in corrosion and protection of magnesium alloys, Adv. Eng. Mater. 7 (2005) 563–586.

[47] R. Zeng, J. Zhang, W. Huang, W. Dietzel, K. Kainer, C. Blawert, et al., Review of studies on corrosion of magnesium alloys, Trans. Nonferrous Met. Soc. China. 16 (2006) s763–s771.

[48] M.C. Zhao, M. Liu, G. Song, A. Atrens, Influence of the β-phase morphology on the corrosion of the Mg alloy AZ91, Corros. Sci. 50 (2008) 1939–1953.

[49] M. Alvarez-Lopez, M.D. Pereda, J. a del Valle, M. Fernandez-Lorenzo, M.C. Garcia-Alonso, O. a Ruano, et al., Corrosion behaviour of AZ31 magnesium alloy with different grain sizes in simulated biological fluids., Acta Biomater. 6 (2010) 1763–71.

[50] N.N. Aung, W. Zhou, Effect of grain size and twins on corrosion behaviour of AZ31B magnesium alloy, Corros. Sci. 52 (2010) 589–594.

[51] J. Liao, M. Hotta, N. Yamamoto, Corrosion behavior of fine-grained AZ31B magnesium alloy, Corros. Sci. 61 (2012) 208–214.

[52] A. Samaniego, I. Llorente, S. Feliu, Combined effect of composition and surface condition on corrosion behaviour of magnesium alloys AZ31 and AZ61, Corros. Sci. 68 (2013) 66–71.

[53] C. Zhong, F. Liu, Y. Wu, J. Le, L. Liu, M. He, et al., Protective diffusion coatings on magnesium alloys: A review of recent developments, J. Alloys Compd. 520 (2012) 11–21. doi:10.1016/j.jallcom.2011.12.124.

[54] J.E. Gray, B. Luan, Protective coatings on magnesium and its alloys - a critical review, J. Alloys Compd. 336 (2002) 88–113.

[55] G. Song, A. Atrens, X. Wu, B. Zhang, Corrosion behaviour of AZ21, AZ501 and AZ91 in sodium chloride, Corros. Sci. 40 (1998) 1769–1791.

[56] X. Li, W. Liang, X. Zhao, Y. Zhang, X. Fu, F. Liu, Bonding of Mg and Al with Mg–Al eutectic alloy and its application in aluminum coating on magnesium, J. Alloys Compd. 471 (2009) 408–411.

[57] H. Yang, X. Guo, G. Wu, S. Wang, W. Ding, Continuous intermetallic compounds coatings on AZ91D Mg alloy fabricated by diffusion reaction of Mg–Al couples, Surf. Coatings Technol. 205 (2011) 2907–2913.

[58] I. Shigematsu, M. Nakamura, N. Saitou, K. Shimojima, Surface treatment of AZ91D magnesium alloy by aluminum diffusion coating, J. Mater. Sci. Lett. 19 (2000) 473–475.

[59] M.X. Zhang, P.M. Kelly, Surface alloying of AZ91D alloy by diffusion coating, J. Mater. Res. 17 (2002) 2477–2479.

[60] L. Zhu, G. Song, Improved corrosion resistance of AZ91D magnesium alloy by an aluminium-alloyed coating, Surf. Coatings Technol. 200 (2006) 2834–2840.

[61] F. Liu, W. Liang, X. Li, X. Zhao, Y. Zhang, H. Wang, Improvement of corrosion resistance of pure magnesium via vacuum pack treatment, J. Alloys Compd. 461 (2008) 399–403.

[62] H.Q. Sun, Y.N. Shi, M.X. Zhang, K. Lu, Surface alloying of an Mg alloy subjected to surface mechanical attrition treatment, Surf. Coatings Technol. 202 (2008) 3947–3953.

[63] H. Huo, Y. Li, F. Wang, Improvement on the corrosion resistance of AZ91D magnesium alloy by aluminum diffusion coating, J. Mater. Sci. Technol. 23 (2007) 379–382.

[64] T. Zhu, W. Gao, Formation of intermetallic compound coating on magnesium AZ91 cast alloy, IOP Conf. Ser. Mater. Sci. Eng. 4 (2009) 012024.

[65] K. Spencer, M. Zhang, Heat treatment of cold spray coatings to form protective intermetallic layers, Scr. Mater. 61 (2009) 44–47.

[66] H. Meifeng, L. Lei, W. Yating, T. Zhixin, H. Wenbin, Corrosion properties of surface-modified AZ91D magnesium alloy, Corros. Sci. 50 (2008) 3267–3273.

[67] C. Zhong, M. He, L. Liu, Y. Wu, Y. Chen, Y. Deng, et al., Lower temperature fabrication of continuous intermetallic coatings on AZ91D magnesium alloy in molten salts, J. Alloys Compd. 504 (2010) 377–381.

[68] H. Yang, X. Guo, G. Wu, W. Ding, N. Birbilis, Electrodeposition of chemically and mechanically protective Al-coatings on AZ91D Mg alloy, Corros. Sci. 53 (2011) 381–387.

[69] M.X. Zhang, H. Huang, K. Spencer, Y.N. Shi, Nanomechanics of Mg–Al intermetallic compounds, Surf. Coatings Technol. 204 (2010) 2118–2122.

[70] G. Song, A. Atrens, Corrosion mechanisms of magnesium alloys, Adv. Eng. Mater. 1 (1999) 11–33.

[71] C.A. Huang, C.K. Lin, Y.H. Yeh, Corrosion behavior of Cr/Cu-coated Mg alloy (AZ91D) in 0.1M H2SO4 with different concentrations of NaCl, Corros. Sci. 52 (2010) 1326–1332.

[72] T. Lei, C. Ouyang, W. Tang, L.F. Li, L.S. Zhou, Enhanced corrosion protection of MgO coatings on magnesium alloy deposited by an anodic electrodeposition process, Corros. Sci. 52 (2010) 3504–3508.

[73] M.J. Zhao, C. Cai, L. Wang, Z. Zhang, J.Q. Zhang, Effect of zinc immersion pretreatment on the electro-deposition of Ni onto AZ91D magnesium alloy, Surf. Coatings Technol. 205 (2010) 2160–2166.

[74] C.A. Huang, T.H. Wang, T. Weirich, V. Neubert, Electrodeposition of a protective copper/nickel deposit on the magnesium alloy (AZ31), Corros. Sci. 50 (2008) 1385–1390.

[75] S. Zhang, F. Cao, L. Chang, J. Zheng, Z. Zhang, J. Zhang, et al., Electrodeposition of high corrosion resistance Cu/Ni–P coating on AZ91D magnesium alloy, Appl. Surf. Sci. 257 (2011) 9213–9220.

[76] Q. Liu, K. Liu, Q. Han, G. Tu, Electrodeposition of Al on AZ31 magnesium alloy in TMPAC-AlCl3 ionic liquids, Trans. Nonferrous Met. Soc. China. 21 (2011) 2104–2110.

[77] Y.F. Jiang, L.F. Liu, C.Q. Zhai, Y.P. Zhu, W.J. Ding, Corrosion behavior of pulse-plated Zn–Ni alloy coatings on AZ91 magnesium alloy in alkaline solutions, Thin Solid Films. 484 (2005) 232–237.

[78] Y. Jiang, C. Zhai, L. Liu, Y. Zhu, W. Ding, Zn-Ni alloy coatings pulse-plated on magnesium alloy, Surf. Coatings Technol. 191 (2005) 393–399.

[79] J. Zhang, C. Yan, F. Wang, Electrodeposition of Al–Mn alloy on AZ31B magnesium alloy in molten salts, Appl. Surf. Sci. 255 (2009) 4926–4932.

[80] T. Jiang, M.J.J. Chollier Brym, G. Dubé, A. Lasia, G.M.M. Brisard, Electrodeposition of aluminium from ionic liquids: Part I—electrodeposition and surface morphology of aluminium from aluminium chloride (AlCl3)–1-ethyl-3-methylimidazolium chloride ([EMIm]Cl) ionic liquids, Surf. Coatings Technol. 201 (2006) 1–9.

[81] T. Jiang, M.J. Chollier Brym, G. Dubé, A. Lasia, G.M. Brisard, Electrodeposition of aluminium from ionic liquids: Part II - studies on the electrodeposition of aluminum from aluminum chloride (AlCl3) - trimethylphenylammonium chloride (TMPAC) ionic liquids, Surf. Coatings Technol. 201 (2006) 10–18.

[82] P. Huang, J.A. Latham, D.R. MacFarlane, P.C. Howlett, M. Forsyth, A review of ionic liquid surface film formation on Mg and its alloys for improved corrosion performance, Electrochim. Acta. (2013).

[83] J.K. Chang, S.Y. Chen, W.T. Tsai, M.J. Deng, I.W. Sun, Electrodeposition of aluminum on magnesium alloy in aluminum chloride (AlCl3)–1-ethyl-3-methylimidazolium chloride (EMIC) ionic liquid and its corrosion behavior, Electrochem. Commun. 9 (2007) 1602–1606.

[84] S. Khireche, D. Boughrara, A. Kadri, L. Hamadou, N. Benbrahim, Corrosion mechanism of Al, Al–Zn and Al–Zn–Sn alloys in 3wt.% NaCl solution, Corros. Sci. 87 (2014) 504–516.

[85] H. Huo, Y. Li, F. Wang, Corrosion of AZ91D magnesium alloy with a chemical conversion coating and electroless nickel layer, Corros. Sci. 46 (2004) 1467–1477.

[86] S.Q. Jia, S.S. Jia, J. Yao, Electroless nickel-plating on die cast magnesium alloy AZ91D, Trans. Nonferrous Met. Soc. China. 17 (2007) s866–s870.

[87] W.J. Cheong, B.L. Luan, D.W. Shoesmith, Protective coating on Mg AZ91D alloy – The effect of electroless nickel (EN) bath stabilizers on corrosion behaviour of Ni–P deposit, Corros. Sci. 49 (2007) 1777–1798.

[88] N. El Mahallawy, A. Bakkar, M. Shoeib, H. Palkowski, V. Neubert, Electroless Ni–P coating of different magnesium alloys, Surf. Coatings Technol. 202 (2008) 5151–5157.

[89] W.X. Zhang, Z.H. Jiang, G.Y. Li, Q. Jiang, J.S. Lian, Electroless Ni-P/Ni-B duplex coatings for improving the hardness and the corrosion resistance of AZ91D magnesium alloy, Appl. Surf. Sci. 254 (2008) 4949–4955.

[90] A. Araghi, M.H. Paydar, Electroless deposition of Ni–P–B4C composite coating on AZ91D magnesium alloy and investigation on its wear and corrosion resistance, Mater. Des. 31 (2010) 3095–3099.

[91] R. Ambat, W. Zhou, Electroless nickel-plating on AZ91D magnesium alloy: effect of substrate microstructure and plating parameters, Surf. Coatings Technol. 179 (2004) 124–134.

[92] A. Rudd, C.B. Breslin, F. Mansfeld, The corrosion protection afforded by rare earth conversion coatings applied to magnesium, Corros. Sci. 42 (2000) 275–288.

[93] C. Blawert, V. Heitmann, W. Dietzel, H. Nykyforchyn, M. Klapkiv, Influence of electrolyte on corrosion properties of plasma electrolytic conversion coated magnesium alloys, Surf. Coatings Technol. 201 (2007) 8709–8714.

[94] H. Ardelean, I. Frateur, P. Marcus, Corrosion protection of magnesium alloys by cerium, zirconium and niobium-based conversion coatings, Corros. Sci. 50 (2008) 1907–1918.

[95] X. Liu, T. Zhang, Y. Shao, G. Meng, F. Wang, In-situ study of the formation process of stannate conversion coatings on AZ91D magnesium alloy using electrochemical noise, Corros. Sci. 52 (2010) 892–900.

[96] A. Frignani, V. Grassi, F. Zucchi, F. Zanotto, Mono-carboxylate conversion coatings for AZ31 Mg alloy protection, Mater. Corros. (2010) NA–NA.

[97] E. Rocca, C. Juers, J. Steinmetz, Corrosion behaviour of chemical conversion treatments on as-cast Mg–Al alloys: Electrochemical and non-electrochemical methods, Corros. Sci. 52 (2010) 2172–2178.

[98] L. Jianrui, G. Yina, H. Weidong, Study on the corrosion resistance of phytic acid conversion coating for magnesium alloys, Surf. Coatings Technol. 201 (2006) 1536–1541.

[99] A.R. Shashikala, R. Umarani, Chemical conversion coating on magnesium alloys - A comparitive study, Int. J. Electrochem. 3 (2008) 993 – 1004.

[100] B.L. Yu, X.L. Pan, J.Y. Uan, Enhancement of corrosion resistance of Mg-9 wt.% Al-1 wt.% Zn alloy by a calcite (CaCO3) conversion hard coating, Corros. Sci. 52 (2010) 1874–1878.

[101] A.S. Hamdy, M. Farahat, Chrome-free zirconia-based protective coatings for magnesium alloys, Surf. Coatings Technol. 204 (2010) 2834–2840.

[102] J. Chen, Y. Song, D. Shan, E. Han, In situ growth of Mg–Al hydrotalcite conversion film on AZ31 magnesium alloy, Corros. Sci. 53 (2011) 3281–3288.

[103] C. Blawert, W. Dietzel, E. Ghali, G. Song, Anodizing Treatments for Magnesium Alloys and Their Effect on Corrosion Resistance in Various Environments, Adv. Eng. Mater. 8 (2006) 511–533.

[104] K. Murakami, M. Hino, M. Hiramatsu, K. Nakai, S. Kobayashi, A. Saijo, et al., Corrosion protection of AZ91D magnesium alloy by anodization using phosphate electrolyte, Mater. Trans. 48 (2007) 3101–3108.

[105] Z. Shi, G. Song, A. Atrens, Corrosion resistance of anodised single-phase Mg alloys, Surf. Coatings Technol. 201 (2006) 492–503.

[106] M. Hino, K. Murakami, A. Saijo, T. Kanadani, Effects of alloying elements on characteristics of anodic oxidized coatings in various Mg-Al-Zn series alloys, Mater. Trans. 49 (2008) 924–930.

[107] H. Ardelean, I. Frateur, S. Zanna, A. Atrens, P. Marcus, Corrosion protection of AZ91 magnesium alloy by anodizing in niobium and zirconium-containing electrolytes, Corros. Sci. 51 (2009) 3030–3038.

[108] A. Manavbasi, S. Nibhanupudi, Improvement of Corrosion Resistance of Magnesium by Anodizing in Alkaline Electrolytes, 2011.

[109] R. Arrabal, E. Matykina, F. Viejo, P. Skeldon, G. Thompson, Corrosion resistance of WE43 and AZ91D magnesium alloys with phosphate PEO coatings, Corros. Sci. 50 (2008) 1744–1752.

[110] E. Cakmak, K.C. Tekin, U. Malayoglu, S. Shrestha, The effect of substrate composition on the electrochemical and mechanical properties of PEO coatings on Mg alloys, Surf. Coatings Technol. 204 (2010) 1305–1313.

[111] Y. Liu, F.W. Yang, Z.L. Wei, Z. Zhang, Anodizing of AZ91D magnesium alloy using environmental friendly alkaline borate-biphthalate electrolyte, Trans. Nonferrous Met. Soc. China. 22 (2012) 1778–1785.

[112] J. Liang, P.B. Srinivasan, C. Blawert, W. Dietzel, Influence of pH on the deterioration of plasma electrolytic oxidation coated AM50 magnesium alloy in NaCl solutions, Corros. Sci. 52 (2010) 540–547.

[113] R.F. Zhang, Film formation in the second step of micro-arc oxidation on magnesium alloys, Corros. Sci. 52 (2010) 1285–1290.

[114] L. Zhao, C. Cui, Q. Wang, S. Bu, Growth characteristics and corrosion resistance of micro-arc oxidation coating on pure magnesium for biomedical applications, Corros. Sci. 52 (2010) 2228–2234.

[115] K. Rie, J. Wo, Plasma-CVD of TiCN and ZrCN films on light metals, Surf. Coatings Technol. 112 (1999) 226–229.

[116] H. Hoche, H. Scheerer, D. Probst, E. Broszeit, C. Berger, Development of a plasma surface treatment for magnesium alloys to ensure sufficient wear and corrosion resistance, Surf. Coatings Technol. 174 (2003) 1018–1023.

[117] M. Carboneras, M.D. López, P. Rodrigo, M. Campo, B. Torres, E. Otero, et al., Corrosion behaviour of thermally sprayed Al and Al/SiCp composite coatings on ZE41 magnesium alloy in chloride medium, Corros. Sci. 52 (2010) 761–768.

[118] Y. Tao, T. Xiong, C. Sun, L. Kong, X. Cui, T. Li, et al., Microstructure and corrosion performance of a cold sprayed aluminium coating on AZ91D magnesium alloy, Corros. Sci. 52 (2010) 3191–3197.

[119] P. Li, M.K. Lei, X.P. Zhu, X.G. Han, C. Liu, J.P. Xin, Wear mechanism of AZ31 magnesium alloy irradiated by high-intensity pulsed ion beam, Surf. Coatings Technol. 204 (2010) 2152–2158.

[120] K. Spencer, M.X. Zhang, The emergence of cold spray as a tool for surface modification, Key Eng. Mater. 384 (2008) 61–74.

[121] A. Pardo, P. Casajús, M. Mohedano, A.E. Coy, F. Viejo, B. Torres, et al., Corrosion protection of Mg/Al alloys by thermal sprayed aluminium coatings, Appl. Surf. Sci. 255 (2009) 6968–6977.

[122] A. Pardo, M.C. Merino, M. Mohedano, P. Casajús, A.E. Coy, R. Arrabal, Corrosion behaviour of Mg/Al alloys with composite coatings, Surf. Coatings Technol. 203 (2009) 1252–1263.

[123] S. Faraji, A.A. Rahim, N. Mohamed, C.S. Sipaut, B. Raja, Corrosion resistance of electroless Cu-P and Cu-P-SiC composite coatings in 3.5% NaCl, Arab. J. Chem. 6 (2013) 379–388.

[124] Z. Zhang, Y. Ding, X. Wang, G. Yang, W. Shen, H. Han, Improvement of surface corrosion resistance for magnesium alloy by combining thermal spray and cast-infiltration, Trans. Nonferrous Met. Soc. China. 20 (2010) 992–996.

[125] X.B. Tian, C.B. Wei, S.Q. Yang, K.Y. Fu, K. Chu, Corrosion resistance improvement of magnesium alloy using nitrogen plasma ion implantation, Surf. Coatings Technol. 198 (2005) 454–458.

[126] B.J. Zheng, X.M. Chen, J.S. Lian, Microstructure and wear property of laser cladding Al+SiC powders on AZ91D magnesium alloy, Opt. Lasers Eng. 48 (2010) 526–532.

[127] G. Abbas, Z. Liu, P. Skeldon, Corrosion behaviour of laser-melted magnesium alloys, Appl. Surf. Sci. 247 (2005) 347–353.

[128] M. Qian, D. Li, S.B. Liu, S.L. Gong, Corrosion performance of laser-remelted Al–Si coating on magnesium alloy AZ91D, Corros. Sci. 52 (2010) 3554–3560.

[129] T.F. Conceicao, N. Scharnagl, C. Blawert, W. Dietzel, K.U. Kainer, Corrosion protection of magnesium alloy AZ31 sheets by spin coating process with poly(ether imide) [PEI], Corros. Sci. 52 (2010) 2066–2079.

[130] T.F. Conceicao, N. Scharnagl, C. Blawert, W. Dietzel, K.U.U. Kainer, On the degradation mechanism of corrosion protective poly(ether imide) coatings on magnesium AZ31 alloy, Corros. Sci. 52 (2010) 3155–3157.

[131] G. Song, M. Liu, The effect of surface pretreatment on the corrosion performance of electroless E-coating coated AZ31, Corros. Sci. 62 (2012) 61–72.

[132] G. Song, M. Liu, The effect of Mg alloy substrate on “electroless” E-coating performance, Corros. Sci. 53 (2011) 3500–3508.

[133] S. Lamaka, M. Montemor, A. Galio, M. Zheludkevich, C. Trindade, L. Dick, et al., Novel hybrid sol–gel coatings for corrosion protection of AZ31B magnesium alloy, Electrochim. Acta. 53 (2008) 4773–4783.

[134] C. Brubaker, Z.K. Liu, Diffusion couple study of the Mg-Al system, in: Magnes. Technol. 2004, 2004: pp. 229–234.

[135] J. Wang, Y. Li, P. Liu, H. Geng, Microstructure and XRD analysis in the interface zone of Mg/Al diffusion bonding, J. Mater. Process. Technol. 205 (2008) 146–150.

[136] J. Wang, Y. Li, H. Wangun, Interface microstructure and diffusion kinetics in diffusion bonded Mg/Al joint, React. Kinet. Catal. Lett. 95 (2008) 71–79.

[137] G. Mahendran, V. Balasubramanian, T. Senthilvelan, Developing diffusion bonding windows for joining AZ31B magnesium–AA2024 aluminium alloys, Mater. Des. 30 (2009) 1240–1244.

[138] G. Mahendran, S. Babu, V. Balasubramanian, Analyzing the effect of diffusion bonding process parameters on bond characteristics of Mg-Al dissimilar joints, J. Mater. Eng. Perform. 19 (2010) 657–665.

[139] K. Spencer, M. Zhang, The use of kinetic metallization to form intermetallic reinforced composite coatings by post-spray heat treatment, Surf. Coatings Technol. 203 (2009) 3019–3025.

[140] R.W. Murray, J.E. Hills, Power coatings on high purity die casting magnesium for appearance and protection, in: NADCA Congr. Expo., Detroit, 1991: pp. 5–11.

[141] D.E. Newbury, N.W.M. Ritchie, Is scanning electron microscopy/energy dispersive X-ray spectrometry (SEM/EDS) quantitative?, Scanning. 35 (2013) 141–168.

[142] SI 1280 Technical Manual, Solartron. (2014).

[143] GalvoGill 12 Data Sheet, ACM Instruments. (2014).

[144] Gill AC Data Sheet, ACM Instruments. (2014).

[145] M. Craig, Manufacturing of novel intermetallic bond coats from the electroplating of ionic liquids, Cranfield University, 2010.

[146] K.N. Kulkarni, A.A. Luo, Interdiffusion and phase growth kinetics in magnesium-aluminum binary system, J. Phase Equilibria Diffus. 34 (2013) 104–115.

[147] H. Okamoto, Al-Mg (Aluminum-Magnesium), J. Phase Equilibria. 19 (1998) 598.

[148] A.G. Beer, M.R. Barnett, Microstructure evolution in hot worked and annealed magnesium alloy AZ31, Mater. Sci. Eng. A. 485 (2008) 318–324.

[149] S.H. Kim, B.S. You, C.D. Yim, Y.M. Seo, Texture and microstructure changes in asymmetrically hot rolled AZ31 magnesium alloy sheets, Mater. Lett. 59 (2005) 3876–3880.

[150] T.C. Chang, J.Y. Wang, C.. M. O, S. Lee, Grain refining of magnesium alloy AZ31 by rolling, J. Mater. Process. Technol. 140 (2003) 588–591.

[151] A. Jäger, P. Lukáč, V. Gärtnerová, J. Haloda, M. Dopita, Influence of annealing on the microstructure of commercial Mg alloy AZ31 after mechanical forming, Mater. Sci. Eng. A. 432 (2006) 20–25.

[152] M. Kohzu, K. Kii, Y. Nagata, H. Nishio, K. Higashi, H. Inoue, Texture randomization of AZ31 magnesium alloy sheets for improving the cold formability by a combination of rolling and high-temperature annealing, Mater. Trans. 51 (2010) 749–755.

[153] B661-06: Standard practice for heat treatment of magnesium alloys, ASTM Int. (2006).

[154] H.S. Kim, W.J. Kim, Enhanced corrosion resistance of ultrafine-grained AZ61 alloy containing very fine particles of Mg17Al12 phase, Corros. Sci. 75 (2013) 228–238.

[155] M. Zhang, P.M. Kelly, Crystallography of Mg17Al12 precipitates in AZ91D alloy, Scr. Mater. 48 (2003) 647–652.

[156] L. Čížek, M. Greger, L. Pawlica, L.A. Dobrzański, T. Tański, Study of selected properties of magnesium alloy AZ91 after heat treatment and forming, J. Mater. Process. Technol. 157-158 (2004) 466–471.

[157] G.L. Makar, J. Kruger, Corrosion of magnesium, Int. Mater. Rev. 38 (1993) 138–153.

[158] E. Ghali, W. Dietzel, K.U. Kainer, General and localized corrosion of magnesium alloys: A critical review, J. Mater. Eng. Perform. 13 (2004) 7–23.

[159] G.S. Frankel, A. Samaniego, N. Birbilis, Evolution of hydrogen at dissolving magnesium surfaces, Corros. Sci. 70 (2013) 104–111.

[160] U.R. Evans, An Introduction to Metallic Corrosion, 1st ed., Edward Arnold & Co., 1948.

[161] M.G. Fontana, Corrosion Engineering, 3rd ed., McGraw-Hill International Editions, 1987.

[162] J.C. Scully, The Fundamentals of Corrosion, 3rd ed., Pergamon Press, 1990.

[163] R. Baboian, ed., NACE Corrosion Engineer's Reference Book, 3rd ed., National Association of Corrosion Engineers, 2002.

[164] A.M. Kauffman, Understanding electrochemcial cells, Solartron. (1997).

[165] G.W. Walter, A review of impedance plot methods used for corrosion performance analysis of painted metals, Corros. Sci. 26 (1986) 681–703.

[166] A. Pardo, S. Feliu, M.C. Merino, R. Arrabal, E. Matykina, Electrochemical estimation of the corrosion rate of magnesium/aluminium alloys, Int. J. Corros. 2010 (2010) 1–8.

[167] S. Feliu Jr, J.C. Galván, A. Pardo, M.C. Merino, R. Arrabal, Native air-formed oxide film and its effect on magnesium alloys corrosion, Open Corros. J. 3 (2010) 80–91.

[168] G. Song, ed., Corrosion of magnesium alloys, Woodhead Publishing, 2011.

[169] K. Jüttner, W.J. Lorenz, Impedance Spectroscopy (EIS)of Corrosion Processes on Inhomogeneous Surfaces, Mater. Sci. Forum. 44-45 (1991) 191–204.

[170] X.K. Zhu, B.N. Leis, Evaluation of burst pressure prediction models for line pipes, Int. J. Press. Vessel. Pip. 89 (2012) 85–97.

[171] T. Ross, B. Hitchen, Some effects of electrolyte motion during corrosion, Corros. Sci. I (1961) 65–75.

[172] M. Pourbaix, Atlas of Electrochemical Equilibria in Aqueous Solutions, 2nd Ed., National Association of Corrosion Engineers, 1974.

[173] B.A. Shaw, Corrosion resistance of magnesium alloys, ASM Handb. Volume 13A (2003).

[174] T. Ishizaki, S. Chiba, K. Watanabe, H. Suzuki, Corrosion resistance of Mg–Al layered double hydroxide container-containing magnesium hydroxide films

formed directly on magnesium alloy by chemical-free steam coating, J. Mater. Chem. A. 1 (2013) 8968.

[175] T. Barnes, I.R. Pashby, Joining techniques for aluminium spaceframes used in automobiles part II — adhesive bonding and mechanical fasteners, J. Mater. Process. Technol. 99 (2000) 72–79.

[176] G. Song, B. Johannesson, S. Hapugoda, D. St John, Galvanic corrosion of magnesium alloy AZ91D in contact with an aluminium alloy, steel and zinc, Corros. Sci. 46 (2004) 955–977.